LOCALISATION OF ATTENUATION EQUATIONS BASED ON STRONG GROUND MOTION DATA FROM DENSE URBAN NETWORKS

by

Fatma Sevil Malcıoğlu

B.S., Geophysical Engineering, İstanbul Technical University, 2007

B.S., Civil Engineering, İstanbul Technical University, 2009

M.S., Earthquake Engineering, İstanbul Technical University, 2011

Submitted to the Kandilli Observatory and Earthquake Research Institute
in partial fulfillment of the requirements for the degree of
Doctor of Philosophy

Graduate Program in Earthquake Engineering

Boğaziçi University

2023

LOCALISATION OF ATTENUATION EQUATIONS BASED ON STRONG GROUND MOTION DATA FROM DENSE URBAN NETWORKS

APPROVED BY:

Assoc. Prof. Ufuk Hancılar (Thesis Supervisor)	.....
Prof. Erdal Şafak (Thesis Co-supervisor)	.....
Prof. Eser Çaktı	.....
Assoc. Prof. A. Özgün Konca	.....
Prof. Ufuk Yazgan	.....
Assist. Prof. Ahu Mutlu	.....

DATE OF APPROVAL: 20.12.2023

ACKNOWLEDGEMENTS

I would like to express my deepest gratitude and heartfelt appreciation to my co-advisor Professor Erdal Şafak. This thesis was launched under his excellent supervision and continued with his extraordinary foresight. I am also really grateful for lots of beneficial comments and feedback from my academic advisor Associate Professor Ufuk Hancılar. I would like to convey my gratitude to the progress and defense committee, Professor Eser Çaktı, Assistant Professor Karin Şesetyan, Professor Ufuk Yazgan, Associate Professor Özgün Konca and Assistant Professor Ahu Mutlu for their insightful comments. During my PhD journey, I was also honoured to be a volunteer member of the EEFIT missions, led by my esteemed colleague and beloved friend Associate Professor Yasemin Didem Aktaş. I am particularly indebted for her invaluable assistance and outstanding inspiration in both the academic and personal facets. I also would like to thank my all friends in the KOERI Earthquake Engineering department for their unremarkable companionship. However, I would like to express my heartfelt gratitude to three of them with whom we experienced many academic firsts in particular. I would like to thank my close friend Kökcan Dönmez, who is always eager to assist with any academic and personal trouble, who never left me without coffee, and who was always there to motivate me with his heartfelt companionship. Also, I would like to thank my dear friend Mustafa Karakaya, who has stood by me in every academic concern, and this academic experience would not have been as enjoyable without his daily humorous messages. I also would like to thank my close friend, Tuğçe Tetik, for her unremarkable friendship on this journey. She was my indispensable companion in my morning coffees, and with whom I attempted to discover both the pleasure of life and academic discipline together. Additionally, I should express my thanks to the nature of Kandilli Campus for providing us with a peaceful medium and to all furry friends, especially to our sweet dog Fındık, whose smiling face always cheers me up, and Scarlet for making me one of the people she can trust again. Last but not least, I would like to express my appreciation to my beloved mother, Semra Zorluer, for her everlasting love, patience, and devotion during my whole scholastic journey.

ABSTRACT

LOCALISATION OF ATTENUATION EQUATIONS BASED ON STRONG GROUND MOTION DATA FROM DENSE URBAN NETWORKS

The regional dependency of ground motions underlines the necessity of adopting a more localized approach in the estimation of ground motion parameters (GMPs). This thesis kicks off with a consistency assessment of the five most suitable regional or global ground motion prediction equations (GMPEs) for the interested area and our local database including 6,534 individual horizontal-component ground motions recorded by the İstanbul Earthquake Rapid Response and Early Warning System (IERREWS) network during 78 small-to-moderate earthquakes. The examination uncovers a systematic overestimation tendency in GMPEs. Using the same database, an analysis is conducted to ascertain whether there are any regional azimuth-dependent effects on ground motions. Due to the vagueness of azimuthal effects, the ground motion recording axes are converted to their principal axes, indirectly introducing the azimuthal influence into the analyses. This thesis suggests a station-specific methodology to refine GMP estimations by isolating regional variations. Evaluation of regression outcomes, distance scalings, and residuals guide the selection of the most appropriate functional forms for the empirical equation. Comparisons of the spatial distribution of peak ground acceleration (PGA) for hypothetical and actual earthquakes serve as the basis for the evaluation of the result consistency. Local variations between GMPEs' estimates and station-specific approximations provide insight into the impact of regional effects on ground motions. The assertion is substantiated by the finding that PGAs calculated from actual earthquake records demonstrate a closer match with station-specific methodology's predictions, especially in regions with observed local differences.

ÖZET

YOĞUN KENTSEL AĞLARDA KAYDEDİLEN KUVVETLİ YER HAREKETİ VERİLERİNE GÖRE AZALIM İLİŞKİLERİNİN YERELLEŞTİRİLMESİ

Yer hareketlerinin bölgesel bağımlılığı, yer hareketi parametrelerinin (GMP'lerin) tahmininde özellikle yerel bir yaklaşımın benimsenmesinin gerekliliğini ortaya koymaktadır. Bu tez, 78 adet küçük ila orta büyüklükteki depremler sırasında İstanbul Deprem Acil Müdahale ve Erken Uyarı Sistemi (IERREWS) ağı tarafından kaydedilen 6,534 tekil yatay bileşenli yer hareketini içeren yerel veritabanımız ve incelenen alan için en uygun beş adet bölgesel ya da küresel yer hareketi tahmin denklemlerinin (GMPE'lerin) tutarlılık değerlendirmesiyle başlar. GMPE'lerde sistematik bir aşırı tahmin eğilimi ortaya çıkmaktadır. Aynı veri tabanı, bölgede yer hareketleri üzerinde azimuta bağlı herhangi bir etkinin olup olmadığını incelemek için de kullanılmıştır. Bölgesel yer hareketlerindeki azimut kaynaklı etkilerin belirsizliği nedeniyle, bu etkiler, yer hareketi kayıt ekseni, asal eksenlerine döndürülerek dolaylı olarak analizlere dahil edilmiştir. GMP'lerin tahminlerini geliştirmek için bölgesel farklılıkları izole ederek istasyon bazlı bir metodoloji bu tez kapsamında önerilmektedir. Ampirik denklemin fonksiyonel formları, regresyon sonuçlarının, mesafeye bağlı değişimin ve residülellerin değerlendirilmesi sonucunda seçilmiştir. Varsayımsal ve gerçek depremler için pik yer hareketi ivmesinin (PGA) mekansal dağılımının incelenmesi, sonuçların tutarlılığının değerlendirilmesinin temelini oluşturur. GMPE ile istasyon bazlı yaklamışımın tahminleri arasındaki lokal farklar, bölgesel etkilerin yer hareketleri üzerindeki etkisinin bir göstergesi olabilir. Bu iddia, gerçek deprem kayıtlarından hesaplanan PGA'ların, özellikle yerel farklılıkların gözlemlendiği bölgelerde istasyon bazlı metodoloji tahminleriyle daha yakın bir eşleşme göstermesi ile desteklenmektedir.

TABLE OF CONTENTS

ACKNOWLEDGEMENTS iii
ABSTRACT iv
ÖZET v
LIST OF FIGURES viii
LIST OF TABLES xxiii
LIST OF SYMBOLS xxiv
LIST OF ACRONYMS/ABBREVIATIONS xxvi
1. INTRODUCTION 1
1.1. Literature Review on Seismic Hazard and Risk Studies for İstanbul . . 1
1.2. Literature Review on Ground Motion Prediction Studies 4
1.3. Objective and Organisation of the Thesis 9
2. COMPILATION OF STRONG MOTION DATA 12
2.1. Overview of IERREWS Network 12
2.2. Compilation of Initial Database 13
2.3. Data Selection Criteria 14
2.4. Strong Motion Data Processing 16
2.5. Characteristics of Final Database 24
3. CONSISTENCY EVALUATION OF GMPEs WITH
STRONG MOTION RECORDS 29
3.1. Main Characteristics of the Selected GMPEs 29
3.2. Consistency Evaluation via Comparison of Distance Scalings 34
3.3. Consistency Evaluation via Residual Analysis 47
3.3.1. Total Residuals with Distance 48
3.3.2. Between-event Residuals with Magnitude 52
3.3.3. Within-event Residuals with Distance 57
3.3.4. Within-event Residuals with Soil Condition Parameter 61
3.3.5. Within-event Residuals with Azimuth 65
4. INVESTIGATION OF AZIMUTHAL EFFECTS 70
4.1. Variation of GMPs with Azimuth 70

4.2. Conversion of Components to Principal Directions 79
5. STATION-SPECIFIC METHODOLOGY 82
5.1. Concept of Station-specific Methodology 82
5.2. Selection of Functional Form 84
5.3. Consistency Evaluation of Station-specific Empirical Equations 103
5.4. Sensitivity Analysis for Magnitude and Soil Condition Parameter . . . 110
5.4.1. Sensitivity of Station-specific Coefficients against Magnitude . . 110
5.4.2. Sensitivity of Station-specific Coefficients against Soil Condition Parameter 117
6. SPATIAL DISTRIBUTION OF ESTIMATIONS VIA STATION-SPECIFIC METHODOLOGY FOR ISTANBUL 120
6.1. 2-D Delaunay Triangulation Grid Meshing 120
6.2. Determination of Cell-based Coefficients 121
6.3. Evaluation of Prediction Performance of the Proposed Methodology . . 131
6.3.1. Comparative Evaluation for Hypothetical Earthquakes 131
6.3.2. Comparative Evaluation for the Largest Actual Event in the Database 134
6.3.3. Comparative Evaluation for an Actual Event without in the Database 140
7. CONCLUSION 147
REFERENCES 151
APPENDIX A: COEFFICIENTS FOR M_L-BASED REGRESSIONS 175
APPENDIX B: RESULTS FOR FUNCTIONAL FORM (5.4) 181
APPENDIX C: RESULTS FOR FUNCTIONAL FORM (5.8) (f = 5.8) 187
APPENDIX D: RESULTS FOR FUNCTIONAL FORM (5.8) (HYBRID) . . . 193

LIST OF FIGURES

Figure 2.1. Spatial Distribution of V_{S30} for İstanbul [117]. 14

Figure 2.2. Database Criteria Scheme. 16

Figure 2.3. Unfiltered Recording of Kaleköy Earthquake (M_L5.3) from TTEML Station. 18

Figure 2.4. Variation of the Slope of Displacements for Different Selected High-pass Filter Frequencies (f_{hp}). 20

Figure 2.5. Graphical User Interface (GUI) for the Strong Ground Motion Processing. 20

Figure 2.6. Strong Ground Motion Time History Processing Scheme (f_{hp} and f_{lp} refer to high-pass and low-pass filter frequency, respectively). . 23

Figure 2.7. Spatial Distribution of Earthquakes (2012-2022) around Marmara Region. 24

Figure 2.8. Histograms of Focal Depth, h of the Earthquakes in the Database. 25

Figure 2.9. Spatial Configuration of the IERREWS Network Stations for (top) European Side of İstanbul, (bottom) Asian Side of İstanbul. 26

Figure 2.10. Histograms of V_{S30} Values at the Recording Sites. 27

Figure 2.11. Distribution of Local Magnitudes (M_L) and Epicentral Distances (R_{EPI}). 28

Figure 3.1. Comparison of GMPEs' Median PGA Estimates with Prediction Curves of this Thesis for V_{S30} = 527 m/s. (Marker colours denote distinct events). 37

Figure 3.2. Comparison of GMPEs' Median PGV Estimates with Prediction Curves of this Thesis for V_{S30} = 527 m/s. (Marker colours denote distinct events). 38

Figure 3.3. Comparison of GMPEs' Median SAs (T=0.4 s, ξ=5%) with Prediction Curves of this Thesis for V_{S30} = 527 m/s. (Marker colours denote distinct events). 39

Figure 3.4. Comparison of GMPEs' Median SAs (T=0.6 s, ξ=5%) with Prediction Curves of this Thesis for V_{S30} = 527 m/s. (Marker colours denote distinct events). 40

Figure 3.5. Comparison of GMPEs' Median SAs (T=1.0 s, ξ=5%) with Prediction Curves of this Thesis for V_{S30} = 527 m/s. (Marker colours denote distinct events). 41

Figure 3.6. Comparison of GMPEs' Median SAs (T=2.0 s, ξ=5%) with Prediction Curves of this Thesis for V_{S30} = 527 m/s. (Marker colours denote distinct events). 42

Figure 3.7. Comparison of GMPE's Median AI Estimates with Prediction Curves of this Thesis for V_{S30} = 527 m/s. (Marker colours denote distinct events). 43

Figure 3.8. Comparison of GMPE's Median CAV Estimates with Prediction Curves of this Thesis for V_{S30} = 527 m/s. (Marker colours denote distinct events). 44

Figure 3.9. Variation of the Total Residuals of PGA and PGV with R_{EPI} for the Selected GMPEs (Zero residuals are shown by the lines in red. Error bars stand for group means with 16^{th} and 84^{th} percentiles). . 49

Figure 3.10. Variation of the Total Residuals of SA (T=0.4 s) and SA (T=0.6 s) with R_{EPI} for the Selected GMPEs (Zero residuals are shown by the lines in red. Error bars stand for group means with 16^{th} and 84^{th} percentiles). 50

Figure 3.11. Variation of the Total Residuals of SA (T=1.0 s) and SA (T=2.0 s) with R_{EPI} for the Selected GMPEs (Zero residuals are shown by the lines in red. Error bars stand for group means with 16^{th} and 84^{th} percentiles). 51

Figure 3.12. Variation of the Total Residuals of AI and CAV with R_{EPI} for the Selected GMPEs (Zero residuals are shown by the lines in red. Error bars stand for group means with 16^{th} and 84^{th} percentiles). . 52

Figure 3.13. Variation of the Between-event Residuals of PGA and PGV with M_L for the Selected GMPEs. (Zero residuals are shown by the lines in red. Error bars stand for group means with 16^{th} and 84^{th} percentiles). 53

Figure 3.14. Variation of the Between-event Residuals of SA (T=0.4 s) and SA (T=0.6 s) with M_L for the Selected GMPEs. (Zero residuals are shown by the lines in red. Error bars stand for group means with 16^{th} and 84^{th} percentiles). 54

Figure 3.15. Variation of the Between-event Residuals of SA (T=1.0 s) and SA (T=2.0 s) with M_L for the Selected GMPEs. (Zero residuals are shown by the lines in red. Error bars stand for group means with 16^{th} and 84^{th} percentiles). 55

Figure 3.16. Variation of the Between-event Residuals of AI and CAV with M_L for the Selected GMPEs. (Zero residuals are shown by the lines in red. Error bars stand for group means with 16^{th} and 84^{th} percentiles). 56

Figure 3.17. Variation of the Within-event Residuals of PGA and PGV with R_{EPI} for the Selected GMPEs. (Zero residuals are shown by the lines in red. Error bars stand for group means with 16^{th} and 84^{th} percentiles). 58

Figure 3.18. Variation of the Within-event Residuals of SA (T=0.4 s) and SA (T=0.6 s) with R_{EPI} for the Selected GMPEs. (Zero residuals are shown by the lines in red. Error bars stand for group means with 16^{th} and 84^{th} percentiles). 59

Figure 3.19. Variation of the Within-event Residuals of SA (T=1.0 s) and SA (T=2.0 s) with R_{EPI} for the Selected GMPEs. (Zero residuals are shown by the lines in red. Error bars stand for group means with 16^{th} and 84^{th} percentiles). 60

Figure 3.20. Variation of the Within-event Residuals of AI and CAV with R_{EPI} for the Selected GMPEs. (Zero residuals are shown by the lines in red. Error bars stand for group means with 16^{th} and 84^{th} percentiles). 61

Figure 3.21. Variation of the Within-event Residuals of PGA and PGV with V_{S30} for the Selected GMPEs. (Zero residuals are shown by the lines in red. Error bars stand for group means with 16^{th} and 84^{th} percentiles). 62

Figure 3.22. Variation of the Within-event Residuals of SA (T=0.4 s) and SA (T=0.6 s) with V_{S30} for the Selected GMPEs. (Zero residuals are shown by the lines in red. Error bars stand for group means with 16^{th} and 84^{th} percentiles). 63

Figure 3.23. Variation of the Within-event Residuals of SA (T=1.0 s) and SA (T=2.0 s) with V_{S30} for the Selected GMPEs. (Zero residuals are shown by the lines in red. Error bars stand for group means with 16^{th} and 84^{th} percentiles). 64

Figure 3.24. Variation of the Within-event Residuals of AI and CAV with V_{S30} for the Selected GMPEs. (Zero residuals are shown by the lines in red. Error bars stand for group means with 16^{th} and 84^{th} percentiles). 65

Figure 3.25. Variation of the Within-event Residuals of PGA and PGV with Azimuth Angle for the Selected GMPEs (Zero residuals are shown by the lines in red. Error bars stand for group means with 16^{th} and 84^{th} percentiles). 66

Figure 3.26. Variation of the Within-event Residuals of SA (T=0.4 s) and SA (T=0.6 s) with Azimuth Angle for the Selected GMPEs (Zero residuals are shown by the lines in red. Error bars stand for group means with 16^{th} and 84^{th} percentiles). 67

Figure 3.27. Variation of the Within-event Residuals of SA (T=1.0 s) and SA (T=2.0 s) with Azimuth Angle for the Selected GMPEs (Zero residuals are shown by the lines in red. Error bars stand for group means with 16^{th} and 84^{th} percentiles). 68

Figure 3.28. Variation of the Within-event Residuals of AI and CAV with Azimuth Angle for the Selected GMPEs (Zero residuals are shown by the lines in red. Error bars stand for group means with 16^{th} and 84^{th} percentiles). 69

Figure 4.1. Variation of the Frequency of Recordings with Azimuth Angle for EQ1-EQ28 (N refers to the total number of recordings for each event). 71

Figure 4.2. Variation of the Frequency of Recordings with Azimuth Angle for EQ29-EQ56 (N refers to the total number of recordings for each event). 72

Figure 4.3. Variation of the Frequency of Recordings with Azimuth Angle for EQ57-EQ78 (N refers to the total number of recordings for each event). 73

Figure 4.4. Variation of the Normalized PGAs with Azimuth and R_{EPI}. 75

Figure 4.5. Variation of the Normalized PGVs with Azimuth and R_{EPI}. 76

Figure 4.6. Variation of the Normalized AIs with Azimuth and R_{EPI}. 77

Figure 4.7. Variation of the Normalized CAVs with Azimuth and R_{EPI}. 78

Figure 4.8. Schematic 2-D Representation of Principal Directions (p_1 and p_2). 80

Figure 5.1. Concept of the Station-specific Analysis Methodology. 83

Figure 5.2. Regression Results for Functional Form (5.3) for Stations TUZL, BOTS and BRGA (a and b refer to regression coefficients and N and R^2 stand for the number of data and coefficient of determination, respectively). 86

Figure 5.3. Distance Scaling of the Functional Form (5.4) for Stations TUZL, BOTS and BRGA (a, b, and c refer to regression coefficients and N and R^2 stand for the number of data and coefficient of determination, respectively). 87

Figure 5.4. Variation of the Total Residuals of PGA with R_{EPI} for the Candidate Functional Forms (Zero residuals are shown by the lines in red. Error bars stand for group means with 16^{th} and 84^{th} percentiles). 91

Figure 5.5. Station-based Coefficient of Determination (R^2) Values and Number of Data (N) (Grey-shaded stations are specifically mentioned in the text). 92

Figure 5.6. Station-based Coefficient of Determination (R^2) Values and Number of Data (N) (Grey-shaded stations are specifically mentioned in the text) (cont.). 93

Figure 5.7. Distance Scaling of the Functional Form (5.5) for Stations TUZL, BOTS and BRGA (a, b, c and d refer to regression coefficients and N and R^2 stand for the number of data and coefficient of determination, respectively). 94

Figure 5.8. Distance Scaling of the Functional Form (5.6) for stations TUZL, BOTS and BRGA (a, b and c refer to regression coefficients and N and R^2 stand for the number of data and coefficient of determination, respectively). 95

Figure 5.9. Distance Scaling of the Functional Form (5.7) for Stations TUZL, BOTS and BRGA (a, b, c and e refer to regression coefficients and N and R^2 stand for the number of data and coefficient of determination, respectively). 96

Figure 5.10. Distance Scaling of the Functional Form (5.8) for Stations TUZL, BOTS and BRGA (a, b, c and f refer to regression coefficients and N and R^2 stand for the number of data and coefficient of determination, respectively). 97

Figure 5.11. Distance Scaling of the Functional Form (5.9) for Stations TUZL, BOTS and BRGA (a, b, c and f refer to regression coefficients and N and R^2 stand for the number of data and coefficient of determination, respectively). 98

Figure 5.12. Distance Scaling of the Functional Form (5.10) for Stations TUZL, BOTS and BRGA (a, b, c, e and f refer to regression coefficients and N and R^2 stand for the number of data and coefficient of determination, respectively). 98

Figure 5.13. Distance Scaling of the Functional Form (5.11) for Stations TUZL, BOTS and BRGA (a, b, c, g and h refer to regression coefficients and N and R^2 stand for the number of data and coefficient of determination, respectively). 99

Figure 5.14. Distance Scaling of the Functional Form (5.12) for Stations TUZL, BOTS and BRGA (a, b, c, g and h refer to regression coefficients and N and R^2 stand for the number of data and coefficient of determination, respectively). 100

Figure 5.15. Distance Scaling of the Functional Form (5.13) for Stations TUZL, BOTS and BRGA (a, b, c, g, h and e refer to regression coefficients and N and R^2 stand for the number of data and coefficient of determination, respectively). 100

Figure 5.16. Distance Scalings of the Functional Form (5.8) (f = 5.8) for Stations TUZL, BOTS and BRGA (a, b and c refer to regression coefficients and N and R^2 stand for the number of data and coefficient of determination, respectively). 102

Figure 5.17. Distance Scalings of the Functional Form (5.8) (hybrid dataset) for Stations TUZL, BOTS and BRGA (a, b, c and f refer to regression coefficients and N and R^2 stand for the number of data and coefficient of determination, respectively). 103

Figure 5.18. Variation of the Total Residuals with Coefficients a, b and c for the Ultimate Functional Form (5.4) and R_{EPI}, Between-event Residuals with M_L and h, the within-event residuals with R_{EPI} and V_{S30} (Zero residuals are shown by the lines in red. Error bars stand for group means with 16^{th} and 84^{th} percentiles). 105

Figure 5.19. Variation of the Total Residuals with Coefficients a, b and c for the Ultimate Functional Form (5.8) (f = 5.8) and R_{EPI}, Between-event Residuals with M_L and h, the within-event residuals with R_{EPI} and V_{S30} (Zero residuals are shown by the lines in red. Error bars stand for group means with 16^{th} and 84^{th} percentiles). 106

Figure 5.20. Variation of the Total Residuals with Coefficients a, b, c and f for the Ultimate Functional Form (5.8) (hybrid) and R_{EPI}, Between-event Residuals with M_L and h, the within-event residuals with R_{EPI} and V_{S30} (Zero residuals are shown by the lines in red. Error bars stand for group means with 16^{th} and 84^{th} percentiles). 107

Figure 5.21. Comparison Between Total Residuals of ASB14 and KAAH15 and Functional Form (5.4) for Stations TUZL, BOTS and BRGA (Grey-shaded areas represent the smaller residuals of the station-specific approach.) 109

Figure 5.22. Comparison Between Total Residuals of ASB14 and KAAH15 and Functional Form (5.8) (f = 5.8) for stations TUZL, BOTS and BRGA (Grey-shaded areas represent the smaller residuals of the station-specific approach.) 109

Figure 5.23. Comparison Between Total Residuals of ASB14 and KAAH15 and Functional Form (5.8) (hybrid dataset) for stations TUZL, BOTS and BRGA (Grey-shaded areas represent the smaller residuals of the station-specific approach.) 110

Figure 5.24. Variation of Station-specific Regression Coefficients with M_L for Functional Form (5.4) (Red lines correspond to the total mean of coefficients and total means are shown by the lines in red. Error bars stand for group means with 16^{th} and 84^{th} percentiles). 111

Figure 5.25. Variation of Station-specific Regression Coefficients with M_L for Functional Form (5.8) (f = 5.8) (Red lines correspond to the total mean of coefficients and total means are shown by the lines in red. Error bars stand for group means with 16^{th} and 84^{th} percentiles). . 112

Figure 5.26. Variation of Station-specific Regression Coefficients with M_L for Functional Form (5.8) (hybrid) (Red lines correspond to the total mean of coefficients and total means are shown by the lines in red. Error bars stand for group means with 16^{th} and 84^{th} percentiles). . 112

Figure 5.27. Cumulative Variation of Subsets' Size with M_L for Station TUZL, BOTS and BRGA. 113

Figure 5.28. Variation of the Normalized Coefficients a, b and c of Functional Form (5.4) with M_L for the Cumulative Subsets of the Stations TUZL, BOTS and BRGA. 114

Figure 5.29. Variation of the Normalized Coefficients a, b and c of Functional Form (5.8) (f = 5.8) with M_L for the Cumulative Subsets of the Stations TUZL, BOTS and BRGA. 115

Figure 5.30. Variation of the Normalized Coefficients a, b and c of Functional Form (5.8) (hybrid) with M_L for the Cumulative Subsets of the Stations TUZL, BOTS and BRGA. 116

Figure 5.31. Variation of the Normalized Coefficient f of Functional Form (5.8) (hybrid) with M_L for the Cumulative Subsets of the Stations TUZL, BOTS and BRGA. 117

Figure 5.32. Variation of Station-specific Regression Coefficients with V_{S30} for Functional Form (5.4) (Total means or regression relations are shown by the lines in red. Error bars stand for group means with 16^{th} and 84^{th} percentiles). 118

Figure 5.33. Variation of Station-specific Regression Coefficients with V_{S30} for Functional Form (5.8) (f = 5.8) (Total means or regression relations are shown by the lines in red. Error bars stand for group means with 16^{th} and 84^{th} percentiles). 119

Figure 5.34. Variation of Station-specific Regression Coefficients with V_{S30} for Functional Form (5.8) (hybrid) (Total means or regression relations are shown by the lines in red. Error bars stand for group means with 16^{th} and 84^{th} percentiles). 119

Figure 6.1. Main Philosophy of 2-D Delaunay Triangulation Meshing and Interpolation Process. 121

Figure 6.2. Variation of Station-specific Coefficients a, b c and f with the Degree of Interpolation for Functional Form (5.8) (hybrid dataset). . 123

Figure 6.3. Spatial Distribution of Interpolated Coefficients for PGA Obtained through Functional Form (5.4). 124

Figure 6.4. Spatial Distribution of Interpolated Coefficients for PGA Obtained through Functional Form (5.8) (f = 5.8). 125

Figure 6.5. Spatial Distribution of Interpolated Coefficients for PGA Obtained through Functional Form (5.8) (hybrid dataset). 126

Figure 6.6. Spatial Distribution of Cell-based Coefficients for PGA Obtained through Functional Form (5.4). 127

Figure 6.7. Spatial Distribution of Cell-based Coefficients for PGA Obtained through Functional Form (5.8) (f = 5.8). 128

Figure 6.8. Spatial Distribution of Cell-based Coefficients for PGA Obtained through Functional Form (5.8) (hybrid dataset). 129

Figure 6.9. Variation of Cell-specific Regression Coefficients with V_{S30} (Regression relations are shown by the lines in red. Error bars stand for group means with 16^{th} and 84^{th} percentiles. 130

Figure 6.10. Spatial Distribution of Cell-based PGAs Obtained through the Station-specific Approach for an M_L5.7 Scenario Earthquake (Yellow circle refers to the epicentre of the earthquake). 132

Figure 6.11. Spatial Distribution of Cell-based PGAs Obtained through the Station-specific Approach for an M_L6.5 Scenario Earthquake (Yellow circle refers to the epicentre of the earthquake). 133

Figure 6.12. Spatial Distribution of Cell-based PGAs Obtained through the Station-specific Approach for the September 26, 2019, M_L5.7 Silivri Earthquake (Yellow circle refers to the epicentre of the earthquake). 135

Figure 6.13. Comparison between PGA Estimations of the Station-specific Methodology and KAAH15 for the 26 September 2019, M_L5.7 Silivri earthquake (Yellow circle refers to the epicentre of the earthquake). . . 137

Figure 6.14. Comparison between PGAs Recorded by IERREWS Stations and Estimations of Station-specific Methodology and KAAH15 for the 26 September 2019, M_L5.7 Silivri Earthquake (Yellow circle refers to the epicentre of the earthquake). 138

Figure 6.15. Comparison between PGAs Recorded by AFAD Stations and Estimations of Station-specific Methodology and KAAH15 for the 26 September 2019, M_L5.7 Silivri Earthquake (Yellow circle refers to the epicentre of the earthquake). 139

Figure 6.16. Spatial Distribution of Cell-based PGAs Obtained through the Station-specific Approach for the November 26, 2022, M_L6.0 Düzce Earthquake. 141

Figure 6.17. Comparison between PGA Estimations of the Station-specific Methodology and KAAH15 for the November 26, 2022, M_L6.0 Düzce Earthquake. 142

Figure 6.18. Comparison between PGAs Recorded by IERREWS Stations and Estimations of Station-specific Methodology and KAAH15 for the November 26, 2022, M_L6.0 Düzce Earthquake. 143

Figure 6.19. Comparison between PGAs Recorded by AFAD Stations and Estimations of Station-specific Methodology and KAAH15 for the November 26, 2022, M_L6.0 Düzce Earthquake. 144

Figure 6.20. Comparison between PGAs Recorded by AFAD Stations around Küçükçekmece Lake and their Estimations of Station-specific Methodology, KAAH15 and ASB14 for the November 26, 2022, M_L6.0 Düzce Earthquake. 145

Figure 6.21. Comparison between PGAs Recorded by IERREWS Stations around Küçükçekmece Lake and Estimations of Station-specific Methodology, KAAH15 and ASB14 for the November 26, 2022, M_L6.0 Düzce Earthquake. 146

Figure B.1. Distance Scalings of the Functional Form (5.4) for All Stations. . . 181

Figure B.2. Distance Scalings of the Functional Form (5.4) for All Stations (cont.).182

Figure B.3. Distance Scalings of the Functional Form (5.4) for All Stations (cont.).183

Figure B.4. Distance Scalings of the Functional Form (5.4) for All Stations (cont.).184

Figure B.5. Distance Scalings of the Functional Form (5.4) for All Stations (cont.).185

Figure B.6. Distance Scalings of the Functional Form (5.4) for All Stations (cont.).186

Figure C.1. Distance Scalings of the Functional Form (5.8) (f = 5.8) for All Stations. 187

Figure C.2. Distance Scalings of the Functional Form (5.8) (f = 5.8) for All Stations (cont.). 188

Figure C.3. Distance Scalings of the Functional Form (5.8) (f = 5.8) for All Stations (cont.). 189

Figure C.4. Distance Scalings of the Functional Form (5.8) (f = 5.8) for All Stations (cont.). 190

Figure C.5. Distance Scalings of the Functional Form (5.8) (f = 5.8) for All Stations (cont.). 191

Figure C.6. Distance Scalings of the Functional Form (5.8) (f = 5.8) for All Stations (cont.). 192

Figure D.1. Distance Scalings of the Functional Form (5.8) (hybrid) for All Stations. 193

Figure D.2. Distance Scalings of the Functional Form (5.8) (hybrid) for All Stations (cont.). 194

Figure D.3. Distance Scalings of the Functional Form (5.8) (f = 5.8) for All Stations (cont.). 195

Figure D.4. Distance Scalings of the Functional Form (5.8) (f = 5.8) for All Stations (cont.). 196

Figure D.5. Distance Scalings of the Functional Form (5.8) (f = 5.8) for All Stations (cont.). 197

Figure D.6. Distance Scalings of the Functional Form (5.8) (f = 5.8) for All Stations (cont.). 198

LIST OF TABLES

Table 3.1. Main features of the selected GMPEs. 33

Table 3.2. Total-database regression coefficients. 36

Table 6.1. Variation of meshing features based on the degree of interpolation. 122

Table A.1. Regression coefficients for M_L-based subsets. 175

LIST OF SYMBOLS

a, b, c, d, e, f, g, h	Regression coefficients
a_{p1}, a_{p2}	Ground accelerations at principal directions
A(f)	Frequency domain representation of ground motion
COV	Covariance matrix
D5-75	Significant duration which are time intervals between 5% and 75% of Arias intensity
D5-95	Significant duration which are time intervals between 5% and 95% of Arias intensity
E(f)	Frequency domain representation of source effects
f_{hp}	High-pass filter frequency
f_{lp}	Low-pass filter frequency
F	Faulting type
G	Instrument sensitivity factor
h	Focal depth
i	Interpolation degree
M	Magnitude
M_L	Local magnitude
M_W	Moment magnitude
$M_{W,hinged}$	Hinged-moment magnitude
p_1	First principal axis
p_2	Second principal axis
P(f)	Frequency domain representation of path effects
R	Source-to-site distance
R^2	Coefficient of determination
R_{EPI}	Epicentral distance
R_{JB}	Joyner-Boore distance
R_{HYP}	Hypocentral distance
R_{RUP}	Rupture distance
N	Number of data

N_{st}	Number of stations
S	Site conditions
S(f)	Frequency domain representation of site effects
Y	Ground motion parameter
VPC	Digitiser Sensitivity Factor
V_{S30}	Average shear-wave velocity in the top 30 m
$V_{S30,REF}$	Reference value of V_{S30}
$V_{S30,CON}$	Lowest V_{S30} in which site amplification is constant
T	Period
α	Angle between recording axes and principal axes
δ_{GMP}	Total residual of interested ground motion parameter
δB_{GMP}	Between-event residual of interested ground motion parameter
δW_{GMP}	Within-event residual of interested ground motion parameter
$\Delta R_{station}$	Distance among stations
ε	Normally distributed random error
ξ	Damping ratio
σ	Standard deviation

LIST OF ACRONYMS/ABBREVIATIONS

2-D	Two Dimensional
ACA	Aegean-Cyprian Arc
AI	Arias Intensity
ASB14	Ground motion model of Akkar et al.
BEA14	Ground motion model of Bindi et al.
CAV	Cumulative Absolute Velocity
EAFZ	East Anatolian Fault Zone
EC8	Euro Code 8
ELER	Earthquake Loss Estimation Routine
EMME	Earthquake Model of the Middle East Region Project
EW	East-West
FAS	Fourier Amplitude Spectra
FN	Fault-Normal
FP	Fault-Parallel
GCF	General Packet Radio Service
GEP	Genetic Expression Programming
GMP	Ground Motion Parameter
GMPE	Ground Motion Prediction Equation
GPRS	General Packet Radio Service
GSM	Global System for Mobile Communications
GUI	Graphical User Interface
Idir	Directivity Factor
IDP	Isochrone Directivity Predictor
IERREWS	Istanbul Earthquake Rapid Response Early Warning System
IM	Intensity Measure
ISMEP	Istanbul Seismic Risk Mitigation and Emergency Preparation Project
KAAH15	Ground motion model of Kale et al.
KOERI	Kandilli Observatory and Earthquake Research Insititute

KS15	Ground motion model of Kuehn and Scherbaum
NAFZ	North Anatolian Fault Zone
NERIES	Network of Research Infrastructures for European Seismology
NF	Normal Fault
NGA	Next Generation Attenuation
NS	North-South
PGA	Peak Ground Acceleration
PGD	Peak Ground Displacement
PGV	Peak Ground Velocity
PreSEIS	Pre-Seismic Shaking
PSHA	Probabilistic Seismic Hazard Analysis
RC	Reinforced Concrete
RESORCE	Reference Database for Seismic Ground Motion in Europe Project
RETMC	Regional Earthquake-Tsunami Monitoring Center
RF	Reverse Fault
SA17	Ground Motion Model of Sandıkkaya and Akkar
SA	Spectral Accelerations
SSF	Strike Slip Fault
UD	Up-Down
TXT	Text

1. INTRODUCTION

The Anatolian plate is extruded in the westward direction as a result of the collision of the Eurasian and Arabian plates, which are controlled by three key tectonic structures; the Aegean–Cyprian Arc (ACA), the North Anatolian Fault Zone (NAFZ) and the East Anatolian Fault Zone (EAFZ). The peculiar tectonic importance and significant seismic activity of the NAFZ constitute one of the most well-known strike-slip faults in the world. Inside the Sea of Marmara, the 1500 km long NAFZ that stretches from Karlıova in the east to Greece in the west is split into two primary strands. The Sea of Marmara is partially crossed by the northern strand of the NAFZ whereas the southern strand extends along the southern shore of the Sea of Marmara and then bends towards the Aegean Sea [1].

1.1. Literature Review on Seismic Hazard and Risk Studies for İstanbul

The distance between the densely-populated districts of İstanbul, which is the most urbanized city of Türkiye with inhabitants of about 15 million [2] and the northern and southern strands of NAFZ is approximately 15 and 70 km based on the active fault map of Türkiye [3]. There is probably a 250-year seismic gap in the south vicinity of Istanbul based on the recurrence interval of the two most recent historical earthquakes, which took place in 1509 and 1766 [4]. Two recent devastating earthquakes (M_W7.4 in Kocaeli, August 1999 and M_W7.2 in Düzce, November 1999 based on KOERI-RETMC [5]) occurred in Istanbul's immediate east caused a significant number of fatalities and massive structural damage. Currently, several researchers point to a strong probability of a catastrophic earthquake with a greater magnitude striking Istanbul and its surroundings fairly soon [6–8]. In this context, numerous studies have attempted to conduct seismic hazard [9–14] and risk [15–18] assessments for the territory to calculate the ground motion parameters (henceforth GMP) using a particularly probabilistic framework and comprehend its potential consequences.

The time-dependent and time-independent probabilistic seismic hazard analyses have recently performed with updated information on the regional seismicity and fault segments. The seismic hazard analysis with Poisson (time-independent) assumption, which means earthquakes occur randomly and independently in time, posits that peak ground acceleration (PGA) for the return periods of 475 years (10% probabilities of exceedance in 50 years) are around 0.3 and 0.4 g. The time-dependent model raised the ground motion estimations for İstanbul [14].

According to seismic risk assessments conducted for Istanbul in 2003 using the intensity-based and spectral displacement-based methodologies, about 5% and 1% of the total number of buildings will respectively experience complete damage (damaged beyond repair) and pancake model collapse together. Moreover, a considerable amount of casualties is anticipated under these circumstances. In addition, the projections include 9% of the overall building inventory experiencing extensive damages and 25% facing moderate damages [15].

Istanbul Earthquake Rapid Response and Early Warning System (IERREWS) has been initiated to mitigate the losses in the case of a disastrous earthquake in Istanbul by the Department of Earthquake Engineering of Boğaziçi University, Kandilli Observatory Earthquake Research Institute (KOERI) with the cooperation of the Governorate of Istanbul, First Army Headquarters and Istanbul Metropolitan Municipality in 2002 [19, 20].

The ensuing progressions in the early warning system operated by the Department of Earthquake Engineering of KOERI are outlined in the research papers [21] and [22].

PreSEIS (Pre-SEISmic Shaking), which has been implemented with the intention of providing early warning of earthquakes, has also been developed and tested using the IERREWS [23].

The Istanbul Seismic Risk Mitigation and Emergency Preparation Project (ISMEP), funded by the World Bank and the European Investment Bank, was launched in 2006 for the execution of the fundamental components of disaster management [24].

Over 4000 buildings, predominantly on the European side of Istanbul near the historical peninsula, are projected to be completely destroyed, according to building damage estimates based on the KOERI Loss Estimation Methodology (KOERILoss) for Istanbul [25].

In 2009, the Earthquake Engineering Department of KOERI developed the first version of the Earthquake Loss Estimation Routine (ELER) methodology and software package which is a damage and loss estimation tool, as a part of the NERIES project to enable the estimation of earthquake losses at regional and urban scale [26–28]. By then integrating ELER into the Istanbul Earthquake Rapid Response System (IERRS), the ELER-IERRS application has been developed, which instantly enables the automatic generation of ground shaking intensity and estimated damage distribution maps in the case of a potential major earthquake around Istanbul [29].

Recently, Hancılar et al. [30] have concentrated on the seismic losses of mid- and high-rise reinforced concrete (RC) buildings that are presumptively constructed in compliance with the Turkish Earthquake Resistant Design Code's requirements (1998) in İstanbul. The total number of buildings in moderate, extensive and complete damage grades varies from around 8% to 22% of interested total mid- and high-rise building stock based on the selected vulnerability model for the earthquake with 10% probabilities of exceedance in 50 years. These figures increase to 30% and 60% for the earthquake with a return period of 2475 years (2% probability of exceedance in 50 years).

The potential earthquake loss estimations booklets on a district basis have been issued for İstanbul by the Istanbul Metropolitan Municipality and the Department of Earthquake Engineering of KOERI [29].

1.2. Literature Review on Ground Motion Prediction Studies

All of the preceding earthquake engineering studies focusing on İstanbul emphasize the vitality of earthquake-resistant design of structures, hazard assessment and development of early warning systems and implementation of contingency plans in order to mitigate the catastrophic consequences before and immediately after an earthquake in Istanbul. These studies indispensably necessitate the most precise estimation of GMPs, which quantify and describe the ground motion characteristics, and their spatial distribution.

According to Douglas [31], which conducts a comprehensive examination of techniques for predicting earthquake ground motions for engineering purposes, the methods can be segregated into four main categories. Black-box, physics-based and hybrid approaches generally aim to generate synthetic ground motion time histories modelling the essential physical structure by using various mathematical approaches. Moreover, ground motion time series are also constructed by some empirical methods, such as scaling actual ground motion traces. However, ground motion prediction equations (henceforth GMPEs), which provide a quick and straightforward prediction of GMPs (e.g. PGA, PGV, PGD, SA at different periods, duration etc.) by considering the different sorts of variabilities, continue to be the most popular approach in engineering practice. A comprehensive overview of attenuation models is presented by the reviews of [32] and [33]. GMPEs are usually produced by regression analyses employing dependent (predictor) variables such as GMPs and independent (explanatory) variables which characterize the earthquake source, wave propagation path between source and site, and local geology and soil beneath the site. A GMPE, which enables computation of the GMPs relevant to a scenario event at a particular site, can be typically expressed in its most basic functional form as follows:

$$\ln(Y) = c_1 + c_2 M - c_3 \ln(f(R, M)) - c_4 R + c_5 F + c_6 S + \varepsilon, \tag{1.1}$$

in which ln(Y) is the natural logarithm of the Y, which refers to a specific GMP. The independent variables M, R, F, and S stand for magnitude, source-to-site distance, faulting type, and parameter characterizing local site circumstances, respectively. ε

serves as the representation for the normally distributed random error in the model. A comprehensive review of the current landscape as well as possible directions for future advances in ground-motion prediction is offered in [34]

The GMPE online compendium of Douglas [35] presents up-to-date documentation consisting of a complete list of empirical ground motion models generated from 1964 to the beginning of 2021 in chronological order along with key details of the methodologies and databases. The earliest-known empirical relation is credited to the study of Esteva and Rosenblueth, which developed it in 1964 [36]. The literature is replete with numerous regional and global empirical ground motion models derived by using different methods such as one-stage regression (e.g. [37,38]), two-stage regression (e.g. [39–42]), one-stage maximum likelihood regression (e.g. [43, 44]), mixed-effect regression (e.g. [45,46]), two-stage maximum likelihood regression (e.g. [46,47]), Bayesian one-stage regression (e.g. [48–50]), neural networks (e.g. [51–54]), genetic expression programming (GEP) (e.g. [55–57]) etc. The most well-known global GMPEs have emerged from the NGA (Next Generation Attenuation) projects, dedicated to formulating GMPEs specifically for shallow crustal events in active tectonic regions of the United States. Comprehensive information on the final products of the NGA projects is accessible through their official websites. An extensive overview of the project is also provided in [58].

The importance of geographical considerations in the compilation of empirical relation databases is underscored by elucidating a significant difference in ground motions between California and Europe [59]. In the context of regional dependency of strong ground motions, the analysis of variance is proposed as an insightful approach [60]. Examining data from different European areas, the study assesses whether strong ground motions exhibit regional dependence within Europe, ultimately concluding that there is limited evidence for such a phenomenon. The study of Ambrasseys [61] is the pioneering study that focuses exclusively on Europe and the Middle East, offering an empirical relationship for horizontal strong ground motions induced by shallow crustal earthquakes in this specific geographic region. Then, a comparative analysis [62] suggests that the estimations from the GMPE, which is later published [63] as a product

of the NGA projects, seem to be in agreement with the estimations of Ambrasseys [61]. The inconsistency in estimations by NGA models is attributed to regional differences, particularly pronounced for small-to-moderate events [64]. In 2016, the study of Campbell [65] also compares the estimations of up-to-date developed GMPEs [66–68] for Europe and the Middle East with those of the ground motion model given in [69], an updated version of their NGA-West2 GMPE generated in 2008. The same study implies that the discrepancies among the estimations of the mentioned GMPEs are negligible from a scientific perspective.

Moreover, researchers frequently compare GMPE estimations focusing on a local area or specific earthquakes. In the paper of Şafak [70], the comparison between PGAs observed in the M_W7.4 Kocaeli earthquake and estimations of the ground motion model of Boore [43] highlights an overestimation of near-field recordings by the empirical relation. Additionally, stations situated around Küçükçekmece Lake, the shores of Bakırköy and Fatih district display larger PGAs than the empirical relation's estimations. The comparison of PGA and SAs from ground motions of the 1999 Chi-Chi, Taiwan earthquake with predictions from four empirical relations also indicates that the empirical ground motion models tend to overpredict GMPs for periods shorter than approximately 1 second [71]. The comparative analysis carried out by [72] investigates the regional dependency through response spectra derived from numerous stochastic models of ground motions. The results point out substantial distinctions in response spectra of several regions. The striking aspect in Figure 10 of [72] is the apparent difference between stochastic response spectra of the Marmara region and Erzincan, even though both are situated within the same country. In another study [73], significantly faster attenuations of GMPs from Italian ground motions are detected at shorter periods ($T \leq 0.2$ - 0.5 s). This discrepancy can be ascribed to the lower frequency-dependent Q values observed in Italian data, which indicate higher crustal damping in the region. The estimation equations for PGAs and PGVs are generated using ground motion data obtained from Türkiye and Italy in [74]. These equations seem to yield lower estimates compared to the predictions derived from global NGA models. The authors attribute this discrepancy to differences in the depth distribution of datasets. The findings in [75] reveal that the PGAs, PGVs, and SAs for the M_W5.7 Silivri earth-

quake in 2019 experience more rapid attenuation than the estimation lines provided by GMPEs such as those from ground motion models presented in [66], [76] and [77]. This behaviour is possibly influenced by distinctive geometrical spreading or anelastic attenuation features in the region.

Several GMPEs have been developed with a focus on seismic activity limited to Türkiye. The pioneering studies of Tezcan [78], Inan et al. [79] and Aydan et al. [80] marks the early attempts to derive empirical ground motion estimation relations for Türkiye. The reliability of these studies remains unverifiable due to the limited amount of data available. In 2002, another study [81] proposes attenuation relations for PGA and SAs, utilizing data from 47 horizontal components of 19 earthquakes in Türkiye. A spatial distribution of PGAs for Türkiye is provided through an attenuation relation formulated with the analysis of 221 ground motion recordings from 122 earthquakes in the same study [82]. The attenuation relation developed by [83] encompasses both PGA and SAs of vertical ground motion recordings of Turkish earthquakes. A random effect regression is implemented to develop an empirical ground motion model for PGA and SAs, utilizing 195 ground motion recordings from 17 earthquakes in northwestern Türkiye in [84]. The ground motion models for northwestern Türkiye are introduced based on the aftershocks of the M_W7.4, 1999 Kocaeli earthquake [85]. GEP is used by [56] to predict PGAs. A two-stage regression analysis is employed on a database comprising 165 ground motion recordings from 49 events to establish an empirical ground motion attenuation relation for the particularly Aegean region of Türkiye [86]. The compatibility analysis of the study's relation with global GMPEs shows that ground motions can exhibit variabilities attributed to the region-specific distinctive physical characteristics despite similar tectonic settings. An attenuation relation is also presented based on 751 horizontal ground motions, primarily recorded in Istanbul and eastern Marmara, from the Kocaeli and Düzce mainshock and aftershocks [87]. Another localized ground motion model for Türkiye incorporates factors such as faulting mechanisms, nonlinearity in local soils, quadratic magnitude term, magnitude dependency of geometrical decay and saturation of short-period ground motions at near-field distances by using 1259 recordings from 573 earthquakes [74]. Various models are also explored through both GEP and ordinary regressions using

a dataset of 120 recordings from 104 earthquakes in Türkiye [57]. The residuals between the estimations of the NGA-West1 GMPEs and the actual GMPs from strong ground motions recorded in Türkiye are assessed by [88]. The analysis of between-event residuals demonstrates a consistent overestimation of GMPs by all NGA-West1 models whereas the within-event residuals do not show any discernible pattern against rupture distance. Hence, the study focuses on modifying the magnitude scaling of the NGA-W1 GMPEs. One of the recent GMPEs, which will be detailed in Chapter 3, introduces empirical ground motion models that are applicable to both Türkiye and Iran [77]. Another recent study [89] concentrates on northwestern Türkiye and utilizes 402 recordings from the mainshocks and aftershocks of the 1999 Kocaeli and Düzce earthquakes to develop a regional attenuation relation. A regional ground motion model is also introduced for western Türkiye, encompassing the Aegean and Marmara regions [90]. The model is developed through ground motion simulations that take into account the region-specific source, path and site characteristics.

Given the specific focus on azimuthal effects on ground motions in the thesis, this paragraph provides a brief literature review on the subject. The variation in the direction in which the seismic waves propagate from the source to the site can modify the temporal and frequency characteristics of ground motion. The geographic distribution of macroseismic data can serve as the preliminary indicator for the azimuthal dependence of ground shaking (e.g [91–93] for Eastern Alp earthquakes) in the early studies. Ongoing research typically emphasizes the spatial distribution of GMPs for the identification of azimuthal dependence, facilitated by the increased availability of instrumental data that ensures comprehensive coverage at similar epicentral distances (e.g. [94] for Nocera Umbra, Central Italy, [95] for 2008 Wenchuan earthquake, [96] for 2009 April L'Aquila earthquakes). Along with the extension of GMP isoseismals in specific directions, azimuthal variation can also have an impact on the frequency content of ground motion [97].

Ground motion components perpendicular to the fault (FN or fault-normal) and particularly aligned with the direction of rupture propagation toward the recording site tend to produce greater ground-motion amplitudes due to directivity effects [98]. The

same study also suggests a technique for modifying the existing attenuation relations to account for the directional effects on ground motion by considering parameters that take into account the geometric relationship between the fault plane and the recording site. By employing a similar technique, the study of Abrahamson [99] modifies the ground motion model proposed in [98] and incorporates the impact of directivity into PSHA. The isochrone theory is used to elucidate the azimuthal dependency of ground motions around a seismic source by introducing the Isochrone Directivity Predictor (IDP) as a function of the isochrones velocity ratio and radiation pattern in [100]. Furthermore, the researchers put forward adjustment factors for ground motion models that do not account for directivity effects. However, the constraints of the Isochrone Directivity Predictor (IDP) are mentioned due to its limited correlation with the residuals in their ground motion model [101]. The GMPE generated in [102] is enhanced in the same study by introducing a directivity factor (Idir) into the explanatory variables, which varies based on the intensity of the directivity signal.

The variability in ground motion estimates demonstrates azimuthal dependence, primarily resulting from directivity effects [103–107] for a variety of regions. A series of studies, which concentrated on the earthquakes in Romania's Vrancea region, propose a methodology for the derivation of the azimuth-dependent GMPE by employing two-step regression analysis. In the first step of the regression, the method yields azimuth-dependent parameters for each earthquake through a parametric analysis. The second regression incorporates the magnitude of all earthquakes while considering the azimuth-corrected distances determined in the prior step [108–110]. Azimuthal dependency of the spectral ratios of ground motions, both recorded and simulated in the Kanto Basin, may also induce amplification owing to the presence of heterogeneous structures beneath the propagation path [111].

1.3. Objective and Organisation of the Thesis

The earlier literature reviews explicitly demonstrate that achieving the most precise estimation of GMPs for a region (e.g. İstanbul) potentially to be exposed to a strong seismic event can significantly enhance the outcomes of earthquake engineer-

ing studies, in which GMPs serve as key input variables. Even with the abundance of regional and global GMPEs, they may fail to capture regionally varying physical processes throughout the entire journey of ground motions, from source to station. Thus, improving the localization of empirical relations may provide a solution to this challenge, particularly with the assistance of densely distributed strong ground motion stations. In this thesis, the dense strong motion network of IERREWS offers an extensive database for testing the estimation capabilities of current empirical models. Additionally, it enables the development of station-specific regressions to enhance GMP estimations, with a particular focus on Istanbul.

In Chapter 2, the processing of strong ground motions is encompassed along with database compilation and database criteria for the selection of reliable ground motion data of earthquakes recorded by the IERREWS network, established and operated by Kandilli Observatory and Earthquake Research Institute (KOERI) of Boğaziçi University.

Empirical equations are introduced in Chapter 3, covering both the complete dataset and subsets categorized by magnitude to explore the conformity with the distance scalings of frequently utilized GMPEs in the vicinity. Additionally, residual analyses are conducted to enhance a complete statistical assessment of the GMPEs' predictive capability.

Chapter 4 is dedicated to the investigation of regional impacts i.e. azimuthal effects on strong ground motion recordings. This chapter also offers a solution to account for the ambiguous effects of azimuth in subsequent analyses by briefly summarizing the process of converting ground motions recorded along the EW-NS coordinate axis frame to those along principal axes.

The previous chapters elucidate and demonstrate the necessity for enhancing GMP estimations for the current database. Hence, Chapter 5 puts forth a station-specific methodology for estimating the GMPs, minimising regional uncertainty and leveraging a sufficient number of recordings from the dense IERREWS network. The

primary focus of this chapter revolves around the choice of the functional form for the station-specific methodology. Furthermore, an investigation into the representativeness of the ultimate relations for the database is conducted, involving residual analysis and a comparison with estimations of the most consistent GMPE for actual data. Chapter 5 concludes by conducting a sensitivity analysis on the coefficients against magnitude and the soil condition parameter.

Chapter 6 initially presents the spatial distribution of cell-based regression coefficients, preceded by general information on 2-D Delaunay triangulation. Then, spatial distribution maps for PGA estimations are produced for both two hypothetical events and actual earthquakes (M_L5.7 Silivri earthquake on September 26, 2019 and M_L6.0 Düzce earthquake on November 23, 2022). The effectiveness of the station-specific methodology is gauged by comparing it with both actual data and the projections provided by the most appropriate GMPE for the database.

2. COMPILATION OF STRONG MOTION DATA

The primary and most indispensable component of GMPs estimation studies is the construction of a robust strong ground motion database. The significant variability in prior attenuation models has been linked with unintentional inconsistencies in the data compilation [112]. A uniform and systematically organized high-quality database facilitates rapid and reliable analyses in earthquake engineering.

2.1. Overview of IERREWS Network

The dense and real-time strong ground motion network of Istanbul Earthquake Rapid Response and Early Warning System (IERREWS), which was initiated for the purpose of the mitigation of losses in the case of a disastrous earthquake in İstanbul, presents an invaluable resource of information for earthquake engineering studies. The strong motion recordings of this dense urban network are employed to localise the attenuation equations for İstanbul in this thesis.

The IERREWS integrates an early warning system and a rapid response unit. For post-earthquake rapid response studies, Istanbul's densely populated areas are equipped with 100 three-channel strong motion accelerometers, which are mostly installed at ground level in low- and medium-height public buildings. GPRS and GSM modems provide access to three-component strong ground motion waveforms that are captured at each station during an earthquake [15,20]. With the support of the Governorship of Istanbul, the rapid response system's total station number has been reached 120 in 2012 with the addition of 20 more sensors [29]. Moreover, since 2012, both fibre-optic data transfer systems via Türk Telekom's network as well as satellite links continuously convey data from 10 strong ground motion stations, which are positioned along the northern shoreline of the Sea of Marmara for early warning studies to the data processing centre [15, 21, 22]. The IERREWS network also incorporates three ocean-bottom stations situated on the Marmara Sea seabed. Güralp's CMG-5T, which are three-component accelerometers equipped with a$\pm$2g dynamic range and a high

sampling rate of 100 Hz [113].

IERREWS network's stations have captured numerous small-to-moderate magnitude ($M_L < 5.7$) earthquakes from 2012 to the present, which did not cause any damage in İstanbul. In this thesis, we have meticulously examined over 30,000 raw horizontal-component recordings.

2.2. Compilation of Initial Database

The metadata tables have been compiled at the beginning of the study before applying any selection criteria and have been gradually updated along with the implementation of the data selection criteria. The metadata tables created are named the "earthquake information table", "recordings information table" and "station information table".

The earthquake information table consists of the origin date and time of the earthquakes, epicentre location in terms of latitude and longitude and the earthquake source characteristics such as faulting mechanism; strike, dip and rake angles; local and moment magnitudes; and focal depth. The earthquake source data are collected from the Boğaziçi University KOERI Regional Earthquake-Tsunami Monitoring Centre (RETMC) [5]. In cases where the source information (particularly moment magnitude, faulting type and geometry parameters) is not accessible in the KOERI-RETMC database, those cells are left empty in the table. An identification (ID) number is also assigned to each earthquake to make it easier to identify the event in the analyses.

The recording information sheet provides a collection of record information for each event such as station name, geographic coordinates of recording sites, record component information and epicentral distance (R_{EPI}). In the database, the finite-fault models and inversions do not exist for the majority of earthquakes. Therefore, the well-known distance metrics, which require the finite-fault model parameters of the event, such as rupture distance (R_{RUP}), defined as the shortest distance to the rupture plane of the fault [114], Joyner-Boore distance (R_{JB}), defined as the closest horizontal

distance to the surface projection of the rupture plane [39], etc., could not be calculated for the events. This table also comprises a column which states the problems related to documentation. They will be fleshed out in the generation of the database.

In the station information table, a summary list has been generated for station information including station code, location in terms of both geographic coordinates and the description of the housing structure in which the instruments are located and average shear-wave velocity in the top 30 m (V_{S30}). The cell-based V_{S30} information is provided for the entire İstanbul by the microzonation project of the Istanbul Metropolitan Municipality for the European and Asian sides of İstanbul as seen in Figure 2.1 [115, 116].

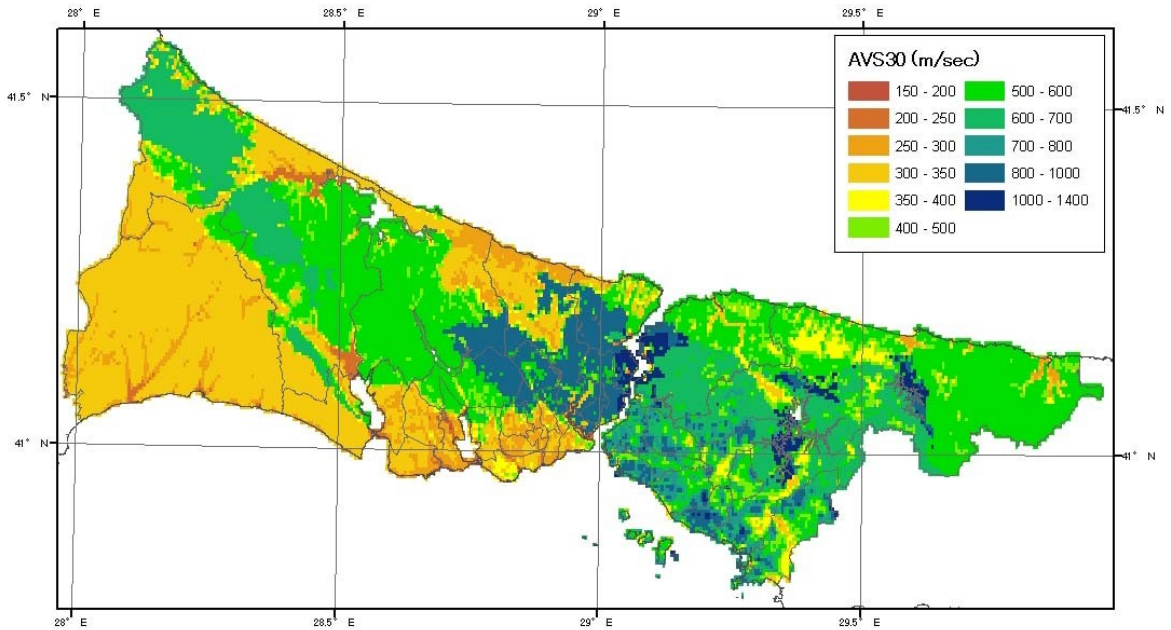


Figure 2.1. Spatial Distribution of V_{S30} for İstanbul [117].

2.3. Data Selection Criteria

The original raw database consists of 224 earthquakes that occurred between March 2012 and June 2022 in the Marmara region and its vicinity. It encompasses 31,054 individual accelerograms (comprising both horizontal components) acquired

from 117 strong motion stations of the IERREWS network. The criteria laid out in Figure 2.2 are implemented into the original data in order to build a reliable and practical database.

The initial step of the database criteria entails two phases associated with the documental material and quality of the database. The meticulous inspection of the database unveils certain documental issues such as earthquake files lacking any recordings, the presence of multiple earthquake folders or multiple files storing the same seismic recordings, files that do not contain both horizontal components as well as recordings from unidentified stations. To start, all earthquakes and recordings are streamlined into individual files by winnowing them from multiple folders and text files. Additionally, any unidentified stations lacking both horizontal components are excluded. During the second stage, the file formats (GCF or TXT File) used for data storage and their structural content are identified for the development of MATLAB [118] routines to utilize in further analyses.

The seismic signals with exceptionally high noise levels, which could not be decontaminated by even data processing, and temporal interruptions are detected through the visual quality inspection of the acceleration time histories. Subsequently, they are eliminated from the database at the second step of the database criteria. Additionally, recordings containing multiple shocks and elongated post-event durations are identified.

The magnitude and distance limitations are considered as the final step of the database criteria. According to personal communication with Dr John Douglas in [66], the data are approximately free of bias for magnitudes greater than 4.0 within a range of up to 200 kilometres Also, the majority of empirical ground motion estimation equations focus on these magnitude and distance thresholds. Hence, this thesis restricts the database within the aforementioned magnitude and distance limits. It also should be stated that similar to the studies of [67] and [77], this thesis embraces the recordings from aftershocks if their characteristics satisfy the database criteria established in the earlier steps.



Figure 2.2. Database Criteria Scheme.

2.4. Strong Motion Data Processing

The data processing of strong ground motions involves operations such as conversion of data format, baseline correction, filtering and the computation of GMPs relevant to this thesis. Some records in the database have been accessed in the format in which they were stored (Güralp compressed GCF File Format). This format is convertible to acceleration values by multiplying the measured count values with the ratio of the digitiser sensitivity factor (VPC in µV/count) and instrument sensitivity factor

(G in V/ms^{-2}) for each station [113]. This calibration information of each instrument in stations is obtained from Calvals Files of Güralp systems. Before data processing, the recordings in GCF format are converted to physical units.

The ground motion signal in the raw data may occasionally be contaminated by undesired random noises. This phenomenon exerts a serious influence on the prospective analyses since the noise content alters the acceleration time signal resulting in physically improbable velocity and displacements as well as response spectra [119,120]. Figure 2.3 demonstrates the effect of noises which leads to large deviations from the baseline of the time series and also non-physical large amplitudes, on the integrated ground velocity and displacements of the EW component of station TTEML for Kaleköy earthquake (M_L5.3) in the database.

Ground motion processing is an essential step in decontaminating the frequency content and acquiring reliable information for earthquake engineering studies. The significance of data correction processes and the inhomogeneous and erroneous effect of subjective choice of corner frequencies on the estimation of GMPs is underlined by various researchers [121–123]. The elastic and inelastic spectra also exhibit differences over the particularly long-period region due to the choice of processing methods [124, 125]. Furthermore, a reliable ground motion dataset is required for displacement-based design and seismic performance assessment methods [126].

The straightforward ground motion processing covers two major applications to make the data utilisable for the analyses; baseline correction and band-pass filtering. Since only filtering could not get rid of non-physical anomalies in the velocity and displacement time series, a pre-filtering baseline correction is systematically applied to all recordings [127, 128]. Subtracting the best straight line fitted to the entire time series is the procedure that is most frequently used to eliminate baseline shifts of integrated velocity and displacement time series [119, 129–132]. All raw accelerations and velocities have been processed with MATLAB's "Detrend" function to get more physically consistent velocities and displacements.

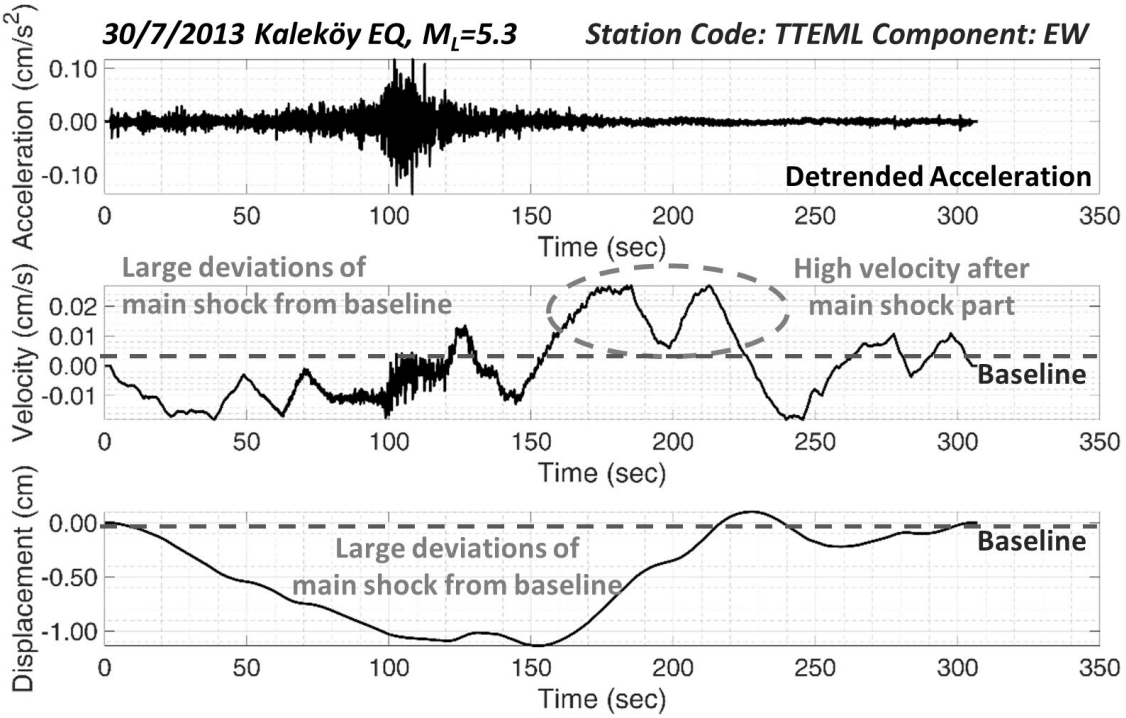


Figure 2.3. Unfiltered Recording of Kaleköy Earthquake (M_L5.3) from TTEML Station.

The non-physical frequency content in the ground motion time series could be possibly due to low and high-frequency noises. The literature provides limited insight into how low-pass filtering affects the GMPs. As stated by Douglas and Boore, 2011 [133], the requirement for low-pass filtering is not typically compulsory operation albeit the high-frequency noise interference in the ground motions. However, the uniform selection of low-pass filter frequency for all recordings, as employed by [61], is a conventional approach in strong ground motion processing. Thus, the low-pass filter frequency (f_{lp}) remains fixed at 20 Hz to suppress high-frequency noise. Unlike the relatively inconsequential impact of high-frequency noise, the presence of low-frequency noise contamination can substantially disrupt the frequency content of strong ground motions, and thereby inaccurate GMPs [133]. The removal of particularly low-frequency noises is critical in seismic performance analyses, which consider the seismic displacement demands. High-pass filtering and its application technique is an essential process in the data processing stage to minimize long-period (low-frequency) noises from the data to achieve as pure ground motions as possible [119, 126, 134]. The selection of the high-

pass filter frequency (f_{hp}) may affect both the peak ground motions and the elastic and inelastic spectral displacements. For magnitudes below 4.5, the high-pass filter frequencies frequently have minimal effect on the peak ordinates. However, it displays a decreasing tendency for larger magnitudes [135]. This dependency of GMPs on the filter corners triggers the motivation for the meticulous selection of high-pass filter corner frequencies.

The high-pass filter frequencies are selected by visual examination on an individual component basis. Beyond the visual inspection of integrated velocity and displacements as well as Fourier amplitude spectra (FAS), the variation in the slope of the displacements for each selected f_{hp} facilitates the selection of a reliable f_{hp}. Each displacement time history, obtained by double integration of acceleration filtered through a variety of high-pass filter frequencies, is subject to a least-squares regression to fit a straight line. If the variation of the slope of the line fitted for each high-pass filter frequency is examined, considerable fluctuations in the slope are observed particularly in low f_{hp} selections (Figure 2.4). In other words, low-frequency noise is responsible for the shifts of displacement time series from the baseline with positive and negative slopes. However, the f_{hp} that culminates in a straight line fit with a zero slope can be considered to be the ideal one. In Figure 2.4, the selection of f_{hp}s corresponding to the grey dots results in notable shifts from the baseline. However, the slope approaches zero at two f_{hp} levels (black dots in Figure 2.4), maintaining the displacement on the baseline. It is evident that the slope weakens, specifically after the second f_{hp} value. Hence, assessing the slope of the displacement time series may provide guidance in the identification of the f_{hp} value. Nevertheless, it should be highlighted that this technique cannot be implemented in earthquakes of significant scale or near-field earthquakes that may induce static displacement. Since the database contains neither near-field (except for a few events) nor large-scale events, this technique can be simply incorporated into our processing scheme.

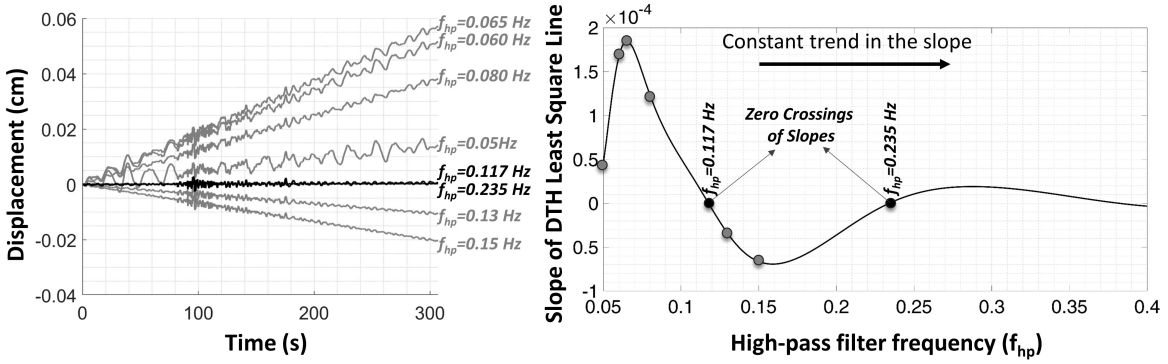


Figure 2.4. Variation of the Slope of Displacements for Different Selected High-pass Filter Frequencies (f_{hp}).

A MATLAB's graphical user interface (GUI) is necessitated as the selection of high-pass filter frequency mostly relies on a subjective judgment as to where low-frequency noise results in deterioration in notably integrated velocity and displacements. The semi-automated interface provides a more practical and faster methodology particularly in the case of processing the large bulk of recordings [136]. Therefore, a GUI has been generated to select high-pass filter corners by processing each component independently (Figure 2.5).

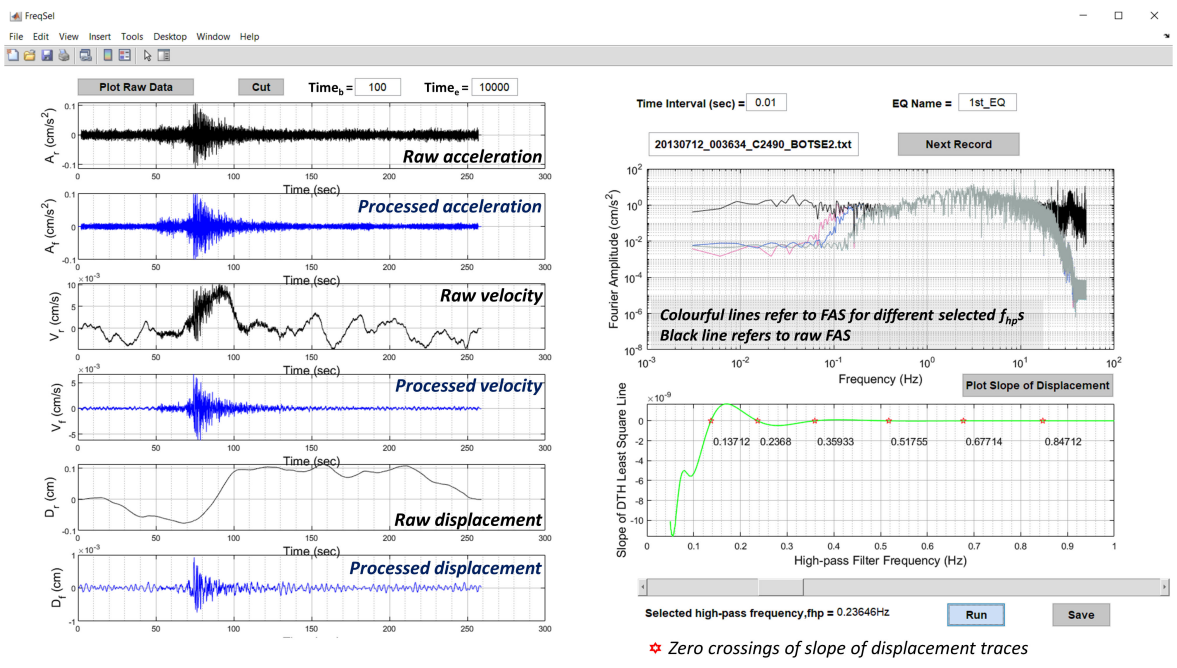


Figure 2.5. Graphical User Interface (GUI) for the Strong Ground Motion Processing.

The workflow for processing the strong ground motion time histories through the user-friendly graphical interface is detailed in Figure 2.6. The GUI algorithm is executed within each earthquake folder, and the "Next Record" button facilitates the analysis on a record-by-record basis. After setting the time interval for each individual record, raw acceleration, velocity and displacement time histories along with the Fourier amplitude spectrum (FAS) are plotted. Additionally, this step addresses the second criterion of the database. If the recording's duration significantly exceeds the earthquake's duration, which may lead to slowing down the analysis, or there are multiple seismic events in the data, the "Cut" button allows for shortening the time series or isolating the main shock from the recording within the desired time interval.

All data processing operations, which cover baseline correction of acceleration and velocity time histories and band-pass filtering of only acceleration time series, on a recording are performed through the "Plot Slope of Displacement" button. The baseline-corrected acceleration time series undergoes 4^{th} order Butterworth band-pass filtering between a range of f_{hp} values from 0 to 1.0 Hz, with a frequency increment of 0.001 Hz, and a constant value of f_{lp} set at 20 Hz. Non-zero digital filtering, known as acausal filtering [119, 125, 134, 137], is accomplished by incorporating zero padding into the time histories prior to filtering, to impede phase shifts. Concurrently, the calculation of the slope for each displacement time history, along with the visualization of them against their corresponding f_{hp} values, as previously expounded, is also accomplished. The slider bar positioned beneath the f_{hp} axis of this slope-f_{hp} graph makes the user drag to change the f_{hp} value. When the user clicks the "Run" button for a selected f_{hp}, the processed time histories and FAS are visualized on the GUI screen. These plotting areas are updated for each f_{hp} value, which is chosen based on a visual assessment of the time histories, FAS, and the slope of the displacement time history. The trials with various f_{hp} values are carried out repeatedly in order to determine the high-pass corner frequency at which the results are visually satisfactory, that is, the processing provides physically plausible time histories and the low-frequency part of FAS seems to be winnowed out undesired noises.

The program generates the two output Excel files and a screenshot by the "Save" button as the results visually meet the desired requirements. A brief table sheet, which is generated for each earthquake, consists of the f_{hp} values chosen, the PGA, PGV, and PGD for both raw and processed recordings, the spectral accelerations (SAs) at different periods (T = 0.2, 0.4, 0.6, 0.8, 1.0, 2.0, 3.0, 4.0, and 5.0 seconds) and the maximum FAS and its corresponding frequency for each horizontal component. Original names of each data file based on their components are also maintained in these tables. By generating the distinct Excel Files for each component, it also permits the storing of processed time histories for acceleration, velocity, and displacement along with the associated response spectra with a 0.5% damping ratio within the period range between 0-5.0 s with the increment of 0.01 s and FAS. The time histories and response spectra will serve as the input for the calculation of other GMPs such as Cumulative Absolute Velocity (CAV), Arias intensity (AI), spectral intensity (SI) etc. in further analyses.

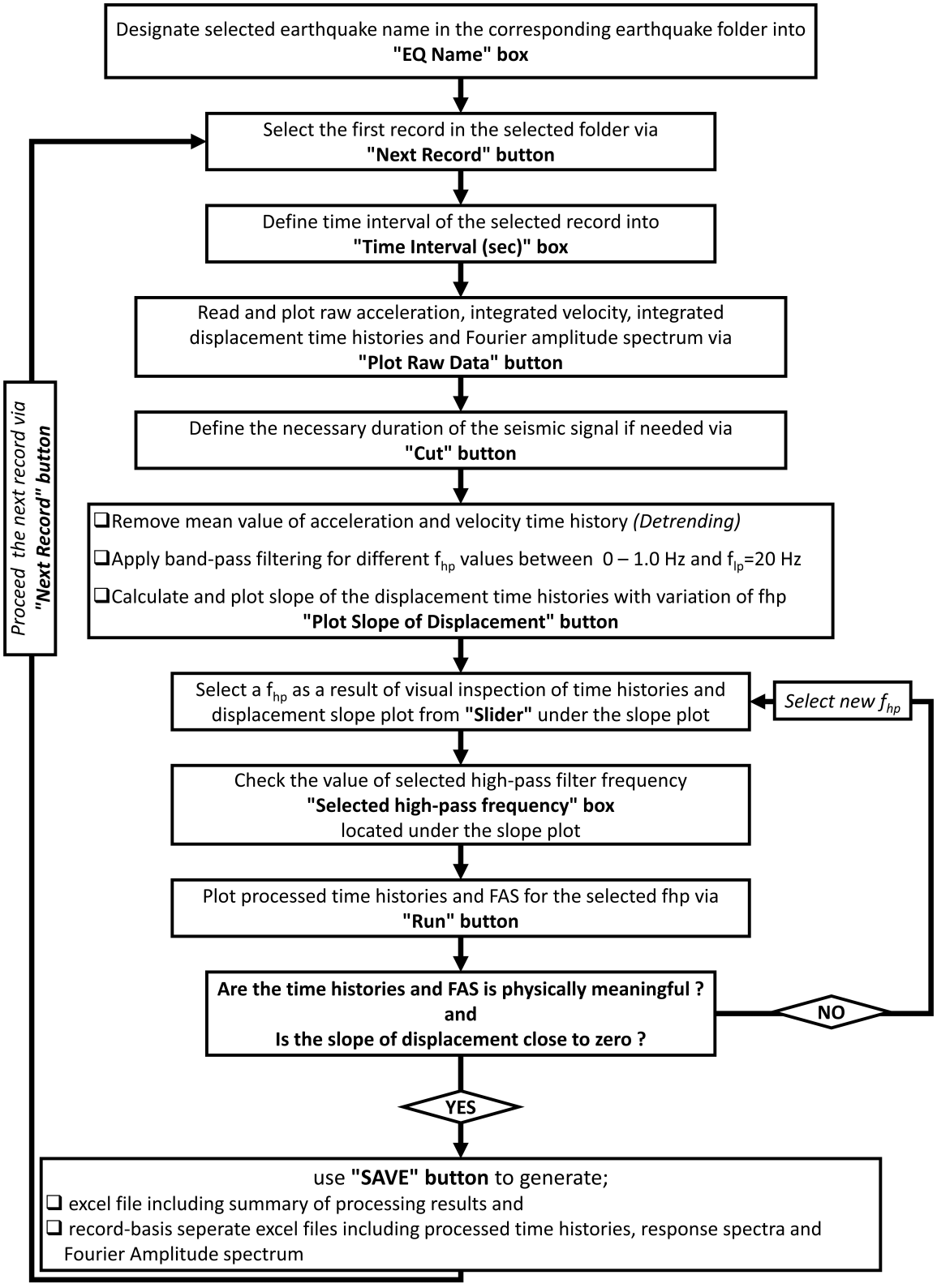


Figure 2.6. Strong Ground Motion Time History Processing Scheme (f_{hp} and f_{lp} refer to high-pass and low-pass filter frequency, respectively).

2.5. Characteristics of Final Database

The final database currently encompasses 6,534 horizontal-component (EW and NS) recordings from 78 seismic events, which took place in the Marmara region between 2012 and 2022, gathered from 108 different IERREWS network stations, following the implementation of database criteria and data processing to the original database. Figure 2.7 shows the nomenclature to be employed across the thesis for the earthquakes, accompanied by their geographic positioning. All earthquakes are located to the South of the IERREWS network, falling within an azimuthal range of approximately ±180 degrees.

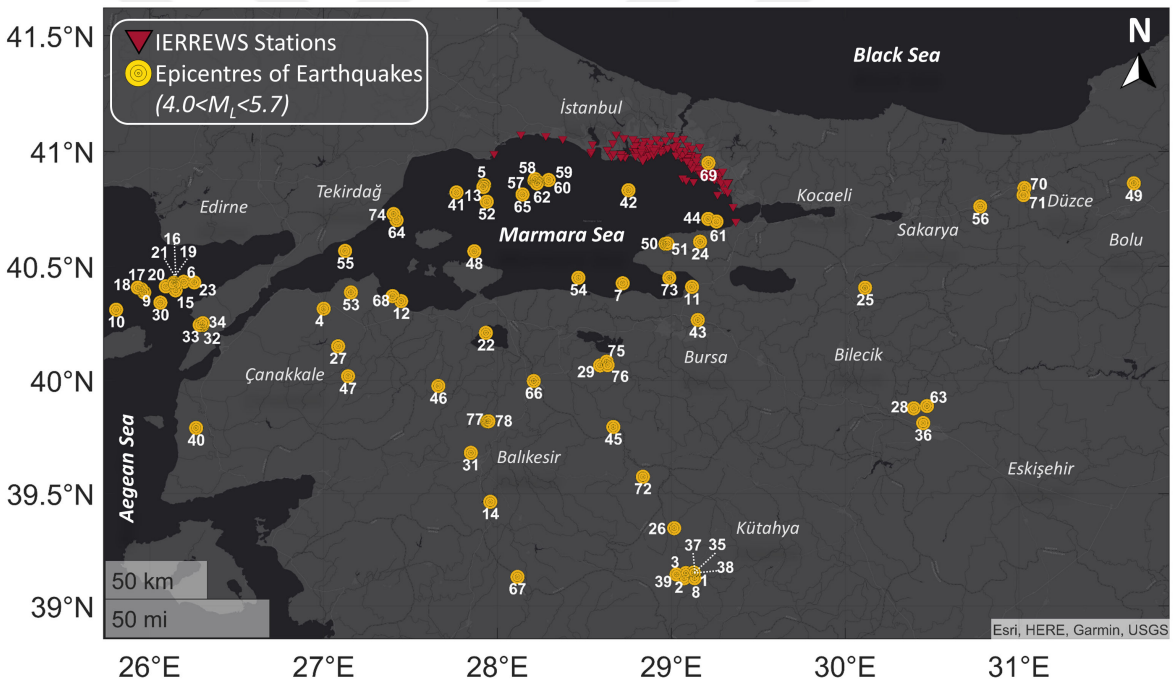


Figure 2.7. Spatial Distribution of Earthquakes (2012-2022) around Marmara Region.

Within the KOERI database, focal mechanism solutions are accessible for merely 29 earthquakes, with the majority of them indicating a strike-slip faulting mechanism, which is conformed with the prevalent mechanism of NAFZ whilst a few events tend to exhibit a normal faulting mechanism with strike slip implications. Earthquakes possess focal depths ranging from 1.8 to 20.2 kilometres, with an average of 10.5 kilometres, signifying a predominance of “shallow depth” events (Figure 2.8).

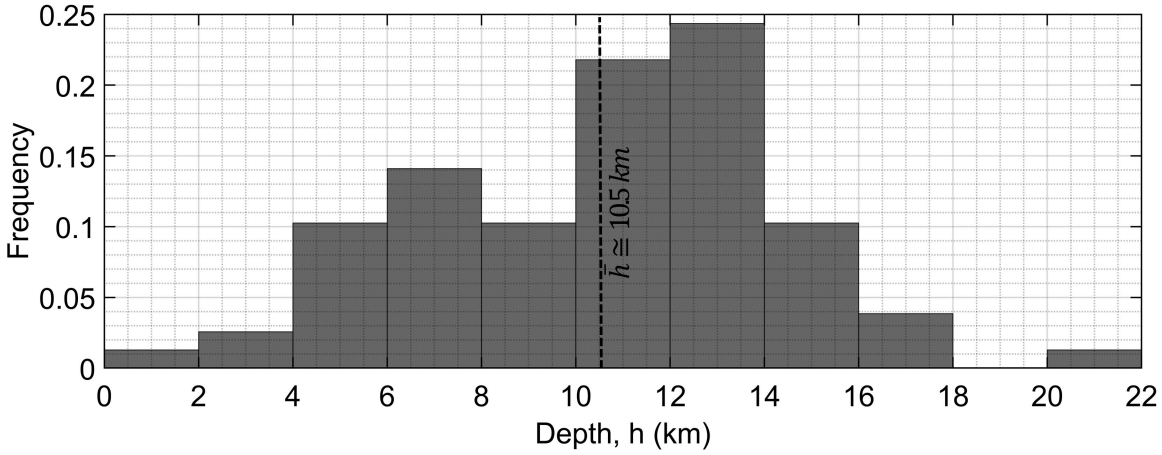


Figure 2.8. Histograms of Focal Depth, h of the Earthquakes in the Database.

The spatial configuration of the IERREWS network's strong ground motion stations seen in Figure 2.9 for both the European and Asian sides of İstanbul explicitly reveals that there is a well-distributed and dense network, particularly in the densely populated residential areas of Istanbul. A significant portion of the stations is strategically deployed along the northern shoreline of the Marmara Sea, which is in close proximity to the potential fault zone of the imminent earthquake within the Marmara Sea. However, the network is deficient in recording sites in the northern and eastern parts of Istanbul particularly beyond the West of Büyükçekmece.

The average shear-wave velocity in the top 30 m (V_{S30}) at the recording sites ranges from 230 to 1082 m/s. In Figure 2.10, the statistical distribution of V_{S30} values for recording sites of IERREWS stations is demonstrated by a histogram. The average value is 527 m/s, with about 23 % of the stations falling into the V_{S30} range of 300 to 350 m/s. Very soft and very stiff soil stations ($V_{S30} < 230$ m/s & $V_{S30} > 950$ m/s, respectively) are relatively underrepresented, with a small amount of data gathered from recording sites with V_{S30} values between 600 and 700 m/s.

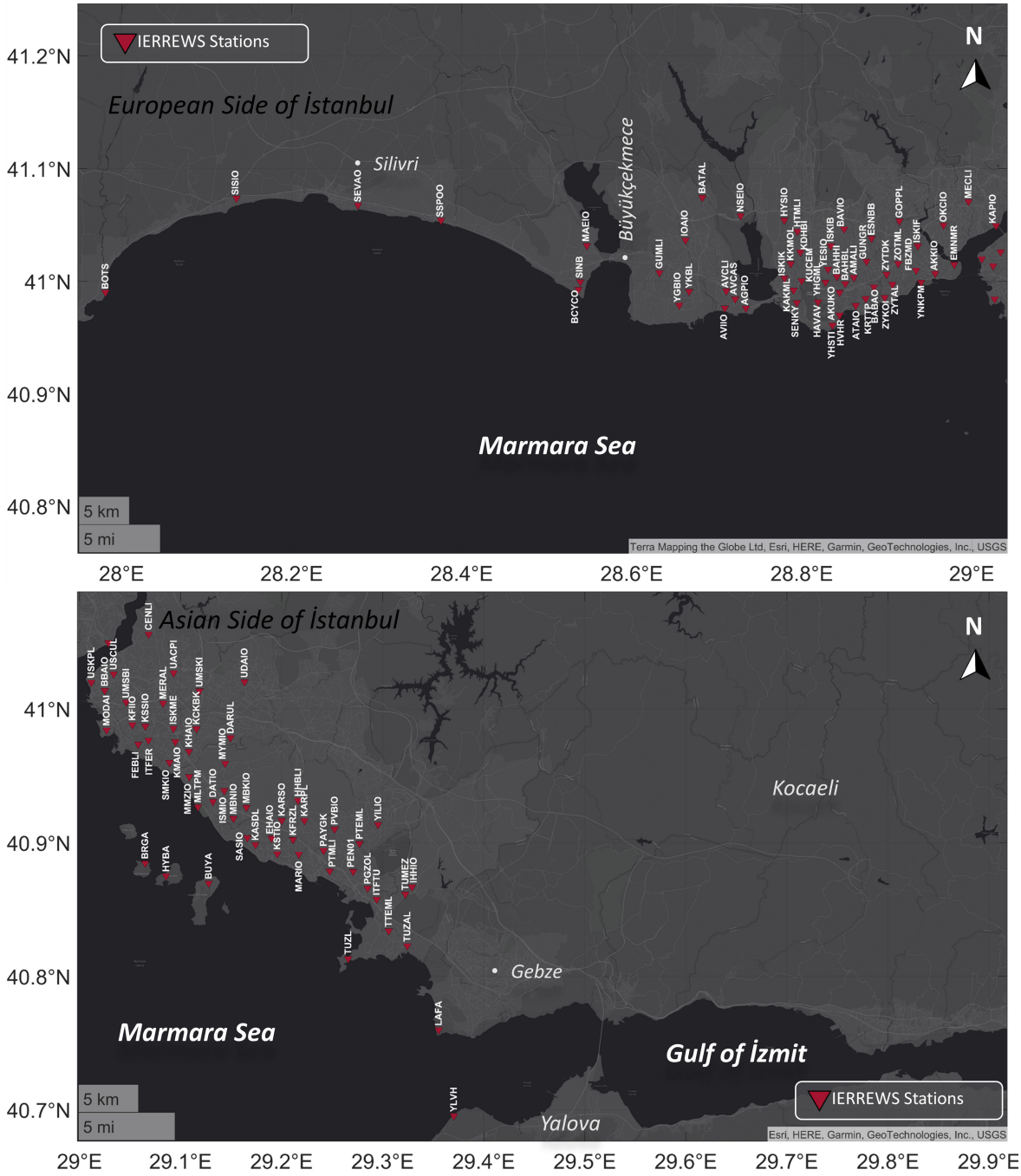


Figure 2.9. Spatial Configuration of the IERREWS Network Stations for (top) European Side of İstanbul, (bottom) Asian Side of İstanbul.

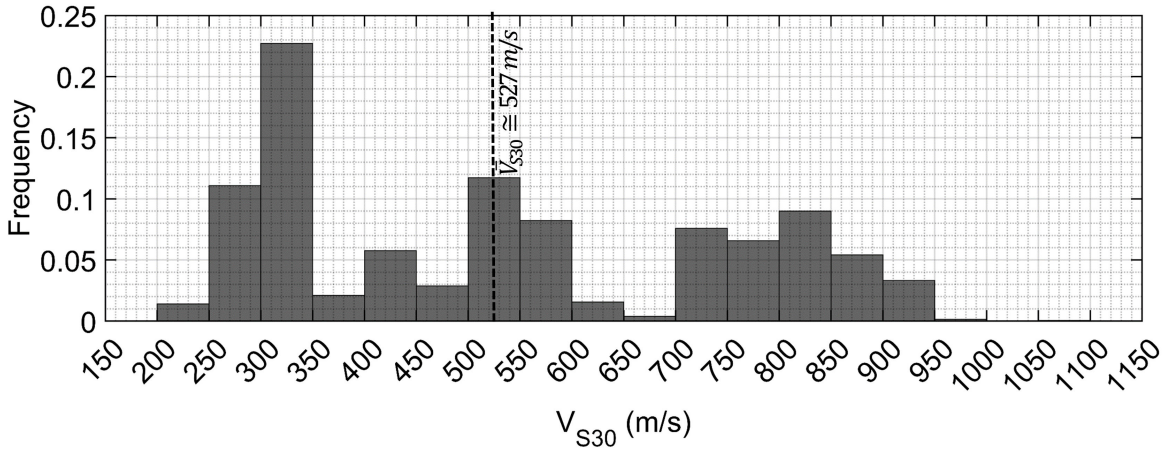


Figure 2.10. Histograms of V_{S30} Values at the Recording Sites.

The scatter plot of the final database concerning local magnitude (M_L) and source-to-site distance (R_{EPI}) can be viewed in Figure 2.11 along with their corresponding statistical distributions. The database comprises earthquakes covering the M_L range from 4.0 to 5.7 ($M_{L,mean} = 4.36$) with R_{EPI} varying from 2.0 to 200 km with a mean of 117 km. Although the maximum magnitude in the database is 5.7, the database suffers from a lack of data for greater magnitudes than M_L5.0. The entire range of R_{EPI} seems to be well-represented for magnitudes up to approximately M_L4.4 and also in M_L4.7. For other magnitudes, the quantity of data accounts for less than 1% of the total dataset. Between 40 and 150 km, R_{EPI} exhibits a more uniform distribution, but in near-field areas, prior to 20 km, there is a relatively low amount of data and at farther distances, beyond 150 km, data distribution shows a slight increase.

The selected low and high-pass filter frequencies may lead to the narrowing of the useable frequency range of response spectra. As previously stated, low-pass filtering seems to have an insignificant effect on spectral amplitudes while the lower bound of the allowable frequency bandwidth, which generally corresponds to the engineering period range, is governed by the high-pass filter frequency. Hence, for spectral amplitudes, a final database elimination is performed for each station based on the selected high-pass filter frequency. If the selected high-pass filter frequency, even if only for one horizontal component, is greater than the structural frequency of interest, that station

is omitted in the computation of spectral amplitudes in this period. In this thesis, a maximum structural period of 2 seconds is taken into account in the computation of spectral ordinates, and all f_{hp}s are chosen below 0.5 Hz. As a result, the application of high-pass filtering does not result in any reduction of the amount of data.

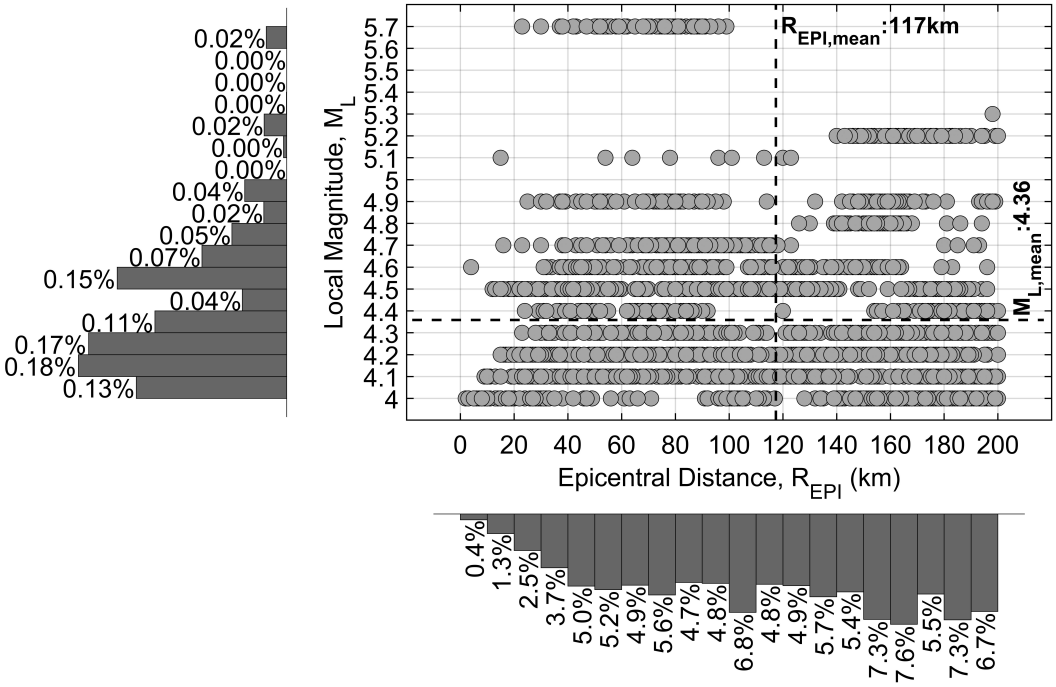


Figure 2.11. Distribution of Local Magnitudes (M_L) and Epicentral Distances (R_{EPI}).

3. CONSISTENCY EVALUATION OF GMPEs WITH STRONG MOTION RECORDS

This chapter investigates the impacts of source, path, and site components on GMPs using a consistency assessment with GMPEs, which are suitable to the regional and local peculiarities of Istanbul and its surroundings. The consistency of the IER-REWS database is performed through median estimates and residual analyses with respect to the selected GMPEs.

3.1. Main Characteristics of the Selected GMPEs

The investigations into attenuation characteristics of ground motions have produced a wide range of diverse empirical estimation models, stemming from varieties in the mathematical-physical models, the type of magnitude and distance metrics, the variables for characterizing local soil conditions, and the different faulting mechanisms and various estimation technique [109]. That's why, a rigorous inspection has been initially performed on the compendium of the Douglas [35], which assembles the GMPEs produced between 1964 and 2021. The GMPE compendium initially undergoes a geographic elimination to ascertain GMPEs whose databases are the most appropriate for the study area. As a result of the selection of GMPEs whose databases contain earthquakes from Europe, Middle-East, the Mediterranean and Türkiye, the number of GMPEs reported in the compendium for PGA, SA, and intensity measure (IM) estimations drops from 485, 316, and 293 to 58, 35, and 28, respectively. These areas' databases include many ground motions from Türkiye, which is why the GMPEs generated for these areas are believed to be the probably best indicative of regional traits.

The second selection criterion is assessing whether the references include details on the quantity of records, earthquakes, magnitude range and scale, distance range and scale, and combination type of horizontal components. The GMPEs are ignored

in the absence of any such details. A further significant issue is that, in order to make the comparison more meaningful, the GMPEs chosen should be as consistent as possible with the earthquake magnitude and source-to-site distance ranges of this study. Since this study's maximum source-to-site distance is 200 km (see Chapter 2), GMPEs that are only applicable for longer distances are not taken into account. Also, the GMPEs that can be used for magnitudes greater than 4.0 are favoured in order to assure relevancy between our database and those of the GMPEs. Since the vertical component of ground motions is outside of the scope of this thesis, the GMPEs developed for them are discarded. We are unable to employ any selection criterion for the upper magnitude limit or the magnitude and distance scales because the remaining GMPEs do not meet the requirements for this kind of selection. Finally, there is just one GMPE left to make a consistent evaluation of Arias Intensity (AI) and Cumulative Absolute Velocity (CAV) while four GMPEs that adopt the same functional form to estimate PGA, PGV, and SA are chosen to facilitate comparison of peak ordinates and SAs. Furthermore, although a considerable amount of events from Türkiye were recognized in the recent GMPE of Kotha et al. [138], this ground motion model is unable to be employed in this thesis due to the unavailability of the regression coefficients.

The primary characteristics of the five GMPEs that were chosen are summed up in Table 3.1, along with their abbreviations that will be used throughout the thesis, the applicable ranges of the dependent and independent parameters that they employ and references. Additionally, the following paragraphs provide a brief overview of the key distinguishing characteristics of the chosen GMPEs. However, the functional forms of the GMPEs selected are not provided herein. Please refer to the respective references for more information about the GMPEs.

The database of ASB14 [66] mostly includes ground motions of mainshocks and aftershocks from Italy, Türkiye, and Greece. Most of the recording sites in their database have V_{S30} values under 800 m/s. Nonlinear site amplification is considered in the functional form of ASB14 by modifying the reference GMP at a rock site ($V_{S30,REF}$ = 750 m/s) with a nonlinear site amplification term which is a function of V_{S30}. Site amplification is presumed to be steady for the sites with V_{S30}s greater than $V_{S30,CON}$=1,000

m/s. The magnitude scaling expression in ASB14 is represented by a Q-hinged model, which reflects the magnitude saturation over the hinged magnitude level ($M_{W,hinged}$ = 6.75 in ASB14). While disregarding the anelastic attenuation, the distance scaling is merely expressed by a magnitude dependent distance scaling function. Regression coefficients are also separately presented for both finite-fault (R_{JB}) and point-source (R_{EPI} and R_{HYP}) distance measures.

BEA14 [67] present ground motion models for two separate datasets obtained from the RESORCE database [139] based on the type of information on soil condition and faulting type. While one subset incorporates events with unidentified focal mechanisms and considers Euro Code soil classes of the recording sites, the other disregards the events with the unknown faulting types and employs V_{S30} as a parameter for soil condition. Turkish and Italian recordings constitute the majority of both subsets and Turkish ground motions in BEA14's database come from recording sites where the V_{S30} values are within the 180 to 800 m/s range. There is no distinction between mainshocks and aftershocks in BEA14 ground motion models. BEA14 separately provides regression coefficients for both R_{HYP} and R_{JB}. Since the strong and proximate events recorded in soft soil conditions, in which the nonlinear effects become prominent, are not adequately represented in their database, the functional form of BEA14 merely comprises linear site amplification expression depending on V_{S30} and reference shear wave velocity ($V_{S30,REF}$ = 800 m/s). Similar to ASB14, the magnitude scaling term of BEA14 contains the hinged-magnitude ($M_{W,hinged}$ = 6.75 in BEA14) and distance scaling reflects the magnitude dependency. Since the research confirms the resemblance between the V_{S30} and EC8-derived ground models using median estimates and standard deviations, the assessment of consistency in this thesis is solely performed on the ground motion model of BEA14, which considers the V_{S30} as a soil condition parameter.

The database of KS15 [50], which is the same repository as the study of [140], encompasses events specifically from Europe. Unlike the ASB14 and BEA14, KS15 abandons the hinged-magnitude in the magnitude scaling term and nonlinear site amplification is neglected as in BEA14. The functional form is relatively straightforward

as articulated in their paper.

Fifty-six per cent of the total number of ground motion recordings in the database of KAAH15 [77] are compiled from 175 events recorded at 163 stations in Türkiye. The rest of the database belongs to the Iranian data. The vast majority of the V_{S30}s in the Turkish dataset fall between 180 m/s and 760 m/s. Strike-slip earthquakes are spread more uniformly, notwithstanding the unequal distribution of reverse-faulting events in the Turkish dataset. The primary goal behind the study is to constitute a predictive model by taking into account potential regional impacts on the GMPs. Despite having remarkably similar tectonic regimes, Türkiye and Iran's sub-datasets demonstrate discrepancies in the magnitude, distance, and type of faulting scalings. The nonlinear soil amplification is considered in the functional form by modifying the regression coefficient of the soil model of [141] ($V_{S30,REF}$ = 750 m/s; $V_{S30,CON}$ = 1000 m/s). By incorporating a hinging-magnitude ($M_{W,hinged}$ = 6.75), magnitude saturation is reflected in the magnitude scaling term. Only ground motions recorded at distances less than 80 km are employed in the computation of regression coefficients for magnitude scaling and faulting style in KAAH15. Geometric decay and anelastic attenuation, the latter of which is presumed to exist at source-to-site distances greater than 80 km, are both incorporated in the distance scaling of KAAH15.

The data of SA17 [142], in which strike-slip and normal faulting mechanisms are prevalent, is evenly dispersed when compared to magnitude, distance, and fault type, particularly for V_{S30} values between 180 and 800 m/s. The entire database of SA17 is identical to that of ASB14. Additionally, except for omitting nonlinear site amplification and breakage at hinged-magnitude, the fundamental functional form of SA17 resembles that of ASB14. The V_{S30} threshold, at which linear soil amplification is accepted to be constant, is 1000 m/s and $V_{S30,REF}$ is equivalent to 750 m/s.

Table 3.1. Main features of the selected GMPEs.

Abbreviation	Database	Site Parameter /Range	Number of Events	Number of Stations	Number of Recordings	Style of Faulting[1]	Magnitude Type /Range	Distance Type /Range	Focal Depth	Ground Motion Parameter[2]	Comb. of Comp.
ASB14	Mediterranean region and the Middle East (A subset of RESORCE[3] Database)	V_{S30} 150-1200 m/s	221	322	1041	NF SSF RF	M_W 4.0-8.0	R_{JB} R_{HYP} R_{EPI} 0 - 200 km	<30 km	PGA PGV SA (T=0.01-4.0 s)	Geo. Mean
BEA14	Europe and the Middle East (Two subsets of RESORCE[3] Database)	Euro Code Soil Classes	365	697	2126	Unknown, NF,SSF,RF	M_W 4.0-7.4	R_{JB} R_{HYP} 0 - 300 km	<35 km	PGA PGV SA (T=0.02-3.0 s)	Geo. Mean
		V_{S30} 100-1000 m/s	255	345	1224	NF,SSF,RF					
KS15	Europe (A subset of RESORCE[3] Database)	V_{S30} 100-2000 m/s [4]	279	251	835	NF RF Other	M_W 4.0-7.64	R_{JB}	<40 km[4,5]	PGA PGV SA (T=0.01-4.0 s)	Geo. Mean[6]
KAAH15	Türkiye and Iran (A subset of EMME[7] Database)	V_{S30} 150-1200 m/s	313	417	1198	NF SSF RF	M_W 4.0-8.0	R_{JB} 200 km	<35 km	PGA PGV SA (T=0.01-4.0 s)	Geo. Mean
SA17	Mediterranean region and the Middle East (A subset of RESORCE[3] Database)	V_{S30} 150-1200 m/s	221	322	1041	NF SSF RF	M_W 4.0-8.0	R_{JB} R_{HYP} R_{EPI} 0 - 200 km	<30 km	AI CAV D5-95 D5-75	Geo. Mean

[1]NF: Normal fault, SSF: Strike slip fault; RF: Reverse fault, [2]PGA: Peak ground acceleration; PGV: Peak ground velocity; SA: Spectral accelerations at the periods (T); AI: Arias Intensity; CAV:Cumulative Absolute Velocity; D5-95 and D5-75: Significant durations, [3]Reference Database for Seismic Ground Motion in Europe project, [4]The parameter range are identified from plots,[5]The focal depth are determined from [140], [6]Information are taken from [35], [7]Earthquake Model of the Middle East Region project.

All of the GMPEs selected use the moment magnitude (M_W) scale rather than the magnitude scale M_L, preferred in our database. In line with the study of [143], the local magnitude (M_L) closely matches the moment magnitude (M_W) for small-to-moderate events. More particularly for Türkiye, the study of [144] put forward an empirical conversion equation from M_W to M_L. M_L values of the earthquakes in this thesis have been converted to M_W based on this equation. However, M_W values provided by KOERI for several events in the database exhibit inconsistency with the M_W estimations. That's why, this thesis favours the assumption of moment and local magnitude equality. Furthermore, as the geometry of fault rupture is missing for the majority of small-to-moderate earthquakes in our database, the consistency analyses incorporate the epicentral distance (R_{EPI}) which can be assumed to be identical to R_{JB} for this magnitude level ($M < 6.0$) [61].

3.2. Consistency Evaluation via Comparison of Distance Scalings

The distance scaling of the PGA, PGV, SAs at various periods, AI and CAV is examined initially in order to assess the compatibility between observed GMPs and empirical model estimations. A two-step nonlinear least squares regression is carried out on the complete database ($M_L \leq 5.7$) as well as on subsets that are grouped according to their earthquake magnitudes with the goal of making the comparison process easier. By emphasizing that the primary objective here is not to formulate a ground motion model for İstanbul, it is not recommended to utilise the produced empirical equation in the estimation of GMPs. The functional forms of all selected GMPEs are mainly similar to each other due to portraying well the physical concepts of a GMP estimation. This fact has prompted us to employ the functional form that are similar to the GMPEs selected rather than seeking a new functional form. The expressions of source and path features are chosen similarly to ASB14 whereas nonlinear soil amplification is disregarded due to inadequate ground motions recorded in soft soils and hinge-magnitude breaking is not incorporated similarly to SA17. The empirical ground motion equations are generated based on the following functional form:

$$\ln(GMP) = f(M_L) + f(M_L, R_{EPI}) + f(V_{S30}). \tag{3.1}$$

Herein, GMP stands for the geometric mean of two horizontal components for the interested parameter such as PGA, PGV, SAs, AI or CAV. $f(\mathrm{M_L})$, $f(\mathrm{M_L},\mathrm{R_{EPI}})$ and $f(\mathrm{V_{S30}})$ can be written as

$$f(M_L) = a_2(M_L - 6.75) + a_3(8.5 - M_L)^2, \quad (3.2)$$

$$f(M_L, R_{EPI}) = [a_4 + a_5(M_L - 6.75)]\{ln(\sqrt{R_{EPI}^2 + a_6^2}), \quad (3.3)$$

$$a_1 = f(V_{S30}) = b_1 + b_2 \ln(V_{S30}), \quad (3.4)$$

and refers to source, path and soil condition terms, respectively. Regression coefficients are depicted by a_1, a_2, a_3, a_4, a_5, a_6, b_1 and b_2. Independent variables are also represented by local magnitude ($\mathrm{M_L}$), epicentral distance ($\mathrm{R_{EPI}}$) and average shear wave velocity for the upper 30 m depth ($\mathrm{V_{S30}}$) in the functional form. The numerical figures, such as $\mathrm{M_{hinge}}$=6.75, have been directly retrieved from ASB14 and are not produced as part of the regression study.

The functional form (3.1) is used to execute a nonlinear regression analysis at the first stage, with the premise that the soil condition term serves as a second constant regression coefficient (a_1, in order to obtain the regression coefficients of the source and path expressions. The second stage regression is performed by using a_1, which is obtained as an outcome of the first step of the regression analysis, through expression (3.4) considering $\mathrm{V_{S30}}$ values of recording sites. As a result of two-stage nonlinear regressions, coefficients for eight GMPs (PGA, PGV, SAs (T=0.4; 0.6; 1.0; 2.0 s, ξ=5%), AI, CAV) are tabulated in Table 3.2 for the regression analysis of the entire database.

Additionally, magnitude-based subgroups are subjected to two-stage regression analyses employing a similar regression framework. However, since the amount of data is not sufficient at each magnitude level, the estimations might not be representative for each sub-dataset. The numerical values of each magnitude-based regression coefficient are not included in the main text of the thesis. To provide the unity of the study, the magnitude-based regression coefficients are provided in Appendix A.

Table 3.2. Total-database regression coefficients.

Ground Motion Parameter	b_1	a_2	a_3	a_4	a_5	a_6	b_2
PGA	14.2428	3.4262	0.1849	-1.4793	0.0173	6.1446	-0.5059
PGV	10.7527	3.7097	0.2817	-0.7863	0.1957	4.8556	-0.8091
SA (T=0.4 s)	16.5390	4.1206	0.2395	-1.1216	0.0253	8.4275	-0.9698
SA (T=0.6 s)	13.4576	3.7392	0.3219	-0.2891	0.2917	7.6062	-1.0900
SA (T=1.0 s)	12.7222	3.9846	0.3681	-0.0386	0.3633	8.5129	-1.2125
SA (T=2.0 s)	13.0681	6.0296	0.4721	-0.5750	0.1042	4.2357	-1.0594
AI	23.2495	7.6536	0.3913	-2.8589	-0.1340	9.2770	-1.3501
CAV	17.3609	5.6631	0.3665	-1.5215	-0.2338	16.6749	-0.7902

The graphs between Figure 3.1 and Figure 3.8 compare the distance scalings of the total and magnitude-based models generated in the current study to the median estimates of the selected predictive models, along with the GMPs (PGA, PGV, SA (T=0.4, 0.6, 1.0, and 2.0), AI and CAV) determined from recorded data. In all comparison graphs, different hues of the data analyzed represent the individual earthquakes at each magnitude level and the median estimations of ground motion models are computed by factoring in the average V_{S30} value ($V_{S30,average}$=527 m/s) of the recording sites. The distance scalings of observed PGA, PGV and SAs for periods of 0.4 s, 0.6 s, 1.0 s and 2.0 s are compared to five ground motion models one of which possesses regression coefficients for both R_{EPI} and R_{JB} whereas only R_{JB}-based SA17 is utilised to check the compatibility with observed data and empirical equation generated in this thesis.

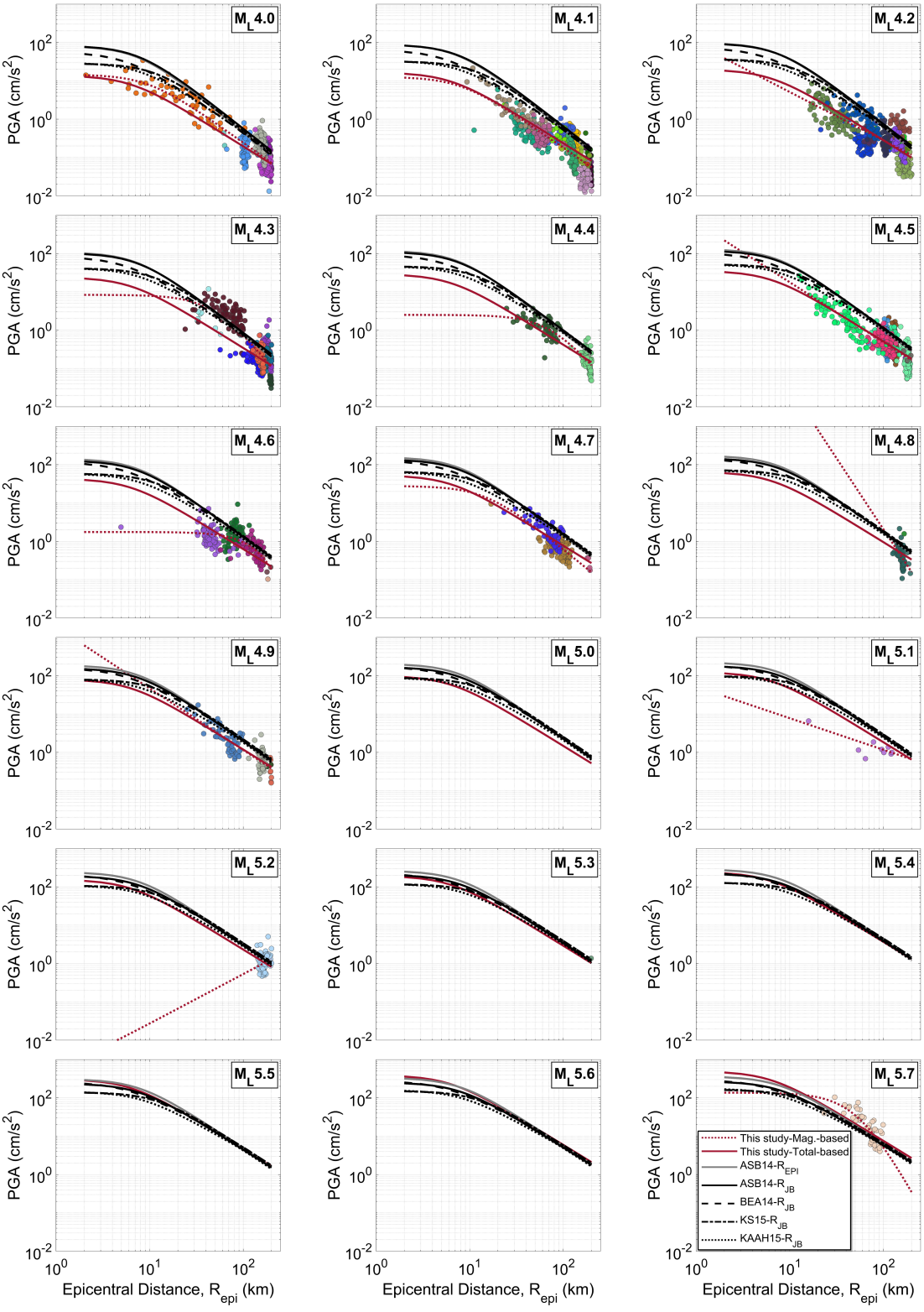


Figure 3.1. Comparison of GMPEs' Median PGA Estimates with Prediction Curves of this Thesis for V_{S30} = 527 m/s. (Marker colours denote distinct events).

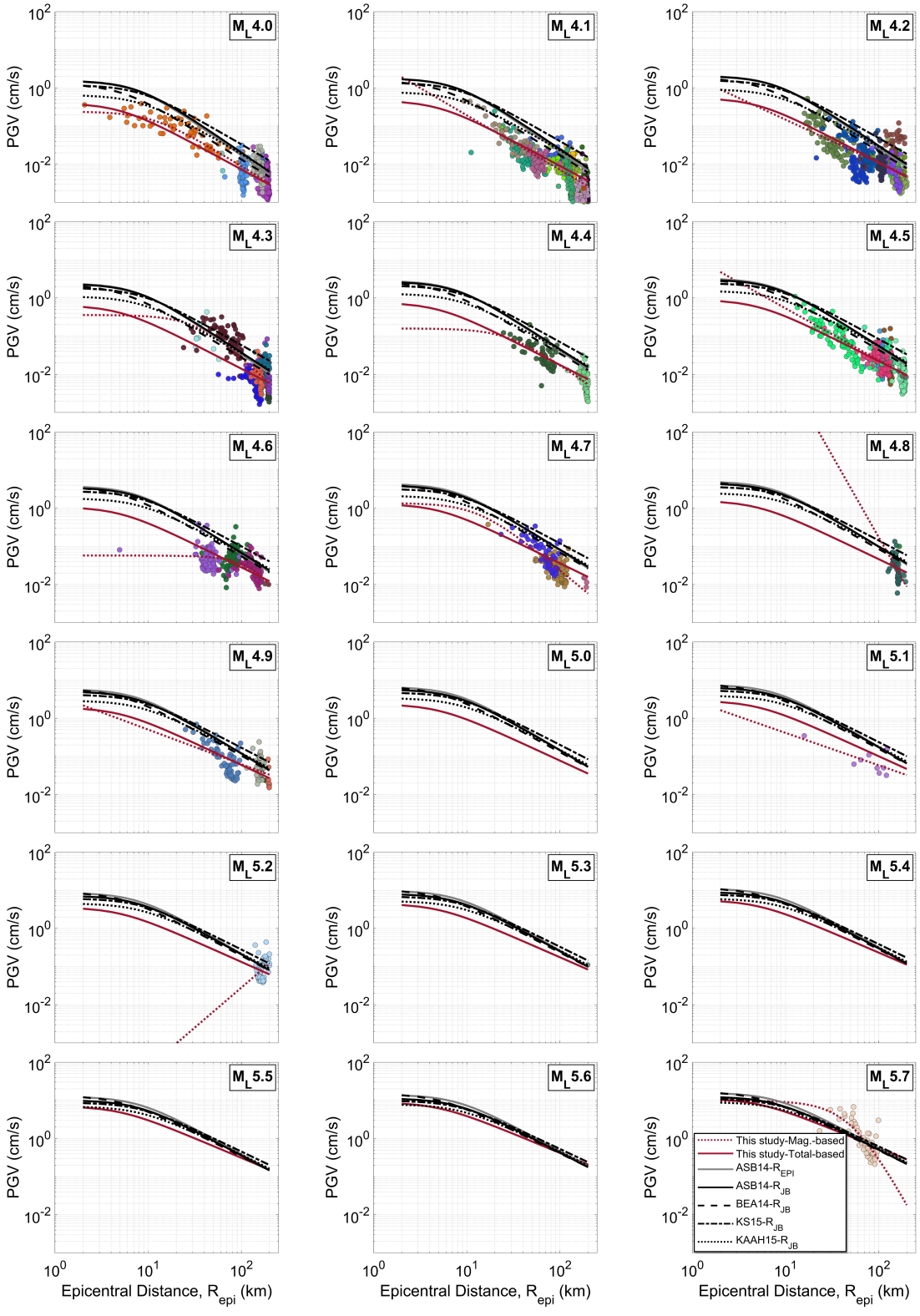


Figure 3.2. Comparison of GMPEs' Median PGV Estimates with Prediction Curves of this Thesis for V_{S30} = 527 m/s. (Marker colours denote distinct events).

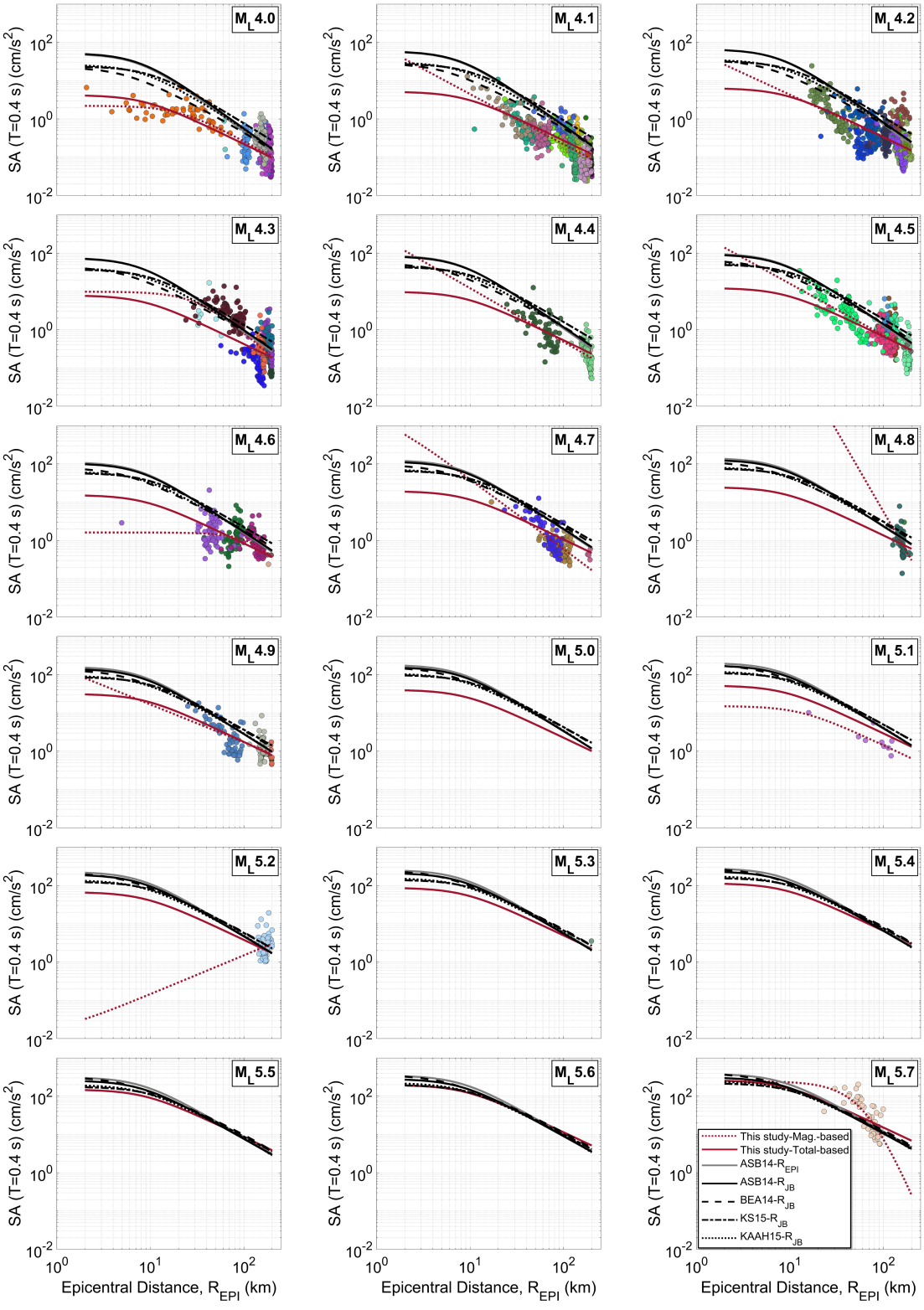


Figure 3.3. Comparison of GMPEs' Median SAs (T=0.4 s, ξ=5%) with Prediction Curves of this Thesis for V_{S30} = 527 m/s. (Marker colours denote distinct events).

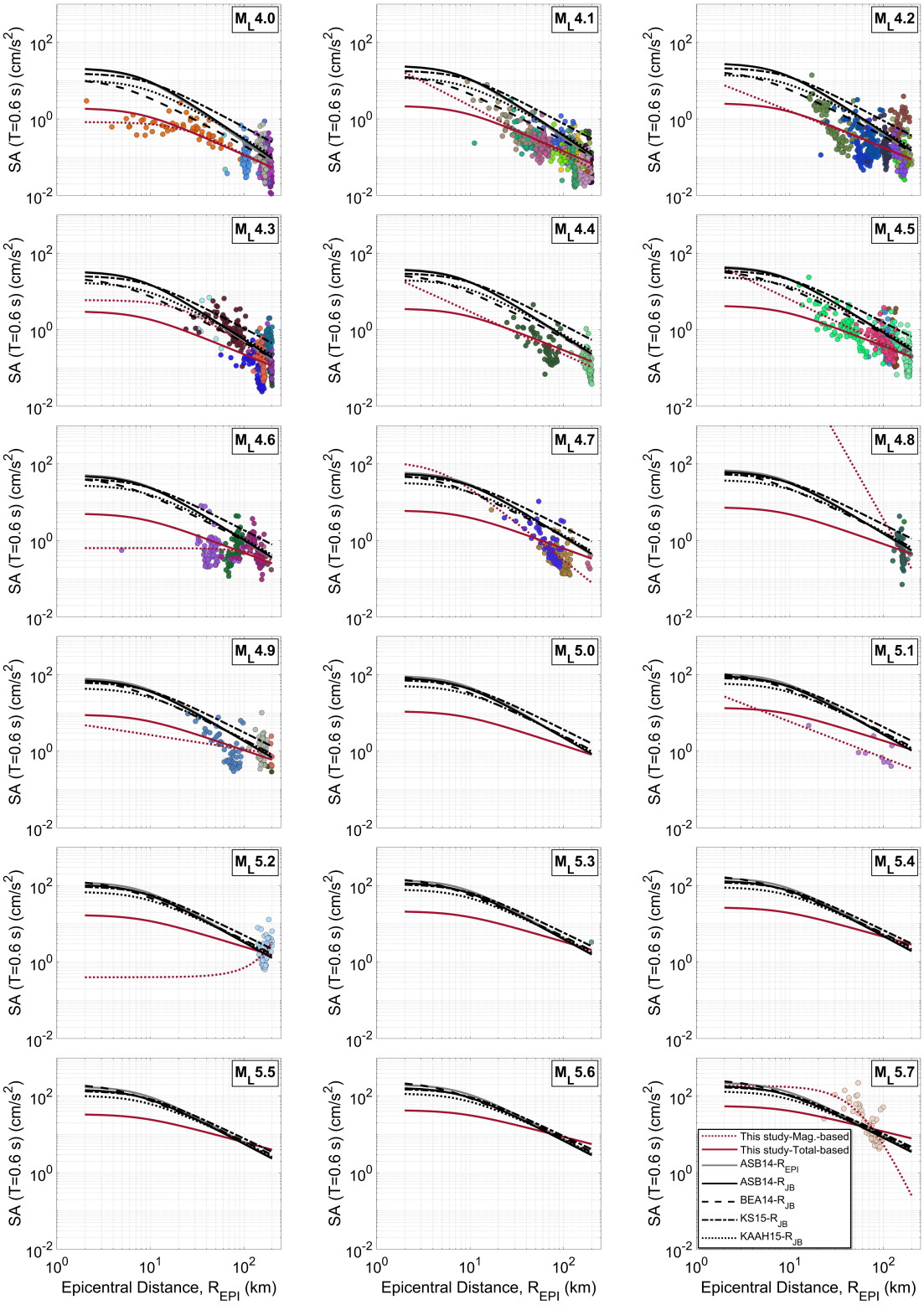


Figure 3.4. Comparison of GMPEs' Median SAs (T=0.6 s, ξ=5%) with Prediction Curves of this Thesis for V_{S30} = 527 m/s. (Marker colours denote distinct events).

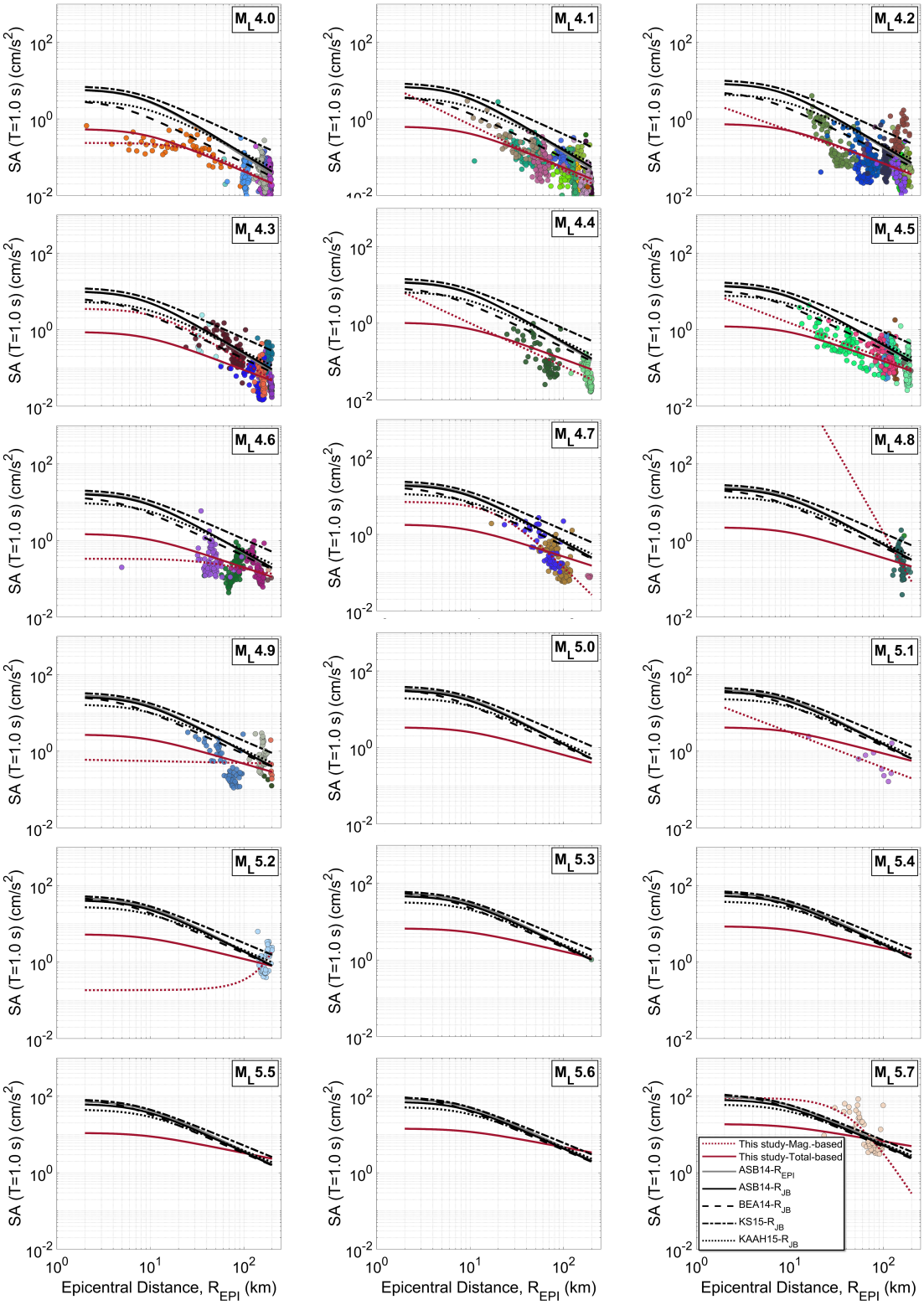


Figure 3.5. Comparison of GMPEs' Median SAs (T=1.0 s, ξ=5%) with Prediction Curves of this Thesis for V_{S30} = 527 m/s. (Marker colours denote distinct events).

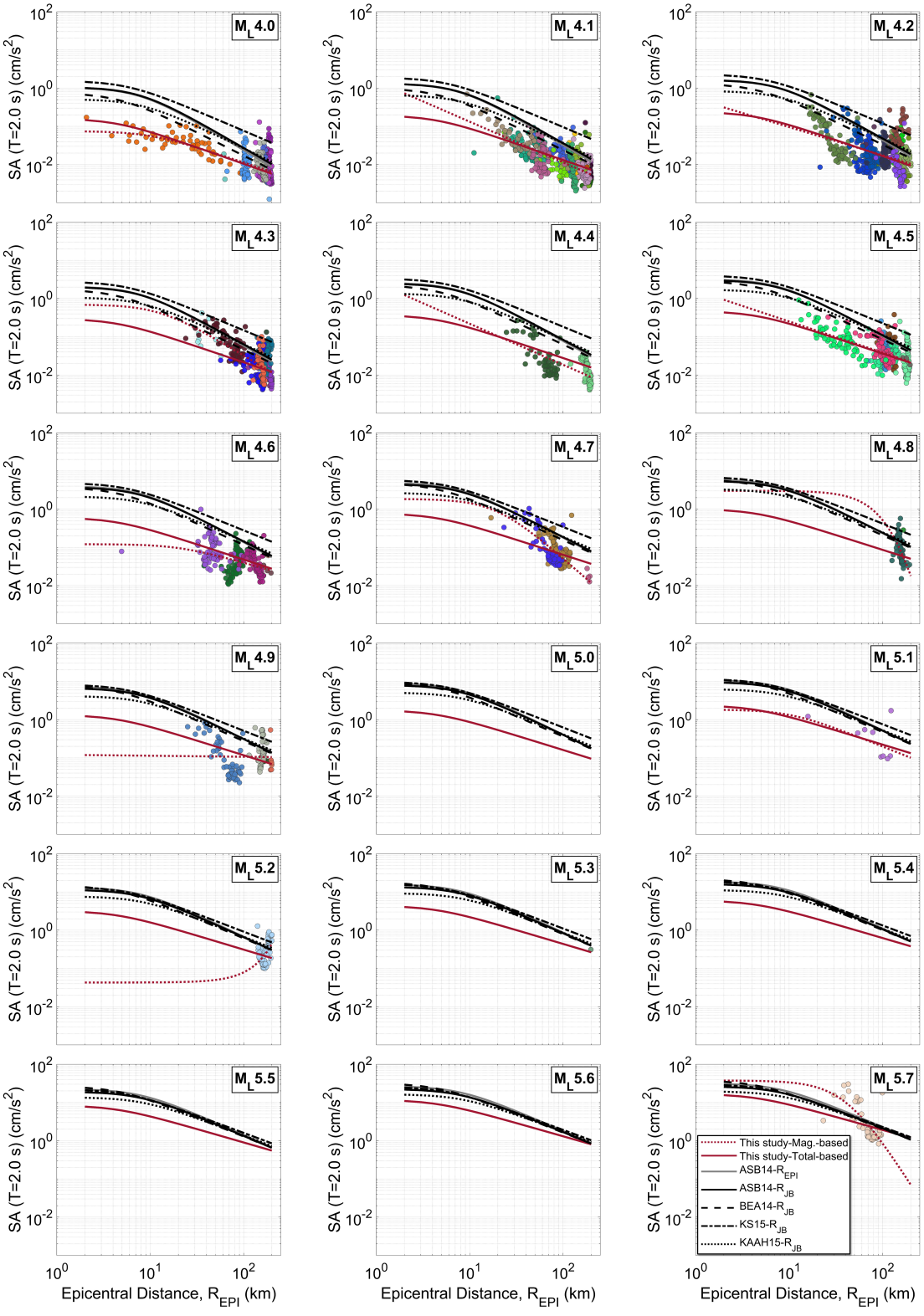


Figure 3.6. Comparison of GMPEs' Median SAs (T=2.0 s, ξ=5%) with Prediction Curves of this Thesis for V_{S30} = 527 m/s. (Marker colours denote distinct events).

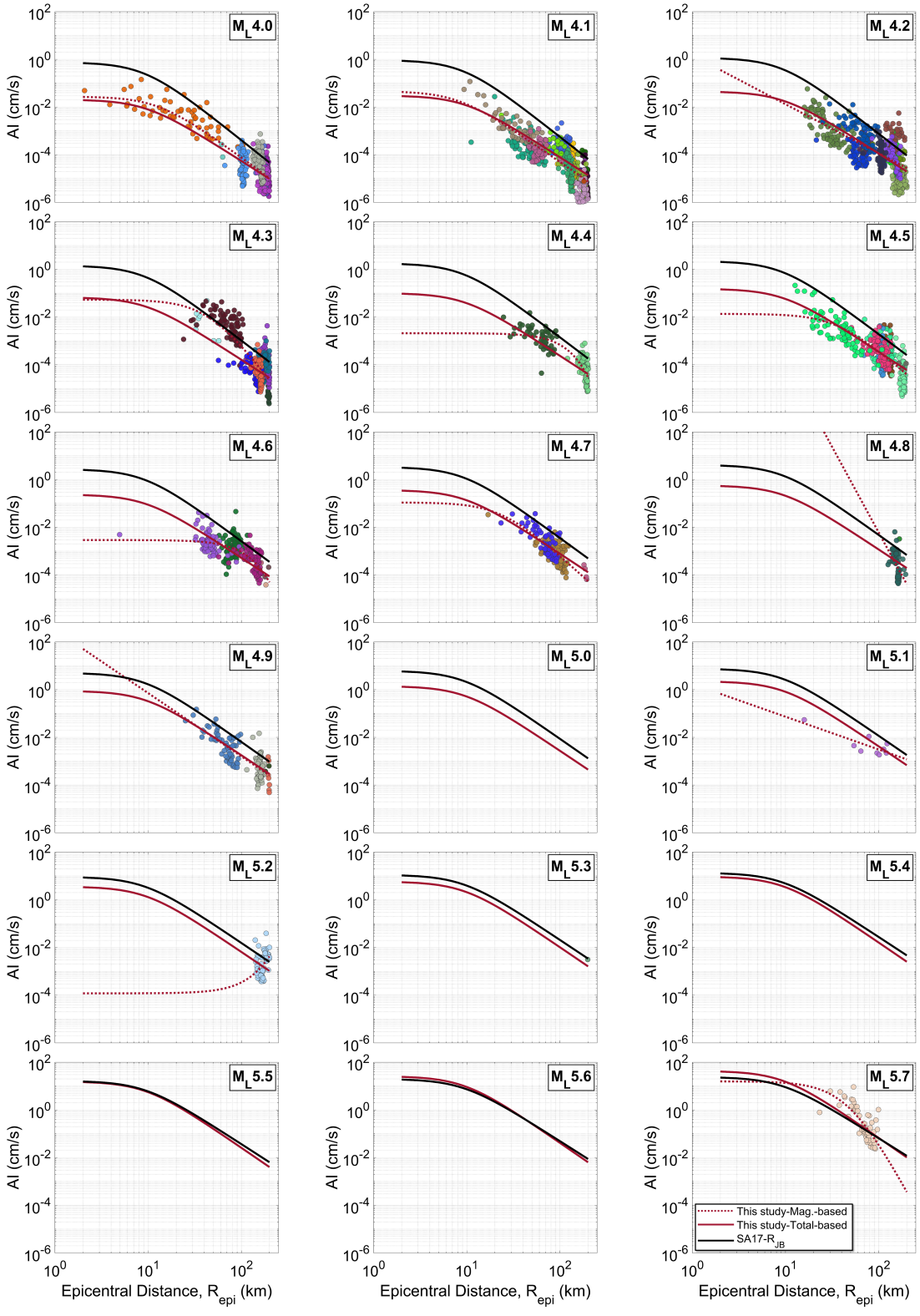


Figure 3.7. Comparison of GMPE's Median AI Estimates with Prediction Curves of this Thesis for V_{S30} = 527 m/s. (Marker colours denote distinct events).

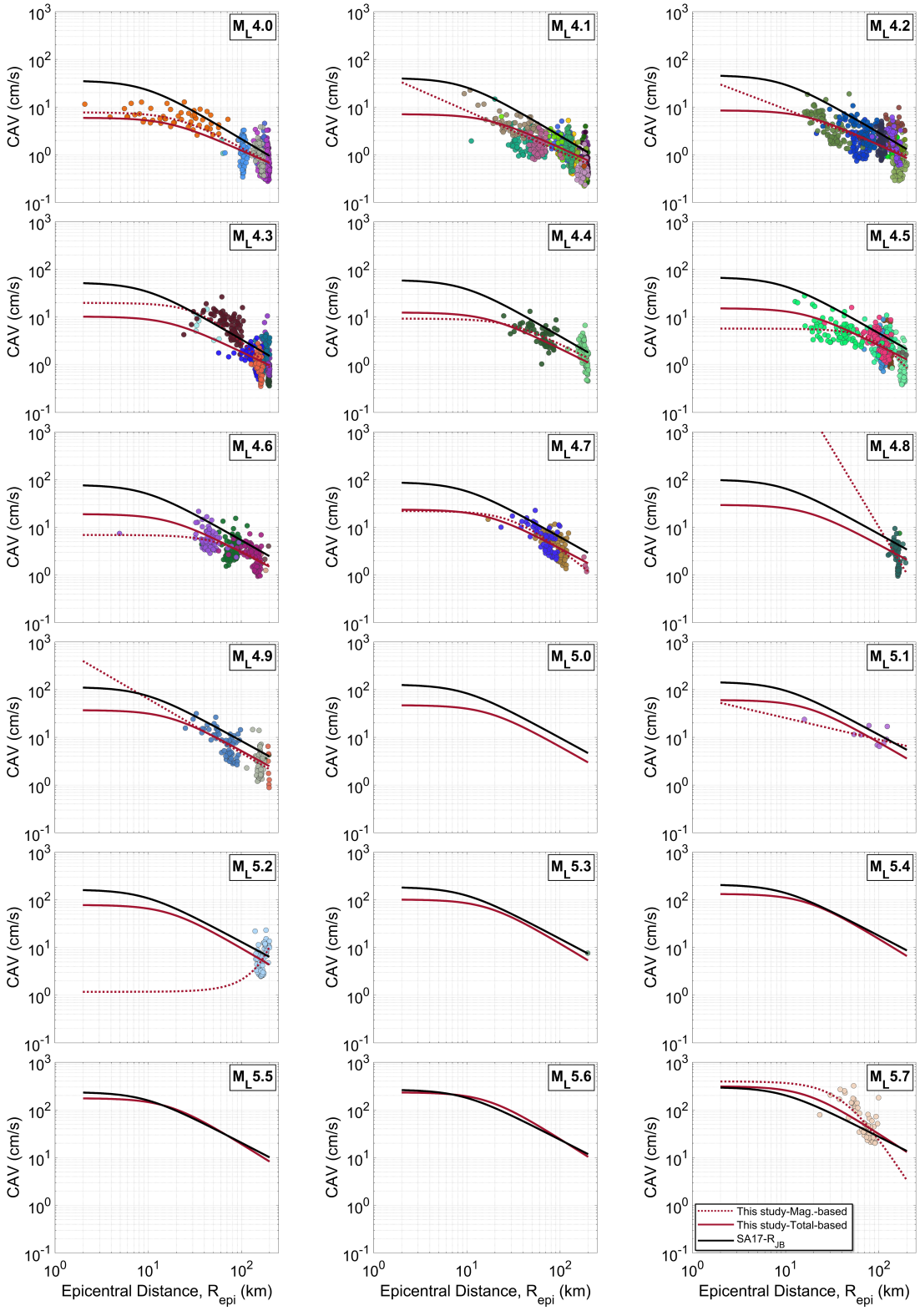


Figure 3.8. Comparison of GMPE's Median CAV Estimates with Prediction Curves of this Thesis for V_{S30} = 527 m/s. (Marker colours denote distinct events).

The attenuation behaviours of total-based regressions seem to match the actual GMPs. However, this is not an unexpected situation since the regression database, which results in total-based estimation lines, includes these same actual data. Meanwhile, the magnitude-based regression estimations for M_L4.0 and M_L4.1 are also congruent with the total-based lines in that the observed data for these magnitude levels appear to be more uniformly spread over R_{EPI} in contrast to data for greater magnitudes. Although our estimates and the data match up, plenty of data points appear to be higher and lower than the total-based estimation line. So, it is not possible to enumerate each GMP precisely for each event at each station, in other words, only one regression line may not accurately reflect all data, since the median estimates are the outcome of a statistical procedure.

The overestimation tendency of GMPEs is explicitly unveiled by comparative figures of attenuation with distance for all parameters inspected herein. This finding is corroborated by the assertion that Turkiye's regional ground motion models feature lower estimations than those of BEA14 in the study of [67]. With the exception of a few data points, the median estimations of all ground motion models yield greater values than the observed GMPs and estimation line of this thesis while they become closer to the estimations of this study with the increase in magnitude. However, it should be reminded that since the database of this study suffers from a lack of data mostly over M_L5.0, one should evaluate this judgment with hesitation for these magnitude levels. The close agreement between the median ASB14 estimations based on the R_{EPI} and the R_{JB} may be a testimony that employing the assumption of $R_{EPI} \approx R_{JB}$ is unlikely to lead to any discrepancies in the consistency evaluation for these magnitude levels.

Up to M_L5.0, this study's estimated PGAs consistently fall below the median lines of GMPEs. Until this level of magnitude, as it gets closer to the epicentre, KAAH15 predicts PGA values that are the closest to the estimation line of this thesis among five ground motion models, but as it gets farther away, all GMPEs produce similar PGAs. Also, the most distant GMPE to the predictions of this thesis seems to be ASB14. Once the M_L exceeds 5.0, our PGA estimates start to align closely with the estimations released by GMPEs and the estimation line of this study slightly surpasses

all GMPEs in the M_L5.7 subgroup, which consists of just one event (the 2019 Silivri earthquake). Hence, all GMPEs demonstrate a consistent inclination to underestimate at this particular magnitude (M_L5.7) level.

Similar to PGA, PGV estimations of this study get closer to the GMPEs' median lines as the magnitude raises. However, they never go beyond them, unlike PGA, at any magnitude level. KAAH15 offers estimations that most closely coincide with the prediction line from this study. While the GMPE that mostly results in the highest PGVs becomes ASB14 at closer distances, KS15 provides mostly the largest PGV estimations at longer distances, whose breaking point goes further with the increase in magnitude.

GMPEs yield the higher SAs at each selected period (T=0.4; 0.6; 1.0; 2.0 s) and their overestimation capacity seems to be more explicit than the PGAs. This finding is also reinforced by [75], which uses IERREWS and AFAD data exclusively for the 2019 Silivri earthquakes (M_L4.5 and M_L5.7). Despite SA estimates of this thesis closely matching and slightly surpassing those of GMPEs for 5.7 at further distances, their overestimation tendency still remains apparent in SA (T=0.4 s). The gaps between the estimation of this study and the median predictions of GMPEs are most pronounced at relatively short-to-medium periods (T= 0.6 and 1.0 s) at close distances, yet these differences seem to narrow at T= 2.0 s. Furthermore, KS15 behaves identically to PGV in terms of having an overestimation capacity for predicting at farther distances for SA (T= 0.4 s). As the period lengthens (T=0.6; 1.0; 2.0 s), this trend begins to also be observed in the near-field region by exceeding the SA estimations of ASB14, which produces the highest PGA estimates.

SA17 tends to overestimate the energy-based GMPs (AI and CAV), which account for the complete duration of ground motion and its frequency content. Parallel to peak ordinates and spectral quantities, the estimation line established in this study approaches the predictions of SA17 as the magnitude gets bigger and slightly exceeds at the magnitude levels 5.6 and 5.7. According to the comparison of SA17 with the AI and CAV estimations of ground motion models proposed in [145] and [146] in the

paper of Sandıkkaya and Akkar [142], SA17 seems to produce the lowest estimations in the magnitude and distance range of the aforementioned study.

3.3. Consistency Evaluation via Residual Analysis

It is feasible to assess the variation of the differences between GMPs observed and estimated through residuals, which is a comparative analysis approach employing the natural logarithmic domain, in order to delve into the potential sources of uncertainties that the empirical ground motion models did not account for, as well as their connection with the main dependent parameters. The predictive capability of a ground motion model outperforms as the residuals approach zero, but an increase in either the negative or positive direction highlights the model's tendency to overestimate or underestimate, respectively. The term "total residual, ($\delta_{GMP,es}$)" stands for the difference between the estimated ($GMP_{estimated,es}$) and observed ($GMP_{observed,es}$) GMP in the natural logarithm domain [147], as expressed by

$$\delta_{GMP,es} = ln(GMP_{observed,es}) - ln(GMP_{estimated,es}). \tag{3.5}$$

Herein "e" and "s" are served as indices to denote different stations and events.Also, $\delta_{GMP,es}$ can be expressed by the sum of the between-event ($\delta B_{GMP,e}$ or inter-event) and within-event residuals ($\delta W_{GMP,es}$or intra-event) [148] as seen below:

$$\delta_{GMP,es} = \delta B_{GMP,e} + \delta W_{GMP,es}. \tag{3.6}$$

Understanding the underlying causes of distinctions between GMPs recorded and estimated may be ensured by the categorization of total residuals into their constituent parts. $\delta W_{GMP,es}$ are indicative of the variability due to path and site impacts for each particular event, whereas $\delta B_{GMP,e}$ account for the variability across different events, primarily due to source effects such as stress-drop, slip irregularities etc.

$$\delta B_{GMP,e} = \frac{\sum_{s=1}^{N_{st}} ln(GMP_{observed,es}) - ln(GMP_{estimated,es})}{N_{st}}. \tag{3.7}$$

The mean difference between the $GMP_{observed,es}$ and the associated $GMP_{estimated,es}$ for each event can provide between-event residuals through a least-squares method, as outlined by [149] (Equation (3.7)).

$\delta W_{GMP,es}$ predominantly portray the role of ground motion variability attributable to crustal heterogeneity, geological disparities, azimuth-dependent directional features, and other site- and path-specific components and can be determined by using equations embodied in (3.5) and (3.6) as follows;

$$\delta W_{GMP,es} = ln(GMP_{observed,es}) - [\ln(GMP_{estimated,es}) + \delta B_{GMP,e}]. \quad (3.8)$$

Total, between-event and within-event residuals calculated by considering GMPs acquired from recordings and their median estimations by the ground motion models chosen for PGA, PGV, SAs (T=0.4; 0.6; 1.0; 2.0 s), AI and CAV will be scrutinized in the subsequent sections. It is essential to underline that the individual V_{S30} values of each station, in lieu of an average V_{S30}, are considered when calculating the GMPs through GMPEs in the residual analysis.

3.3.1. Total Residuals with Distance

The analysis results of total residuals are presented in Figure 3.9 through Figure 3.12 for the GMPs mentioned in the previous section. The individual total residuals exhibit a distribution across both negative and positive residual ranges, with a notable concentration in the negative zone for all GMPs.

Additionally, a basic statistical assessment is conducted on the total residuals for distance intervals spanning 10 kilometres. The 16^{th} (-1σ), 50^{th} (mean) and 84^{th} ($+1\sigma$) percentile of the normal distribution for each distance bin are depicted by the error bars in the figures. The mean and 16^{th} percentile total residual variations of each bin appear to systematically be in the negative zone, clearly demonstrating the overestimation patterns of ground motion models for all GMPs. As well, a significant portion of the total residuals at the 84^{th} percentile predominantly possess negative values, with only a small number barely crossing the zero threshold. The overestimation attenuation patterns of GMPEs stated in the preceding section are bolstered by the findings deduced from the examination of total residuals.

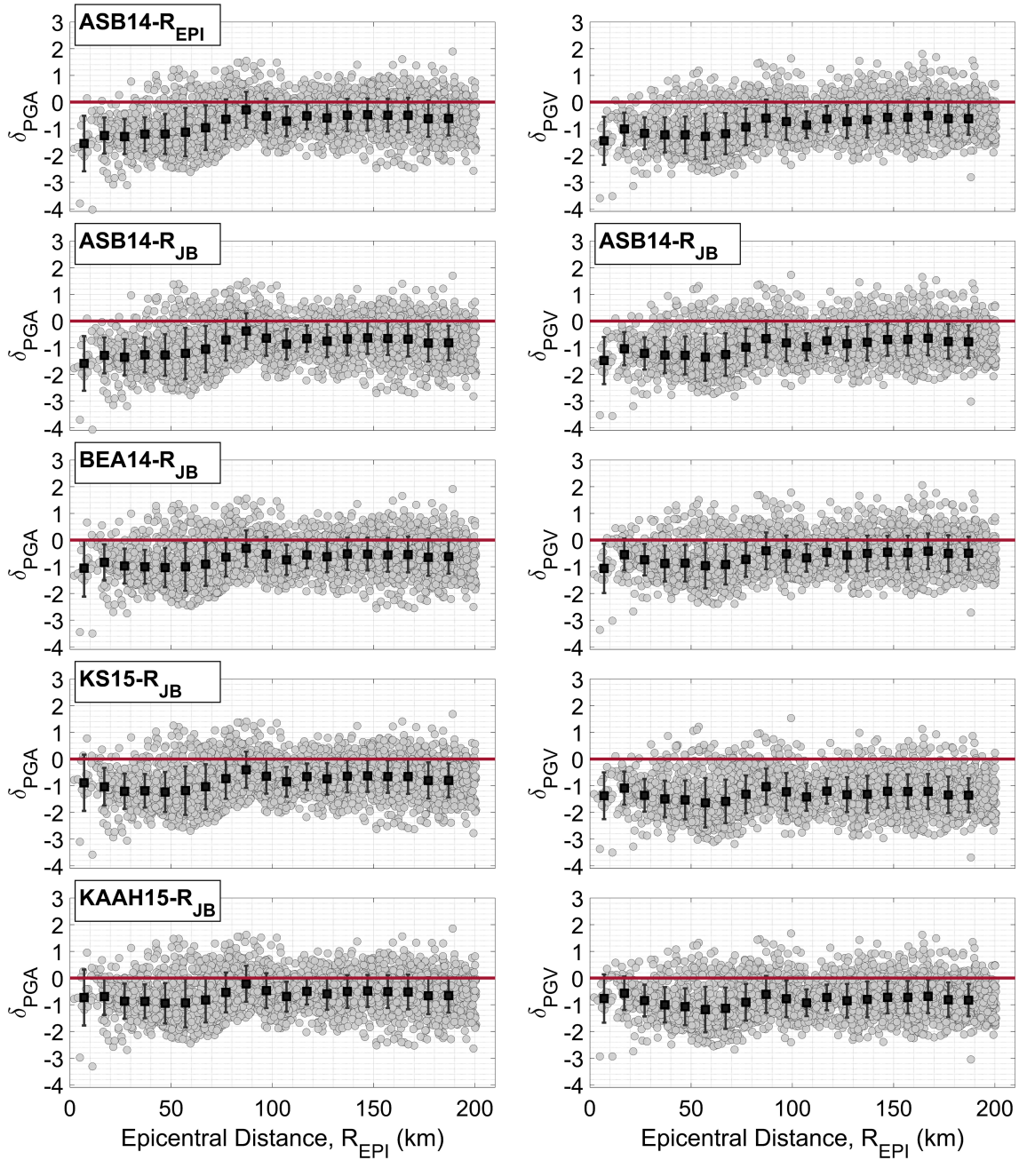


Figure 3.9. Variation of the Total Residuals of PGA and PGV with R_{EPI} for the Selected GMPEs (Zero residuals are shown by the lines in red. Error bars stand for group means with 16^{th} and 84^{th} percentiles).

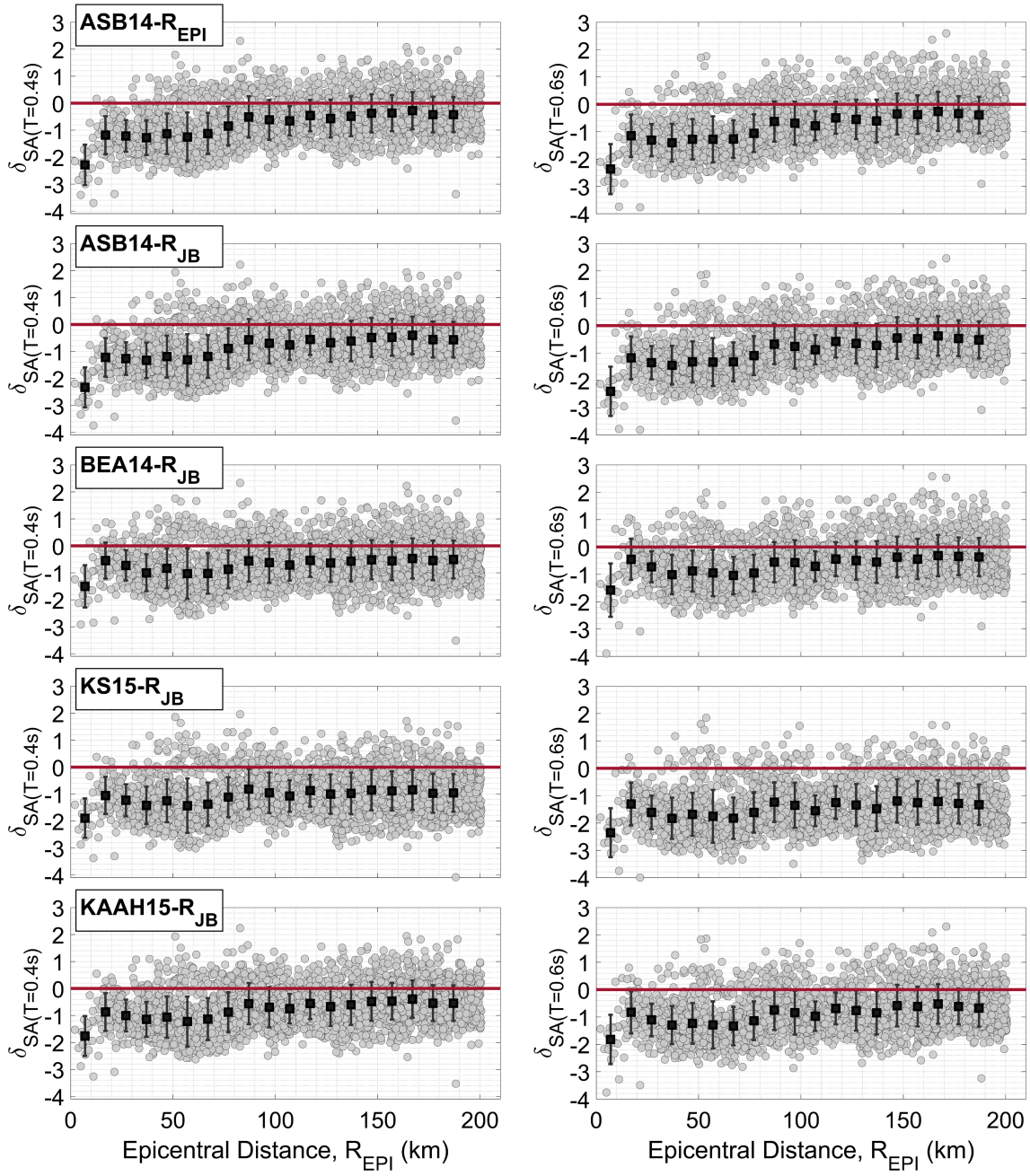


Figure 3.10. Variation of the Total Residuals of SA (T=0.4 s) and SA (T=0.6 s) with R_{EPI} for the Selected GMPEs (Zero residuals are shown by the lines in red. Error bars stand for group means with 16^{th} and 84^{th} percentiles).

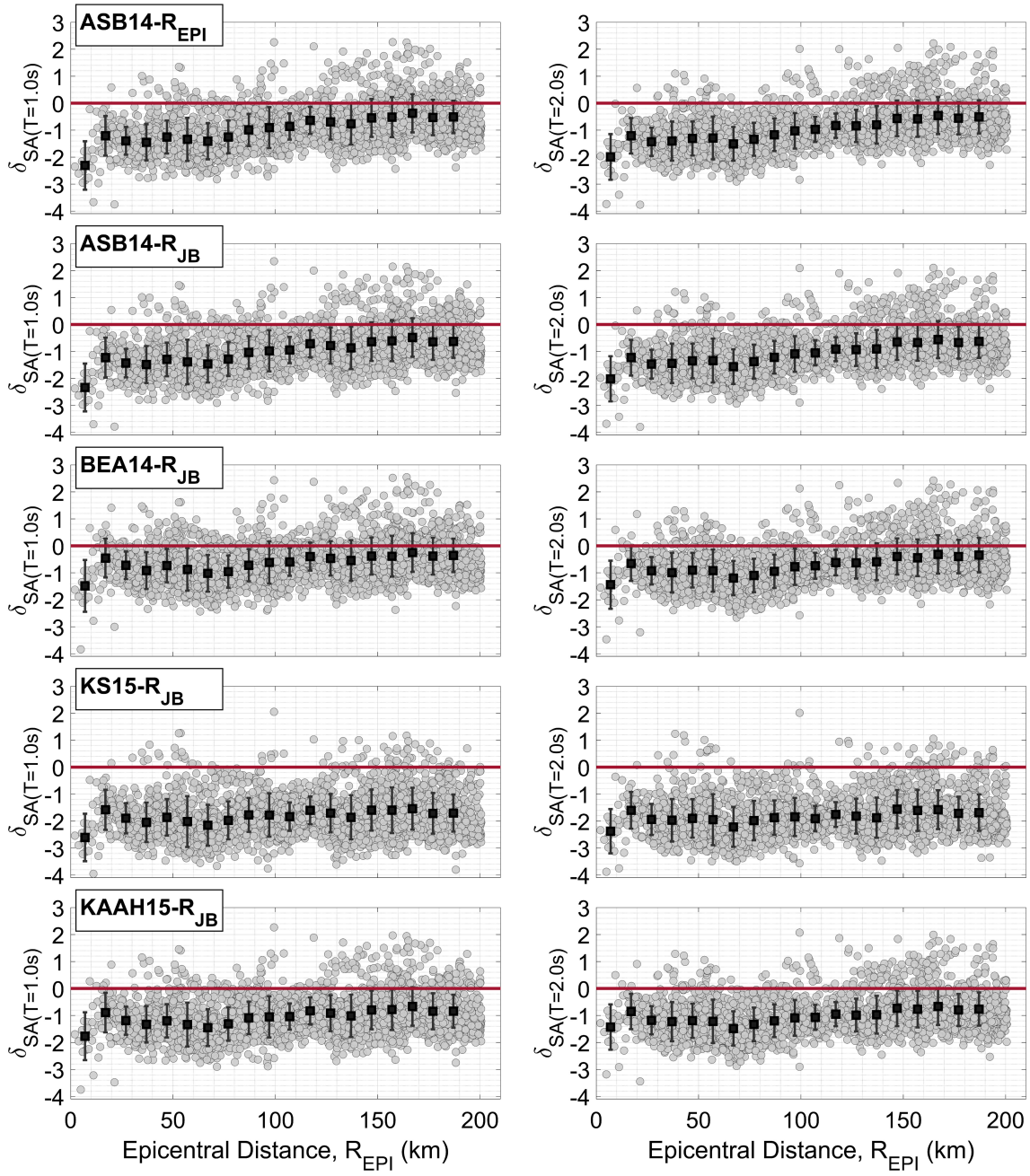


Figure 3.11. Variation of the Total Residuals of SA (T=1.0 s) and SA (T=2.0 s) with R_{EPI} for the Selected GMPEs (Zero residuals are shown by the lines in red. Error bars stand for group means with 16^{th} and 84^{th} percentiles).

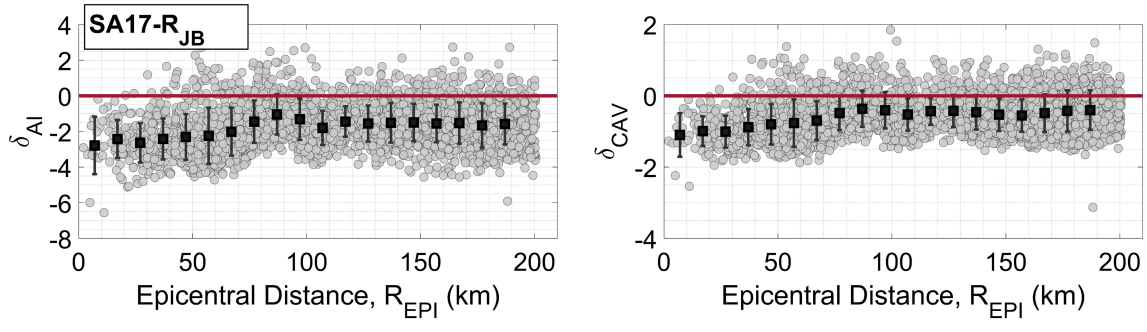


Figure 3.12. Variation of the Total Residuals of AI and CAV with R_{EPI} for the Selected GMPEs (Zero residuals are shown by the lines in red. Error bars stand for group means with 16^{th} and 84^{th} percentiles).

The fluctuations and relatively large negative residual tendency observed in the total residual plots of all GMPs before the 80 km deserve particular attention, while the total residuals appear to stabilize beyond this distance threshold. Through the entire range, peak ordinates and spectral accelerations appear to have relatively better agreement with KAAH15 and BEA14. The total residuals for AI and CAV seem to gradually converge toward the zero line while moving away from the epicentre, and after 80 km they remain relatively constant with an overprediction tendency.

3.3.2. Between-event Residuals with Magnitude

The between-event residuals are presented in Figure 3.13 to Figure 3.16, demonstrating the relationship with magnitude for all GMPs. The majority of the between-event residuals seem to be beneath the zero line. Similarly, the overestimation tendency can be identified in the mean of between-event residuals for bins with an interval of Δ_L=0.1 and their corresponding values that are 16^{th} and 84^{th} percentiles away from the mean. Also, it should be stated that since each bin group contains just one event, it is not able to compute the standard deviations for magnitude bins greater than M_L4.9. Moreover, the presence of single outlier data with larger between-event residuals in the M_L4.0 and M_L4.8 subsets leads to unusually large standard deviations in those cases.

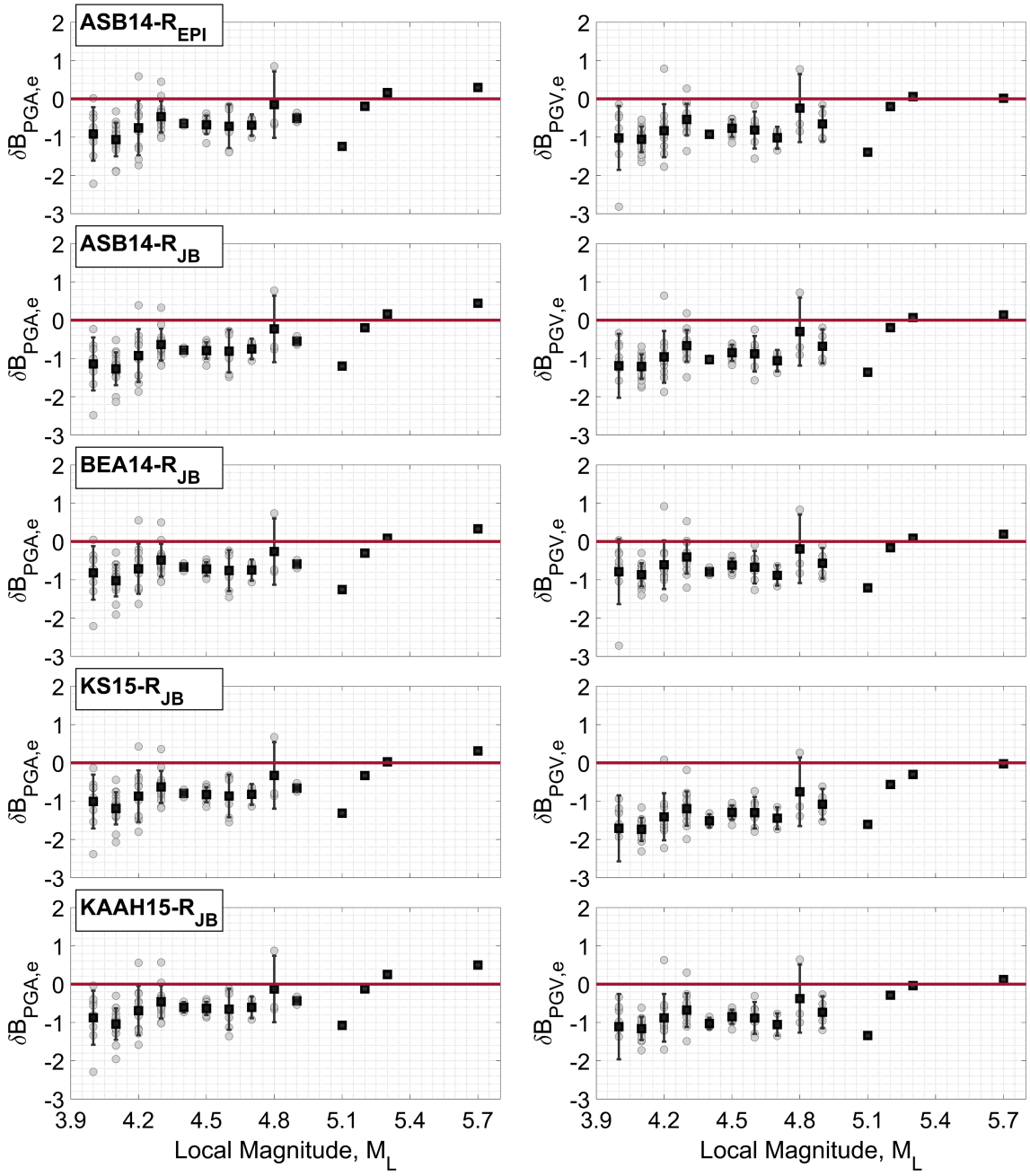


Figure 3.13. Variation of the Between-event Residuals of PGA and PGV with M_L for the Selected GMPEs. (Zero residuals are shown by the lines in red. Error bars stand for group means with 16^{th} and 84^{th} percentiles).

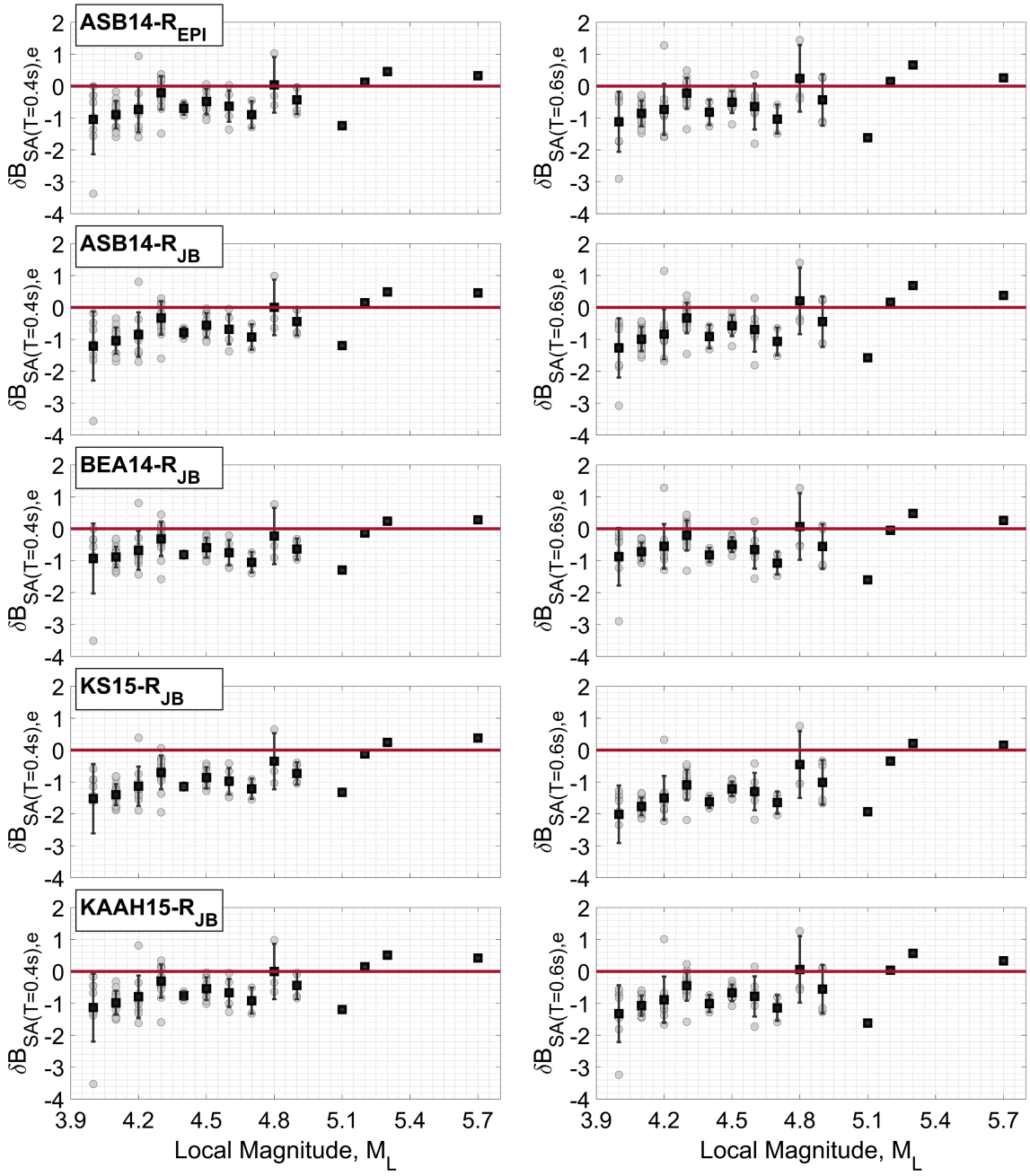


Figure 3.14. Variation of the Between-event Residuals of SA (T=0.4 s) and SA (T=0.6 s) with M_L for the Selected GMPEs. (Zero residuals are shown by the lines in red. Error bars stand for group means with 16^{th} and 84^{th} percentiles).

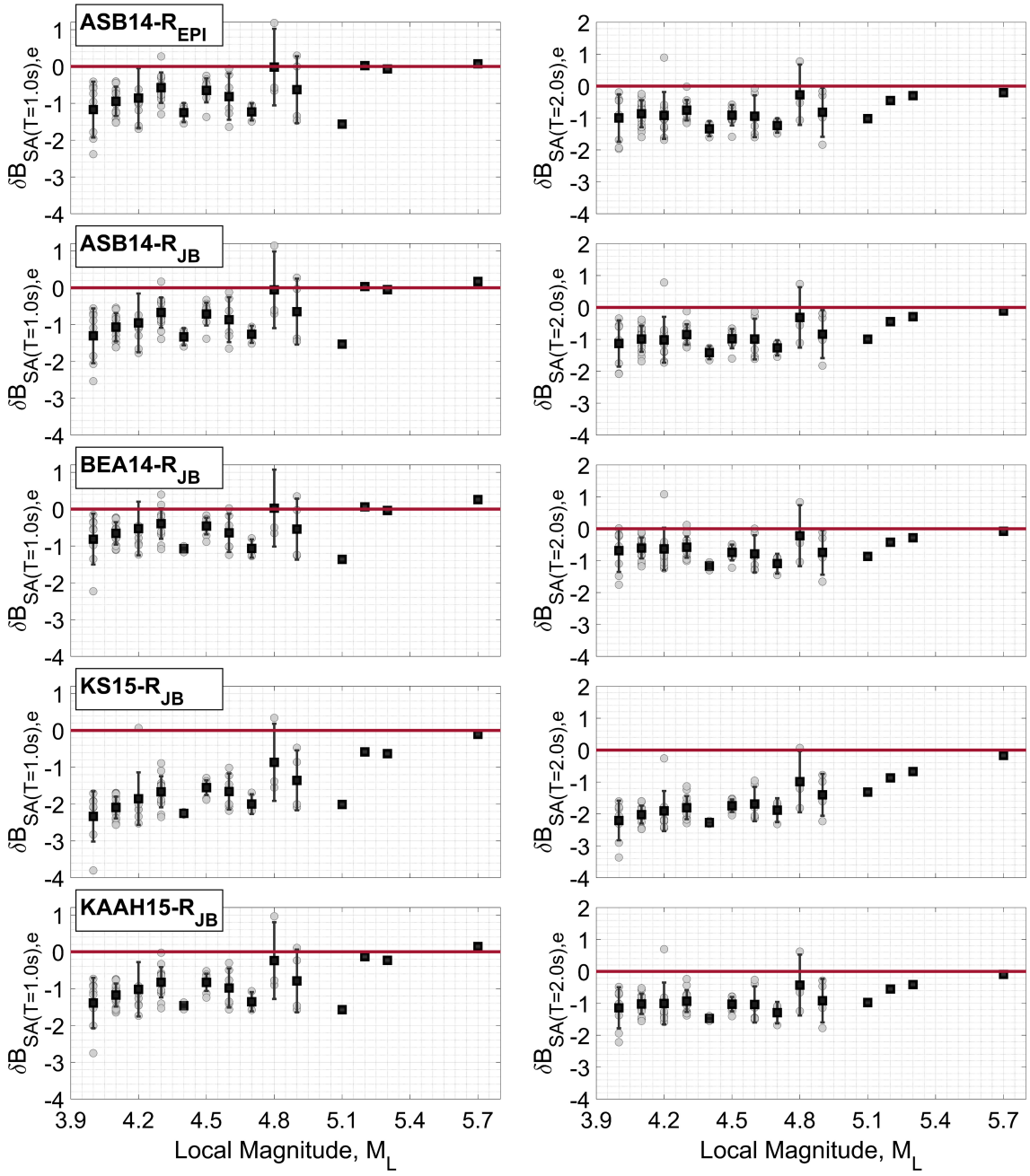


Figure 3.15. Variation of the Between-event Residuals of SA (T=1.0 s) and SA (T=2.0 s) with M_L for the Selected GMPEs. (Zero residuals are shown by the lines in red. Error bars stand for group means with 16^{th} and 84^{th} percentiles).

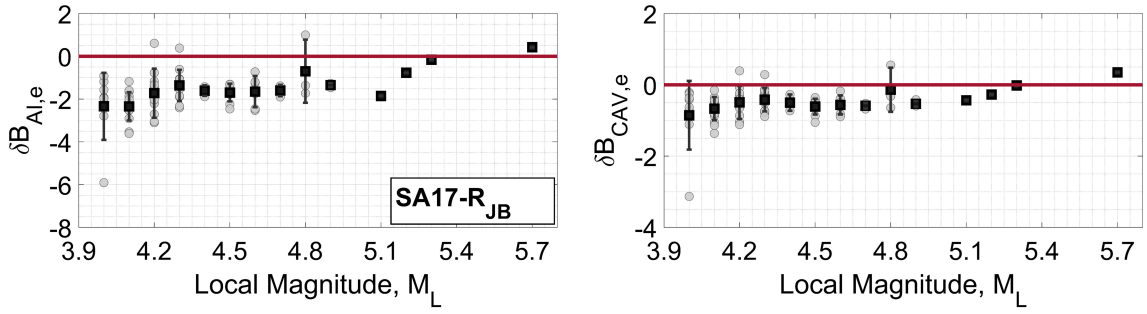


Figure 3.16. Variation of the Between-event Residuals of AI and CAV with M_L for the Selected GMPEs. (Zero residuals are shown by the lines in red. Error bars stand for group means with 16^{th} and 84^{th} percentiles).

It is challenging to pinpoint a precise systematic change in this overestimation pattern with respect to magnitude. This ambiguous variation with magnitude may be attributed to inadequate data for $M_L \geq 5.0$. The considerable dispersive trait of between-event residuals in Turkish data is also highlighted in [77], particularly when contrasted with data from Iran, despite the close geographic proximity of the two regions. Additionally, the comparison between the estimates of BEA14 and the GMPE of Akkar and Çağnan [74], which is derived from a database consisting of Turkish events, reveals a greater between- event sigma in the estimates of the Türkiye-based GMPE as emphasized in Bindi et al. [67]. These inferences announced by [77] and [67] reinforce the argument of this study that the scattered pattern in between-event residuals could be attributable to local source-related peculiarities.

While KAAH15 and BEA15 stands out for its relatively better performance by offering relatively smaller between-event residuals, KS15 is the ground motion model that exhibits the poorest ability to capture source-dependent variability for peak ordinates and spectral accelerations. As for the evaluation of energy-based parameters, SA17 appears to be better capable than AI in detecting the source-dependent variability in CAV.

3.3.3. Within-event Residuals with Distance

The within-event residuals, which are attributed to the variations arising from the propagation path and site-specific characteristics, display oscillations near the zero line, encompassing both negative and positive residual regions, with respect to source-to-site distance as observed in Figure 3.17 through Figure 3.20. This unbiased tendency with regard to R_{EPI} is more evident in the mean within-event residuals for each 10 km interval bin along the entire distance range regardless of the type of GMPs and for all ground motion models. However, irregular trends of within-event residuals with relatively higher $\pm 1\sigma$ are recognized in close proximity to the earthquake source particularly within the 20 km range which could be possibly linked to the insufficient near-field recordings.

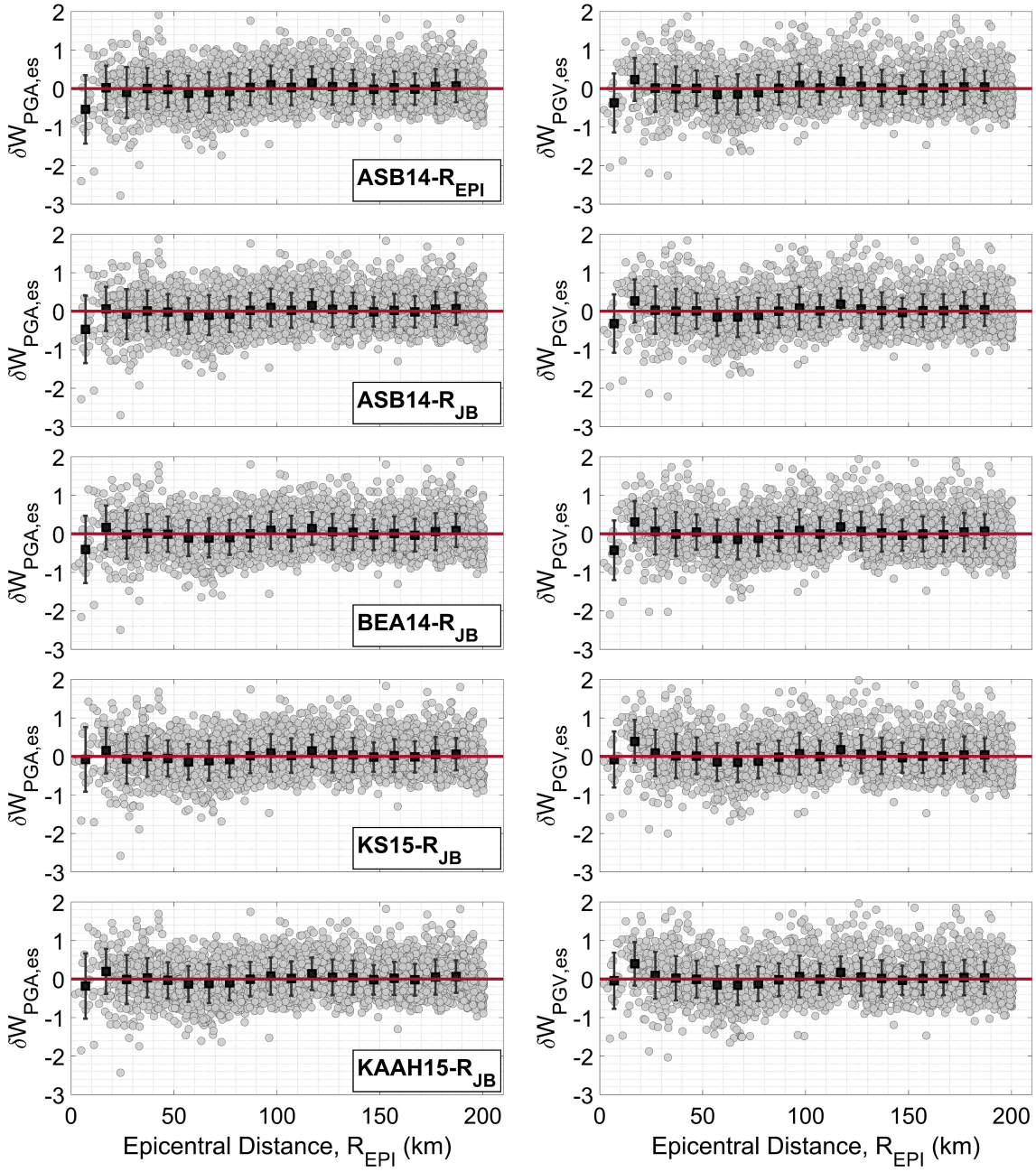


Figure 3.17. Variation of the Within-event Residuals of PGA and PGV with R_{EPI} for the Selected GMPEs. (Zero residuals are shown by the lines in red. Error bars stand for group means with 16^{th} and 84^{th} percentiles).

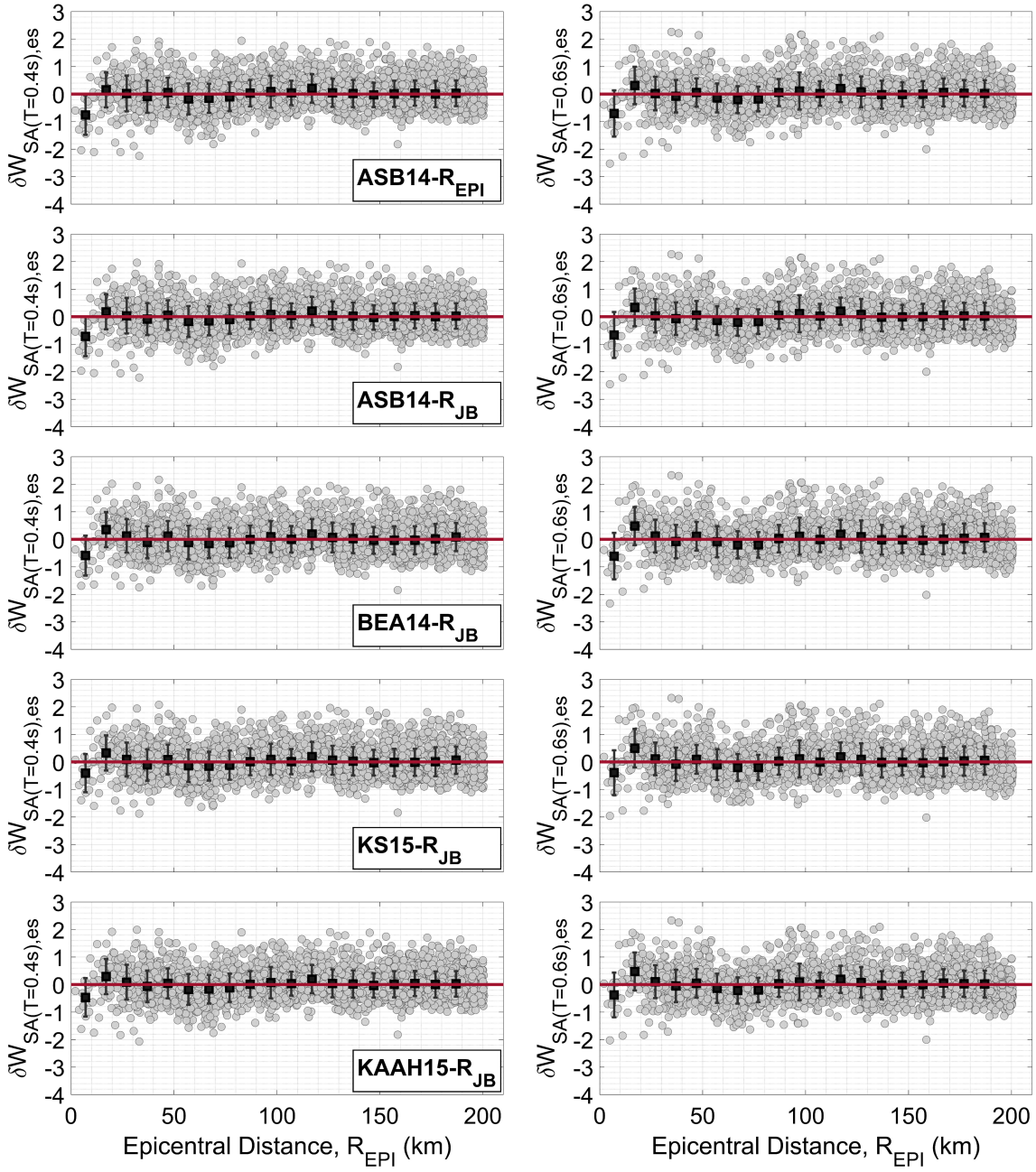


Figure 3.18. Variation of the Within-event Residuals of SA (T=0.4 s) and SA (T=0.6 s) with R_{EPI} for the Selected GMPEs. (Zero residuals are shown by the lines in red. Error bars stand for group means with 16^{th} and 84^{th} percentiles).

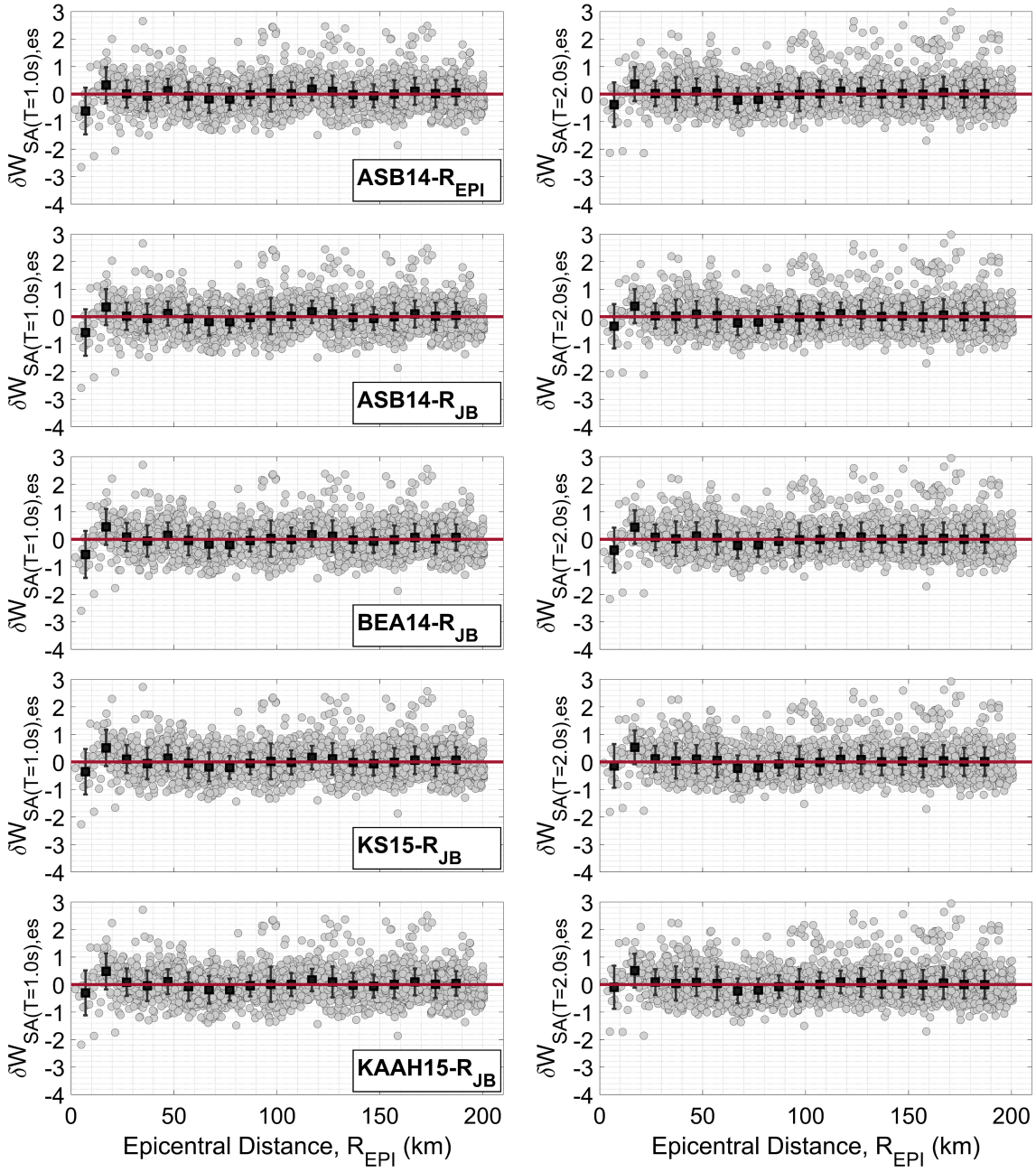


Figure 3.19. Variation of the Within-event Residuals of SA (T=1.0 s) and SA (T=2.0 s) with R_{EPI} for the Selected GMPEs. (Zero residuals are shown by the lines in red. Error bars stand for group means with 16^{th} and 84^{th} percentiles).

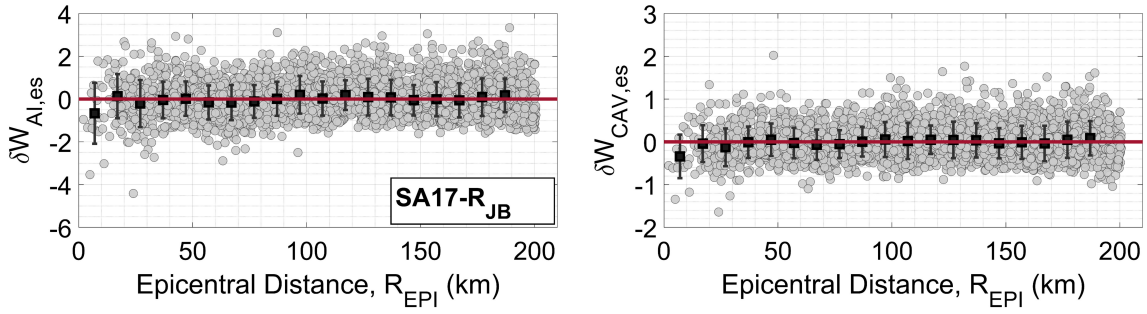


Figure 3.20. Variation of the Within-event Residuals of AI and CAV with R_{EPI} for the Selected GMPEs. (Zero residuals are shown by the lines in red. Error bars stand for group means with 16^{th} and 84^{th} percentiles).

3.3.4. Within-event Residuals with Soil Condition Parameter

The level of agreement between the observed GMPs and the predictions of GMPEs is also delved into estimator parameters related to soil conditions, such as V_{S30} in Figure 3.21 through Figure 3.24. There are no discernible patterns in the within-event residuals as a function of V_{S30}. The within-event residuals are additionally categorized into various V_{S30} subgroups, whose intervals are selected as 200 m/s, to figure out the variation of the average residuals for each GMP. The mean within-event residuals regarding V_{S30} display fairly similar trends to their variations as a function of R_{EPI}. Nevertheless, the most notable deviation of within-event residuals from the zero line is visible at V_{S30} = 500 m/s, which roughly corresponds to the average V_{S30} value across all stations. Subsequently, the variation in within-event residuals with regard to V_{S30} does not yield the clear statistical ramifications as those observed with R_{EPI}.

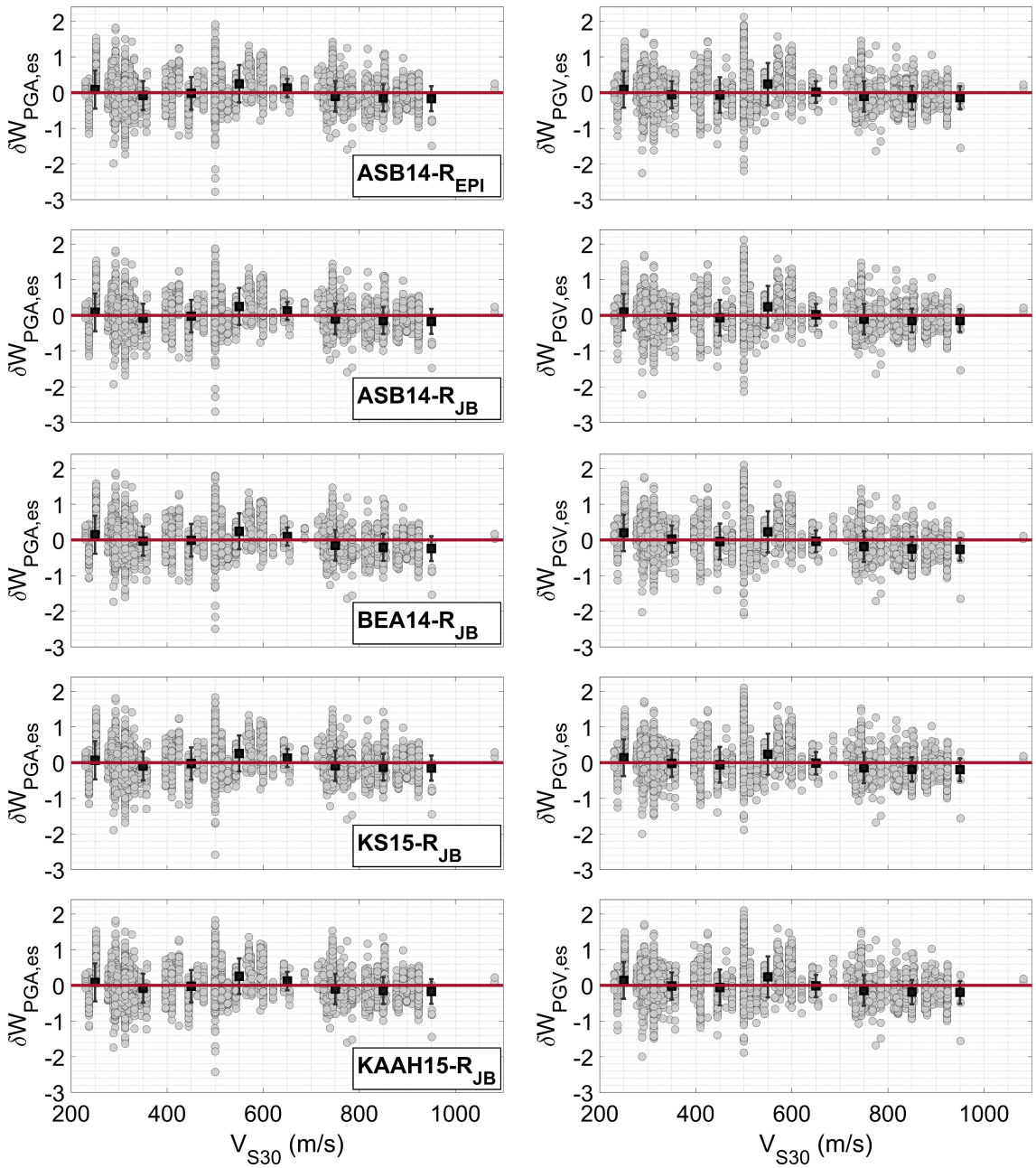


Figure 3.21. Variation of the Within-event Residuals of PGA and PGV with V_{S30} for the Selected GMPEs. (Zero residuals are shown by the lines in red. Error bars stand for group means with 16^{th} and 84^{th} percentiles).

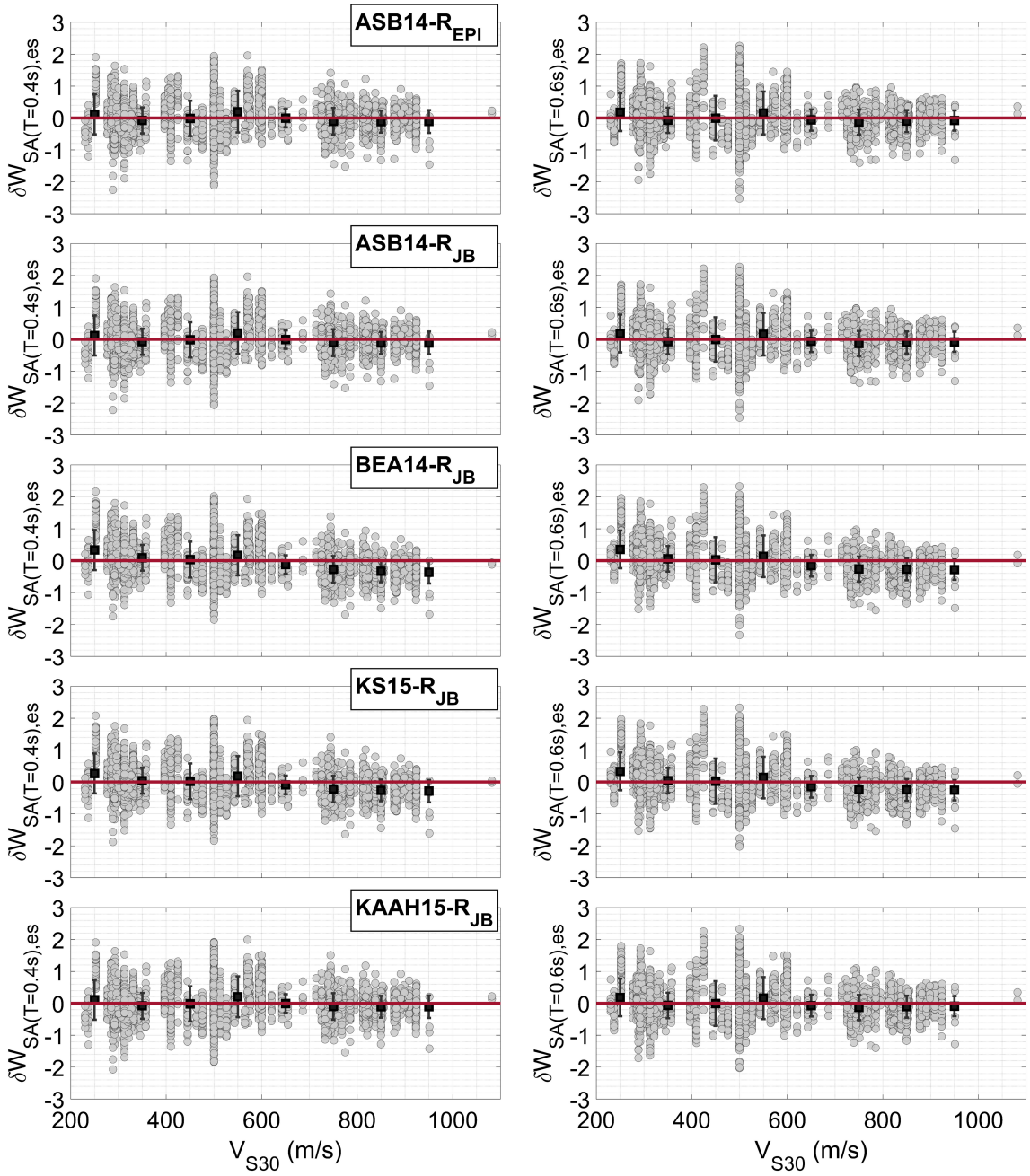


Figure 3.22. Variation of the Within-event Residuals of SA (T=0.4 s) and SA (T=0.6 s) with V_{S30} for the Selected GMPEs. (Zero residuals are shown by the lines in red. Error bars stand for group means with 16^{th} and 84^{th} percentiles).

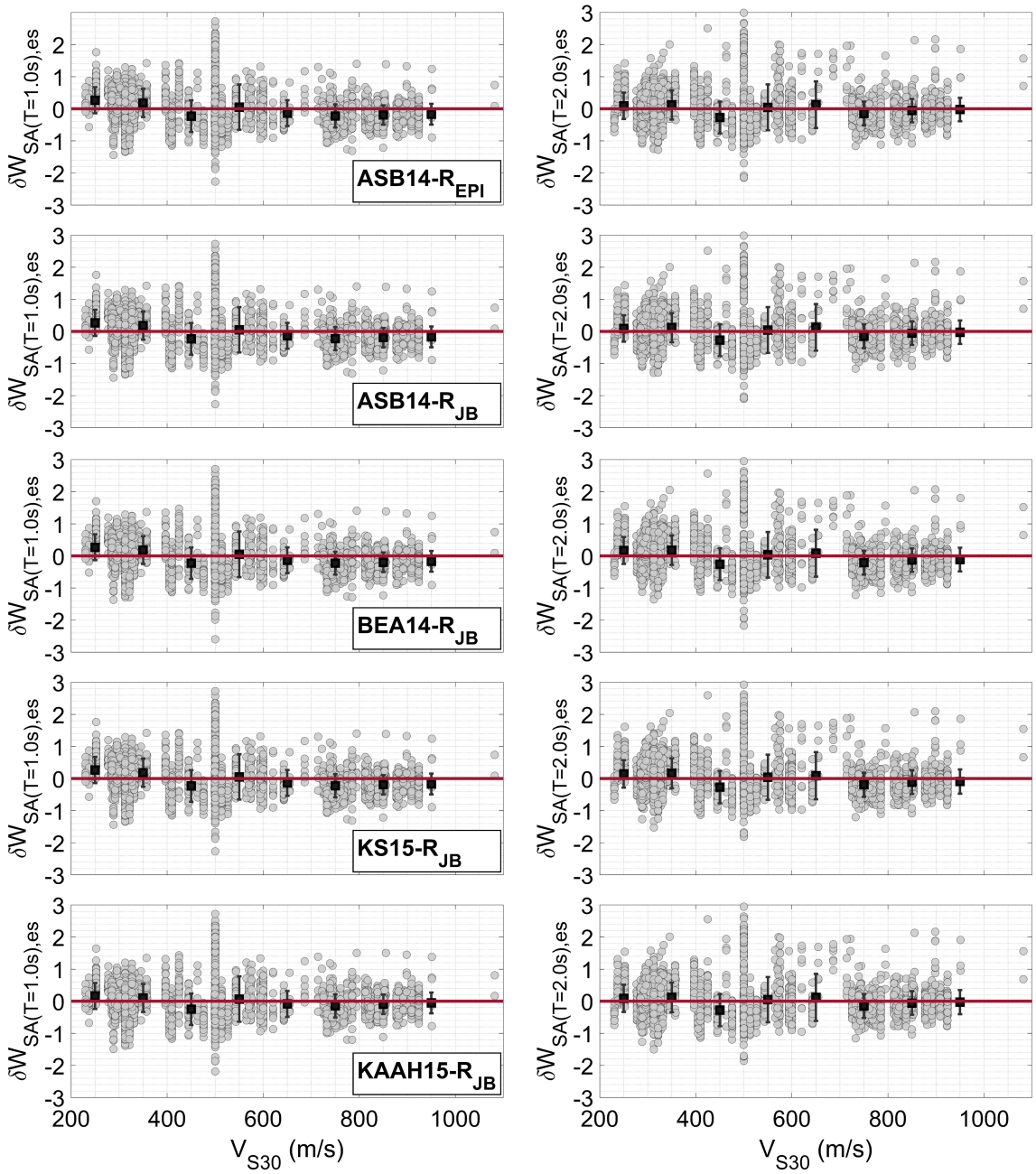


Figure 3.23. Variation of the Within-event Residuals of SA (T=1.0 s) and SA (T=2.0 s) with V_{S30} for the Selected GMPEs. (Zero residuals are shown by the lines in red. Error bars stand for group means with 16^{th} and 84^{th} percentiles).

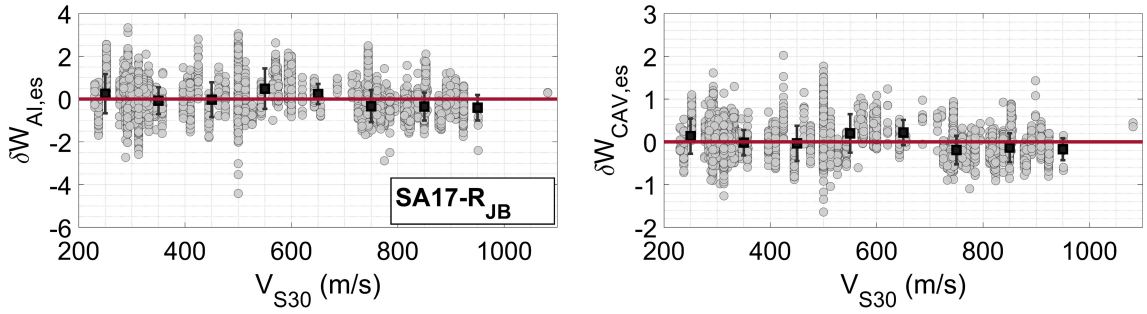


Figure 3.24. Variation of the Within-event Residuals of AI and CAV with V_{S30} for the Selected GMPEs. (Zero residuals are shown by the lines in red. Error bars stand for group means with 16^{th} and 84^{th} percentiles).

Another striking observation is that the within-event residuals of KS15 and BEA14, which account for only linear site effects in the ground motion model, behave in a manner similar to other GMPEs that incorporate nonlinear soil amplification. Apart from that, the within-event residuals of KAAH15, which reflects more Türkiye-based regionality, do not exhibit visible distinctions from other ground motion models with a more global focus as a function of the main path and site estimator parameters.

3.3.5. Within-event Residuals with Azimuth

This section solely focuses on the outcome of the residual analysis based on azimuth angles, as the azimuthal dependence of the database will be comprehensively tackled in the next section. The variation of within-event residuals versus azimuth angle is expressed in Figure 3.25 through Figure 3.28 to analyse the existence of potential biases in the within-event residuals resulting from source-to-site directionality that is not integrated into the functional forms of the GMPEs chosen.

An azimuth interval of 20 degrees is chosen to comprehend how the mean of each bin and their corresponding error bars vary along with the entire azimuth range. The absence of any discernible patterns and large fluctuations of within-event residuals between [-180 -100] and [100 180] degrees can be attributed to data scarcity. Nonetheless, there is a substantial volume of data within the -100 to +100 degree range that oscil-

lates around the zero line. As in the case of the statistical evaluations of within-event residuals as a function of R_{EPI} and V_{S30}, the variation of within-event residuals against azimuth is unable to detect any discernible impact of the directionality on any GMPs.

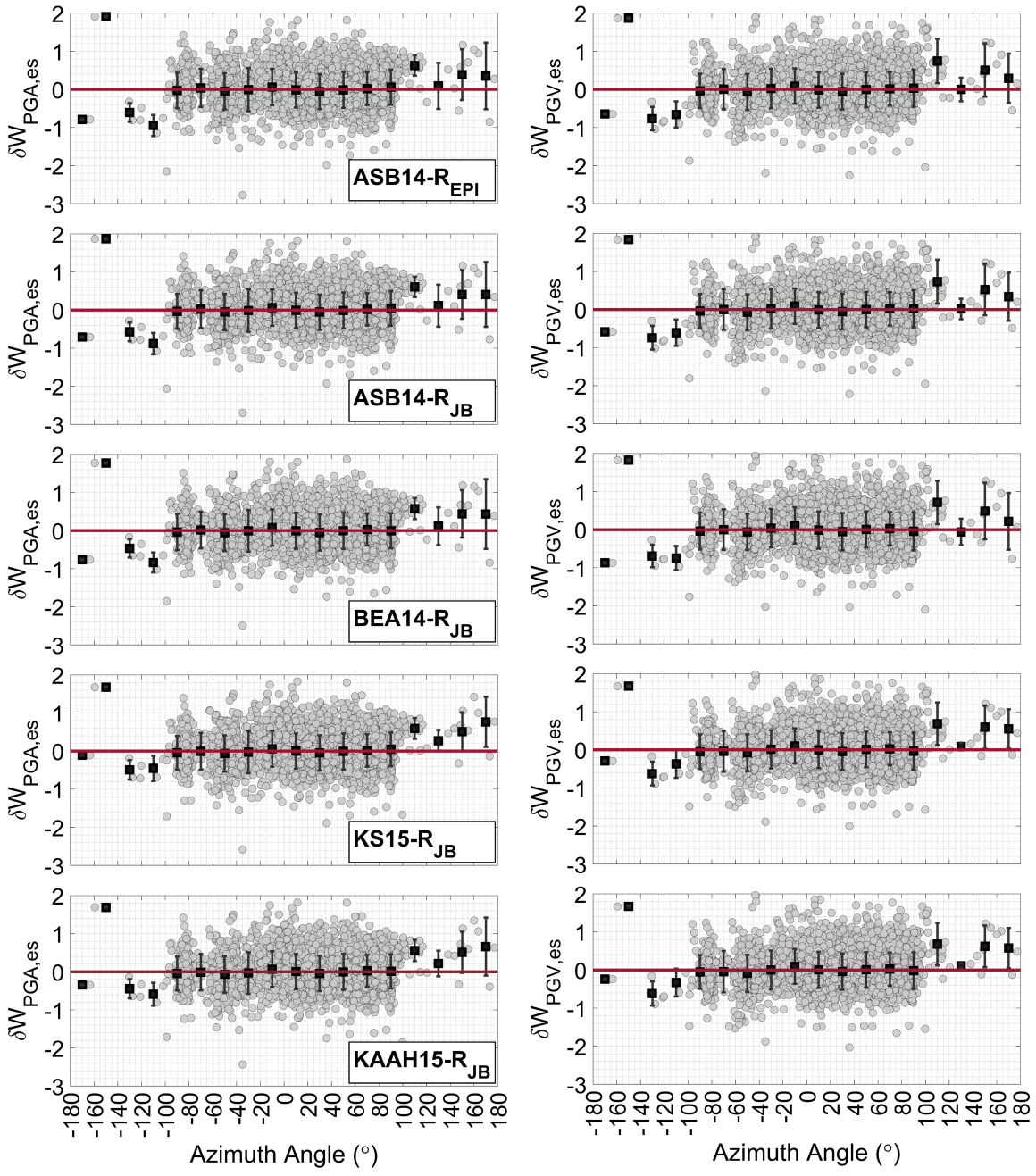


Figure 3.25. Variation of the Within-event Residuals of PGA and PGV with Azimuth Angle for the Selected GMPEs (Zero residuals are shown by the lines in red. Error bars stand for group means with 16^{th} and 84^{th} percentiles).

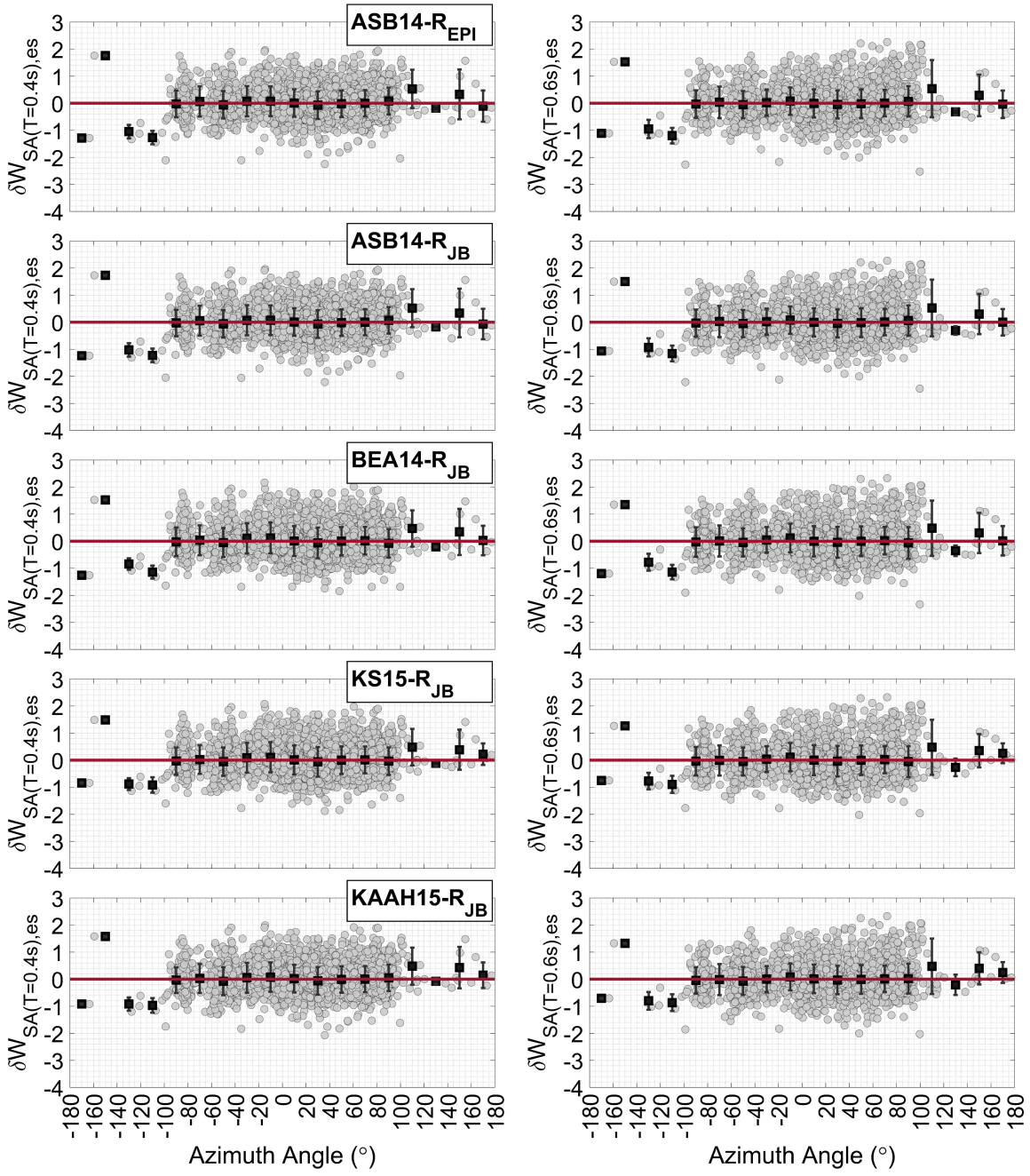


Figure 3.26. Variation of the Within-event Residuals of SA (T=0.4 s) and SA (T=0.6 s) with Azimuth Angle for the Selected GMPEs (Zero residuals are shown by the lines in red. Error bars stand for group means with 16^{th} and 84^{th} percentiles).

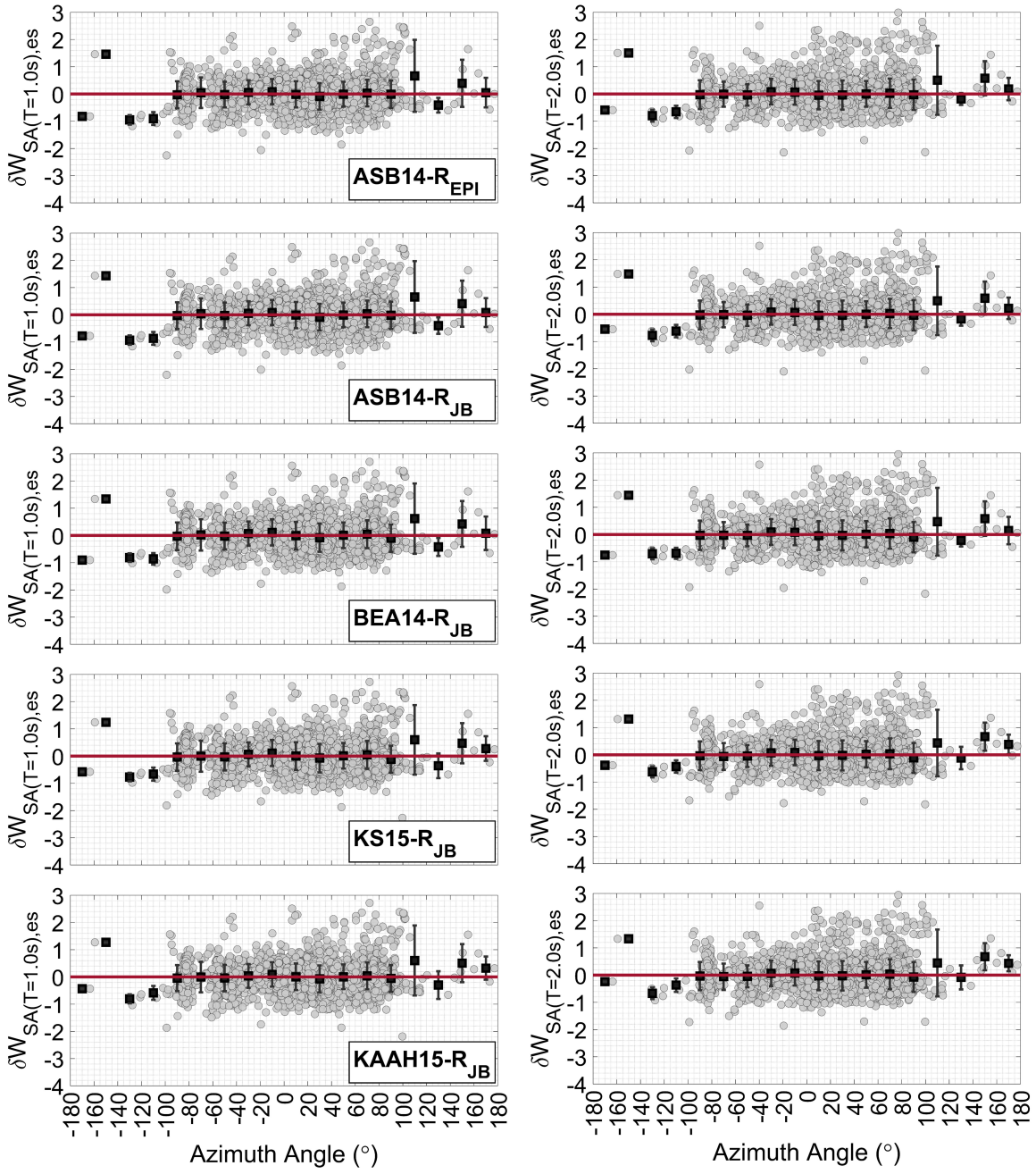


Figure 3.27. Variation of the Within-event Residuals of SA (T=1.0 s) and SA (T=2.0 s) with Azimuth Angle for the Selected GMPEs (Zero residuals are shown by the lines in red. Error bars stand for group means with 16^{th} and 84^{th} percentiles).

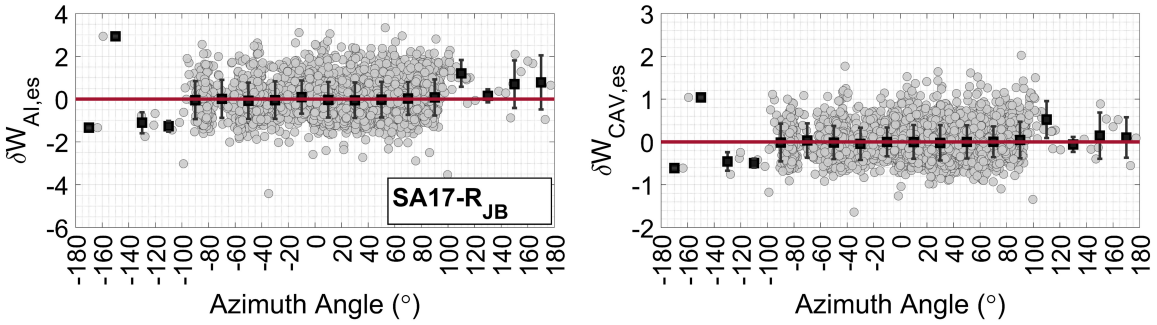


Figure 3.28. Variation of the Within-event Residuals of AI and CAV with Azimuth Angle for the Selected GMPEs (Zero residuals are shown by the lines in red. Error bars stand for group means with 16^{th} and 84^{th} percentiles).

4. INVESTIGATION OF AZIMUTHAL EFFECTS

4.1. Variation of GMPs with Azimuth

It is valuable to investigate more intently the azimuthal variability of GMPs for earthquakes with relatively broad station coverage although the variation of residuals does not specifically indicate any tendency with azimuth as discussed in the previous chapter.

The commonly accepted definition of source-to-site azimuth primarily refers to the angle formed between the fault's strike or plane and a vector connecting the earthquake source with the specific site of interest (e.g. [98, 107, 150]). However, there are also a limited number of studies defining the azimuth as the angle between the geographic North and the line connecting the epicentre and the recording site with a point source approximation [95, 151]. Even though the first definition is more comprehensible and efficient, particularly in illustrating directivity effects, this thesis employs the second, more straightforward definition because the precise strike angles of all earthquakes in our database are not available. Nonetheless, assessing earthquakes individually may provide insights into whether significant GMPs intensify at particular azimuth angles as an initial evaluation.

Figure 4.1 through Figure 4.3 illustrate the distribution of the number of recordings with azimuth in 30-degree intervals around the epicentre for each earthquake. Most of the events (grey-shaded slices in the figures) do not encompass a wide azimuthal range that would allow for the detection of azimuthal variations in GMPs. However, sixteen earthquakes (black-shaded slices in the figures) possessing data for a minimum of the 90-degree segment are regarded as having comparatively adequate information to ascertain the azimuthal dependence.

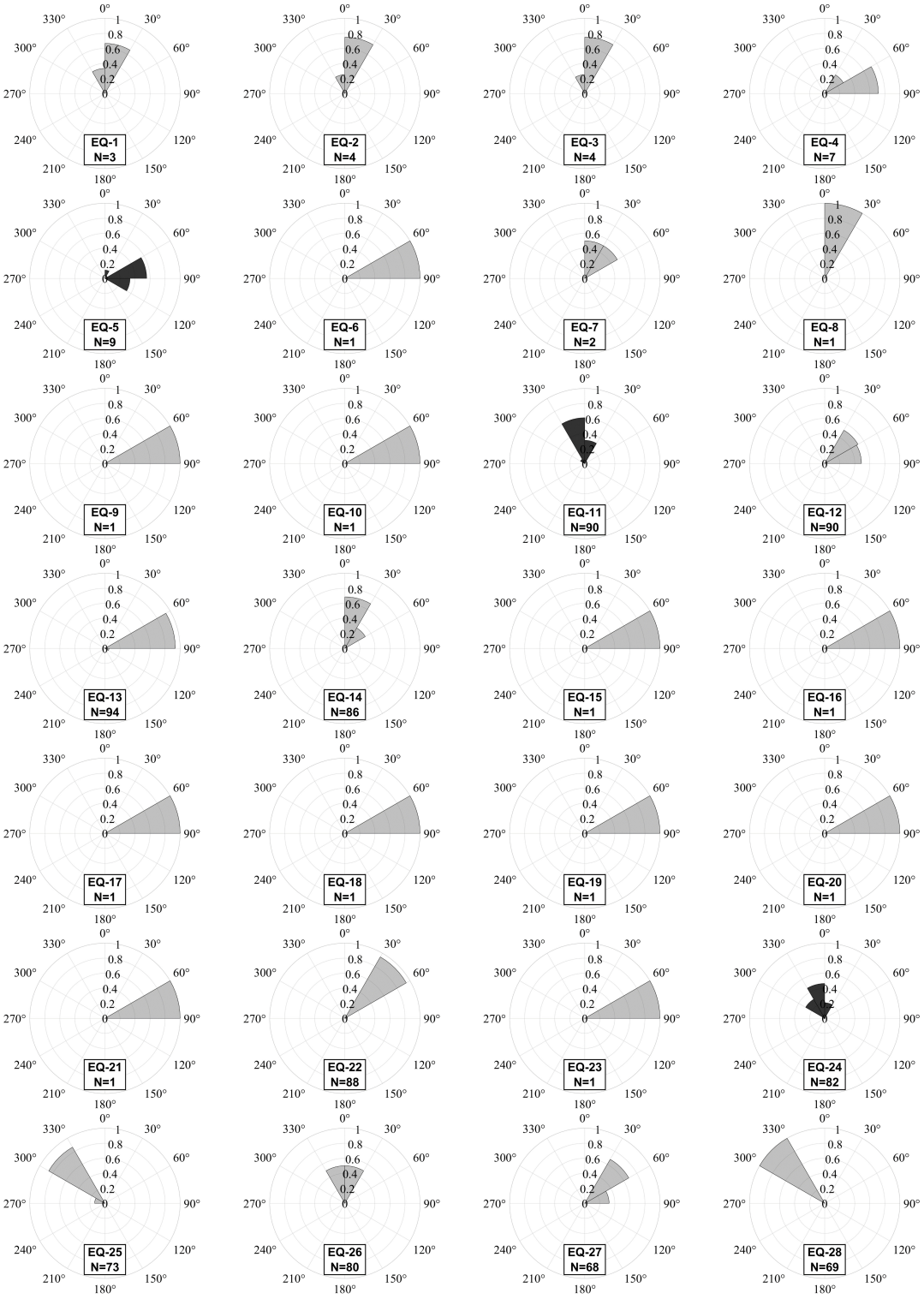


Figure 4.1. Variation of the Frequency of Recordings with Azimuth Angle for EQ1-EQ28 (N refers to the total number of recordings for each event).

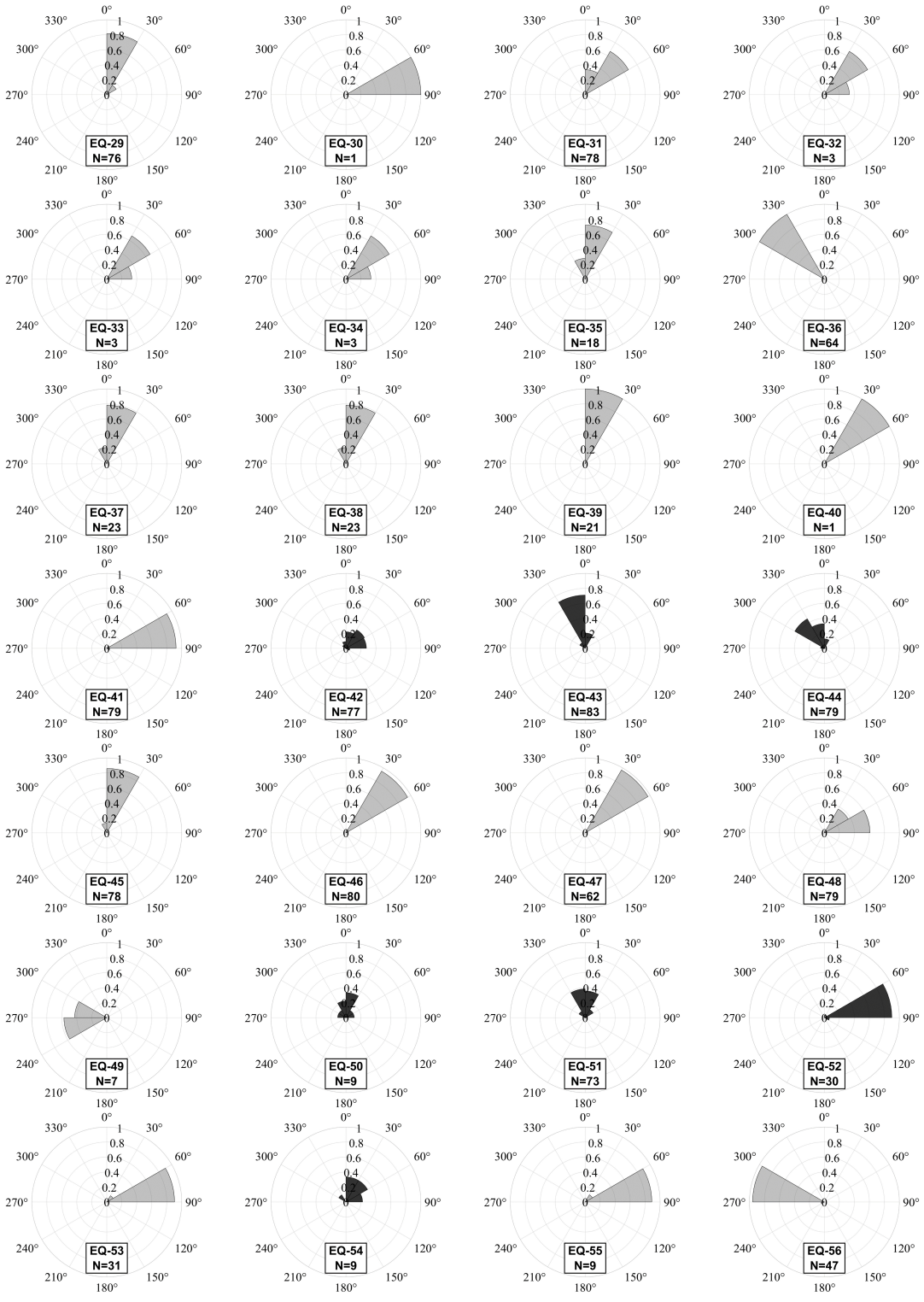


Figure 4.2. Variation of the Frequency of Recordings with Azimuth Angle for EQ29-EQ56 (N refers to the total number of recordings for each event).

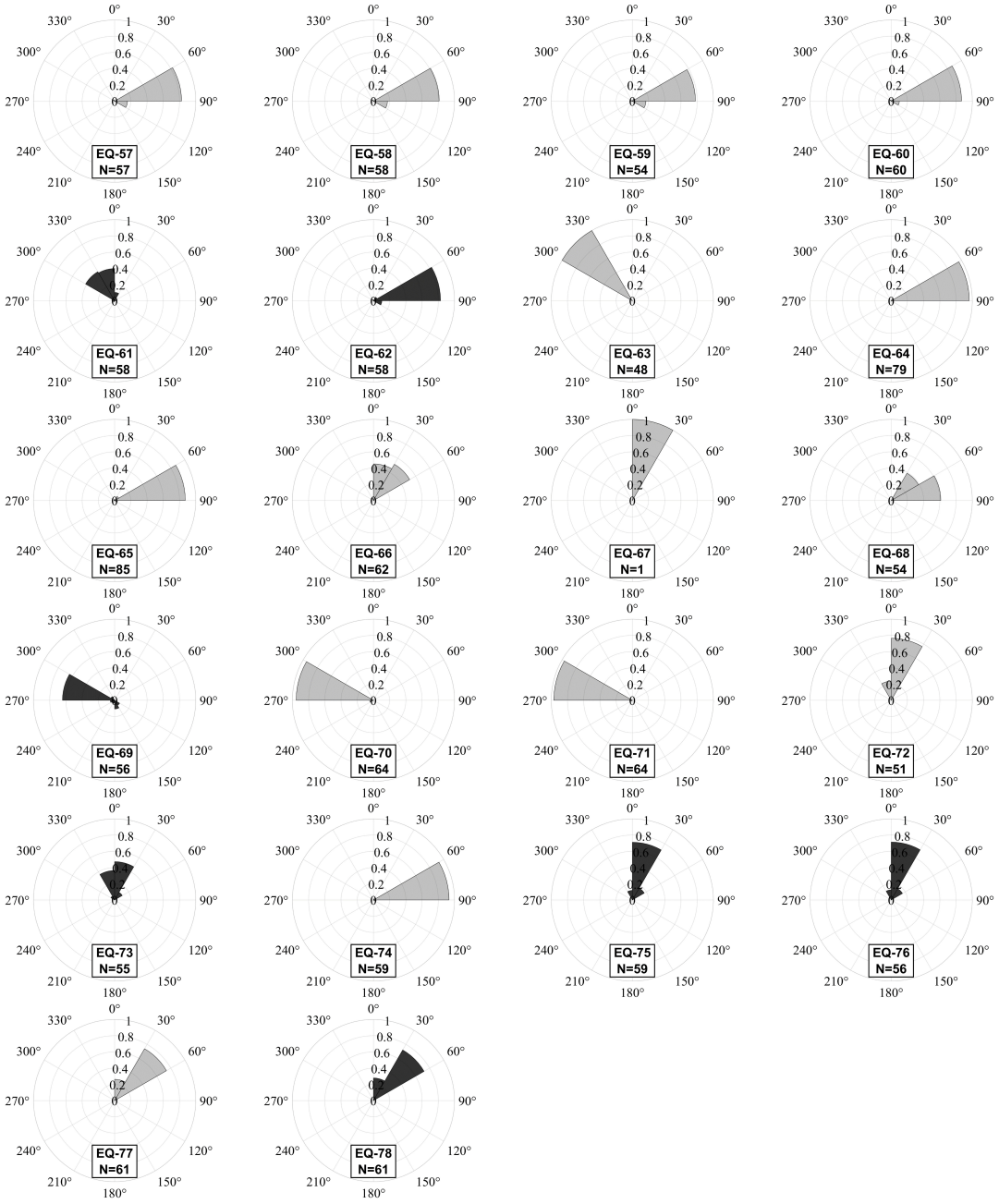


Figure 4.3. Variation of the Frequency of Recordings with Azimuth Angle for EQ57-EQ78 (N refers to the total number of recordings for each event).

The figures, from Figure 4.4 through Figure 4.7, illustrate the changes in the normalized PGA, PGV, AI, and CAV with azimuth regarding R_{EPI} for the earthquakes under consideration. Herein, GMPs are normalized by dividing each geometric mean of GMP by its maximum value associated with the respective earthquake to enhance the clarity of detecting the intensification of large amplitudes in a specific direction.

In EQ-5, a single data point stands out with the highest value within the 10° to 60° azimuth range, while the remaining data, with comparatively lower values, is clustered between 70° and 100°. The inadequate number of data within limited azimuthal coverage makes it challenging to precisely assess the azimuthal dependence of all GMPs from EQ-5 as well as EQ-50, EQ-52 and EQ-54.

The upward trend is relatively tracked in the amplitudes of EQ-11, EQ-24, EQ-42, EQ-44, EQ-51, EQ-61, and EQ-62 at specific azimuths within the positive range. However, this rise cannot be solely attributed to directional effects, as it may also be closely connected to the proximity of the recording sites to the epicentre. Exceptionally, the recording sites of the EQ-42 are uniformly distributed around the maximum amplitude of GMPs ($\approx 30°$ of azimuth angle) throughout the azimuth range of -50 to 200 degrees. Between distances of 20 to 40 kilometres, the PGAs reach 80% of the maximum PGA recorded ($PGA_{normalized} = 0.8$) at approximately 30° of azimuth. Conversely, their values at azimuths of -40° and 80° are only 7% of the maximum PGA recorded at equivalent distances. The other GMPs, namely PGV, AI, and CAV, showcase parallel patterns as well. This finding could potentially be an indication of the azimuthal dependence in the region; however, a more comprehensive analysis is needed for a precise inference, as the evaluation of a single event is insufficient.

In the case of EQ-43, the GMPs result in slightly higher values (indicated by green circles in the plots; $80 \leq R_{EPI} \leq 100$ km) within the range of -40 and 0 degrees of azimuths while stations at even relatively closer distances to the epicentre, but with different azimuths (from -60° to 0°), yield smaller amplitudes (indicated by yellow circles in the plots; $60 \leq R_{EPI} \leq 80$ km). This result may also be a sign of regional azimuthal dependence, albeit not an unambiguous one.

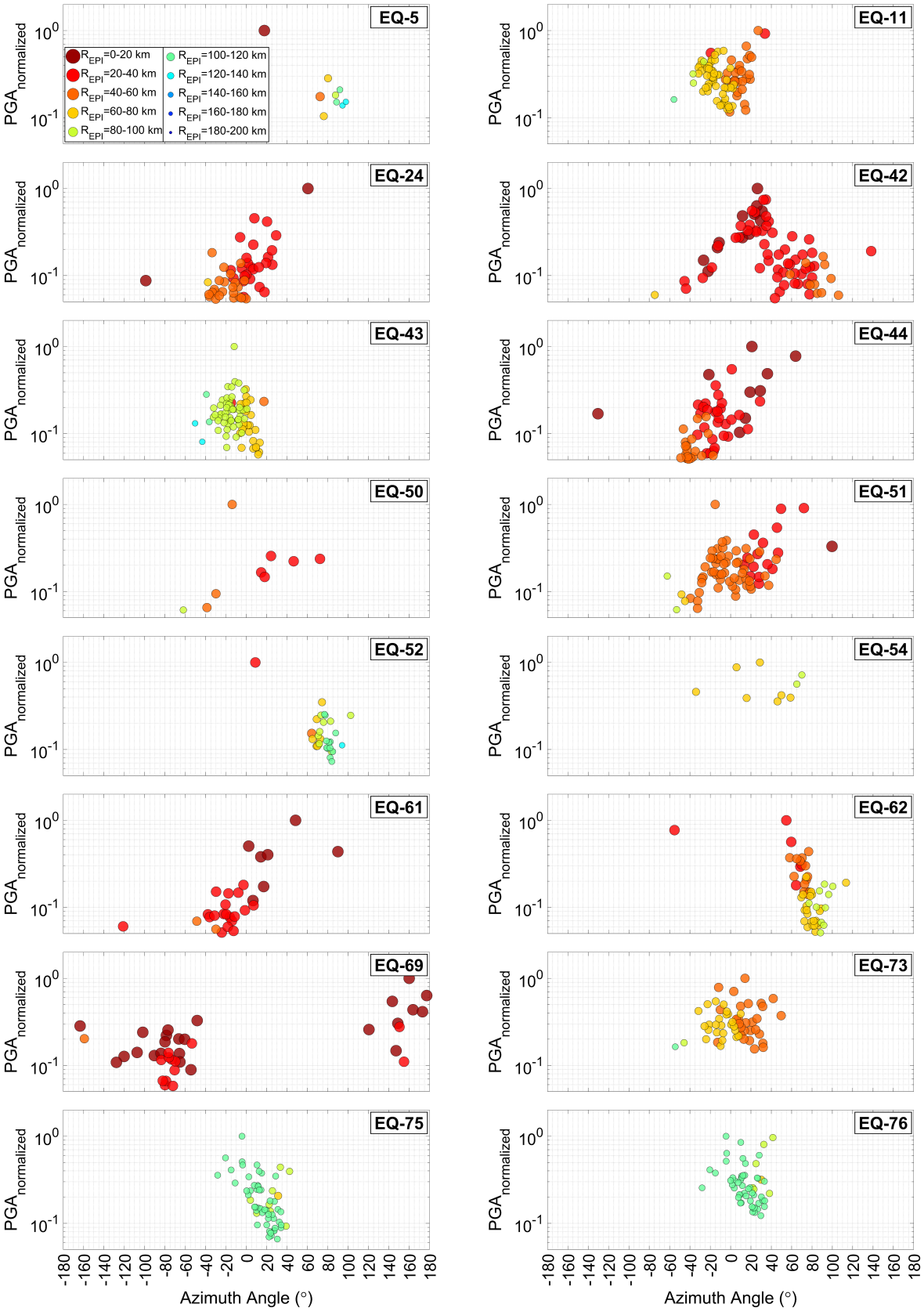


Figure 4.4. Variation of the Normalized PGAs with Azimuth and R_{EPI}.

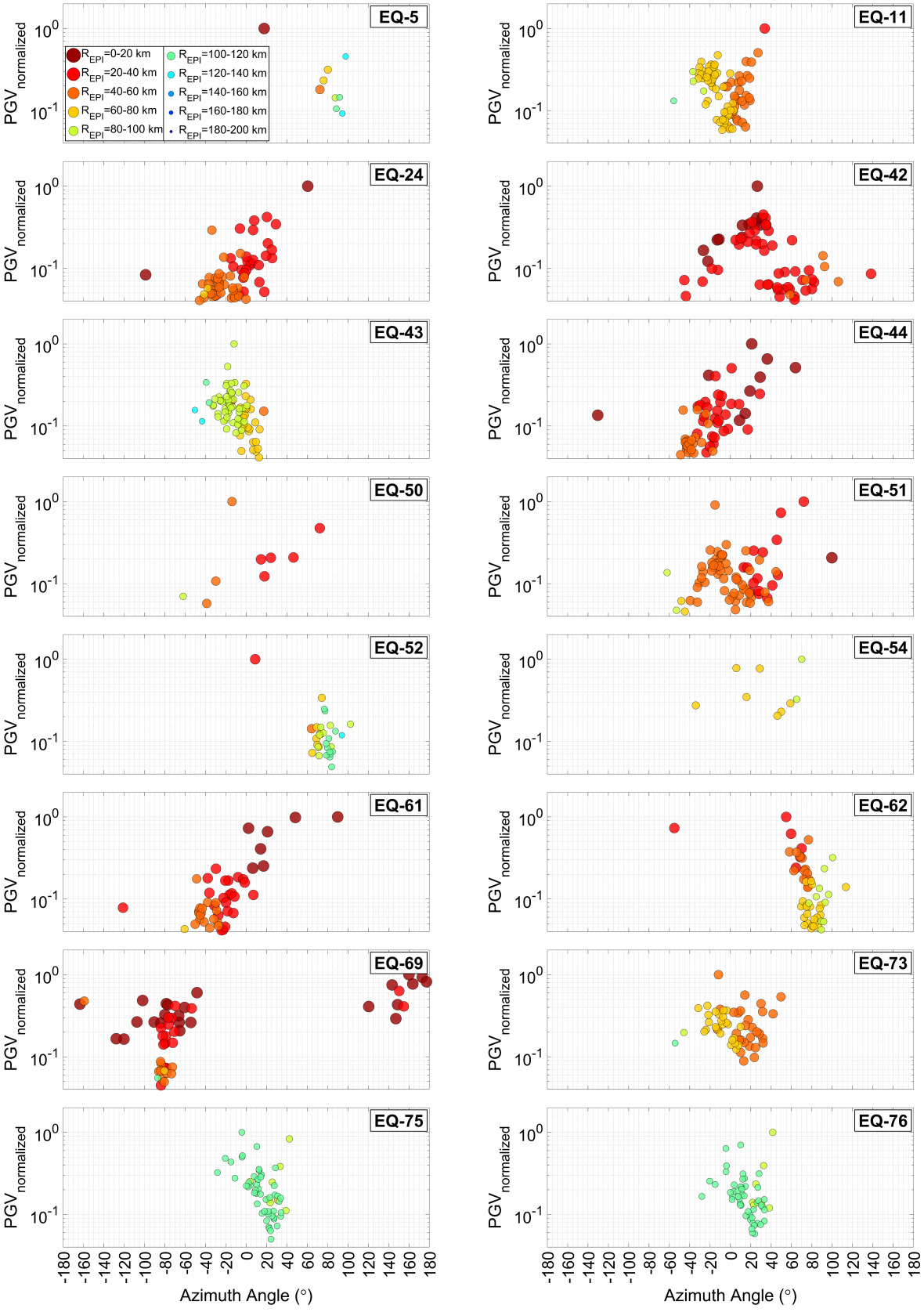


Figure 4.5. Variation of the Normalized PGVs with Azimuth and R_{EPI}.

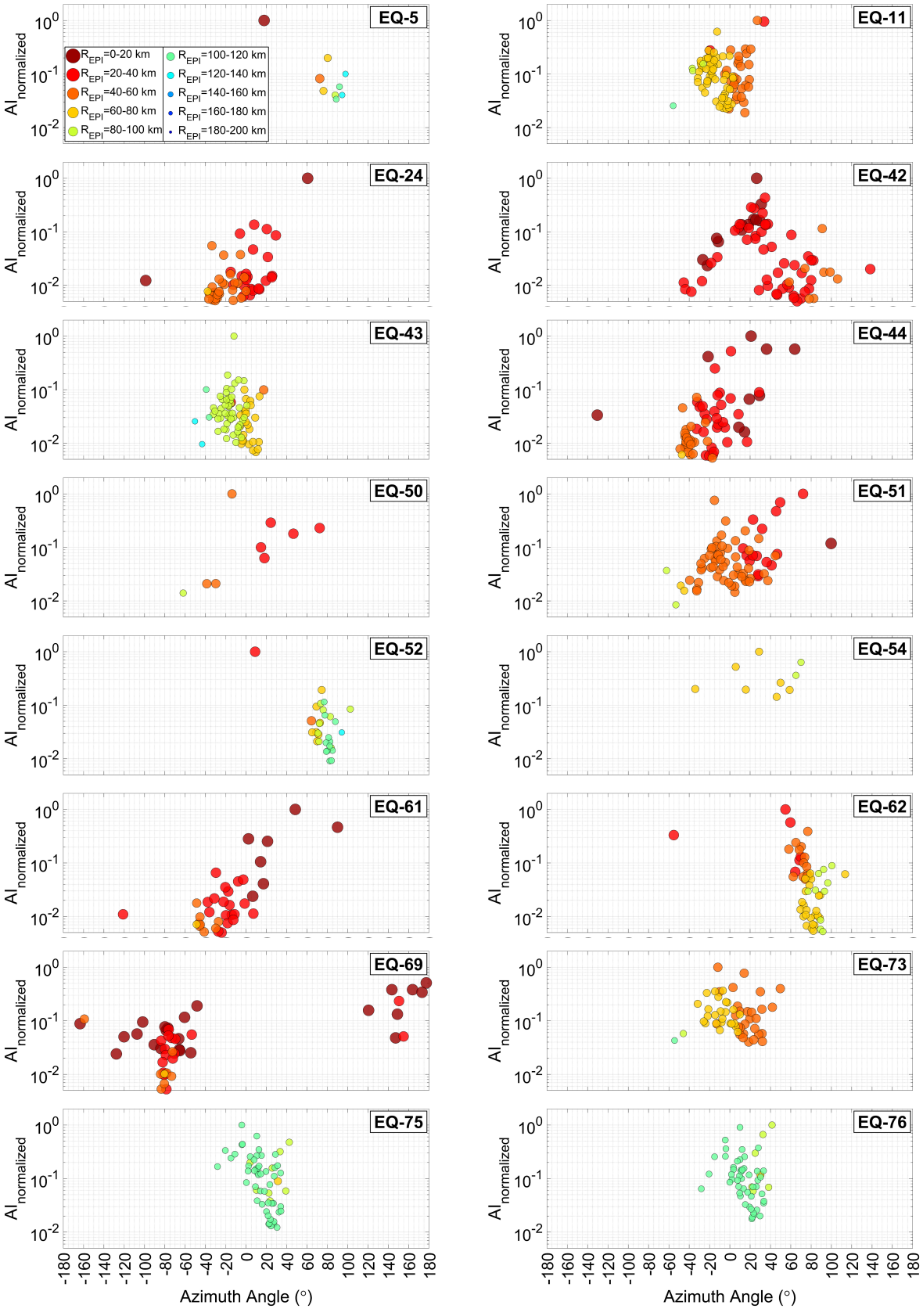


Figure 4.6. Variation of the Normalized AIs with Azimuth and R_{EPI}.

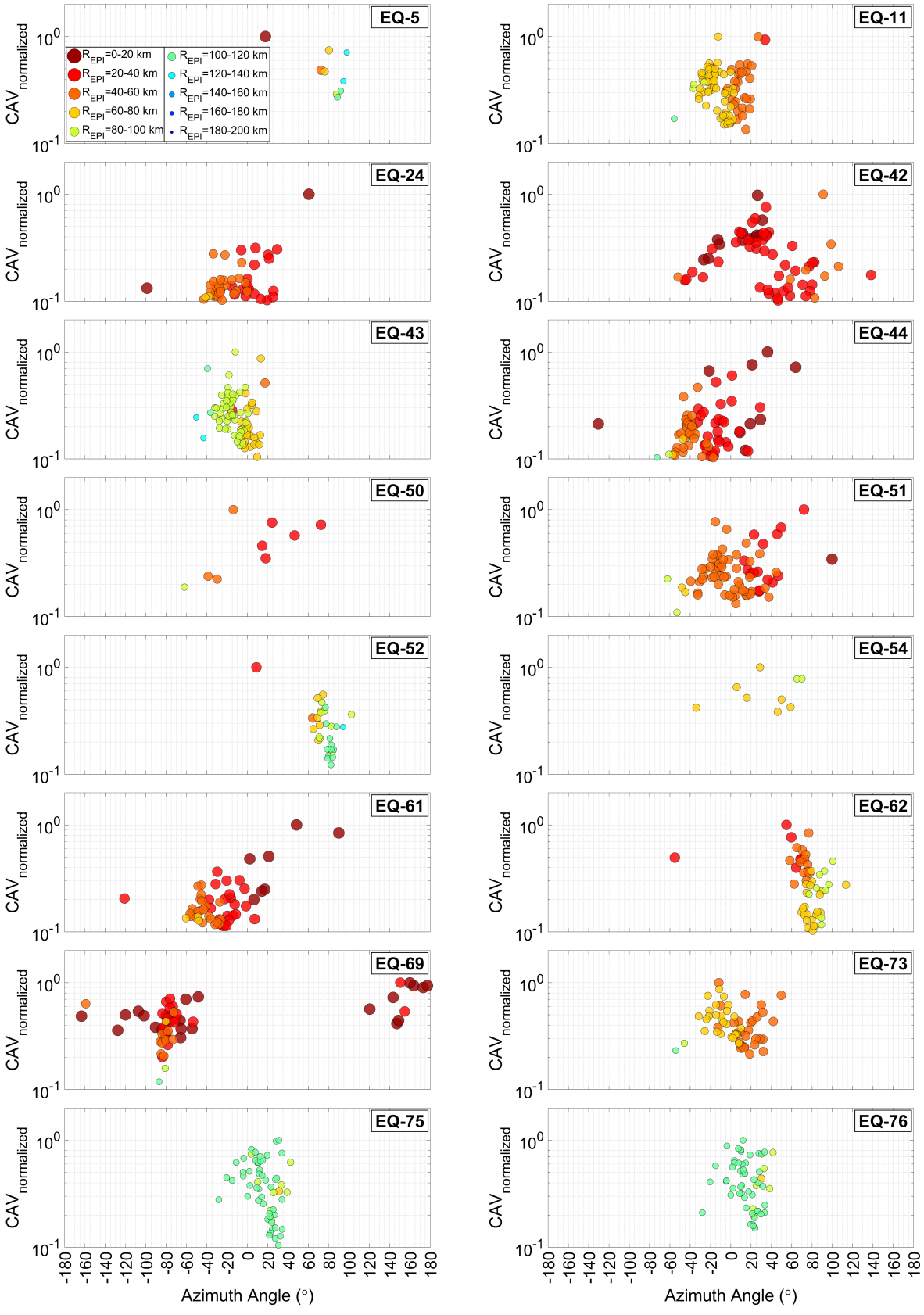


Figure 4.7. Variation of the Normalized CAVs with Azimuth and R_{EPI}.

The data set for EQ-73, encompassing R_{EPI} between 40-60 km and 60-80 km, yields similar values for GMPs. As such, it is difficult to make accurate judgments about the azimuthal implications for this event.

EQ-75 and EQ-76 are positioned at a distance of 100 to 140 kilometres from the IERREWS network. This relatively homogenous distribution of R_{EPI} may explain the trend of amplitudes increasing towards 0° that is potentially associated with the directional dependency. Nevertheless, the scarcity of data impedes a precise deduction on this matter.

Overall, the azimuthal dependency of ground motions should be assessed in conjunction with other primary variables, such as source-to-site distance and parameters characterizing soil condition. The proximity of R_{EPI} and the soft soil conditions could potentially account for the surge in the amplitudes of GMPs and obstruct the recognition of azimuthal dependence. Hence, a significant amount of data is required at similar R_{EPI} and uniform soil conditions for a genuine assessment of azimuthal effects. Therefore, any effects of azimuths on GMPs derived from the majority of earthquakes in the database of this study could not be able to concretely observed. The reasons are either there has been an increase in distance in parallel with the variation in azimuth or the GMPs have remained within small azimuth angle ranges due to the position of the earthquakes and stations.

4.2. Conversion of Components to Principal Directions

The ambiguity in azimuthal effects on ground motions of the database of this thesis prompts us to discover another way to reflect the directionality of the region on GMPs. Any potential variations in the GMPs resulting from azimuthal implications are accommodated by the conversion of ground motions from the direction of East-West (EW) and North-South (NS) to principal directions of the ground motion time series.

The principal directions achieved through a specific coordinate transformation may signify the orientations in which GMPs attain their maximum and minimum values [152, 153]. Figure 4.8 schematically illustrates this type of coordinate transformation. p_1 and p_2 denote the principal directions, which are acquired by transforming the EW-NS recording axes at an angle of α.

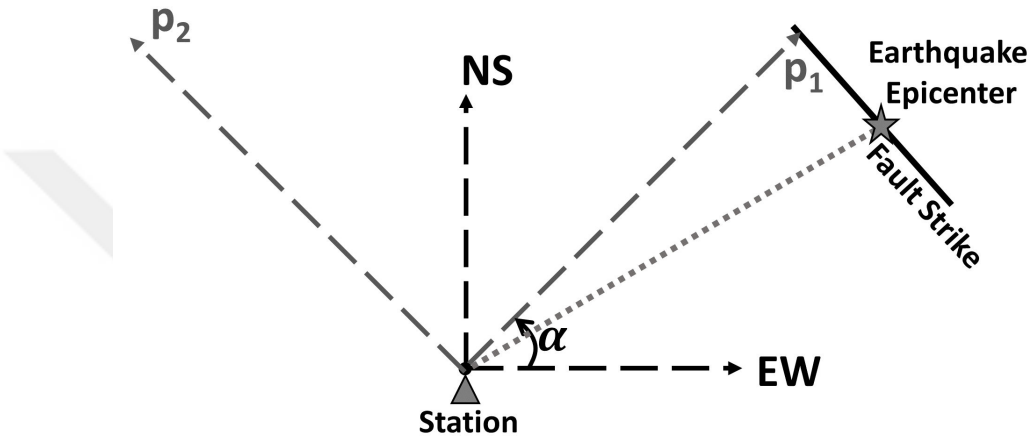


Figure 4.8. Schematic 2-D Representation of Principal Directions (p_1 and p_2).

The highest and lowest values (ignoring the UD direction) of ground motions are predominantly witnessed in the fault-normal direction (perpendicular to the fault strike) and the fault-parallel (parallel to the fault strike) direction, respectively. Hence, the fault-normal direction (represented as "p_1" in Figure 4.8) can be associated with one component of the principal directions, resulting in greater amplitudes, whereas the fault-parallel direction may correspond to the other component (represented as "p_2" in Figure 4.8).

The covariances of ground motions at recording directions can be expressed as

$$COV = \begin{bmatrix} \sigma_{EW,EW} & \sigma_{EW,NS} \\ \sigma_{NS,EW} & \sigma_{NS,NS} \end{bmatrix}, \tag{4.1}$$

in which, $\sigma_{EW,EW}$ and $\sigma_{NS,NS}$ represent the variances of ground motions recorded at the EW and NS directions, respectively whereas $\sigma_{EW,NS}$ and $\sigma_{NS,EW}$ refer to covariances. The angle α between the principal coordinate system and the EW-NS coordinate sys-

tem can be computed by diagonalizing the covariance matrix (COV), which is given by Equation (4.1), of the ground motion series such that the off-diagonal terms ($\sigma_{EW,NS}$ & $\sigma_{NS,EW}$) become zero. This ensures that ground motions along principal axes are uncorrelated with each other [153, 154].

Then, the angle α, in the counterclockwise direction, between the principal coordinate system and the recorded EW-NS coordinate system is calculated as follows:

$$\alpha = \frac{1}{2}\tan^{-1}\left(\frac{2\cdot\sum_{i=1}^{n} a_{EW,i}a_{NS,i}}{\sum_{i=1}^{n} a_{EW,i} - \sum_{i=1}^{n} a_{NS,i}}\right), \tag{4.2}$$

where, i=1, 2... n corresponds to each data number of the ground motion time series. a_{EW} and a_{NS} refer to the ground accelerations recorded at the EW and NS directions, respectively. For each station, the EW-NS records are rotated around the Z-axis in the counterclockwise direction as

$$\begin{bmatrix} a_{p1} \\ a_{p2} \end{bmatrix} = \begin{bmatrix} a_{EW} & a_{NS} \end{bmatrix} \begin{bmatrix} \cos\alpha & -\sin\alpha \\ \sin\alpha & \cos\alpha \end{bmatrix}. \tag{4.3}$$

Herein, a_{p1} and a_{p2} represent the ground accelerations in two principal axes.

The regional azimuthal dependence of ground motions will be indirectly incorporated into further analyses by employing ground motions aligned with the primary directions.

5. STATION-SPECIFIC METHODOLOGY

Regional variations may be responsible for the discrepancies noticed between the estimations of GMPEs and the actual GMPs calculated from recorded data, as well as the nonlinear regression relationships derived from the regional database as explored in Chapter 3. The current chapter will propose and discuss a methodology adopted to estimate GMPs by isolating local factors linked to station positions of the urban dense network of İstanbul.

5.1. Concept of Station-specific Methodology

The seismic source, the propagation path of waves from seismic origin to a spot on the earth's surface and the local site circumstances all contribute to identifying the physical nature of a ground motion at a particular location. The following frequency domain multiplication of these three controlling parameters is utilized to represent this.

$$A(f) = E(f) \cdot P(f) \cdot S(f), \tag{5.1}$$

in which, A(f) refers to ground motion in the frequency domain at a particular location, E(f), P(f) and S(f) represent the source, path and site effects, respectively [155, 156]. The most prevalent GMPs (or dependent variables of empirical equations) refer to the parameters obtained from ground motion recorded at a specific location as a result of source, site, and path effects. These dependent parameters also encompass the local considerations in tandem with their fundamental physical processes. The key independent variables, which are the main input of empirical ground motion models, attempt to encapsulate the physical principles underlying these effects. Empirical ground motion models are generated by applying mathematical methods to various combinations of functional forms, incorporating independent parameters, to estimate GMPs. However, addressing particularly the region-dependent variants with just one model poses a challenging issue.

This thesis proposes to perform a station-specific regression analysis to capture the local effects as thoroughly as possible and enhance the practicality of the empirical estimation equations. It should be noted that an essential prerequisite for this methodology is the availability of sufficient data at each recording site. This concept can be mathematically expressed as

$$A_{es}(f) = E_{es}(f) \cdot P_{es}(f) \cdot S_s(f). \tag{5.2}$$

In this context, e and s are indices to represent different events and stations. The e^{th} ground motion in the s^{th} station's database corresponds to the wave originating from the e^{th} source ($E_{es}(f)$) and following its propagation path ($P_{es}(f)$). Hence, source and path parameters become only variants whereas the soil condition parameters ($S_s(f)$) remain constant for a single-station case. Equation (5.2), a modified version of Equation (5.1) for a single station case, and Figure 5.1 portray the methodology's fundamental concept.

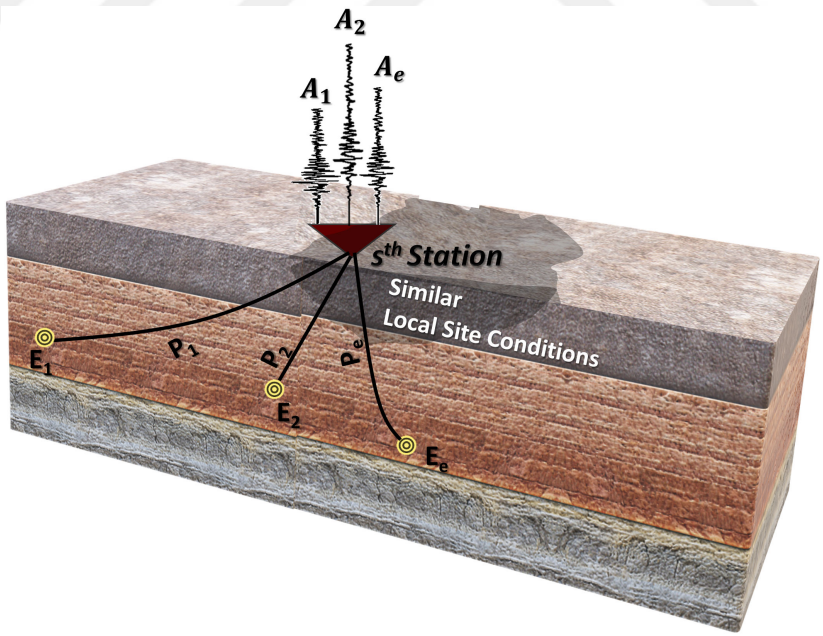


Figure 5.1. Concept of the Station-specific Analysis Methodology.

Owing to variations in V_{S30}'s determination methodology and scepticism relating to its representativeness to actual soil conditions, it stands out as the model parameter with the most substantial influence on aleatory variability [157]. As such, this methodology enables to reduce the level of uncertainty arising from variations in soil conditions. Additionally, ground motions, which arrive at the same station, from neighbouring earthquakes travel almost identical paths. Therefore, this methodology has the potential to minimize uncertainties associated with the path effects. Potential azimuthal effects, representing another local feature that impacts ground motions, are also managed by converting ground motion time series in principal directions, as elaborated in Chapter 4.

5.2. Selection of Functional Form

With the enhancement of data acquisition systems, the ground motion databases encompass more data. This advance might prompt researchers to establish more intricate functional forms particularly incorporating more independent variables to fulfill more representative empirical models. However, studies indicate neither the aleatory variability nor the estimation accuracy of empirical ground motion models is enhanced by constructing the functional formulas more complicated [33, 157, 158]. Thus, the functional forms being considered here are firstly chosen to be as straightforward as possible. Then, the complexity of the form is gradually enhanced, incorporating the terms regarding only the most essential estimation parameters that align with the physical characteristics of ground motion. A variety of functional forms have been tested for station-specific regression analyses, by employing the independent-variable terms in the well-established forms of ground motion estimation models frequently found in the literature. The upcoming paragraphs will deliberate on the functional forms and independent variables that are examined, along with the evaluation of total residuals and coefficient of determination (R^2) values for the trial regressions. Then, distance scalings of PGA will be given for the three stations (TUZL, BOTS and BRGA), chosen due to their substantial data volume. Trial regressions are solely conducted for PGA to select the most appropriate functional form.

Numerous studies specifically indicate that reverse faulting events result in more significant ground motions [40, 114, 159] whereas any much discernible variation in ground motions arising from events with strike-slip and normal mechanisms is not noticed in several studies [160,161]. Given that most of the earthquakes in the database of this thesis are associated with either strike-slip mechanisms or normal mechanisms with a strike-slip tendency, the faulting style within this study's database is assumed as homogenous. That's why, the style of faulting (SoF) term is not integrated into the functional form.

The study of Campbell [162] investigates the effect of focal depth, within a similar range (h=1.8-24.3 km) to that of this study's database and does not witness a notable impact of focal depth on PGAs despite the slightly larger tendency from a limited number of events with $h > 15$ km. As the depth range ($1.8 \leq h \leq 20.2$ km) within the database of this thesis primarily corresponds to shallow events, the depth parameter is also disregarded in the functional form.

Given that regression studies have been carried out for every single station, the functional form is regardless of soil condition parameter (e.g. V_{S30}) and includes terms regarding only source and path characteristics. Therefore, these aspects can be incorporated into regression models with straightforward but representative parameters, such as magnitude and distance between the earthquake source and the recording site.

The linear relationship between logarithmic GMPs and magnitude, stemming from the exponential connection between the energy unleashed by an earthquake and its magnitude [163], is typically integrated into the functional form by multiplying the magnitude (M_L) by a positive regression coefficient. Also, the geometric spreading of ground motions, described by lessening amplitudes of propagating waves as distance increases, is typically expressed in the functional equation through a term involving a negative power of distance [164–166]. Firstly, a very straightforward two-coefficient functional form is tried for the station-specific analysis to accomplish both exponential dependency on magnitude and geometric spreading. The predictor variables are merged

as the ratio of magnitude to the source-to-site distance as follows:

$$ln(GMP) = a + b \cdot \ln\left(\frac{M_L}{R_{EPI}}\right). \tag{5.3}$$

Figure 5.2 depicts the linear regression results based on Functional Form (5.3). The attenuation relation with both magnitude and distance is represented by a single coefficient, b as a result of the unified predictor variable (M_L/R_{EPI}) choice in this functional form. Hence, this form may not allow the accurate separation of the influences stemming from the magnitude and distance at a constant value of (M_L/R_{EPI}). For instance, the ratio of M_L/R_{EPI} remains constant at a fixed value, such as 0.03, for both a hypothetical M_L6.0 event recorded at 200 km of R_{EPI} and the M_L4.0 event recorded at 133 km of R_{EPI}. This implies the resulting PGAs (e.g. $\approx$ 0.28 cm/s^2 for station TUZL) are obtained fairly similar despite a considerable rise in magnitude and relatively small differences in the R_{EPI}. Consequently, this functional form leads to unrealistic estimations.

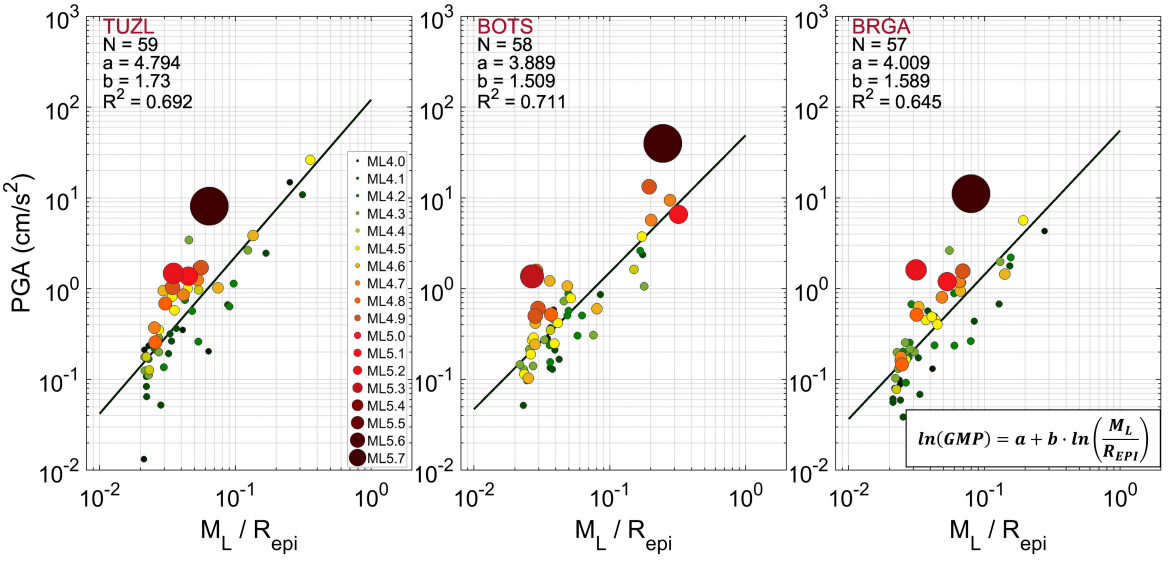


Figure 5.2. Regression Results for Functional Form (5.3) for Stations TUZL, BOTS and BRGA (a and b refer to regression coefficients and N and R^2 stand for the number of data and coefficient of determination, respectively).

The second attempt to establish the functional form involves assigning distinct coefficients (b and c, respectively) for both magnitude and distance variables as follows:

$$\ln(GMP) = a + b \cdot M_L + c \cdot \ln(R_{EPI}). \tag{5.4}$$

The disconnection of magnitude and distance terms by separating the coefficients in the functional form leads to improved estimations with higher values of the coefficient of determination (R^2) (Figure 5.3). While actual GMPs are captured with sufficient accuracy, particularly for the far-field, the shape of the estimation lines seems inappropriate for representing the physical features of the ground motion behaviour in the near-field. Even at a magnitude of 5.7, the estimated PGA climb as high as about 5000 cm/s^2 (or 5g) at a distance of 2 kilometres from the epicentre of the earthquake for station TUZL as a result of linear increase in PGA with decreasing R_{EPI}. Similar unrealistic estimations are valid for the regression results obtained from other stations as well.

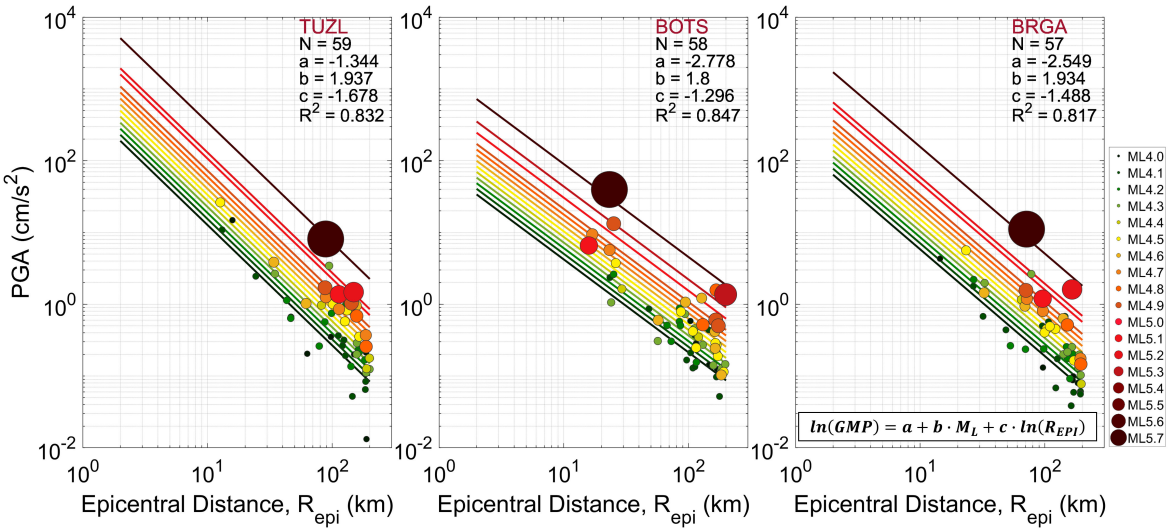


Figure 5.3. Distance Scaling of the Functional Form (5.4) for Stations TUZL, BOTS and BRGA (a, b, and c refer to regression coefficients and N and R^2 stand for the number of data and coefficient of determination, respectively).

To assess the impact of altering the functional form on the performance of the regression, adjustments are made to the Functional Form (5.4) by incorporating terms related to the nature of ground motions. Hereafter, the Functional Form (5.4) is assumed to be the fundamental function and by adjusting this base functional form, the influence of each term is examined individually.

Ground motions exhibit a nonlinear magnitude dependency (known as magnitude saturation), which implies that as the size of an earthquake increases, ground motions rise more slowly [167]. This is typically incorporated into a functional form with a quadratic magnitude term ($d \cdot M^2$) with a negative coefficient d. Nonetheless, as stated in [33], an accurate assessment of the quadratic relationship between earthquake magnitude and GMPs can be attained by having a significant number of large earthquakes in the dataset. Even in the absence of adequate large magnitude events in the database of this thesis, attempts have been made to include this term in the functional form of the regressions by modifying the Functional Form (5.4) as given below:

$$\ln(GMP) = a + b \cdot M_L + c \cdot \ln(R_{EPI}) + d \cdot M_L^2. \tag{5.5}$$

Compared to larger earthquakes, the geometrical decay of GMPs from smaller events demonstrates a more rapid decrease with distance, with a steeper slope [168, 169]. In light of this fact, the magnitude-dependent geometric decay is accounted for by modifying the coefficient of $\ln(\mathrm{R_{EPI}})$ with a term that is a function of magnitude in [61]. The magnitude-dependent geometric decay is incorporated into the functional forms of many ground motion model developers [32, 50, 66, 67, 77, 170]. Despite the extremely narrow magnitude range in this study's database, the geometric decay term in Functional Form (5.4) is just converted into a magnitude-dependent form similar to the aforementioned studies through multiplication with $\mathrm{M_L}$, as embodied in below:

$$\ln(GMP) = a + b \cdot M_L + c \cdot M_L \cdot \ln(R_{EPI}). \tag{5.6}$$

The anelastic attenuation resulting from the inherent characteristics of the Earth's crust during wave propagation is typically expressed in empirical ground motion models as a multiplicative factor of distance with a corresponding regression coefficient [32, 39, 77, 170]. On the other hand, in several studies, the coefficient of the anelastic term is acquired to be positive, implying a growth of GMPs with distance. This unrealistic

outcome compels these studies to disregard the anelastic term [37,66,171]. In order to check the effect of the anelastic term on the model, the foundational Functional Form (5.4) is adapted by incorporating a term in the form of $e \cdot R_{EPI}$ as expressed below:

$$\ln(GMP) = a + b \cdot M_L + c \cdot \ln(R_{EPI}) + e \cdot R_{EPI}. \tag{5.7}$$

The distance parameter has been directly employed in the previous functional forms. However, GMPEs usually incorporate an increased distance ($\sqrt{R_{EPI}^2 + f^2}$) into the functional form, as ground motions exhibit unexpectedly high amplitudes at very close distances to the seismic source [33, 114]. The most common and physically comprehensible approach is to introduce a regression coefficient, f representing a hypothetical depth and treat the hypotenuse as a new distance parameter (e.g. [39,50,66,67,69,77, 138,170]). Hence, this concept (known as distance saturation) results in a smaller geometric decay in the near-fields, while exhibiting a steeper slope of the estimation line in the far-fields. Even if the previous Functional Form (5.4), which considers an unmodified distance term, provides reasonable values for intermediate and far distances, the estimations at close distances are tested by implementing this distance modification as given below:

$$\ln(GMP) = a + b \cdot M_L + c \cdot \ln(\sqrt{R_{EPI}^2 + f^2}). \tag{5.8}$$

Regression analyses are also repeated after adjusting the distance terms in the Functional Forms of (5.6) and (5.7), including magnitude-dependent geometric attenuation and anelastic attenuation terms as follows:

$$\ln(GMP) = a + b \cdot M_L + c \cdot M_L \cdot \ln(\sqrt{R_{EPI}^2 + f^2}), \tag{5.9}$$

$$\ln(GMP) = a + b \cdot M_L + c \cdot \ln(\sqrt{R_{EPI}^2 + f^2}) + e \cdot (\sqrt{R_{EPI}^2 + f^2}). \tag{5.10}$$

Distance saturation may also have a magnitude dependence, signifying that it predominates more at greater distances with the increase in magnitude [172, 173]. The term f, representing pseudo-depth in the distance saturation term is expressed as an exponential function of magnitude in several studies [87, 160, 174–177]. Although the lack of near-field and large magnitude earthquakes challenges capturing the impact

of magnitude on distance saturation in this study, the coefficient f in the Functional Forms (5.8), (5.9) and (5.10) is converted to a multiplicative exponential function of magnitude, introducing supplementary coefficients g and h ($f = g \cdot \exp(h \cdot M_L)^2$) as expressed below:

$$\ln(GMP) = a + b \cdot M_L + c \cdot \ln(\sqrt{R_{EPI}^2 + (g \cdot \exp(h \cdot M_L))^2}), \quad (5.11)$$

$$\ln(GMP) = a + b \cdot M_L + c \cdot M_L \cdot \ln(\sqrt{R_{EPI}^2 + (g \cdot \exp(h \cdot M_L))^2}), \quad (5.12)$$

$$\ln(GMP) = a + b \cdot M_L + c \cdot \ln(\sqrt{R_{EPI}^2 + (g \cdot \exp(h \cdot M_L))^2}) + e \cdot (\sqrt{R_{EPI}^2 + (g \cdot \exp(h \cdot M_L))^2}). \quad (5.13)$$

The efficiency of these candidate functional forms is initially evaluated by examining the variation of total residuals with respect to actual PGAs. The total residuals, depicting the differences between the logarithm of observed data and PGAs estimated using the Functional Forms (5.4) through (5.13) with station-specific regression coefficients, are plotted against R_{EPI} in Figure 5.4. The effects of alternative models on the total residuals seem to be minimal. Nevertheless, total residuals for the Functional Forms (5.11) and (5.12) show more notable fluctuations, particularly at shorter distances of 70 km.

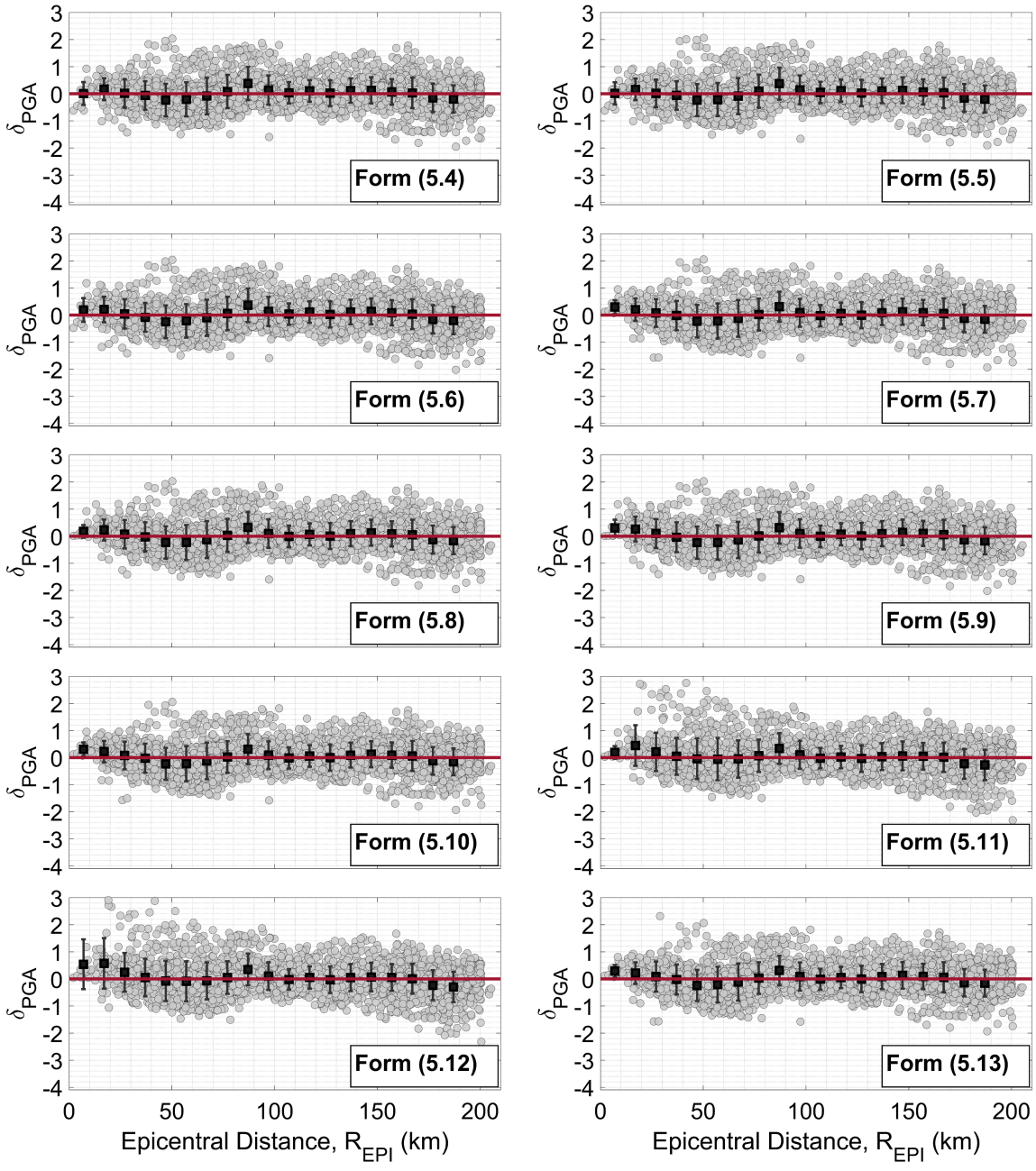


Figure 5.4. Variation of the Total Residuals of PGA with R_{EPI} for the Candidate Functional Forms (Zero residuals are shown by the lines in red. Error bars stand for group means with 16^{th} and 84^{th} percentiles).

The variation of station-specific R^2 values is also investigated to ascertain the final functional form together. Figure 5.5 displays the R^2 values for each functional form along with the corresponding number of data points (N) at each station. The stations with low data ($N \leq 10$) and relatively low R^2 (only station BCYCO) for all functional

forms, shown by red shading in Figure 5.5 and Figure 5.6, are eliminated completely due to the reduction of the estimations' robustness. Alternative functional models serve as almost equivalent R^2 values and comparable estimating performance in most cases except for 12 stations (grey-shaded in Figure 5.5 and Figure 5.6). The Functional Forms (5.11), (5.12) and also (5.13) stand out in these stations with relatively lower R^2 values, in parallel to the assessment of the total residuals. As a result, these three functional forms are not included in subsequent inquiries that aim to identify the ultimate functional forms.

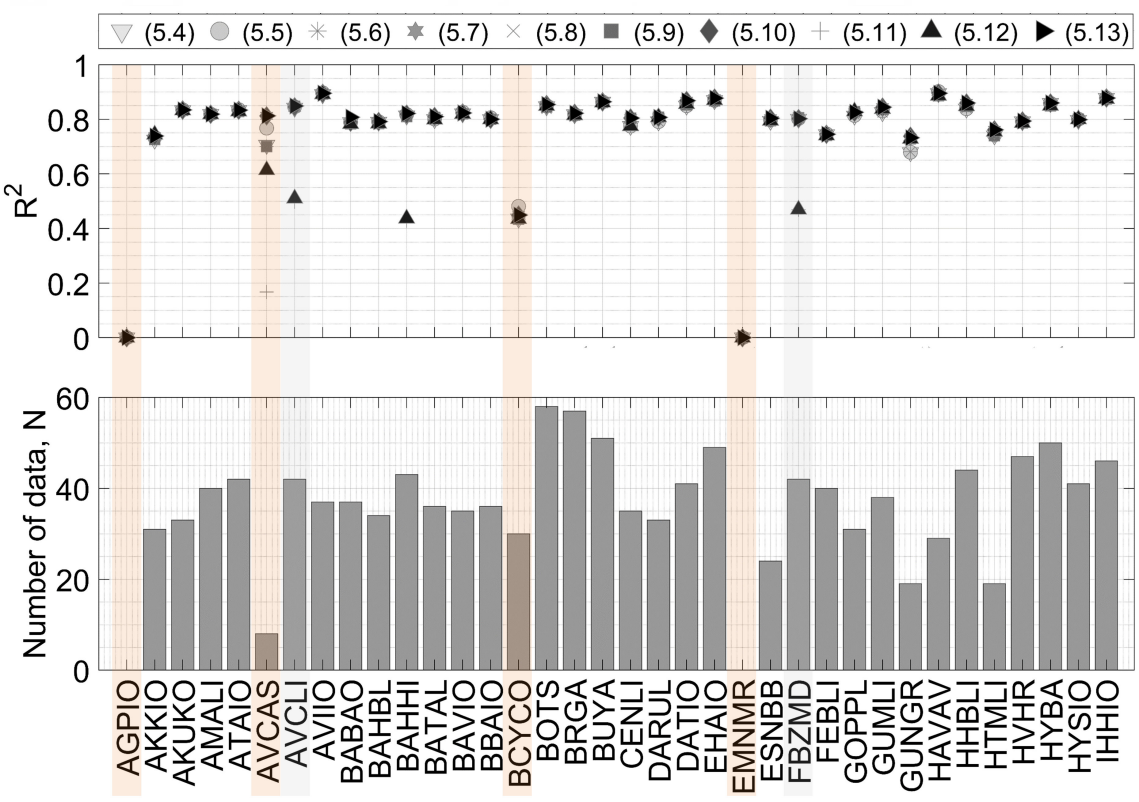


Figure 5.5. Station-based Coefficient of Determination (R^2) Values and Number of Data (N) (Grey-shaded stations are specifically mentioned in the text).

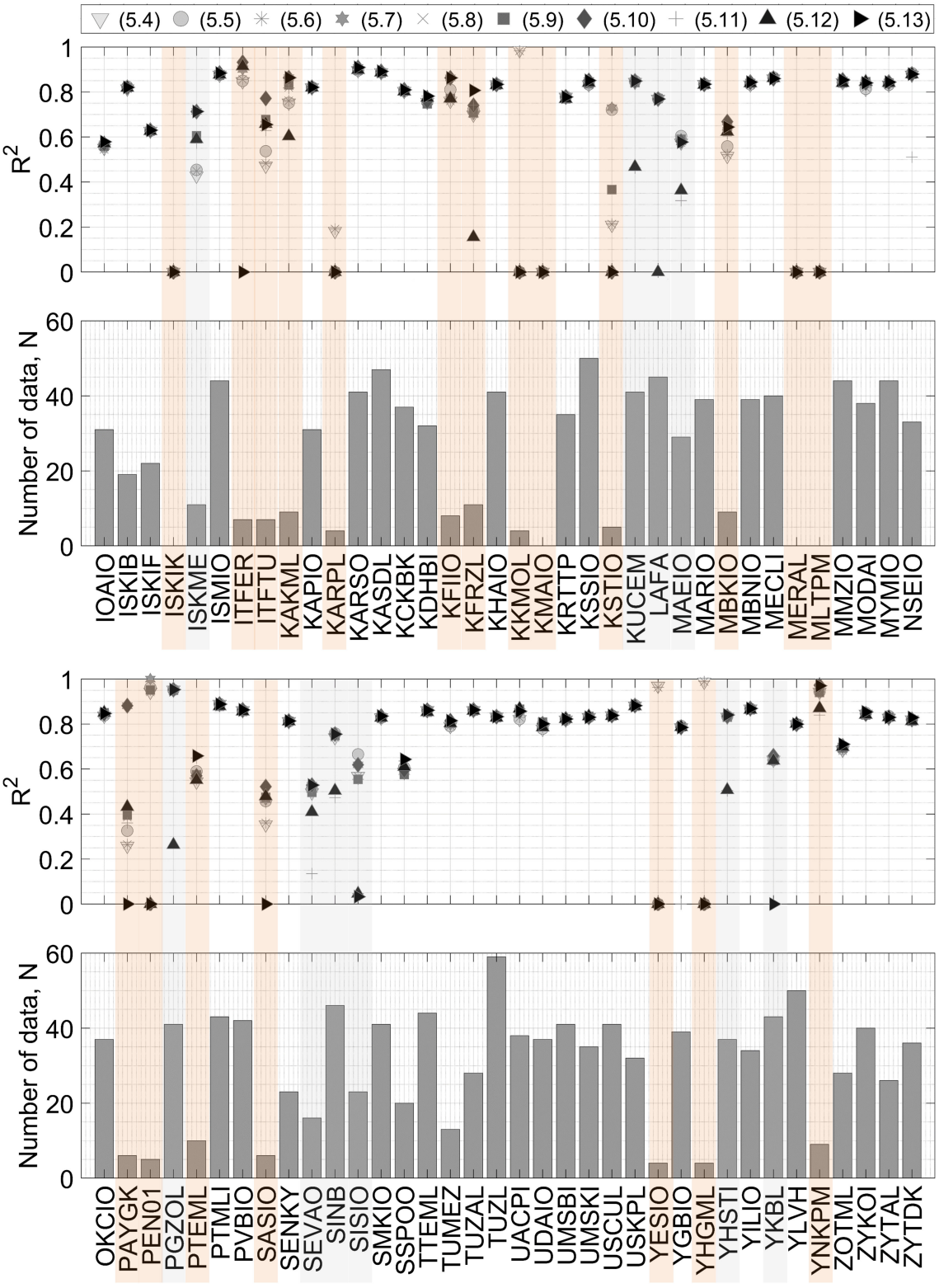


Figure 5.6. Station-based Coefficient of Determination (R^2) Values and Number of Data (N) (Grey-shaded stations are specifically mentioned in the text) (cont.).

The inspection of total residuals and station-specific R^2 values reveals that, despite the enhancing complexity of the functional forms, their predictive capabilities remain competitive. This situation favours defining the most data-representative and straightforward functional form. Therefore, an evaluation will be conducted by reviewing the distance scaling plots for each station visually and also assessing the coefficients associated with each term. The subsequent paragraphs will provide details of the final review process, by exemplifying the station-specific distance scaling of the aforementioned functional forms to formulate the ultimate functional form.

The inclusion of quadratic magnitude term relatively augments the estimation capacity compared to the base Functional Form (5.4) (Figure 5.3) almost for all stations. However, the coefficients of the terms including M_L (b and d) do not consistently yield a physically meaningful sign for each station (Figure 5.7). This inconsistency may be associated with the uneven magnitude distribution for each station and the lack of large magnitude events.

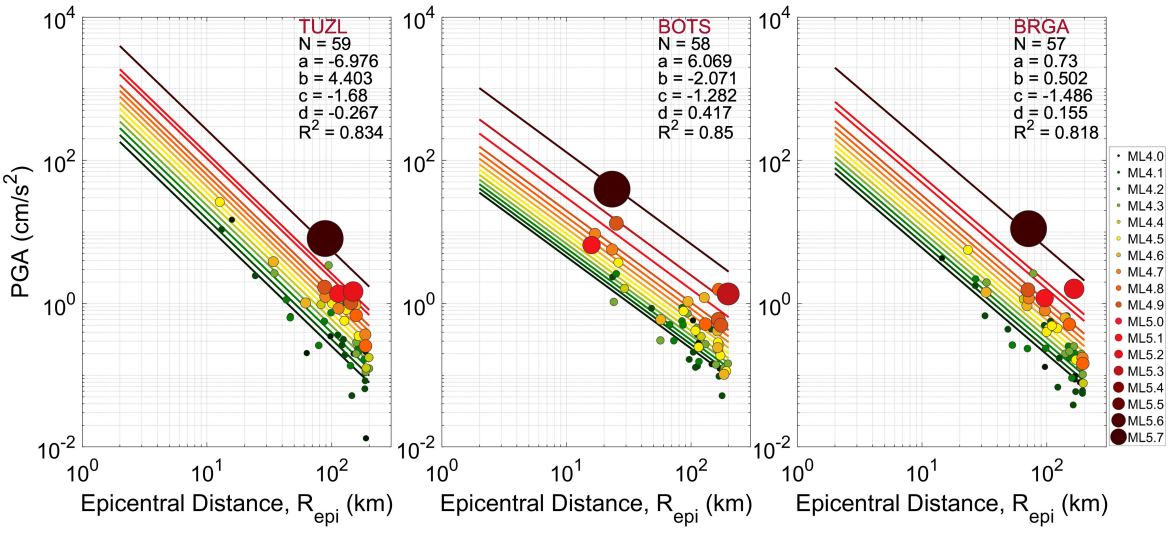


Figure 5.7. Distance Scaling of the Functional Form (5.5) for Stations TUZL, BOTS and BRGA (a, b, c and d refer to regression coefficients and N and R^2 stand for the number of data and coefficient of determination, respectively).

The influence of the magnitude-dependent geometric decay term is evident in all stations, whereas the R^2 values slightly reduce when compared to those of the base functional form (Figure 5.8). The expansion between the estimation lines in the near-field, attributed to magnitude dependency of distance term, cannot be verified due to the absence of near-field data and contributes to unacceptably large near-field amplitudes. Hence, this term is neglected in the final functional form.

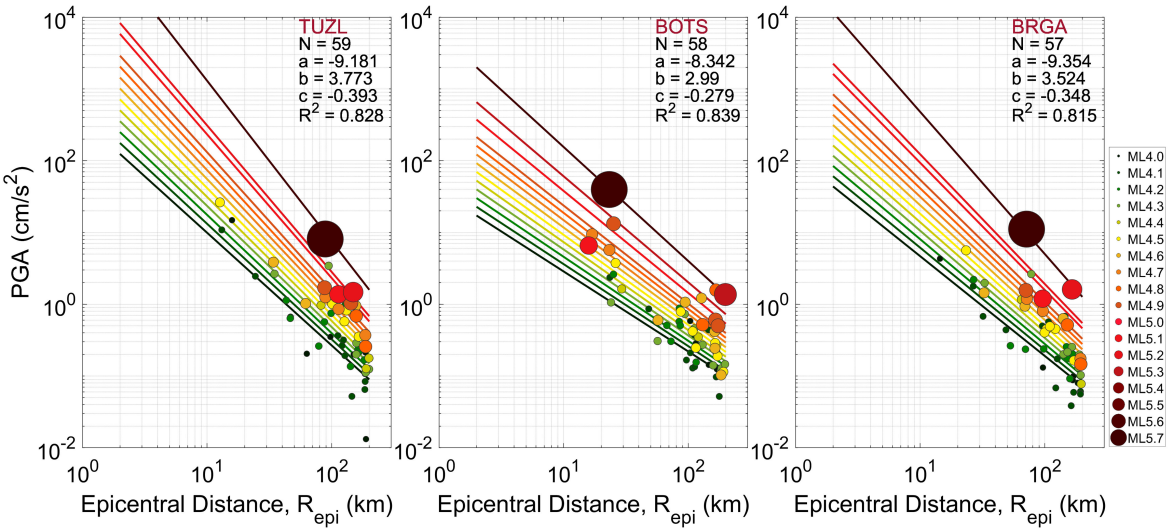


Figure 5.8. Distance Scaling of the Functional Form (5.6) for stations TUZL, BOTS and BRGA (a, b and c refer to regression coefficients and N and R^2 stand for the number of data and coefficient of determination, respectively).

The influence of the anelastic attenuation term, which is expressed in the Functional Form (5.7), is not evident at station TUZL, likely due to the close-to-zero value of coefficient e (Figure 5.9). The linear tendency of the relation seems to be protected in both near- and far-field distances. At stations BOTS and BRGA, the behaviour of the equation at far distances seems to be relatively more controlled by the anelastic attenuation term, especially when compared to Figure 5.3, which is plotted without incorporating the anelastic attenuation term. While the negative sign of the coefficient e holds the physical meaning of the term in the majority of stations, the relatively low values of this coefficient do not significantly impact the total estimation capacity. As

a result, the final functional form does not need to embrace the anelastic attenuation term.

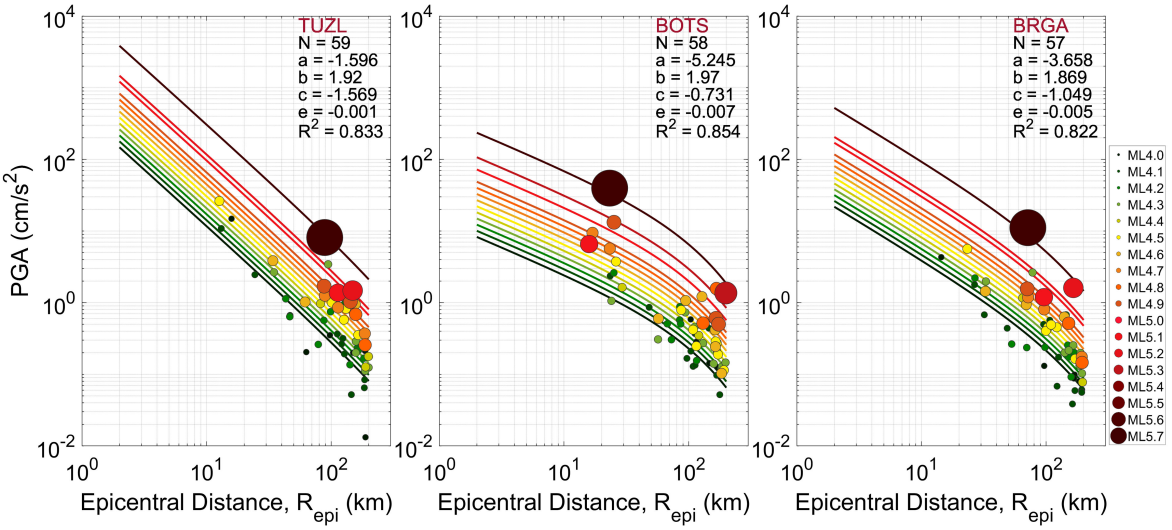


Figure 5.9. Distance Scaling of the Functional Form (5.7) for Stations TUZL, BOTS and BRGA (a, b, c and e refer to regression coefficients and N and R^2 stand for the number of data and coefficient of determination, respectively).

The variation of PGA estimations employing Functional Form (5.8) with respect to R_{EPI} is presented in Figure 5.10. For stations TUZL and BRGA, where the majority of the data are concentrated at distances greater than approximately 80 km, the coefficients a, b, and c are found to be identical to the values presented in Figure 5.3, which takes the unmodified distance term into account in its functional form. Hence, the outcomes of this functional form do not demonstrate any near-field distance saturation in these stations. The impact of the modified distance approach is clearly evident in station BOTS as it comprises a bulk of data at relatively closer distances, specifically between 10 and 30 km. Since this functional form is unable to yield consistently reliable values for coefficient f due to a lack of near-field recordings for every station, this type of implementation for distance modification still does not address the issue of near-field features for all stations. Nevertheless, a further discussion will be conducted regarding the inclusion of this term in the final functional form to provide more meaningful near-field PGAs.

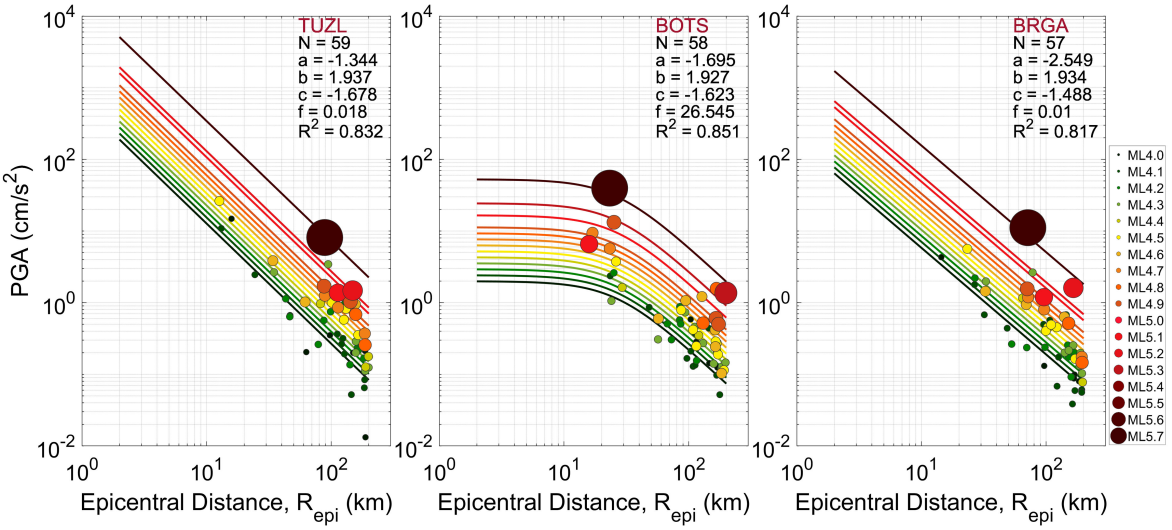


Figure 5.10. Distance Scaling of the Functional Form (5.8) for Stations TUZL, BOTS and BRGA (a, b, c and f refer to regression coefficients and N and R^2 stand for the number of data and coefficient of determination, respectively).

The implications of distance modification in the Functional Form (5.9) regarding magnitude-dependency of geometric decay term are clearly visible at station BOTS, (Figure 5.11), similar to what Figure 5.10 illustrates. However, stations TUZL and BRGA provide identical results as observed in the functional forms where unmodified distance is considered (Figure 5.8). The magnitude-dependent factor for modified distance is left out in the final functional form as there is no appreciable improvement in the estimating capacity of PGA and near-field characteristics differ from station to station.

The regression results of the Functional Form (5.10) with the modified distance and anelastic attenuation are presented in Figure 5.12. The effect of the modified distance seems to be negligible when compared to Figure 5.10, which directly takes into account the epicentral distance. As a result, it seems unlikely that incorporating this term into the ultimate functional form would significantly enhance the estimations.

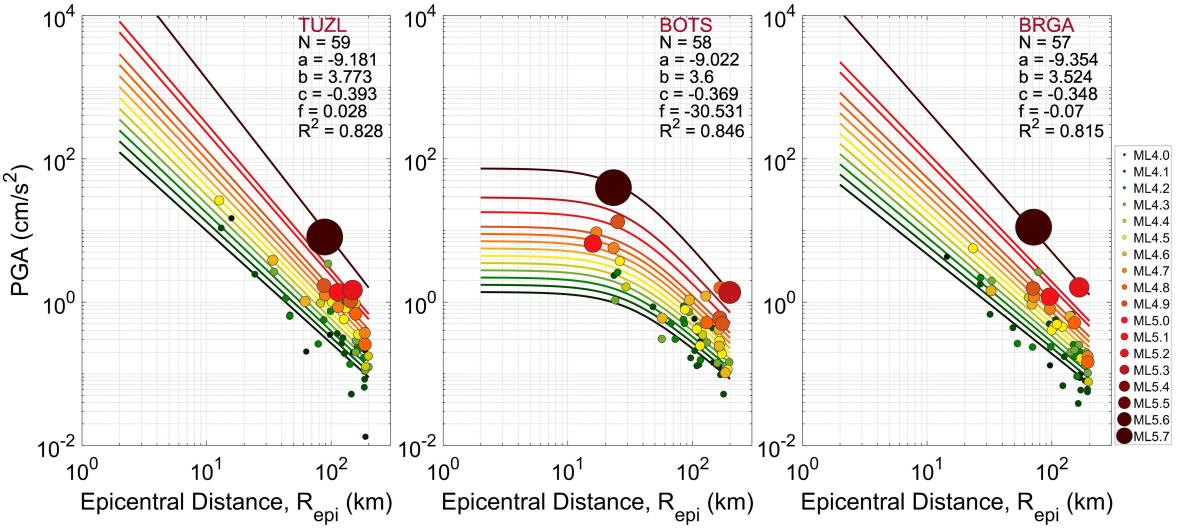


Figure 5.11. Distance Scaling of the Functional Form (5.9) for Stations TUZL, BOTS and BRGA (a, b, c and f refer to regression coefficients and N and R^2 stand for the number of data and coefficient of determination, respectively).

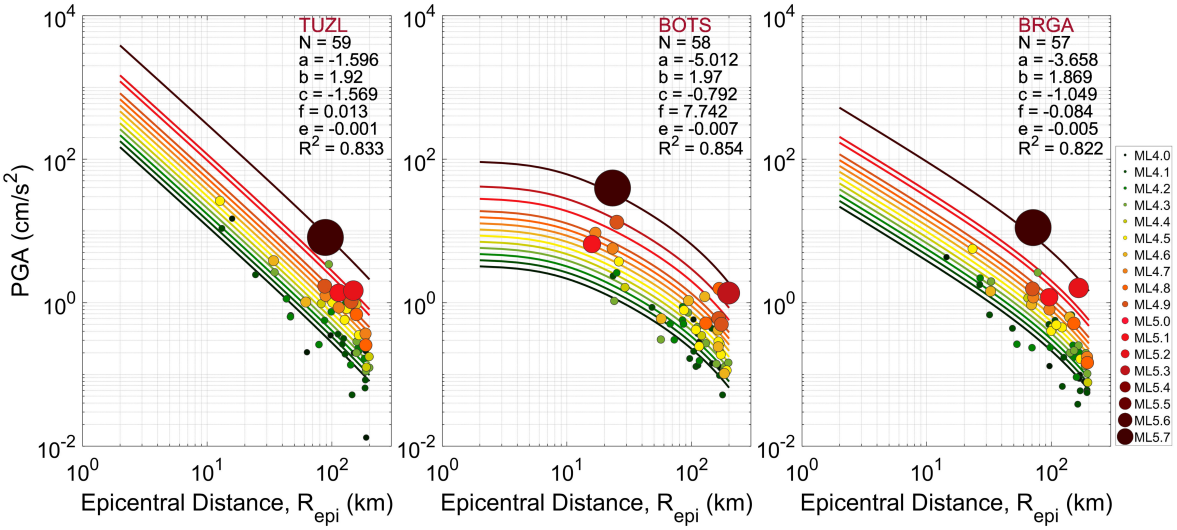


Figure 5.12. Distance Scaling of the Functional Form (5.10) for Stations TUZL, BOTS and BRGA (a, b, c, e and f refer to regression coefficients and N and R^2 stand for the number of data and coefficient of determination, respectively).

Even though the Functional Forms (5.11), (5.12) and (5.13) have been dismissed from the final functional form due to fluctuations in total residuals and inadequate R^2 values, their distance scalings are presented here for the sake of integrity. The regression results performed on the Functional Form (5.11) are seen in Figure 5.13. The regression curves unequivocally point out the absence of any noticeable impact of magnitude-dependent distance saturation for the station-specific subsets. As for Functional Form (5.12), the coefficients a, b, c, and R^2 values for stations TUZL and BRGA (Figure 5.14) are acquired in exactly accordance with those resulting from the regression analysis executed with the Functional Form (5.9) (Figure 5.11. On the other hand, station BOTS showcases a modest impact of distance saturation that varies with magnitude, notably in the near field. The regression results of the Functional Form (5.13) are depicted in Figure 5.15. Although the Functional Form (5.13) including terms associated with magnitude-dependent geometric attenuation, magnitude-dependent distance saturation and anelastic attenuation seems to be the most complex functional form introduced thus far, it does not demonstrate superior estimation performance compared to the fundamental Functional Form (5.4).

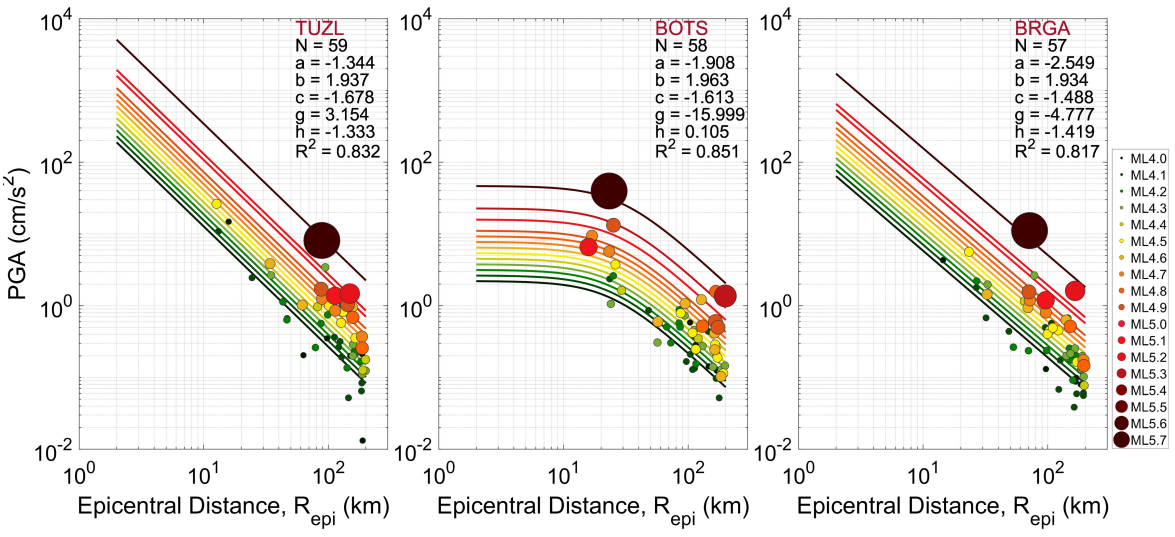


Figure 5.13. Distance Scaling of the Functional Form (5.11) for Stations TUZL, BOTS and BRGA (a, b, c, g and h refer to regression coefficients and N and R^2 stand for the number of data and coefficient of determination, respectively).

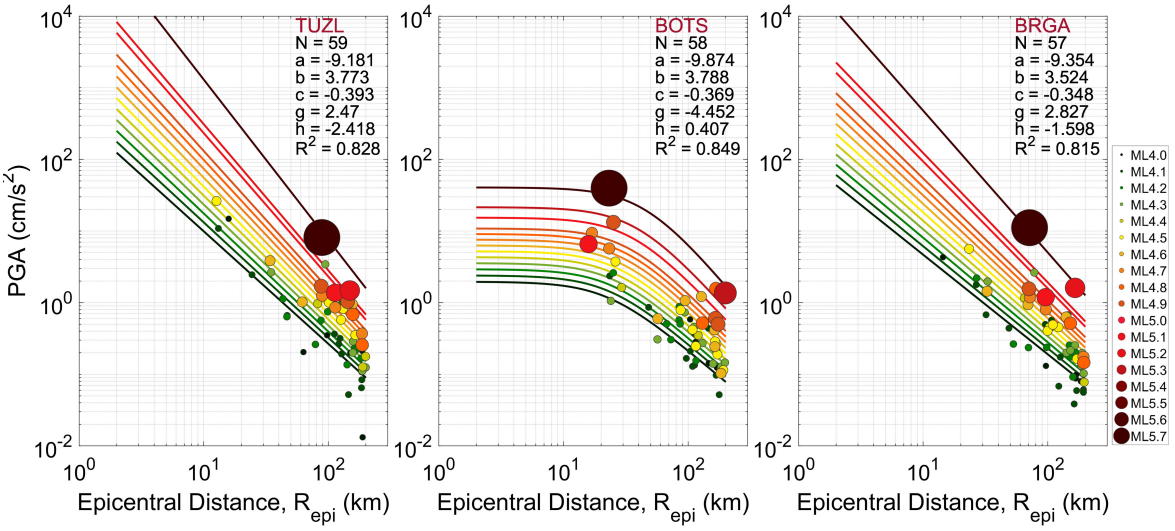


Figure 5.14. Distance Scaling of the Functional Form (5.12) for Stations TUZL, BOTS and BRGA (a, b, c, g and h refer to regression coefficients and N and R^2 stand for the number of data and coefficient of determination, respectively).

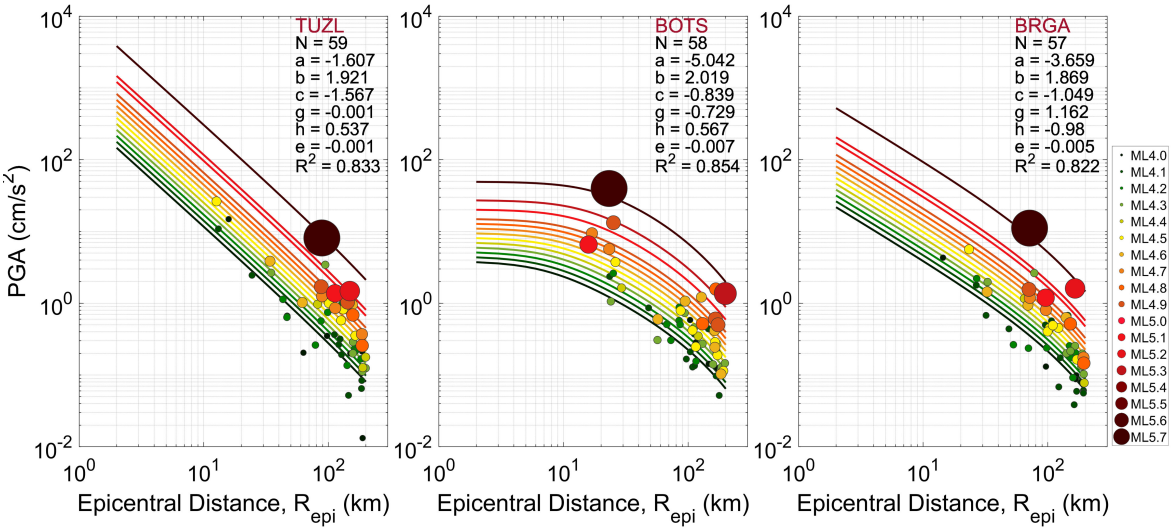


Figure 5.15. Distance Scaling of the Functional Form (5.13) for Stations TUZL, BOTS and BRGA (a, b, c, g, h and e refer to regression coefficients and N and R^2 stand for the number of data and coefficient of determination, respectively).

Relying on the previous discussions, the final functional form comprises the terms representing exponential dependencies on the magnitude, as well as geometric decay since incorporating other terms neither results in a substantial enhancement of the estimation capacity nor yields a consistently reliable value for regression coefficients. Hence, Functional Form (5.4), which notably offers reliable estimations for intermediate and far-field distances, is considered one of the final functional forms in this thesis. However, near-field estimations remain a challenging issue within this functional form. Furthermore, the lack of recordings at distances shorter than 20 km, prevents accurate derivation of coefficient f through regression analyses and estimating near-field GMPs via Functional Form (5.8). That issue of misleading near-field estimations via Functional Form (5.8) can be partially resolved by implementing two different approaches for the derivation of the coefficient f. One approach is to conduct a regression analysis on the complete database using the Functional Form (5.8) and determine a single value for the coefficient f representing the entire database. This assumption enables a straightforward solution for portraying the near-field flattening of GMPs, with minimal impact on estimation capacity. The application of regression to the entire database for the Functional Form (5.8) results in the numerical value of the coefficient f as 5.8. The variable f is set to 5.8, representing the fictitious depth value of events in the database of this thesis. Even though this approach provides a practical solution for near-field estimations, enforcing a single f value for each subset may lead to contradictions in the station-specific relations. Hence, this thesis also puts forth an alternative approach by incorporating a hybrid dataset into the regression analysis to provide more flexible constraints for near-field areas. To accomplish this, initially, a regression analysis is conducted on the complete database by using the functional form given in Chapter 3. The choice of this form is motivated by its relative consistency with the selected GMPEs, particularly for near-field distances. This empirical relation is then used to compute near-field estimates for a limited number of distances (R_{EPI}=7 and 10 km) for each station. Hybrid datasets are then constructed by combining these near-field estimations with the station-specific actual dataset. Finally, each station-specific hybrid dataset is subjected to regression analysis for the Functional Form (5.8). Nevertheless, it should be stated that the fundamental principles of the station-specific methodology may not be strictly maintained with the incorporation of near-field data estimated

through total-based regressions. Figure 5.16 and Figure 5.17 present the distance scalings of the PGA determined through the Functional Form (5.8) by considering f=5.8 and hybrid dataset approach for stations TUZL, BOTS and BRGA, respectively.

Appendix B, C and D present the distance scalings of station-based regressions using the final Functional Forms (5.4), (5.8) (f = 5.8) and (5.8) (hybrid dataset), respectively, for the remaining 84 stations since 24 stations have been expelled from the database because of insufficient data points and comparatively low R^2 values.

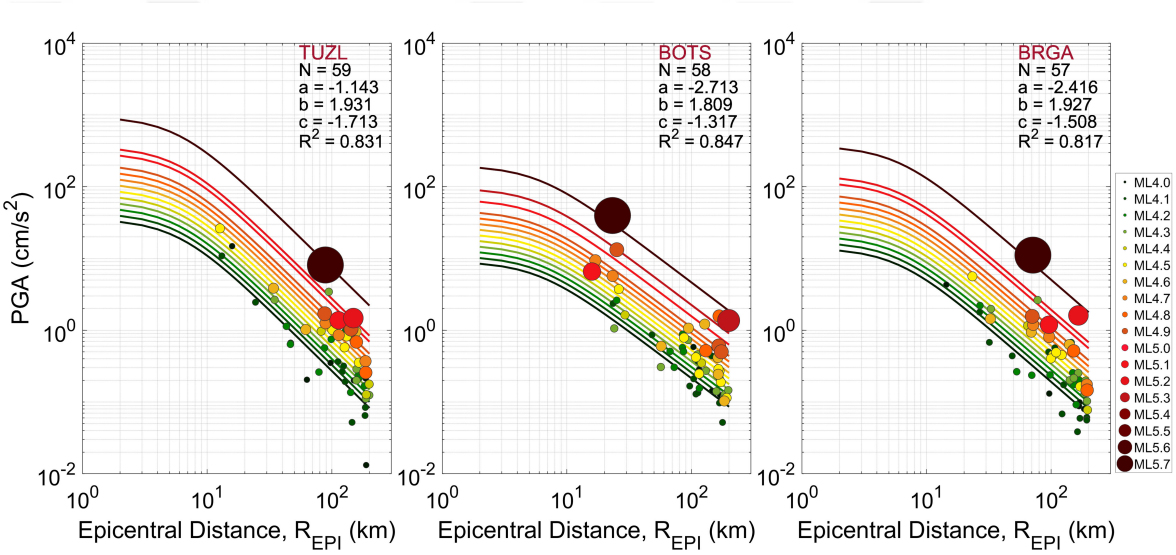


Figure 5.16. Distance Scalings of the Functional Form (5.8) (f = 5.8) for Stations TUZL, BOTS and BRGA (a, b and c refer to regression coefficients and N and R^2 stand for the number of data and coefficient of determination, respectively).

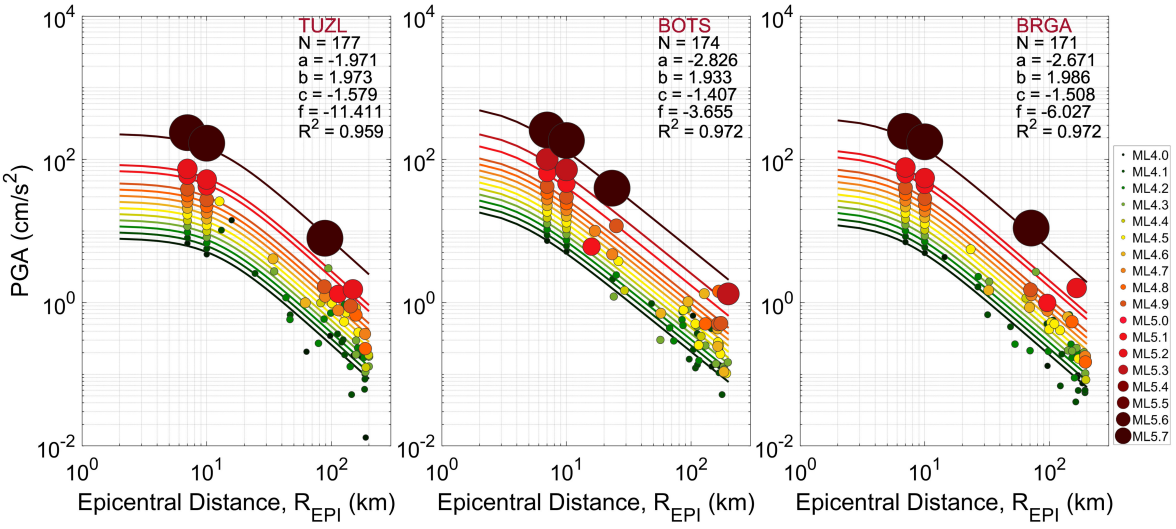


Figure 5.17. Distance Scalings of the Functional Form (5.8) (hybrid dataset) for Stations TUZL, BOTS and BRGA (a, b, c and f refer to regression coefficients and N and R^2 stand for the number of data and coefficient of determination, respectively).

5.3. Consistency Evaluation of Station-specific Empirical Equations

The analysis of residuals is firstly executed to appraise the variation of misfit between estimations of the station-specific regression analysis and actual PGAs with regression coefficients (a, b, c and f), epicentral distance and local magnitude, depth and soil condition parameter (Figure 5.18 through Figure 5.20).

The dispersion of total residuals (δ_{PGA}) around the zero line does not point out any clear correlation with regression coefficients (a, b, c and f) and R_{EPI} for three functional forms. Even so, the overestimation tendency of total residuals, which is seen in the comparison with the selected GMPEs in Chapter 3, is abolished in the predictions of this study, resulting in almost zero mean. As compared to the other two functional forms, the near-field total residuals of the Functional Form (5.8) in the hybrid dataset feature a slight tendency toward underestimation. This implies that there might be a small discrepancy between the limited number of actual near-field PGAs and those that have been externally transferred to the dataset.

Considering station-specific methodology, between-event residuals quantify the average difference between the actual GMP of a specific earthquake and the median prediction of the station under consideration. As each station acquires only a single data entry from each earthquake, the total residuals can be directly linked to the between-event residuals for each station-specific relation. However, adhering to the procedures outlined in Chapter 3, the average of total residuals across all stations is designated as the between-event residual for each earthquake. Concurrently, within-event residuals are computed in a similar approach, allowing for a systematic comparison with the residual analyses conducted for GMPEs.

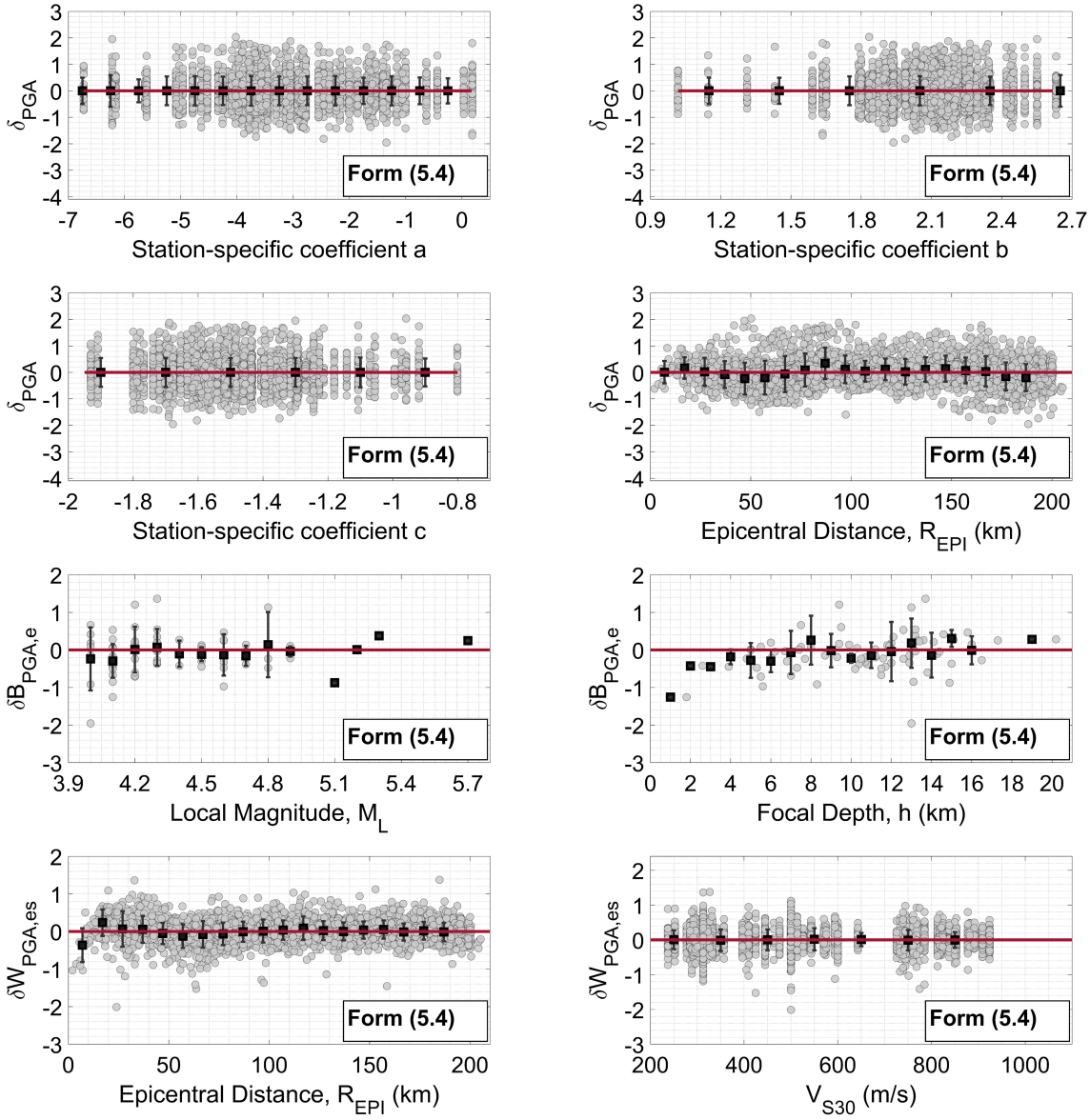


Figure 5.18. Variation of the Total Residuals with Coefficients a, b and c for the Ultimate Functional Form (5.4) and R_{EPI}, Between-event Residuals with M_L and h, the within-event residuals with R_{EPI} and V_{S30} (Zero residuals are shown by the lines in red. Error bars stand for group means with 16^{th} and 84^{th} percentiles).

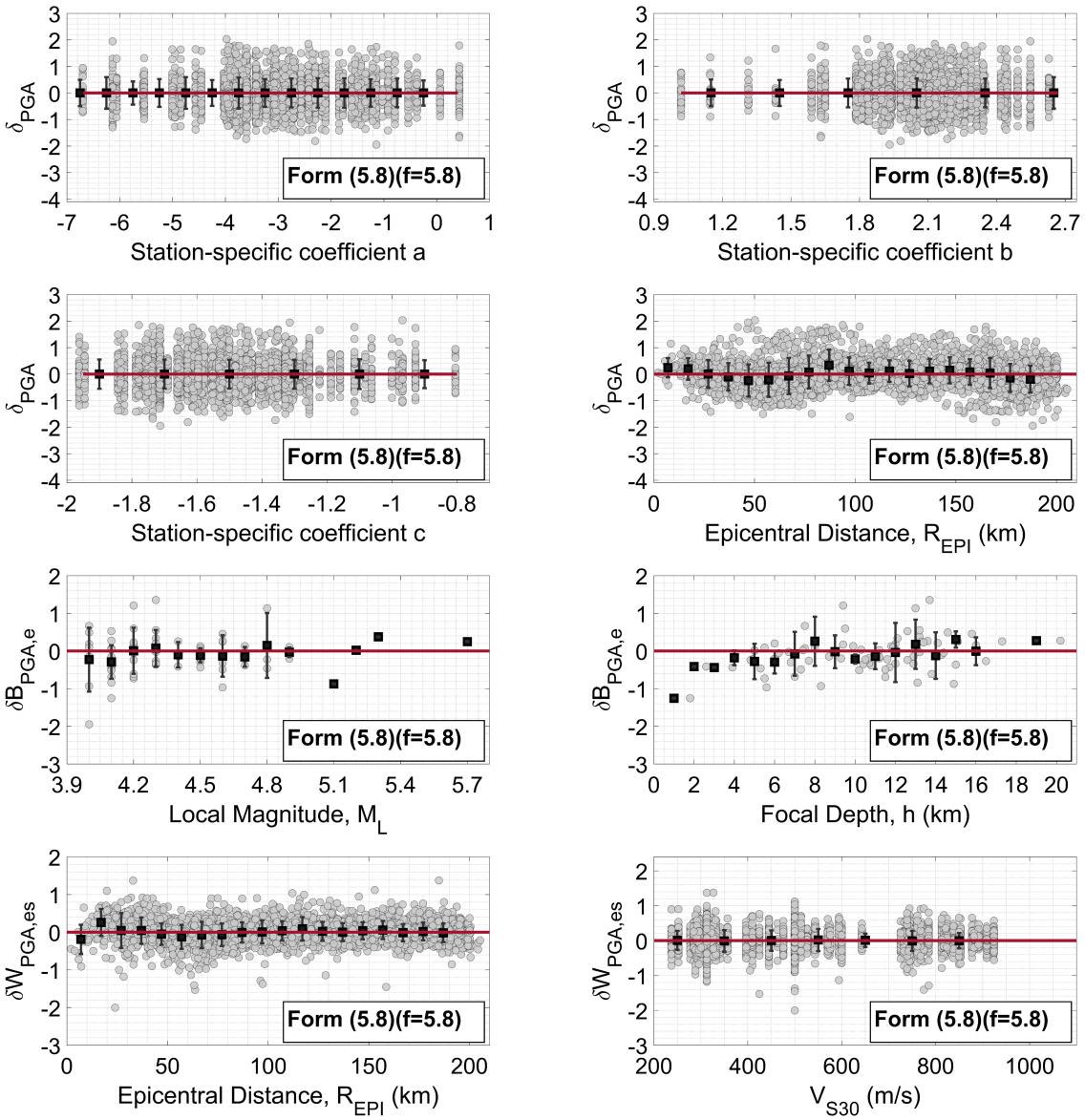


Figure 5.19. Variation of the Total Residuals with Coefficients a, b and c for the Ultimate Functional Form (5.8) (f = 5.8) and R_{EPI}, Between-event Residuals with M_L and h, the within-event residuals with R_{EPI} and V_{S30} (Zero residuals are shown by the lines in red. Error bars stand for group means with 16^{th} and 84^{th} percentiles).

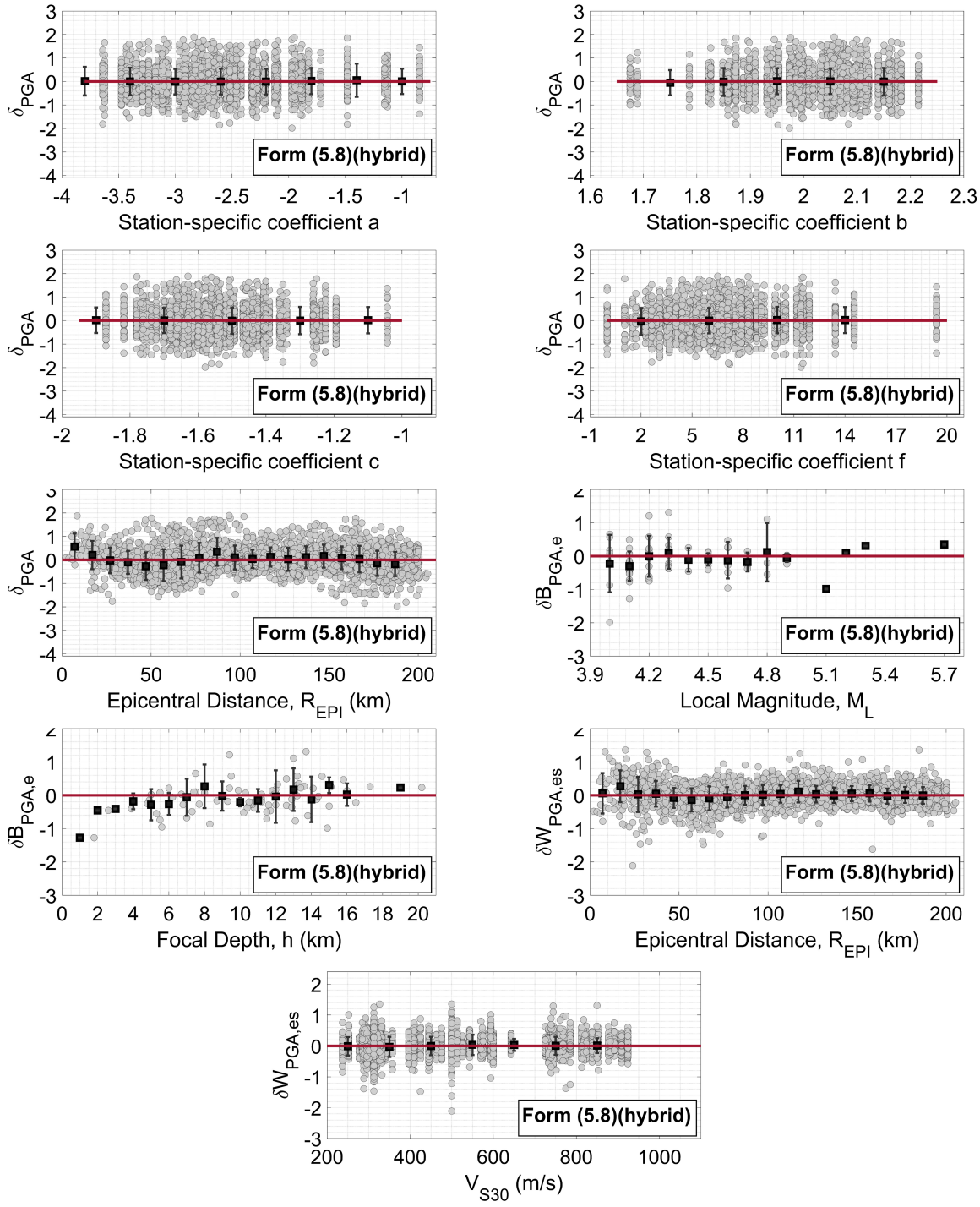


Figure 5.20. Variation of the Total Residuals with Coefficients a, b, c and f for the Ultimate Functional Form (5.8) (hybrid) and R_{EPI}, Between-event Residuals with M_L and h, the within-event residuals with R_{EPI} and V_{S30} (Zero residuals are shown by the lines in red. Error bars stand for group means with 16^{th} and 84^{th} percentiles).

Similar to the evaluation of total residuals, the between-event residuals ($\delta B_{PGA,e}$) against M_L, which mostly fluctuates around zero, do not exhibit overestimation, which is witnessed in the consistency assessment with GMPEs in Chapter 3. On the other hand, the M_L4.0 and M_L4.8 bins exhibit a notable standard deviation of between-event residuals. The deviation of between-event residuals from zero-line is seen within a very shallow depth range (h < 3 km), likely attributed to the limited number of events.

Furthermore, the within-event residuals ($\delta W_{GMP,es}$) do not offer any insights into the correlation with the entire range of R_{EPI} and V_{S30}. However, slight deviations emerge at close distances, which are consistent with the trends found in the total residuals.

A comparative analysis is also conducted between the total residuals obtained from the estimations of ASB14 and KAAH15, which seems to be the most appropriate empirical model as detailed in Chapter 3, and those derived from the station-specific approach. Total residuals of the GMPEs against the residuals of the station-specific methodology are presented in Figure 5.21 through Figure 5.23 for three final functional forms. The plotting area is segmented into four sections delineated by the 1:1 and 1:-1 lines to improve clarity. The grey-shaded areas at the upper and bottom of the plots highlight that the total residuals of GMPEs exceed those measured in the current study. In other words, the station-specific methodology outperforms the GMPEs in terms of estimation capacity in these shaded areas. Furthermore, the negative and positive signs of residuals denote the underestimation and overestimation, respectively, of the actual GMPs. In the most of stations, the majority of data is clustered in the bottom grey-shaded area, suggesting relatively superior estimations of the station-specific methodology compared to KAAH15 and ASB14. Nevertheless, a balanced inclination for both overestimation and underestimation tendency is commonly noted. Furthermore, there typically seems to be a linear relationship between this study's and GMPEs' estimations. The data appears to be shifted from the 1:1 line in parallel, yet the extent of this deviation varies from station to station.

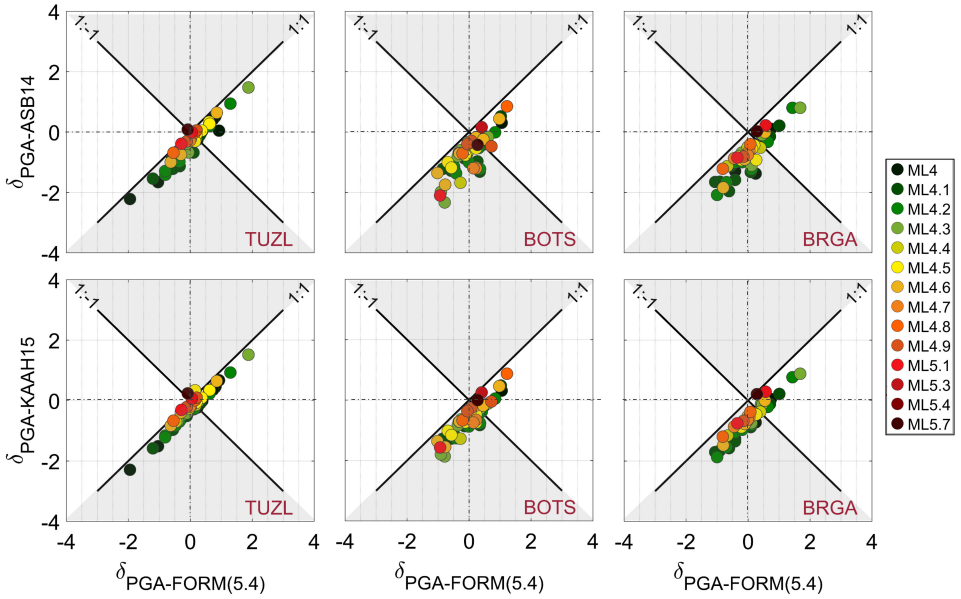


Figure 5.21. Comparison Between Total Residuals of ASB14 and KAAH15 and Functional Form (5.4) for Stations TUZL, BOTS and BRGA (Grey-shaded areas represent the smaller residuals of the station-specific approach.)

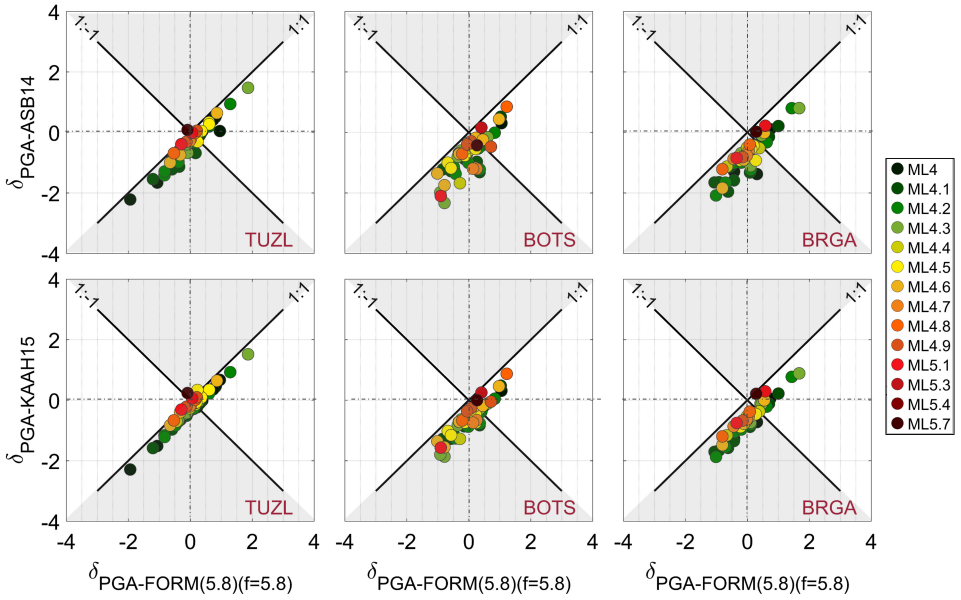


Figure 5.22. Comparison Between Total Residuals of ASB14 and KAAH15 and Functional Form (5.8) (f = 5.8) for stations TUZL, BOTS and BRGA (Grey-shaded areas represent the smaller residuals of the station-specific approach.)

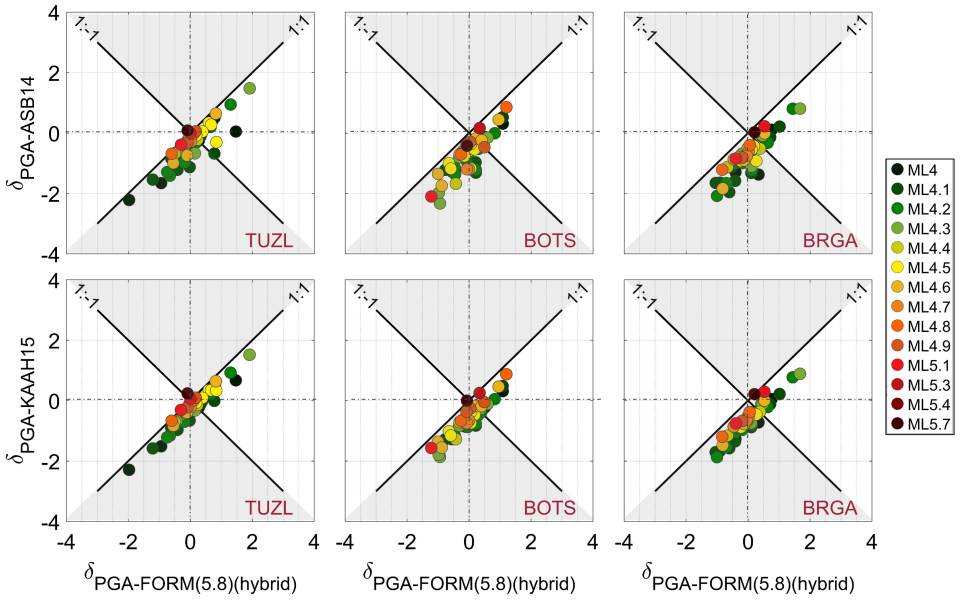


Figure 5.23. Comparison Between Total Residuals of ASB14 and KAAH15 and Functional Form (5.8) (hybrid dataset) for stations TUZL, BOTS and BRGA (Grey-shaded areas represent the smaller residuals of the station-specific approach.)

5.4. Sensitivity Analysis for Magnitude and Soil Condition Parameter

5.4.1. Sensitivity of Station-specific Coefficients against Magnitude

The variation of the station-specific regression coefficients with magnitude is examined in this section due to the low amount of moderate and large magnitude events ($M_L > 4.7$) in the database of this thesis as discussed in Chapter 3. The highest magnitude (M_L5.7) in the database belongs to the earthquake that took place off Silivri on September 26, 2019. In the context of the station-specific approach, it's worth noting that not all the stations under consideration might have recorded events of the same highest magnitude level. Simply stated, the maximum magnitude recorded at each station might not always match M_L5.7. These circumstances may introduce a contradiction in the estimations for magnitudes that fall outside the scope of the regression analyses. The standard deviations of coefficients a, b and c reduce when the hybrid dataset is incorporated in the regressions of Functional Form (5.8) regressions. However, among all coefficients of the Functional Form (5.8) using the hybrid

dataset, coefficient f reveals the largest standard deviations. The coefficient b displays slightly larger standard deviations for $M_L < 5.3$, while those corresponding to larger magnitudes show smaller deviations from the total mean (Figure 5.24 through Figure 5.26). This may be attributed to the incorporation of a limited number of events at this relatively large magnitude level.

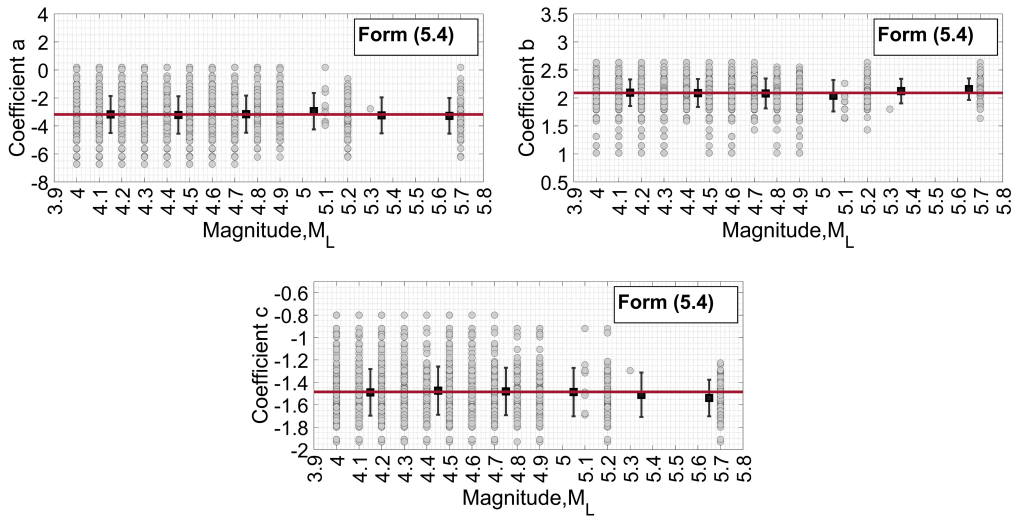


Figure 5.24. Variation of Station-specific Regression Coefficients with M_L for Functional Form (5.4) (Red lines correspond to the total mean of coefficients and total means are shown by the lines in red. Error bars stand for group means with 16^{th} and 84^{th} percentiles).

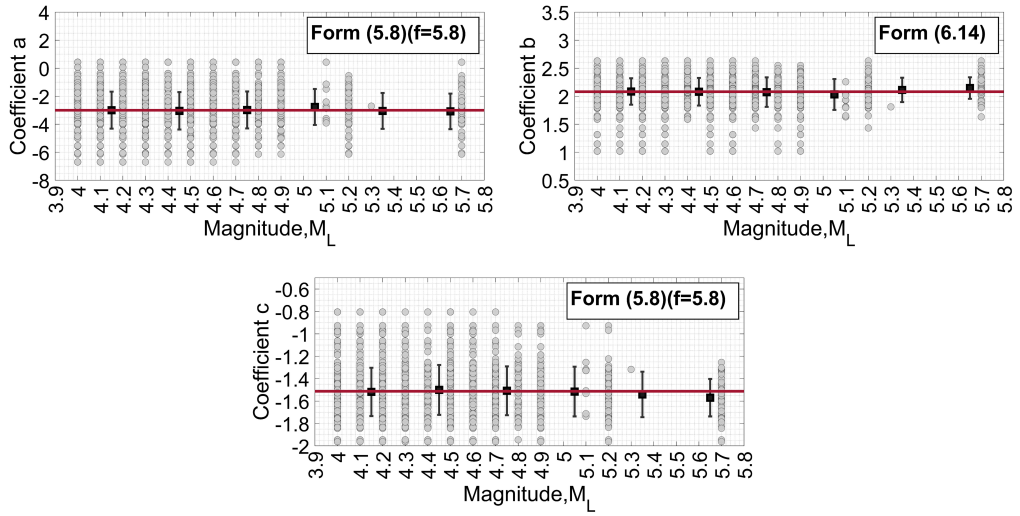


Figure 5.25. Variation of Station-specific Regression Coefficients with M_L for Functional Form (5.8) (f = 5.8) (Red lines correspond to the total mean of coefficients and total means are shown by the lines in red. Error bars stand for group means with 16^{th} and 84^{th} percentiles).

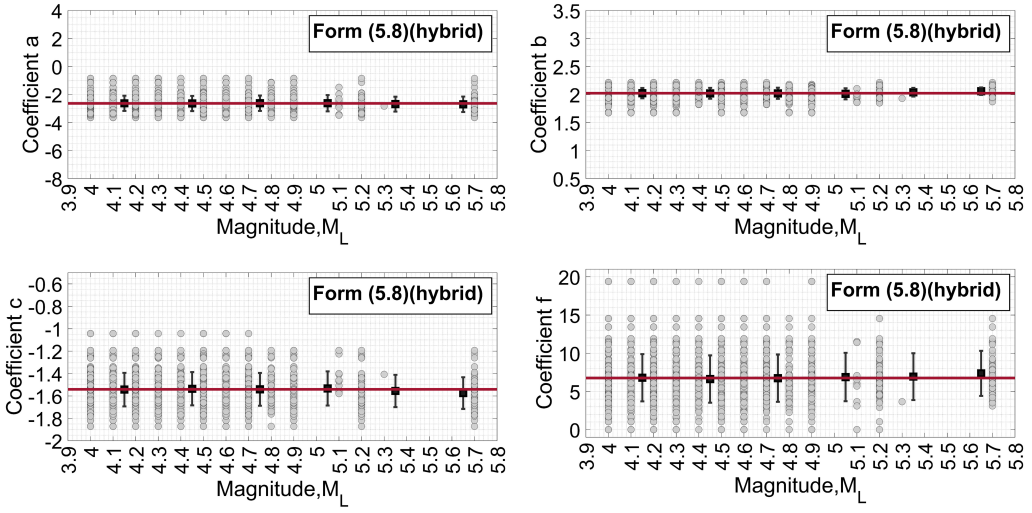


Figure 5.26. Variation of Station-specific Regression Coefficients with M_L for Functional Form (5.8) (hybrid) (Red lines correspond to the total mean of coefficients and total means are shown by the lines in red. Error bars stand for group means with 16^{th} and 84^{th} percentiles).

Figure 5.27 exemplifies the variation in the cumulative number of data with the increase in magnitude levels for stations TUZL, BOTS, and BRGA. The rate of increase in the cumulative number of data diminishes as the magnitude levels rise. The variations in the regression coefficients on a station basis are investigated by incorporating the data with a magnitude increment of 0.1 to figure out the effect of each magnitude level in the regression analysis. The station-specific regression analyses are reiterated for each subset generated with a cumulative increase in the number of data. The variation of the regression coefficients normalized to their maxima with magnitude is displayed in Figure 5.28 through Figure 5.31. The normalized coefficients point out fluctuations, specifically in the small magnitude range (up to M_L4.3). Still, they maintain remarkable stability beyond M_L4.3. This may be a precursor to the possibility this station-specific methodology is extended to events of greater magnitude.

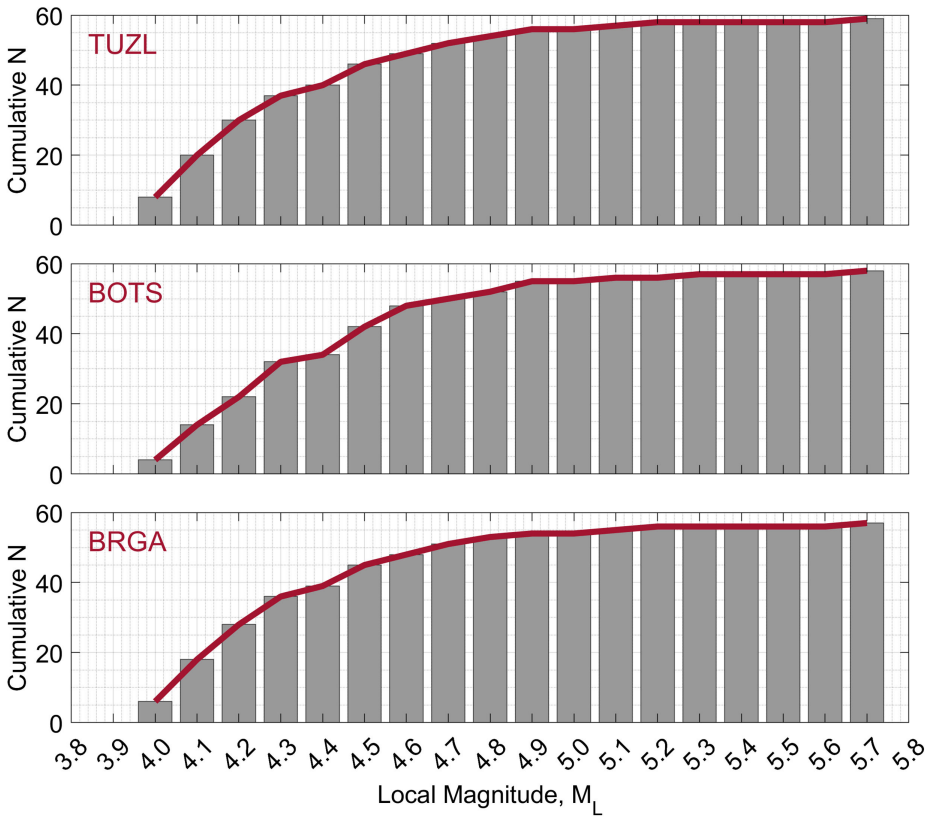


Figure 5.27. Cumulative Variation of Subsets' Size with M_L for Station TUZL, BOTS and BRGA.

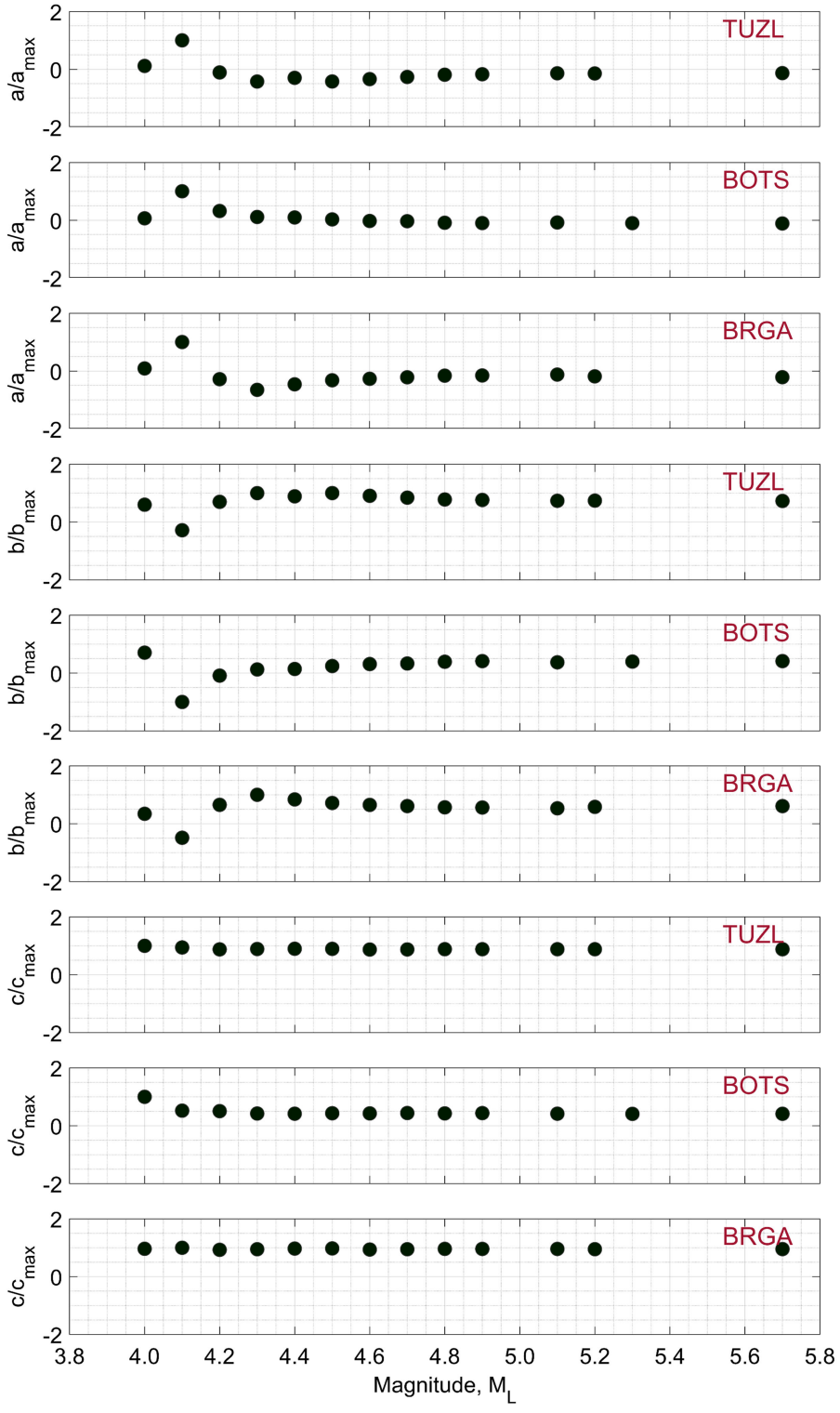


Figure 5.28. Variation of the Normalized Coefficients a, b and c of Functional Form (5.4) with M_L for the Cumulative Subsets of the Stations TUZL, BOTS and BRGA.

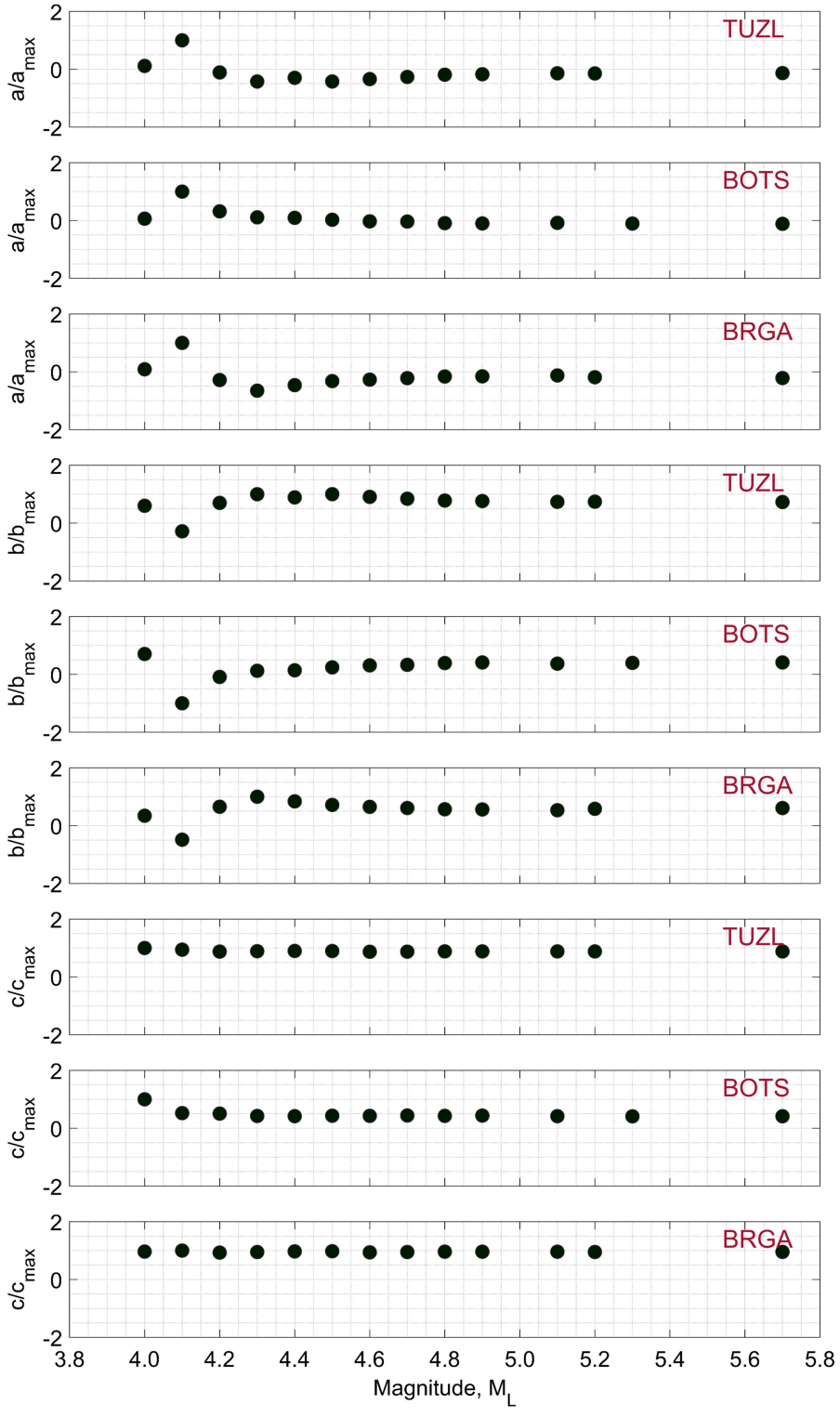


Figure 5.29. Variation of the Normalized Coefficients a, b and c of Functional Form (5.8) (f = 5.8) with M_L for the Cumulative Subsets of the Stations TUZL, BOTS and BRGA.

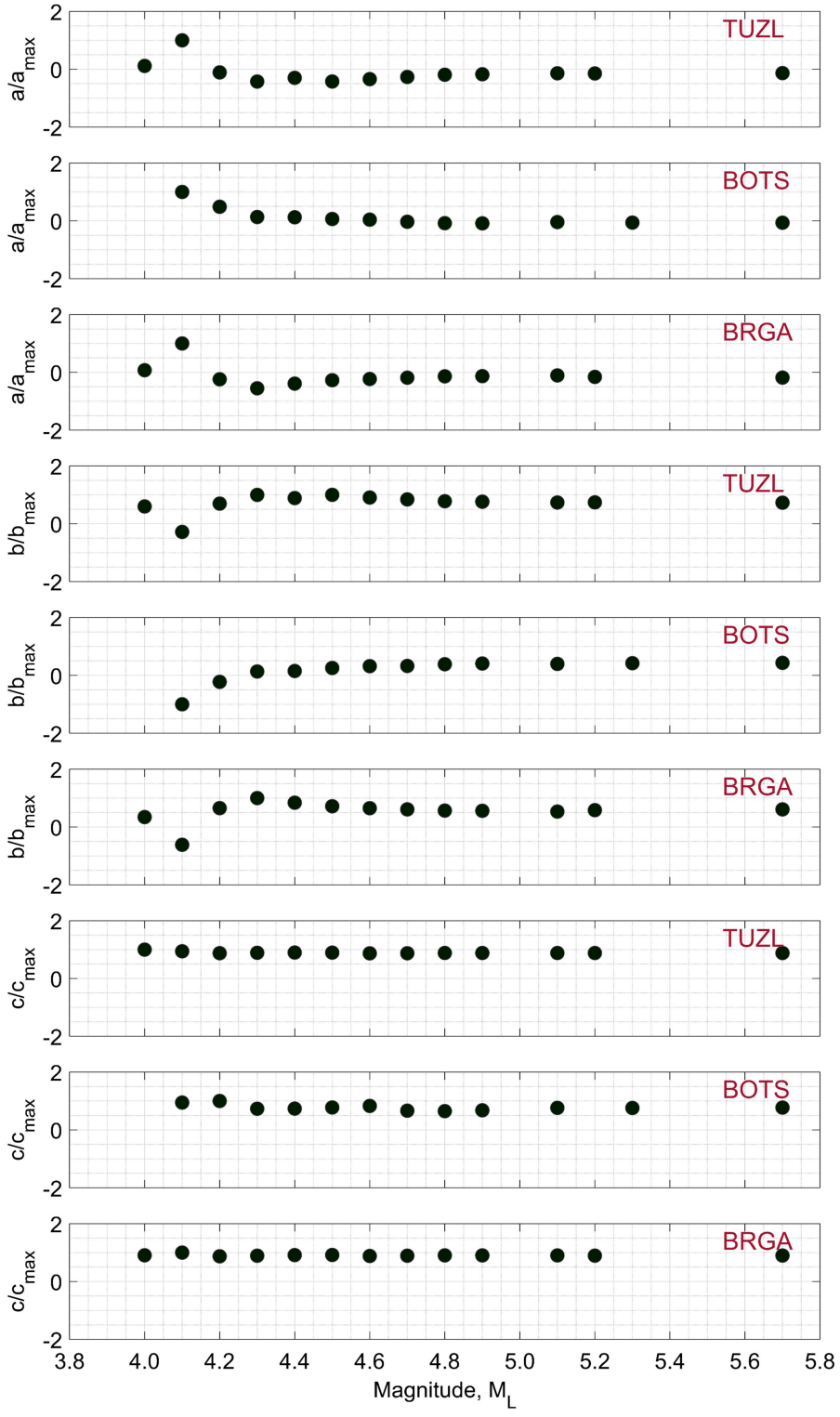


Figure 5.30. Variation of the Normalized Coefficients a, b and c of Functional Form (5.8) (hybrid) with M_L for the Cumulative Subsets of the Stations TUZL, BOTS and BRGA.

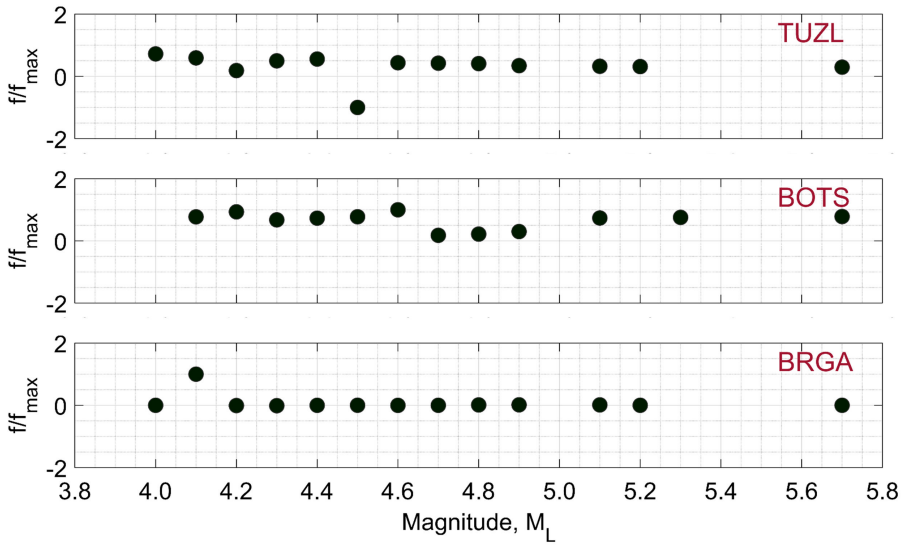


Figure 5.31. Variation of the Normalized Coefficient f of Functional Form (5.8) (hybrid) with M_L for the Cumulative Subsets of the Stations TUZL, BOTS and BRGA.

Additionally, station-based datasets are split into two subsets, each containing an equal number of data, to conduct magnitude sensitivity analysis. One subset comprises small-magnitude events, displaying an unstable tendency as expressed in the previous analysis, while the second subset represents the intermediate-magnitude range (up to M_L5.7). A stable coefficient value for both subsets could not be found due to the non-homogeneous distribution of magnitudes and the insufficient number of data in each station-specific subset.

5.4.2. Sensitivity of Station-specific Coefficients against Soil Condition Parameter

The sensitivity of the regression coefficients regarding V_{S30} is also tested since the station-specific regressions do not necessitate the soil condition parameter (e.g. V_{S30}). Figure 5.32 through Figure 5.34 displays the changes in all regression coefficients of three functional forms concerning V_{S30}. The coefficient a tends to yield values below the mean in relatively softer soils ($V_{S30} < 500$ m/s), while it floats around the average value in stiffer soils for Functional Form (5.4) and (5.8) (f=5.8). In the case of incorporation

of the hybrid dataset, the coefficient a seems to be stable through the entire V_{S30} range. Coefficient b which signifies the magnitude dependency, does not demonstrate any discernible trend with respect to V_{S30} and predominantly remains around the mean value of b for all functional forms. However, coefficient c, specifying the amount of geometric attenuation, shows a linear increasing tendency in the negative region as V_{S30} grows. This linear pattern of coefficient c is less pronounced with smaller R^2 in the Functional Form (5.8) utilizing the hybrid dataset. However, there is a linear upward trend in coefficient f as soil conditions enhance.

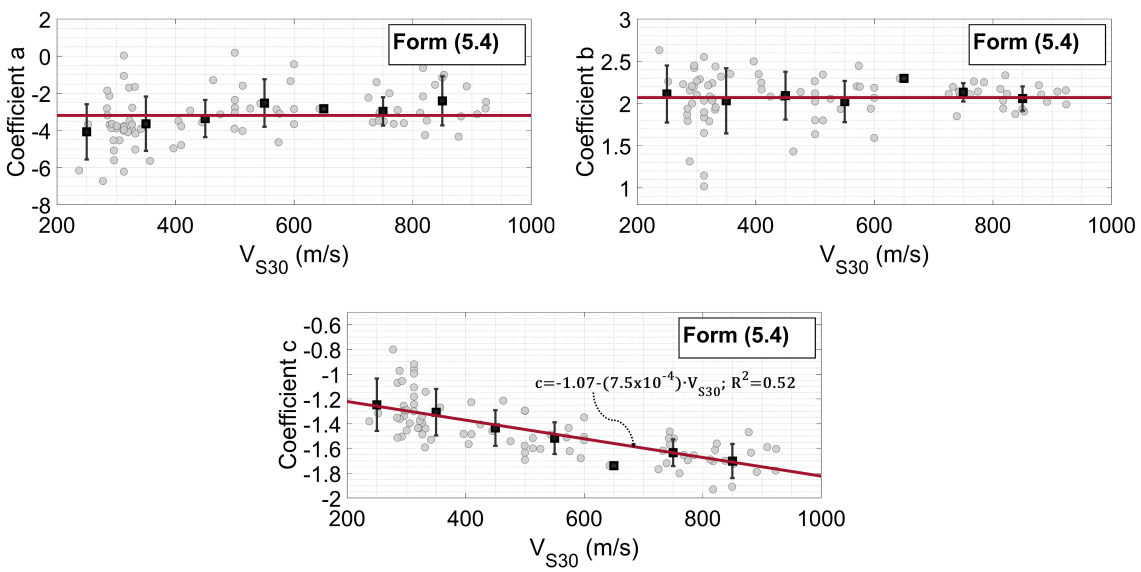


Figure 5.32. Variation of Station-specific Regression Coefficients with V_{S30} for Functional Form (5.4) (Total means or regression relations are shown by the lines in red. Error bars stand for group means with 16^{th} and 84^{th} percentiles).

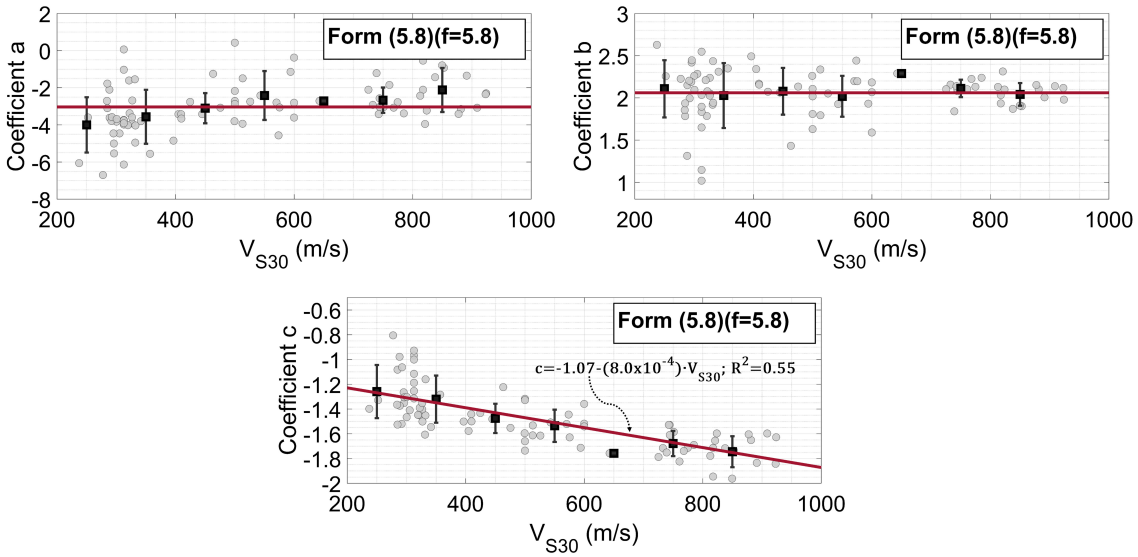


Figure 5.33. Variation of Station-specific Regression Coefficients with V_{S30} for Functional Form (5.8) (f = 5.8) (Total means or regression relations are shown by the lines in red. Error bars stand for group means with 16th and 84th percentiles).

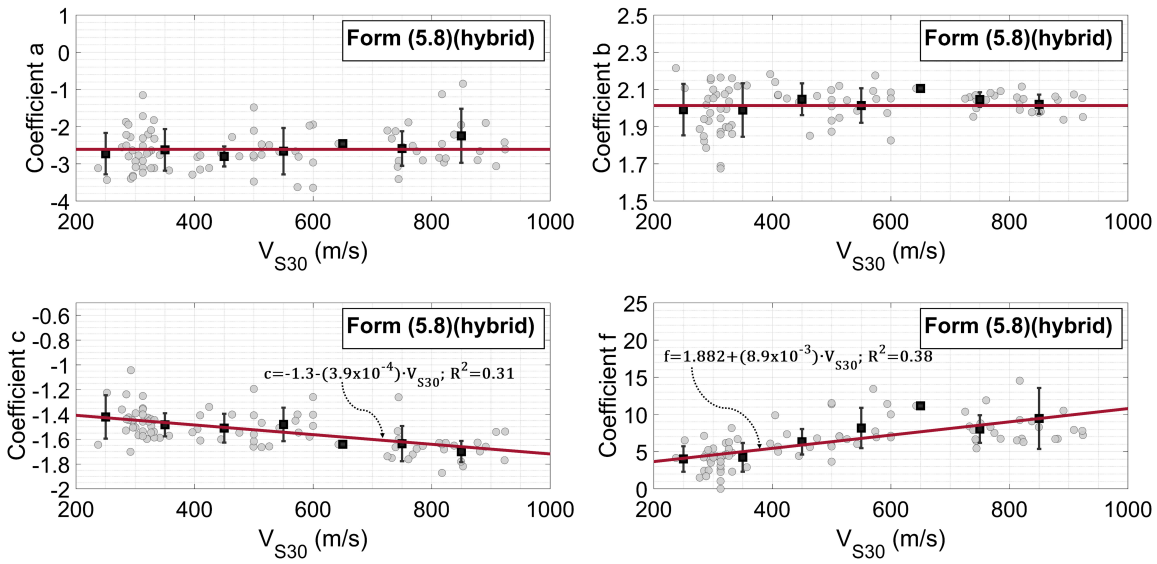


Figure 5.34. Variation of Station-specific Regression Coefficients with V_{S30} for Functional Form (5.8) (hybrid) (Total means or regression relations are shown by the lines in red. Error bars stand for group means with 16th and 84th percentiles).

6. SPATIAL DISTRIBUTION OF ESTIMATIONS VIA STATION-SPECIFIC METHODOLOGY FOR ISTANBUL

The primary objective of this chapter is to create spatial distribution maps of PGA, derived from station-specific methodologies, for particularly southern part of İstanbul.

6.1. 2-D Delaunay Triangulation Grid Meshing

The station-specific coefficients are available for the recordings sites and the estimation of GMPs can be simply accomplished using the station-specific equations derived in Chapter 5. Yet, it is essential to procure the supplementary coefficients in locations where station-specific regression analysis could not manage to produce the required coefficients for generating a spatial distribution of GMPs.

In many regions, the spacing between strong-motion stations is typically sparse, with the majority being more than 10 km apart from the other [178]. In areas where coefficients are not available, the estimator parameters regarding source, path, and site, along with the resulting GMPs, may demonstrate spatial variability, particularly when the inter-station distances are significant. Nevertheless, the presence of a dense strong ground motion network diminishes spatial variability and allows for the utilization of conventional interpolation methods. Hence, the dense coverage of the IERREWS network (0.7 km $< \Delta R_{station} <$ 16 km) and the station-specific approach allow a basis for assuming that missing information at a given random point can be calculated through simple interpolation using the results from three neighbouring stations. In particular, triangular grid meshing is preferred for the spatial distribution of station-specific coefficients to minimize the impact of the irregular station distribution. Larger triangles provide approximate estimates in areas where the distribution of stations is sparse, whereas smaller triangles serve to take into account the impact of denser station populations. The densely populated southern part of Istanbul, housing IERREWS stations, is divided into non-overlapping triangles encircled by a convex hull through

MATLAB's Delaunay triangulation meshing algorithm. The outer convex hull offers a practical advantage by particularly excluding areas where IERREWS stations are not deployed. Initially, the algorithm designates the station points as the vertices of each triangle. Next, the Delaunay triangulation meshing is accomplished by maximizing the minimum angle of all triangles [179]. The algorithm assigns the mean value of coefficients at the vertices of each triangle to the point where the bars of the newly generated triangles intersect as exemplified in Figure 6.1.

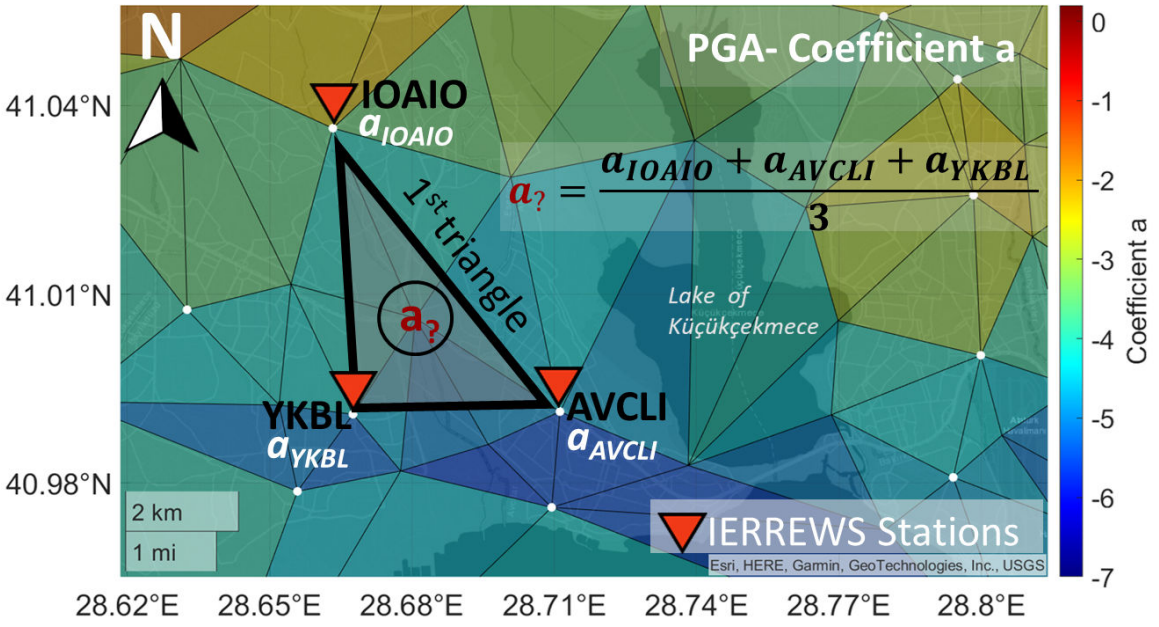


Figure 6.1. Main Philosophy of 2-D Delaunay Triangulation Meshing and Interpolation Process.

6.2. Determination of Cell-based Coefficients

Istanbul is subdivided into a grid with a size of 0.005°×0.005°, covering approximately 420 km in longitude and 556 km in latitude. However, the region must be constrained to a latitudinal border enacted by the northernmost stations due to the absence of recording sites in those areas of Istanbul. The restricted area is divided into 4,714 cells. The coefficient value for each cell is determined by assigning the interpolated point that is closest to the centre. However, if the cell consists of one

of the IERREWS stations, its station-specific coefficient is directly allocated to the cells. Finally, a unique attenuation equation characterised by the distinct coefficients is formulated for each cell.

To ascertain the optimal number of interpolation repetitions, a sensitivity analysis is conducted on triangle grid meshings, specifically focusing on the variation of the coefficients determined in each cell. The interpolation process is optimized by increasing the number of interpolation points to ensure that cell coefficients in the current step closely match those obtained in the previous step. Therefore, the interpolation is iteratively repeated 6 times, progressively increasing the number of points and triangles. The variation of geometrical meshing features with the repetition of interpolation is summarized in Table 6.1. The points used in the first meshing is identical to the final number of station ($N_{st} = 83$). It is important to emphasize that station YLVH, situated outside the study area, is excluded due to its potential to provide misleading results that could disrupt the interpolation process. With each interpolation, there is a threefold increase in the number of triangles generated compared to the previous step.

Table 6.1. Variation of meshing features based on the degree of interpolation.

Degree of Interpolation	**0**	**1**	**2**	**3**	**4**	**5**	**6**
Number of points	83	238	703	2,098	6,283	18,838	56,503
Number of triangles	155	465	1,395	4,185	12,555	37,665	112,995

Figure 6.2 illustrates the change of each cell-based coefficient between two sequential interpolations against degrees of interpolation for Functional Form (5.8) (hybrid dataset) as an example. Large deviations are mostly evident up to the 4^{th} degree of interpolation. Subsequently, the coefficients stabilize and exhibit greater constancy at the 6^{th} degree of interpolation. Hence, the interpolation process is optimized with the greatest number of interpolation points, providing as possible as similar cell coefficients as in the previous interpolation step. Similar approaches are applied to the

other functional forms. As a result, the 6th degree of triangulation is employed to generate cell-based coefficient maps. A total of 56,503 interpolated points together with 83 stations and 112,995 triangles are produced.

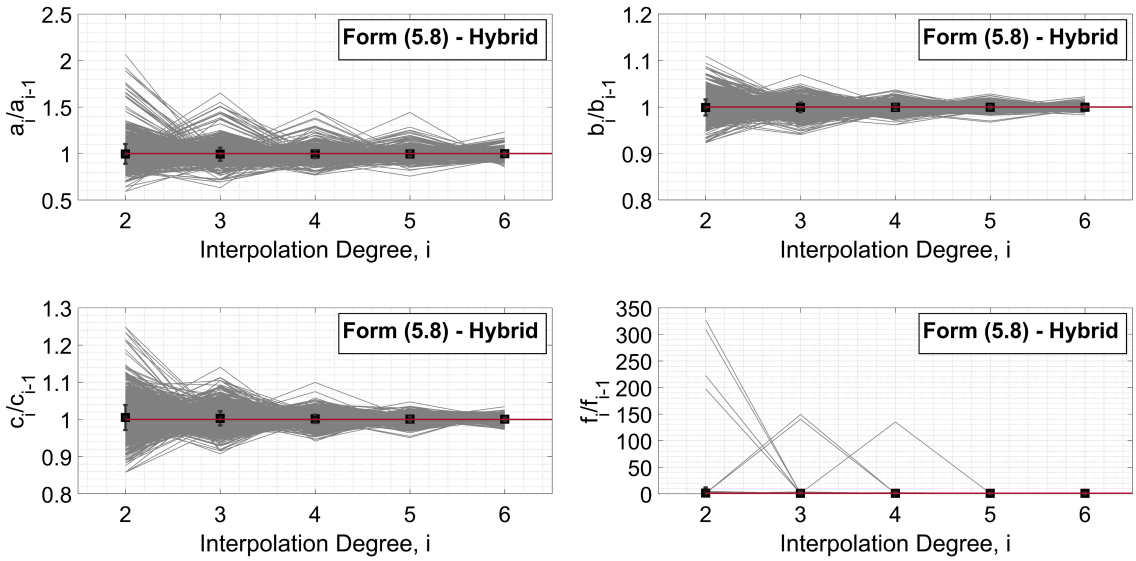


Figure 6.2. Variation of Station-specific Coefficients a, b c and f with the Degree of Interpolation for Functional Form (5.8) (hybrid dataset).

Figure 6.3 through Figure 6.5 displays the ultimate triangular distribution of all coefficients (a, b, c and f) of three functional forms for the 6th degree of interpolation. Ultimately, three cell-based maps are produced for coefficients a, b, c and f as illustrated in Figure 6.6 through Figure 6.8.

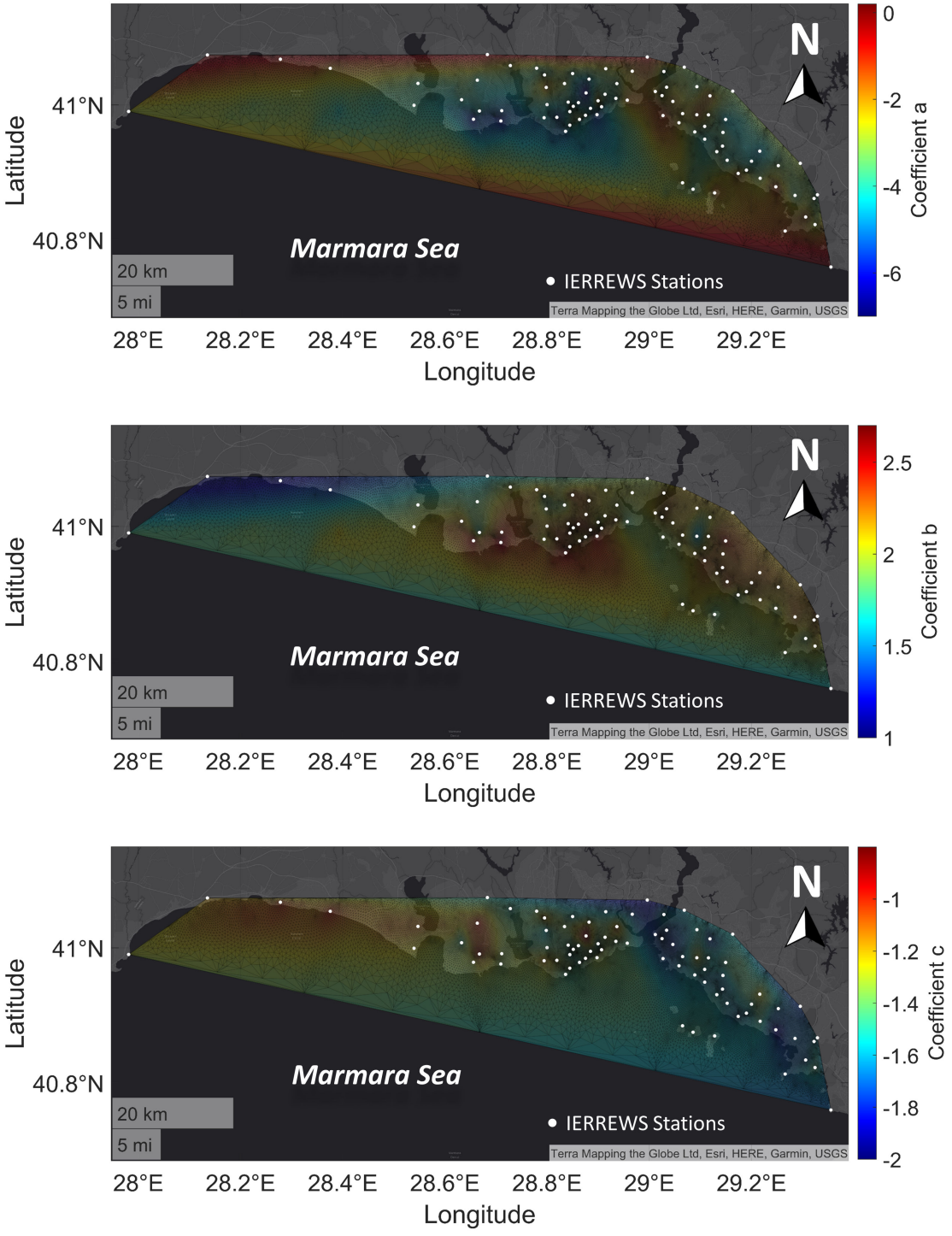


Figure 6.3. Spatial Distribution of Interpolated Coefficients for PGA Obtained through Functional Form (5.4).

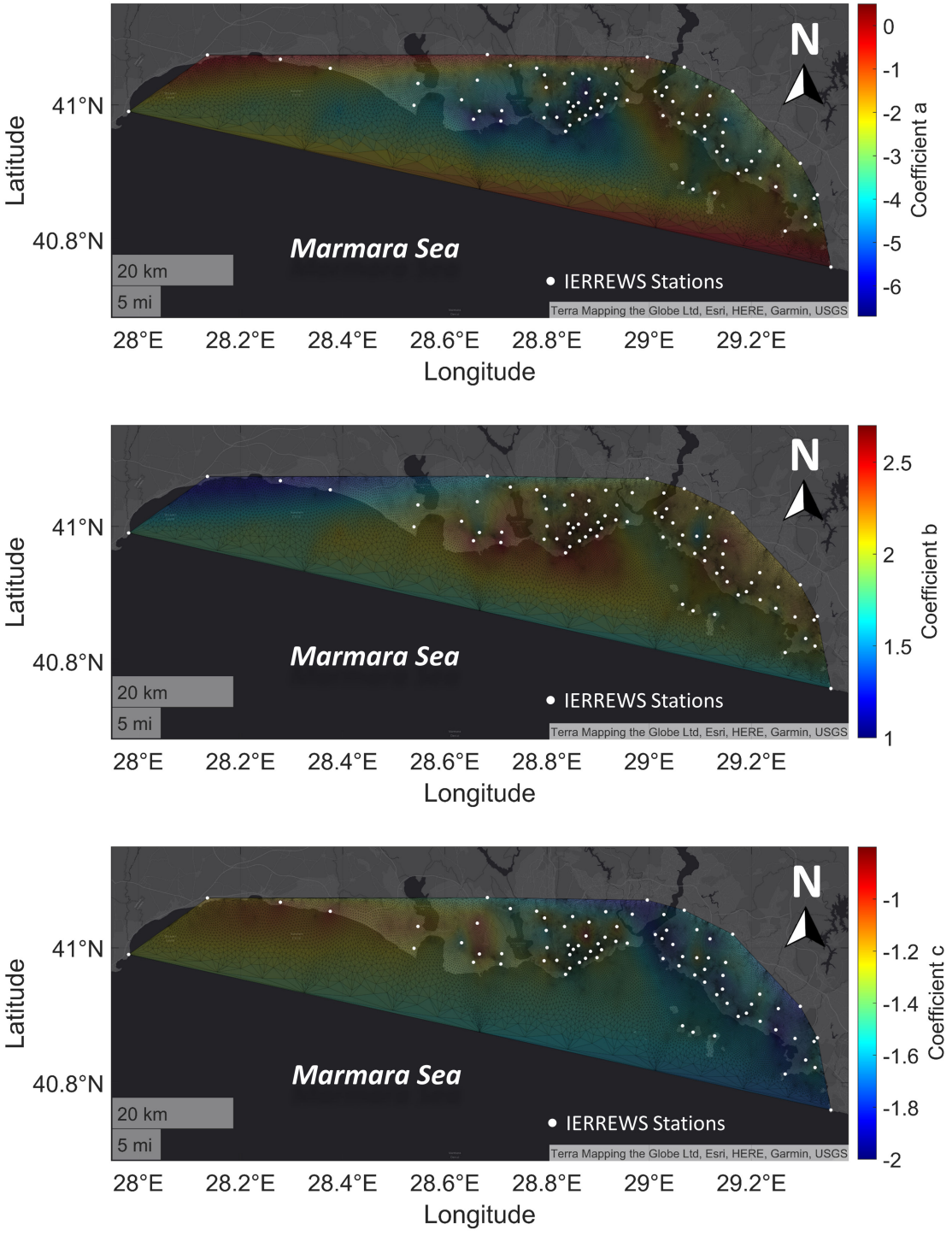


Figure 6.4. Spatial Distribution of Interpolated Coefficients for PGA Obtained through Functional Form (5.8) (f = 5.8).

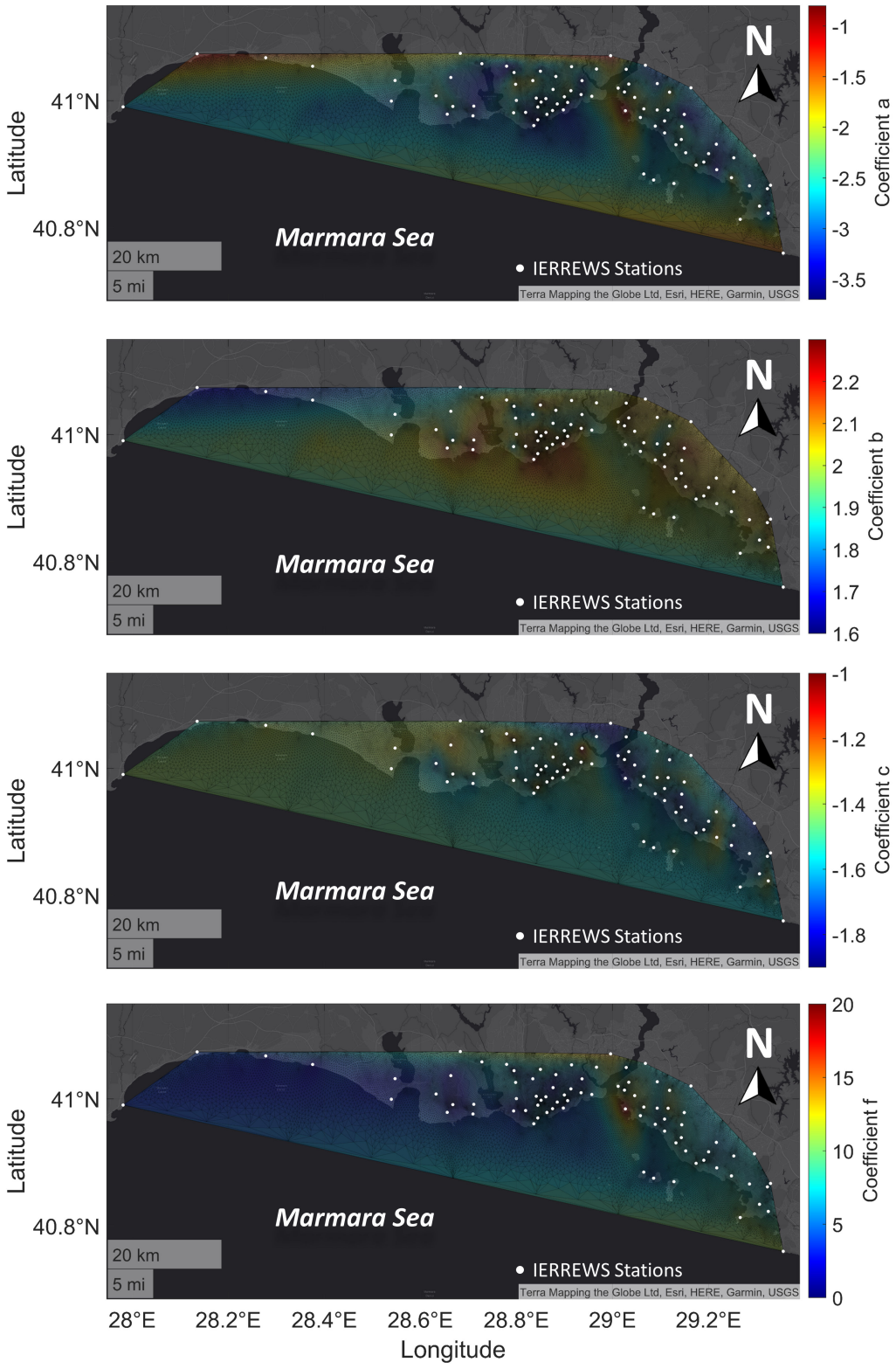


Figure 6.5. Spatial Distribution of Interpolated Coefficients for PGA Obtained through Functional Form (5.8) (hybrid dataset).

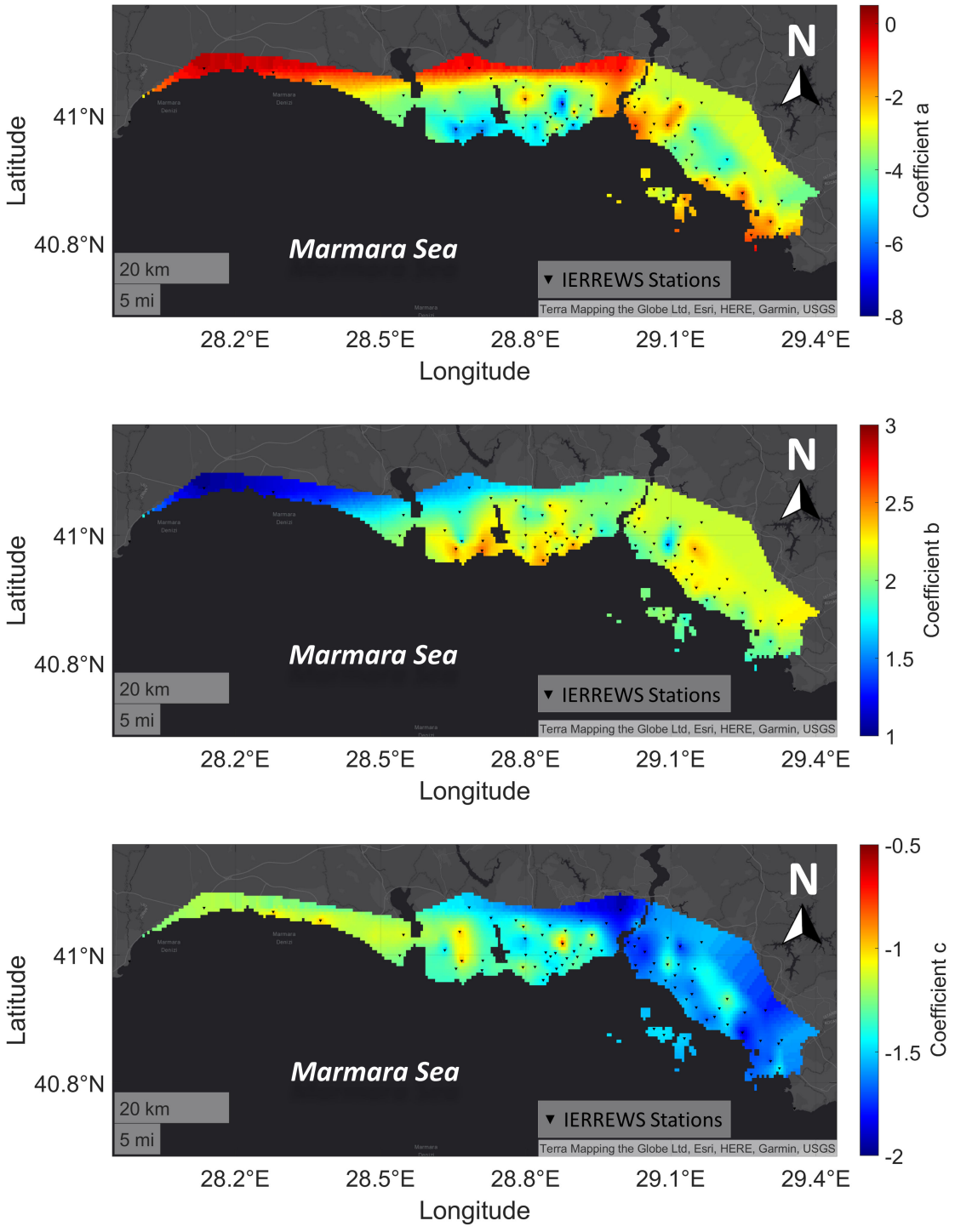


Figure 6.6. Spatial Distribution of Cell-based Coefficients for PGA Obtained through Functional Form (5.4).

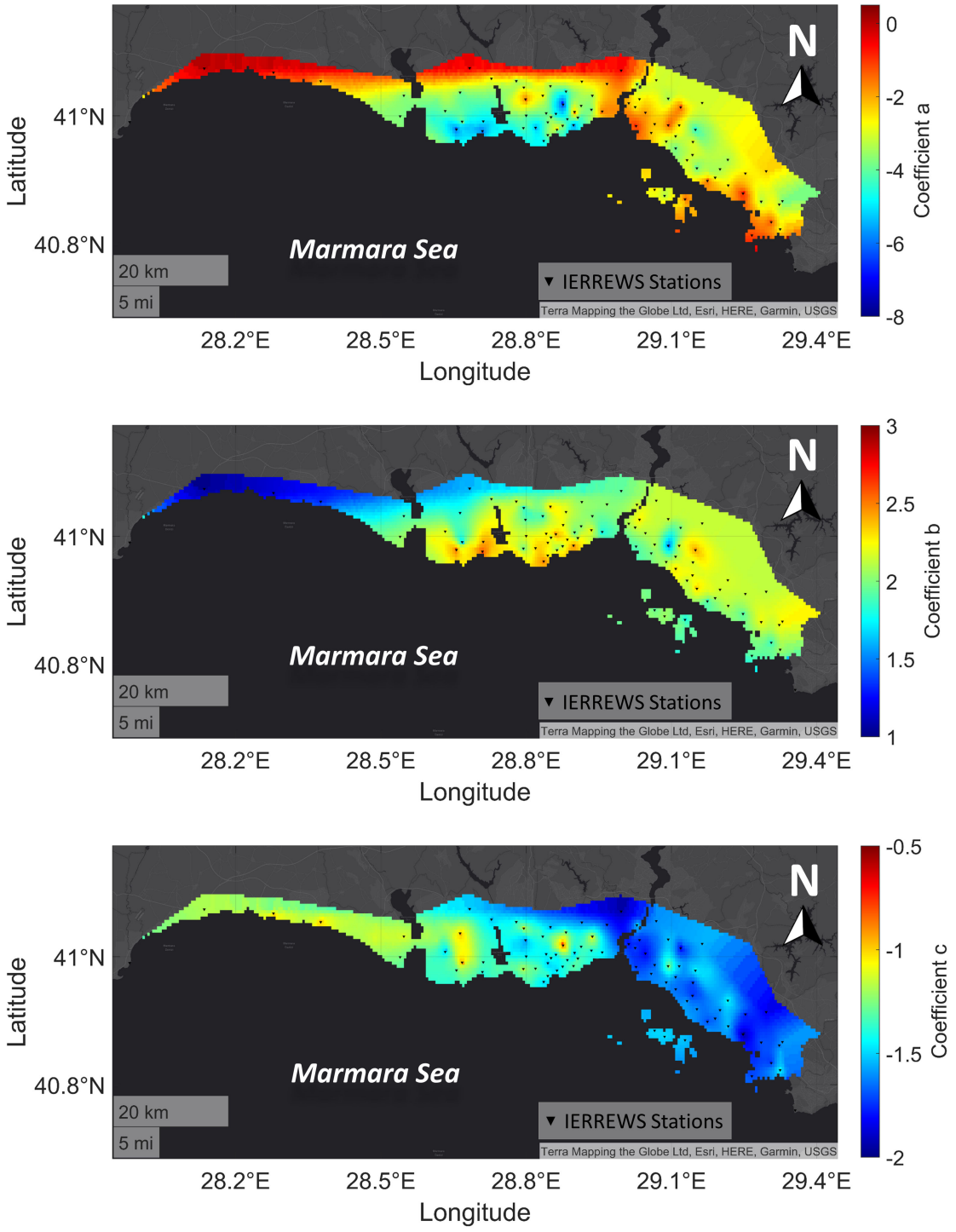


Figure 6.7. Spatial Distribution of Cell-based Coefficients for PGA Obtained through Functional Form (5.8) (f = 5.8).

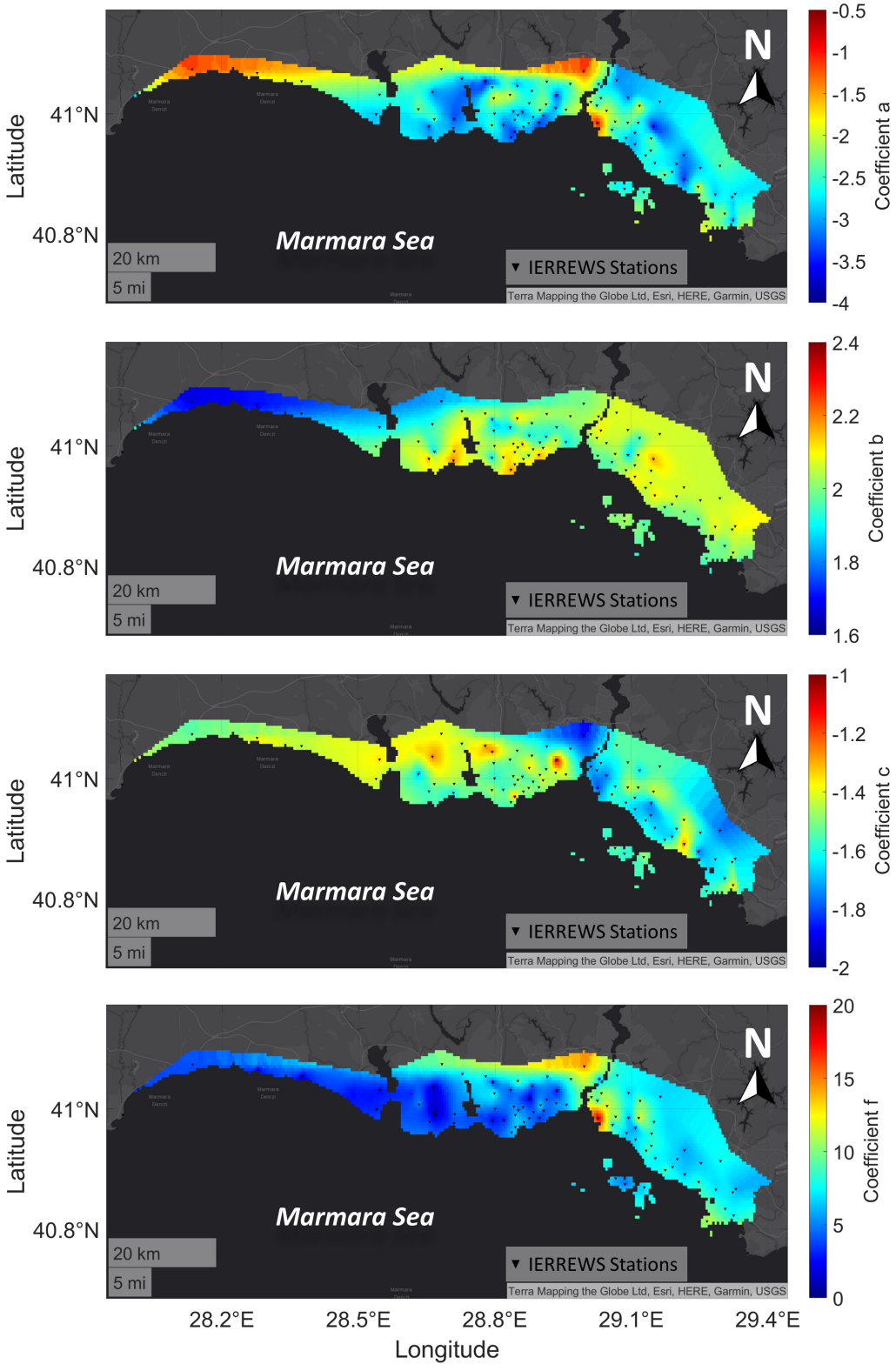


Figure 6.8. Spatial Distribution of Cell-based Coefficients for PGA Obtained through Functional Form (5.8) (hybrid dataset).

A concern has been raised regarding the integration of V_{S30} into the interpolation process, given that coefficients c and f demonstrate a dependency on V_{S30}, as emphasized in Chapter 5. Before diving into the modification of the interpolation stage for the soil condition parameter, it is checked whether the relationship between these coefficients and V_{S30} is preserved after the interpolation stage. Figure 6.9 shows the relationship between interpolated c and f values and the corresponding V_{S30} for each cell. The regression relations between these coefficients and V_{S30} appear to closely align with those derived solely for station locations in Chapter 5. Additionally, the very slightly different R^2 values support and validate this inference. Hence, the interpolation process can be considered partially successful in distributing the V_{S30} dependency of coefficients c and f. This success may be attributed to the proximity of stations, facilitating an effective distribution of soil condition differences. That's why, the interpolation process in this thesis does not incorporate any modifications regarding soil conditions.

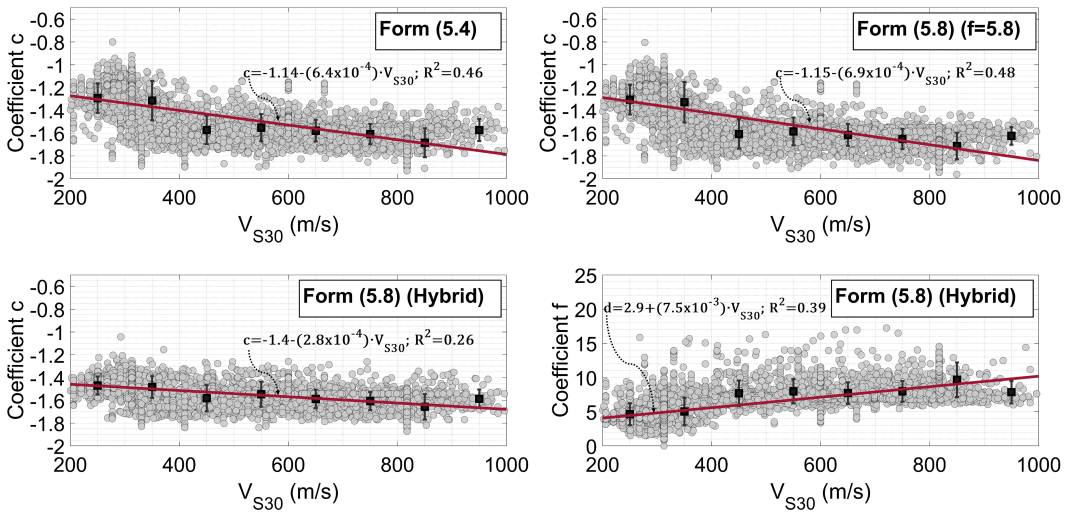


Figure 6.9. Variation of Cell-specific Regression Coefficients with V_{S30} (Regression relations are shown by the lines in red. Error bars stand for group means with 16^{th} and 84^{th} percentiles.

6.3. Evaluation of Prediction Performance of the Proposed Methodology

The station-specific methodology's performance to predict PGAs is assessed by examining spatial distribution maps for both hypothetical and actual earthquakes and comparing them to those generated by the GMPE of KAAH15, which seems to be less inappropriate for the database used in this thesis for PGA.

6.3.1. Comparative Evaluation for Hypothetical Earthquakes

Two hypothetical earthquakes of moderate and large magnitudes, 5.7 and 6.5 on the local scale, are assumed to take place at the identical epicentre. The epicentre of the earthquakes has been intentionally chosen to be about in the approximate middle of all IERREWS stations. This selection also considers ensuring that there are stations at various distances capable of testing the near-field PGAs. The Functional Forms (5.4) and (5.8) (for both f=5.8 and hybrid dataset approach) are executed by utilising the cell-based regression coefficients acquired through the interpolation procedure for these scenario events. In the following step, PGAs are calculated individually for each cell using cell-specific equations. Figure 6.10 and Figure 6.11 show the spatial distribution of PGAs estimated by three functional forms of the station-specific methodology and KAAH15.

In the case of an M_L5.7 event, the maximum PGA is computed as 232 cm/s^2 using the Functional Form (5.4) in the northwest of the epicentre ($R_{EPI} \approx$ 14 km –around station HVHR-). Using the Functional Form (5.8), with the parameter f set to 5.8, the resulting calculation yields a slight decrease in the maximum PGA value to 222 cm/s^2 at the same R_{EPI}. The Functional Form (5.8) with station-specific f values, achieved through the implementation of hybrid datasets, results in a PGA of 148 cm/s^2 at the identical location. In contrast, the KAAH15 model estimates the maximum PGA as 75 cm/s^2 at 3 km west of station HVHR.

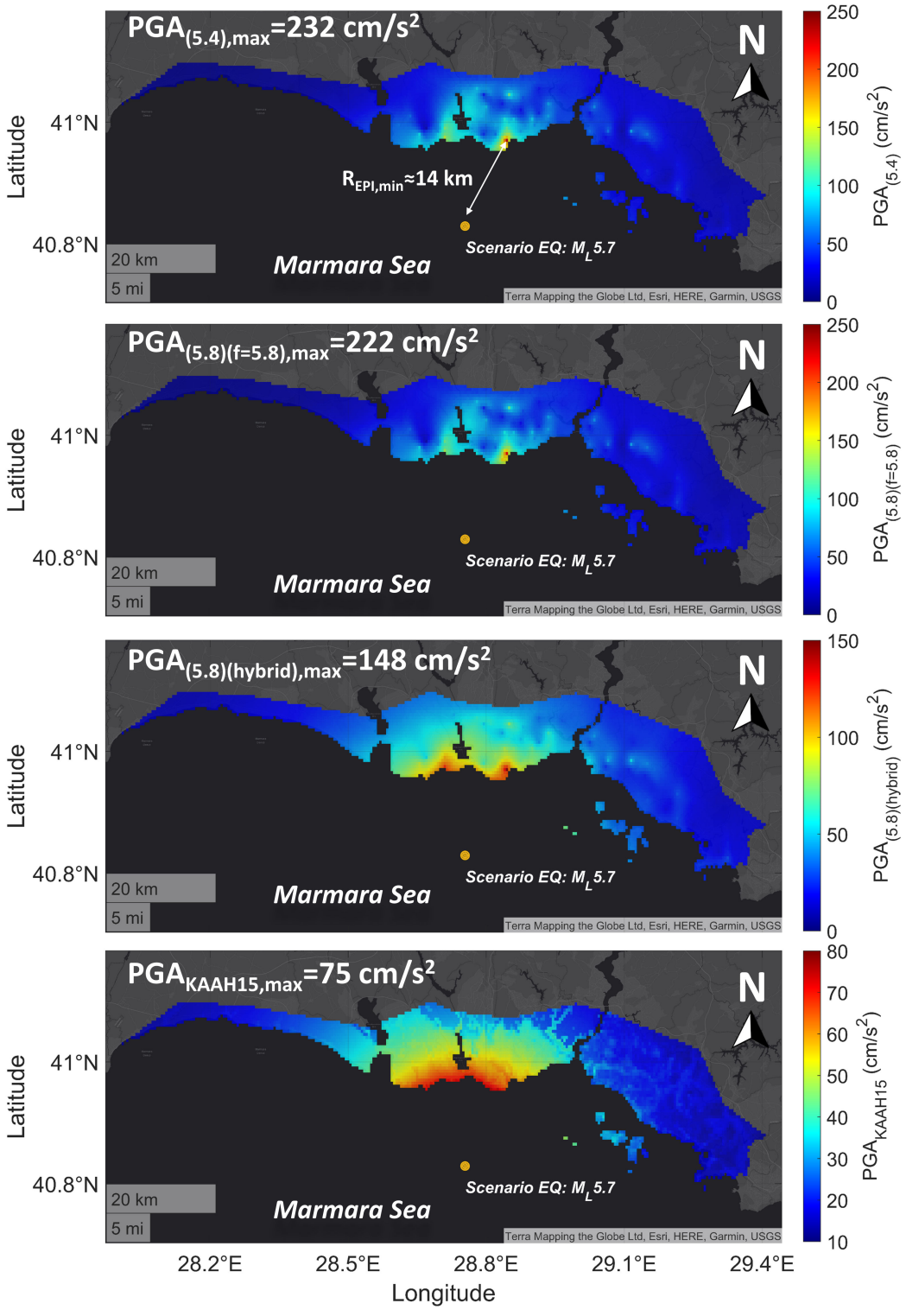


Figure 6.10. Spatial Distribution of Cell-based PGAs Obtained through the Station-specific Approach for an M_L5.7 Scenario Earthquake (Yellow circle refers to the epicentre of the earthquake).

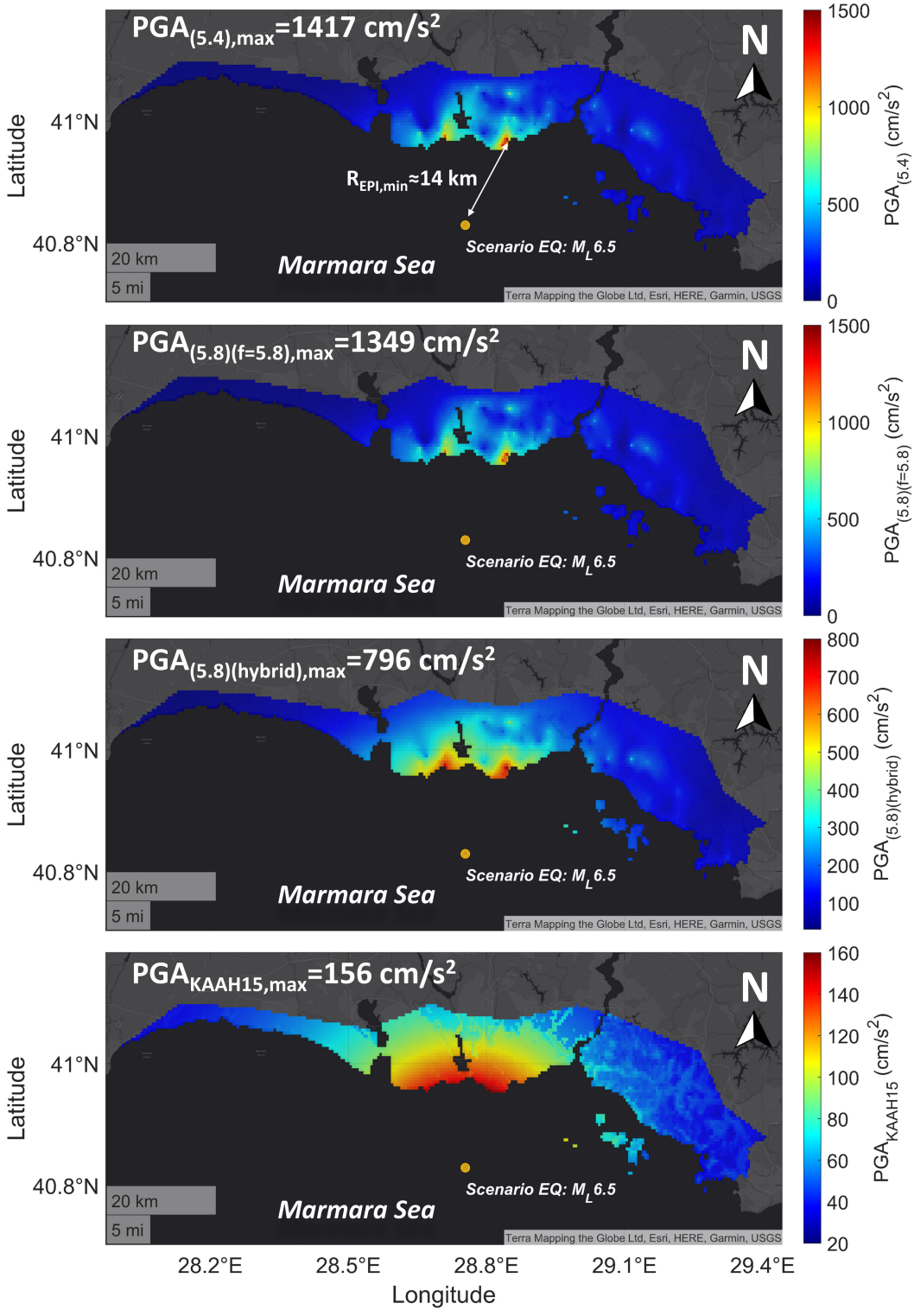


Figure 6.11. Spatial Distribution of Cell-based PGAs Obtained through the Station-specific Approach for an M_L6.5 Scenario Earthquake (Yellow circle refers to the epicentre of the earthquake).

Secondly, the construction of spatial distributions of PGAs is repeated by increasing the magnitude of the event to 6.5 at the same epicentre. In this case, the maximum PGA are obtained at the same location as before. The estimations through the first two functional forms result in a significant increase in the maximum PGA, reaching 1400 cm/s^2. However, the hybrid dataset approach yields more reasonable results, with the maximum PGA at a level of 800 cm/s^2. Nevertheless, when compared to the predictions of KAAH15, a five-fold difference between maximum PGAs is notable. This significant discrepancy may be an indicator of either persisting near-field issues in the hybrid dataset approach or could be attributed to M_L6.5 falling outside the magnitude range of this thesis' database. Regardless of these challenges and uncertainties, the regional differences may have contributed to an increase in PGAs in several specific areas. Hence, the upcoming sections will compare spatial distributions of PGAs for real earthquakes to comprehend the reason for the earlier contradiction.

6.3.2. Comparative Evaluation for the Largest Actual Event in the Database

The spatial PGA distribution maps are generated for the M_L5.7 Silivri earthquake through both station-specific methodology and KAAH15 (Figure 6.12). The estimations of the Functional Forms (5.4) and (5.8) (f=5.8) provide the largest PGA ($\approx$ 53 cm/s^2) at approximately 53 km from the epicentre and the spatial distribution seems to be similar for both functional forms. However, Functional Form (5.8) regarding hybrid datasets results in the highest PGA ($\approx$ 47 cm/s^2) at the closest vicinity to the epicentre ($R_{EPI} \approx$ 21 km) similar to estimations of KAAH15 ($PGA_{KAAH15,max} \approx$ 54 cm/s^2 at $R_{EPI} \approx$ 21 km). This finding may be a supporting result that the challenges in near-field estimations through the station-specific methodology might be mitigated, at least partially, by adopting the hybrid dataset approach. However, a large PGA ($\approx$ 40 cm/s^2) at 53 km from the epicentre is still estimated by the hybrid dataset approach in contrast to the estimation of KAAH15 ($\approx$ 17 cm/s^2). This region coincides with the area showing significant disparities in estimations of hypothetical earthquakes. Therefore, the notable discrepancies between estimations of the station-specific methodology and KAAH15 in this specific area may be attributed to regional factors.

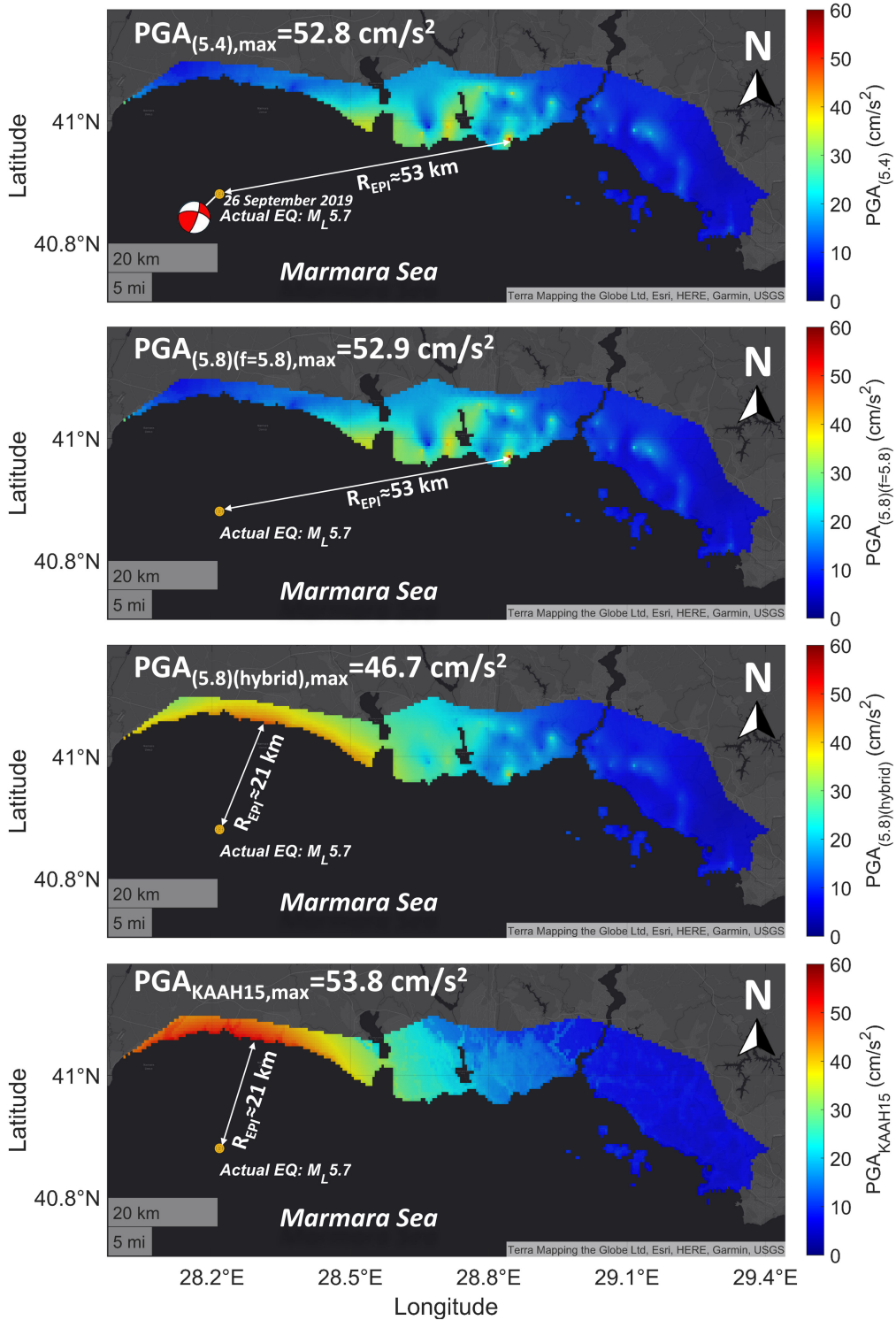


Figure 6.12. Spatial Distribution of Cell-based PGAs Obtained through the Station-specific Approach for the September 26, 2019, M_L5.7 Silivri Earthquake (Yellow circle refers to the epicentre of the earthquake).

Figure 6.13 allows for identifying the differences between the station-specific methodology estimations and KAAH15 by displaying the geographic distribution of residuals, which represent the differences between the logarithms of PGA estimations. Significant variations are evident in the vicinity of Küçükçekmece Lake, the shores of Bakırköy, the western shorelines of Haliç on the European side of Istanbul, and the surrounding areas of Kartal and Dudullu on the Asian side. Even though these local deviations from PGA projections of KAAH15 seem to be less prominent in the estimations of the Functional Form (5.8) employing the hybrid dataset approach, they might be important indicators of the influence of regional variations on PGA.

Comparative evaluations are also conducted between cell-based estimations and the PGAs obtained from both IERREWS (Figure 6.14) and AFAD (Figure 6.15) stations. The optimal estimations for two near-field stations are provided by the Functional Form (5.8) with the hybrid dataset approach. However, at the majority of the other stations, the station-specific methodology's estimations exhibit relative superiority over those of KAAH15. Total residuals appear to be higher on the European side and the western part of the Asian side of Istanbul, predominantly characterized by positive residuals, indicating underestimation. Additionally, these areas seem to be comparatively better estimated by Functional Forms (5.4) and (5.8) with $f = 5.8$ when compared to the other two estimations. This outcome may be linked to the near-field modification of Functional Form (5.8) through hybrid datasets, potentially resulting in a reduced capacity in the estimations for medium and far-field regions. All considered relationships demonstrate relatively acceptable predictive performance for the south-eastern part of Istanbul's Asian side. Given that the data from IERREWS stations has participated in the regression analysis for deriving station-specific coefficients, an additional comparison is carried out for the PGAs recorded by AFAD stations (Figure 6.15). The station-specific estimations, particularly with the hybrid dataset approach, appear to outperform those of KAAH15. The comparatively higher residuals of the station-specific methodology in the close proximity of the M_L5.7 Silivri earthquake's epicentre may be linked to the considerable distances between IERREWS stations, which are incorporated into the regression analyses, in this specific vicinity.

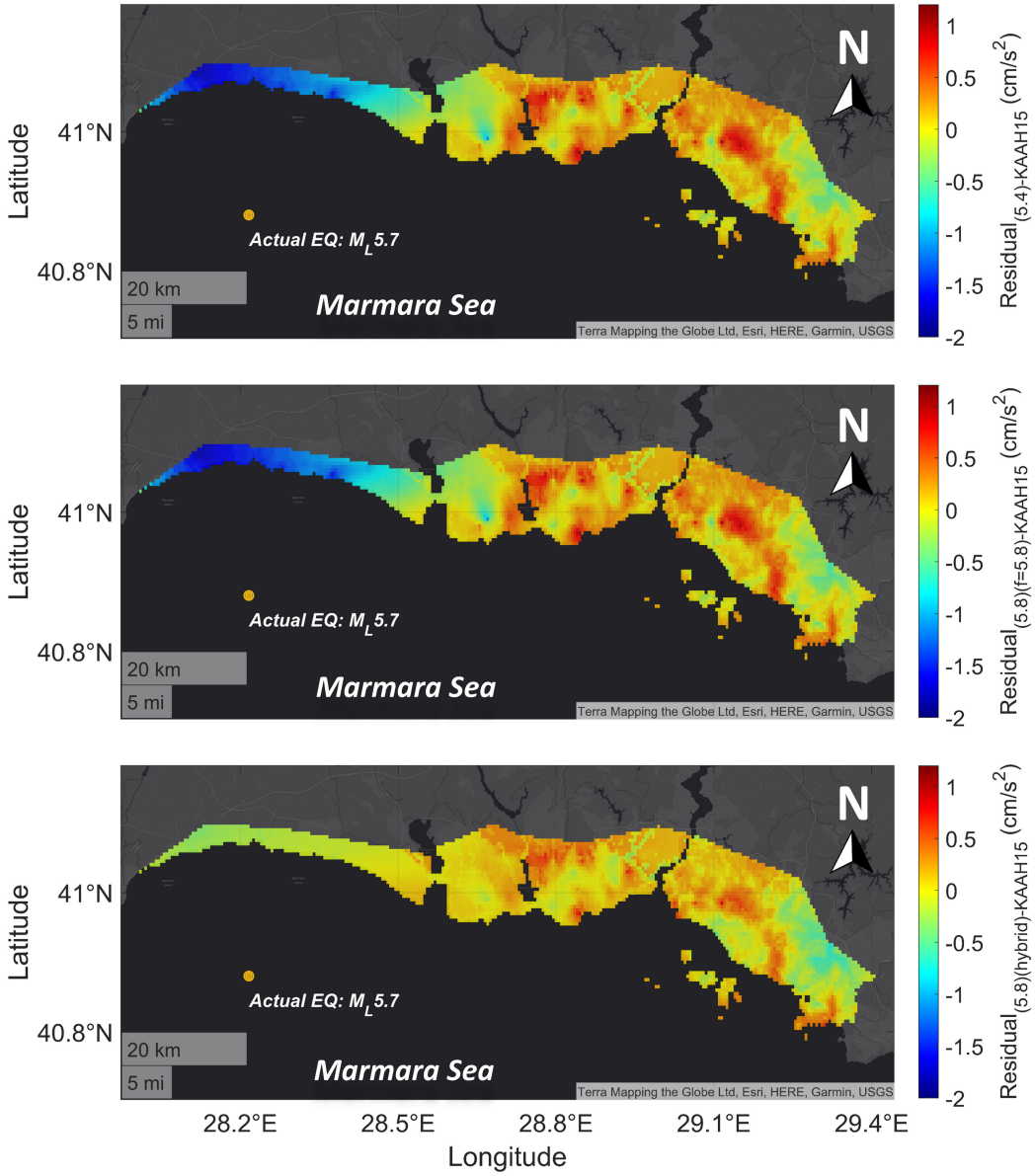


Figure 6.13. Comparison between PGA Estimations of the Station-specific Methodology and KAAH15 for the 26 September 2019, M_L5.7 Silivri earthquake (Yellow circle refers to the epicentre of the earthquake).

R

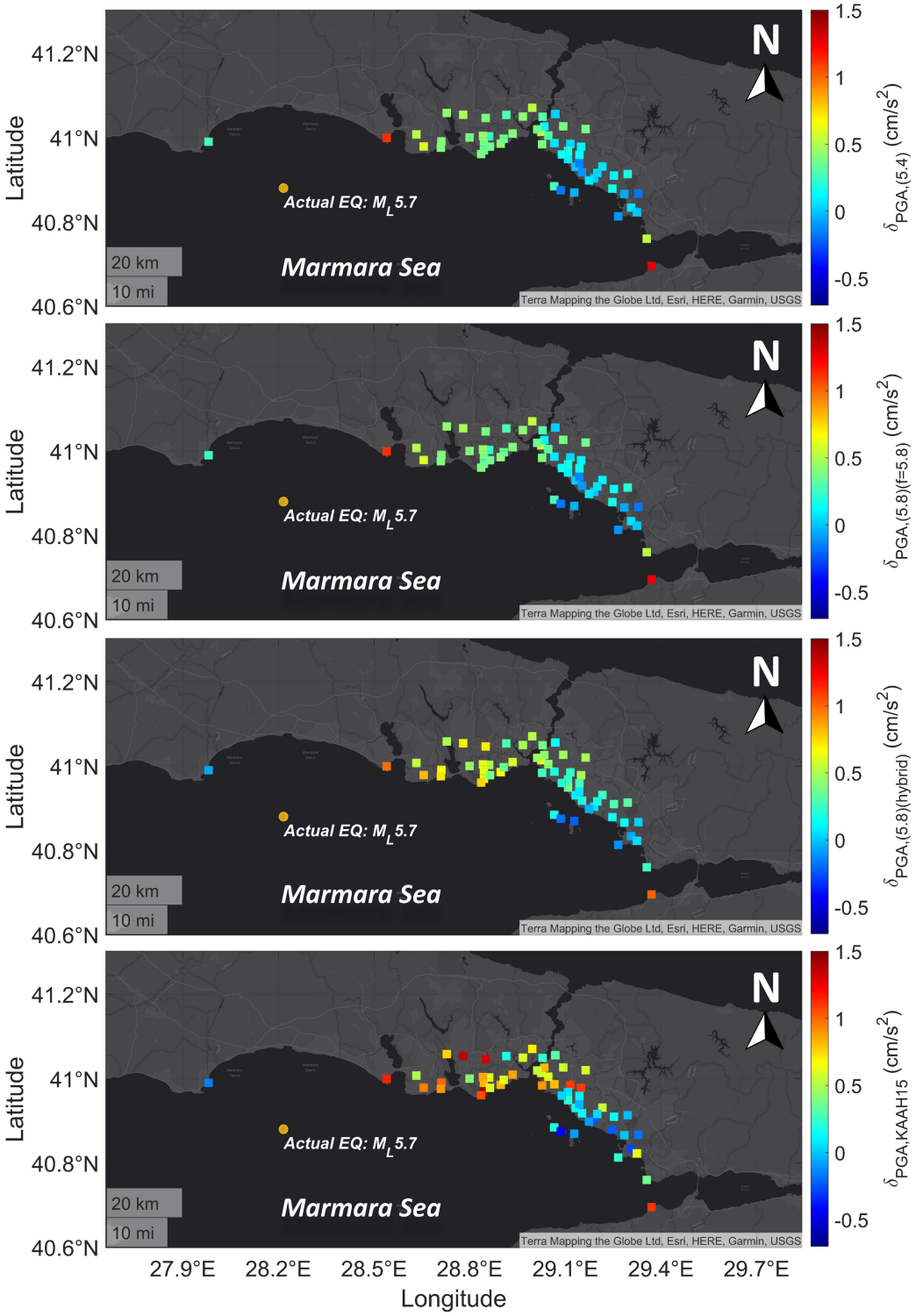


Figure 6.14. Comparison between PGAs Recorded by IERREWS Stations and Estimations of Station-specific Methodology and KAAH15 for the 26 September 2019, M_L5.7 Silivri Earthquake (Yellow circle refers to the epicentre of the earthquake).

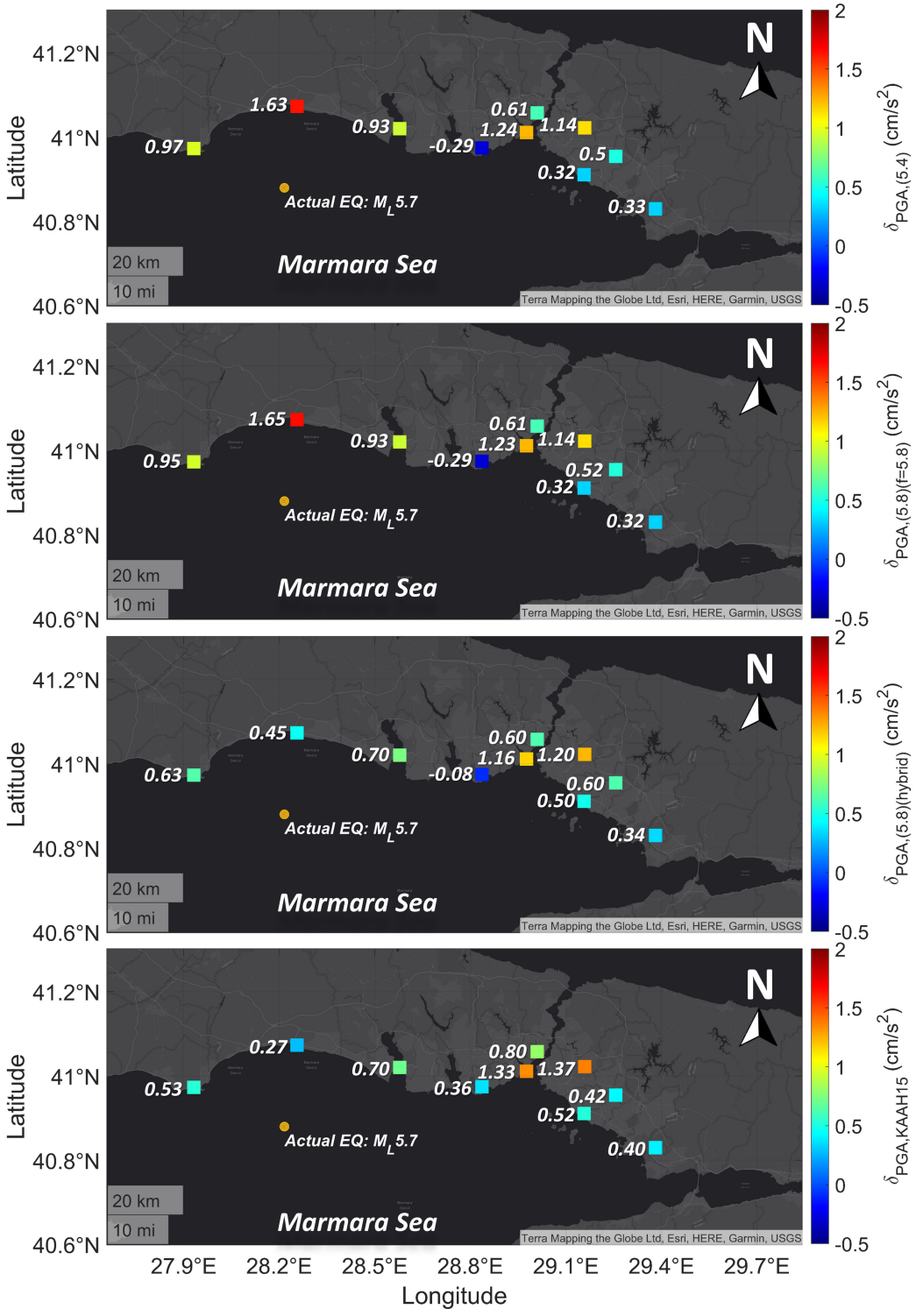


Figure 6.15. Comparison between PGAs Recorded by AFAD Stations and Estimations of Station-specific Methodology and KAAH15 for the 26 September 2019, M_L5.7 Silivri Earthquake (Yellow circle refers to the epicentre of the earthquake).

6.3.3. Comparative Evaluation for an Actual Event without in the Database

The ultimate comparative analysis concentrates on the M_L6.0 Düzce earthquake that took place on November 23, 2022 despite having a slightly larger magnitude than the highest magnitude level in the database. Since this earthquake has not been incorporated into the regression analysis, the results may provide a more reliable assessment of the estimation capabilities of the station-specific methodology. The map illustrating a geographic distribution of PGA estimations from both station-specific methodology and KAAH15 is presented in Figure 6.16 for Istanbul. The southeastern end of Istanbul yields the highest PGA ($\approx$ 6.7 cm/s^2) estimation of KAAH15. In contrast, the results of this study indicate that the central south of İstanbul's European side has the highest PGA similar to previous evaluations. The PGA estimations of Functional Forms (5.4) and (5.8) with f=5.8 surpass the level of 20 cm/s^2 whereas functional form (5.8) with a hybrid dataset approach yields a PGA of 17.1 cm/s^2. In the same location, the estimation of KAAH15 stands at 4.6 cm/s^2. The station HVHR of the IERREWS network is situated in this area that experienced a significant discrepancy in estimations. Specifically, the PGA value recorded at the HVHR station during the M_L6.0 Düzce earthquake seems to be 19.1 cm/s^2, which is in agreement with the estimations of the station-specific methodology proposed in this thesis. This finding enforces the idea that regional factors have a significant impact on GMPs and conventional GMPEs may fail to accurately capture these effects. The residual distribution map for M_L6.0 Düzce earthquake in Figure 6.17 explicitly highlights the localized discrepancies between the estimations of the station-specific methodology and KAAH15 as discussed earlier. The consistency evaluation of estimations with actual PGAs of other IERREWS stations and also AFAD stations are performed by employing total residuals in Figure 6.18 and Figure 6.19, respectively. The total residuals from the station-specific methodology indicate lower values, implying a better estimation capacity compared to KAAH15 for both IERREWS and AFAD stations situated around these discrepancies, particularly on the European side of Istanbul. In the rest of the stations, especially in the Asian section of Istanbul, the total residuals of the KAAH15 and the station-specific methodology exhibit a mostly equivalent estimation capability for PGA prediction for IERREWS stations. In contrast, the estimations of KAAH15

stand out as more effective for the limited number of AFAD stations on the Asian side.

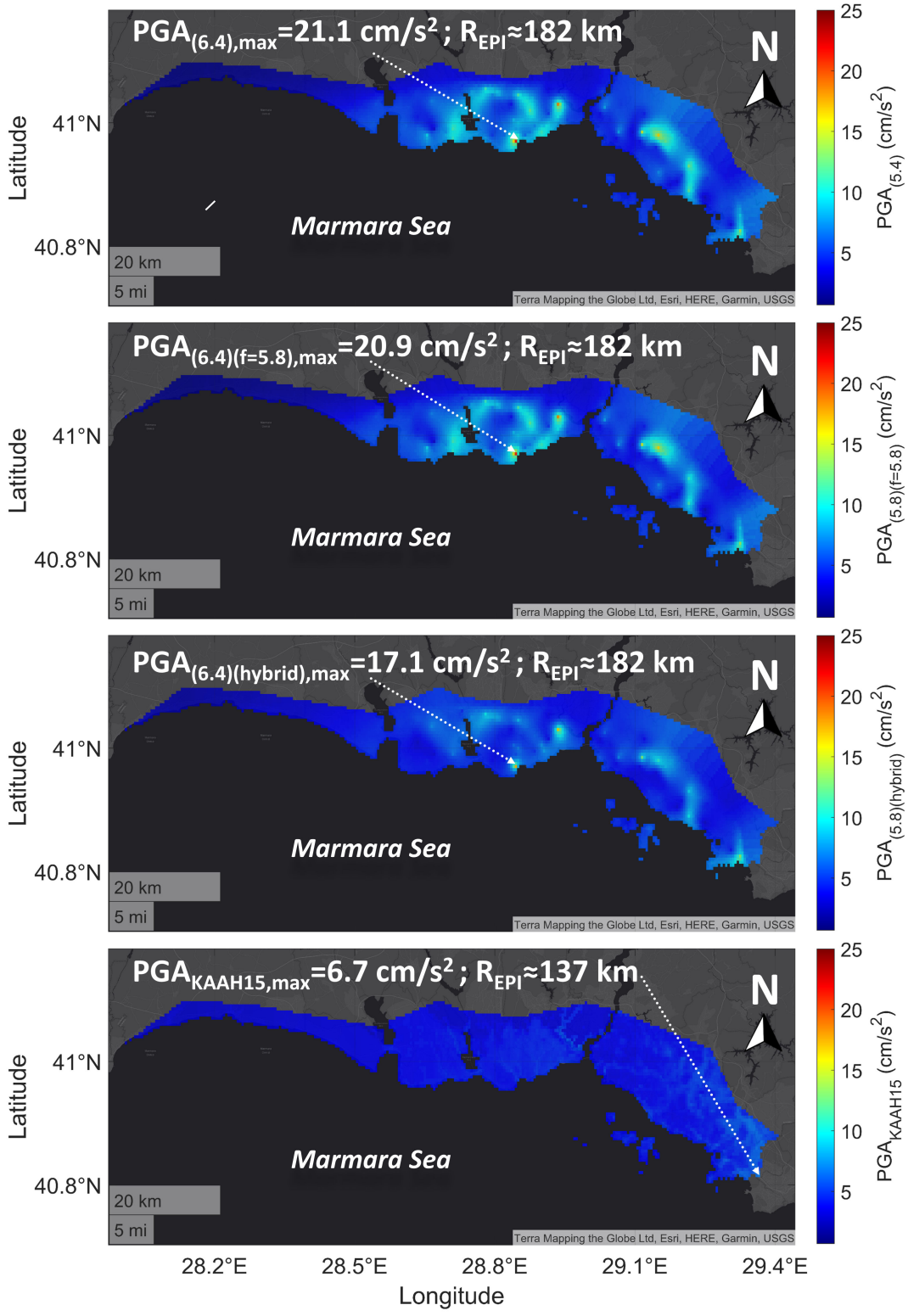


Figure 6.16. Spatial Distribution of Cell-based PGAs Obtained through the Station-specific Approach for the November 26, 2022, M_L6.0 Düzce Earthquake.

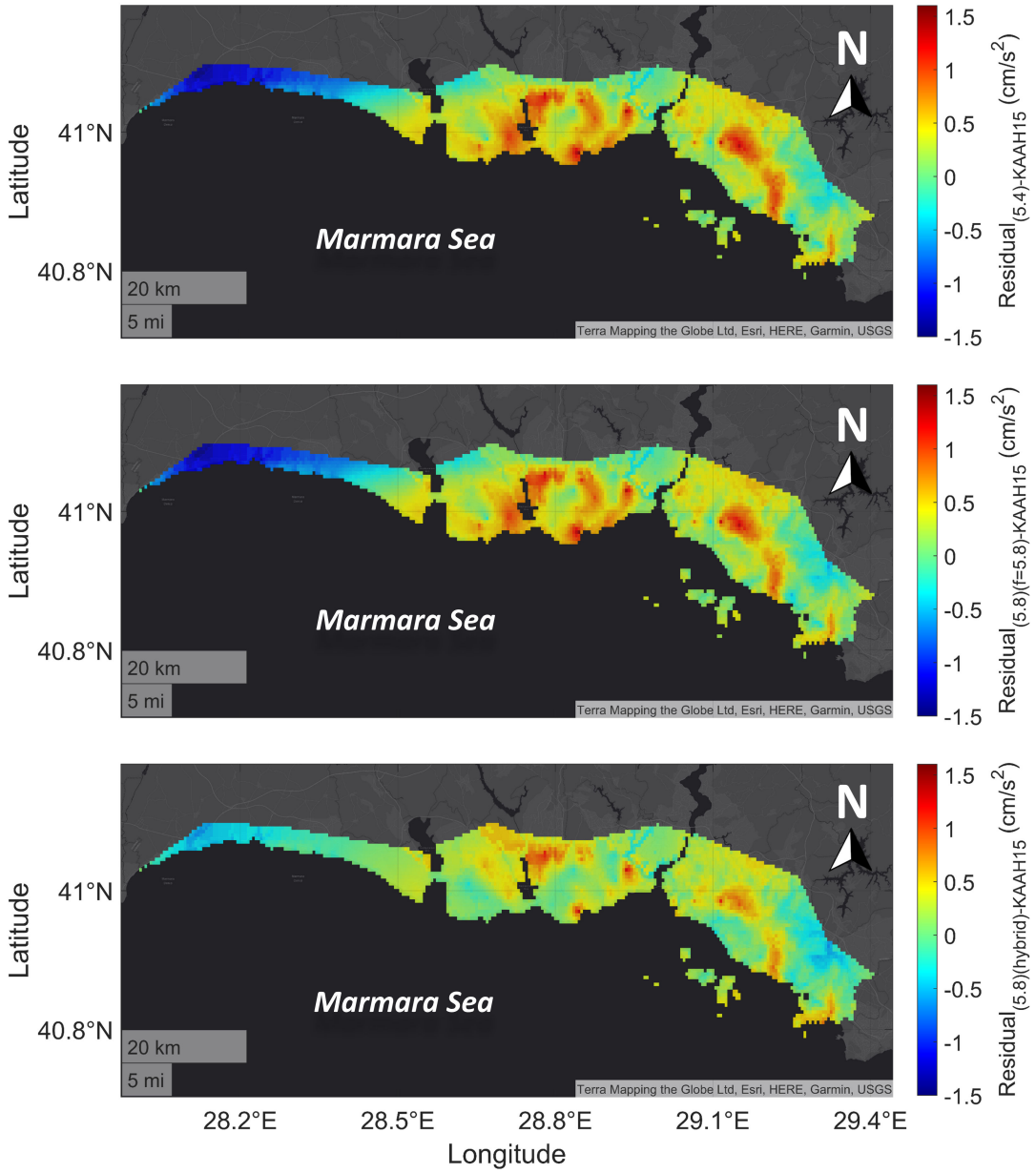


Figure 6.17. Comparison between PGA Estimations of the Station-specific Methodology and KAAH15 for the November 26, 2022, M_L6.0 Düzce Earthquake.

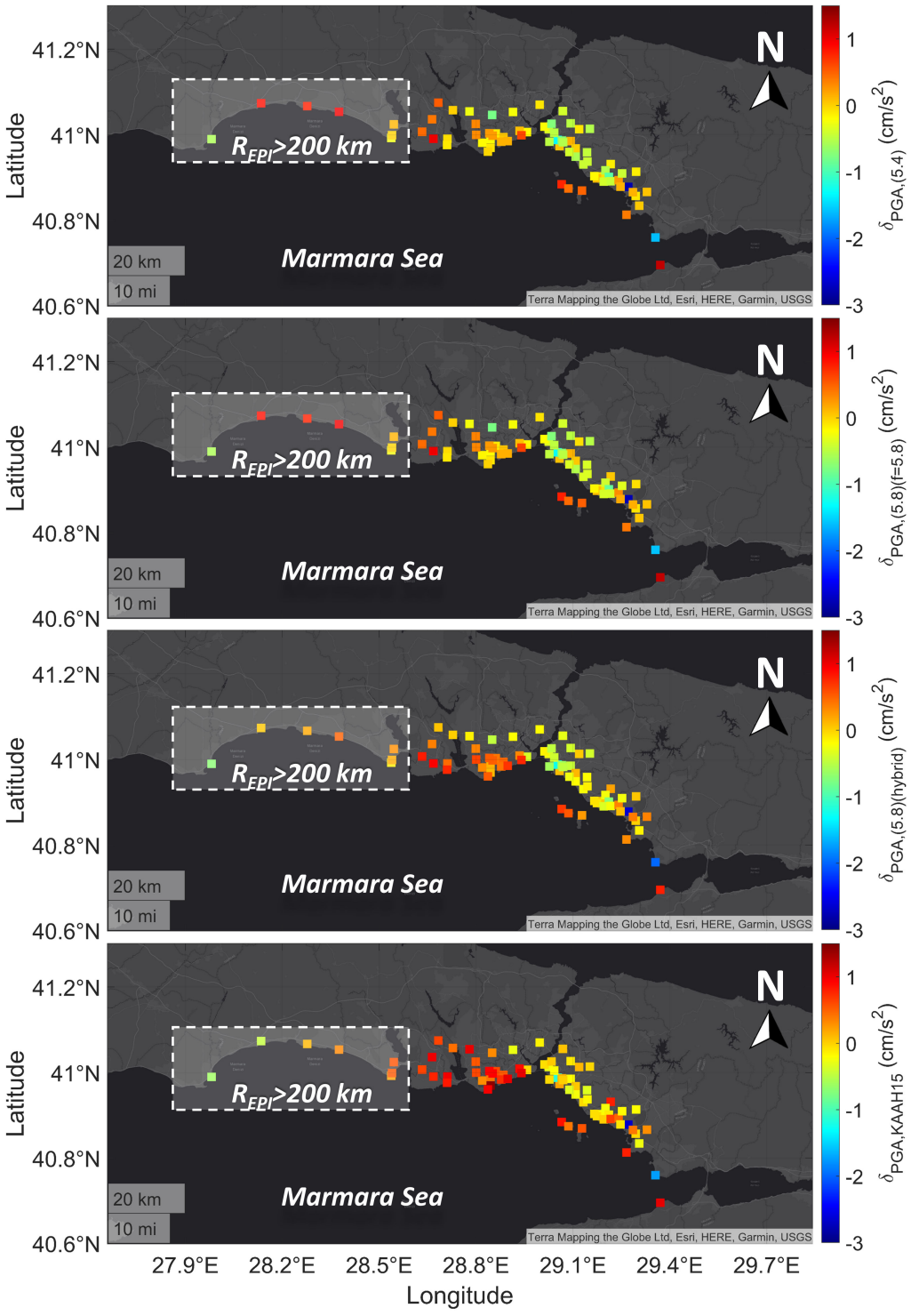


Figure 6.18. Comparison between PGAs Recorded by IERREWS Stations and Estimations of Station-specific Methodology and KAAH15 for the November 26, 2022, M_L6.0 Düzce Earthquake.

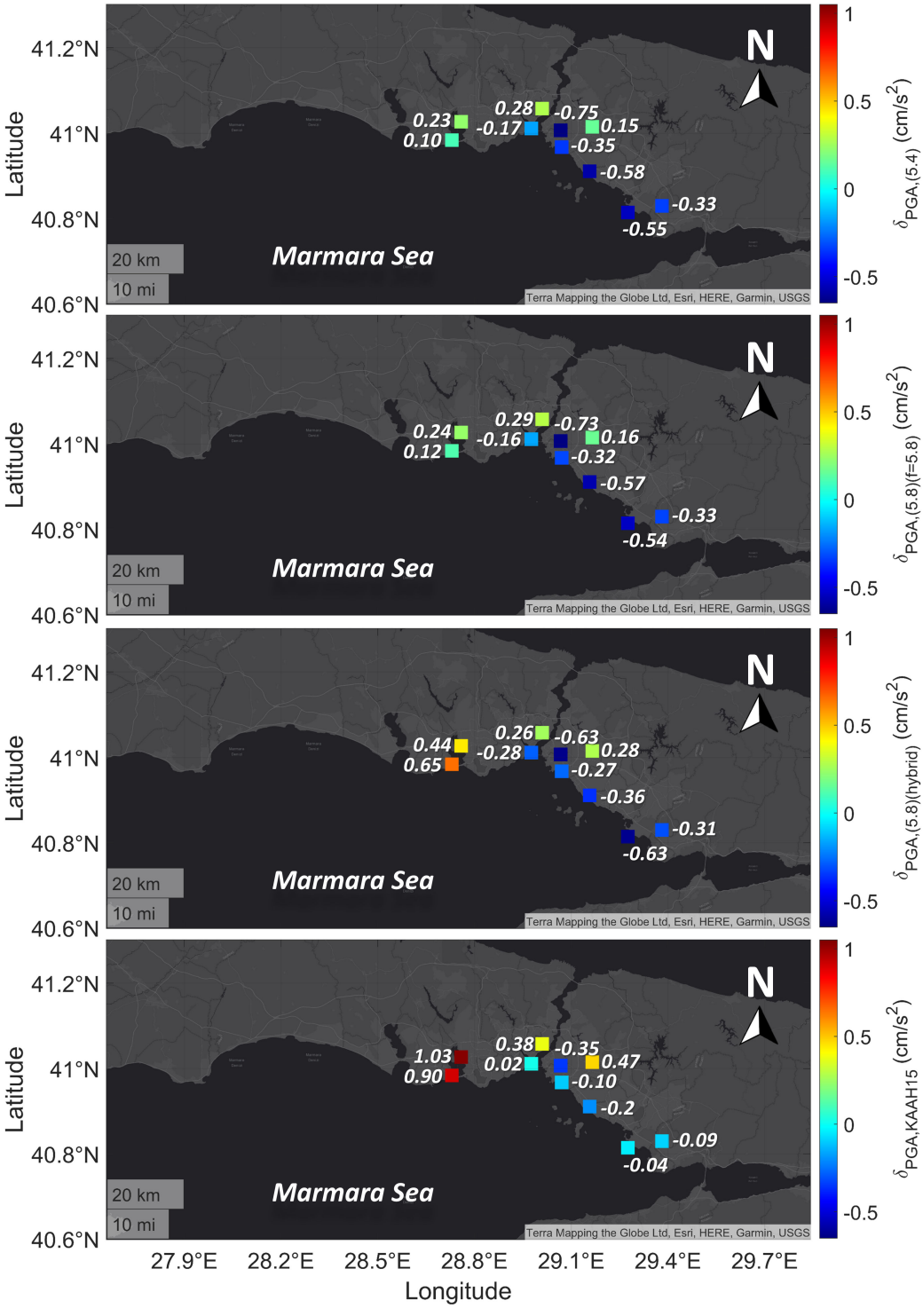


Figure 6.19. Comparison between PGAs Recorded by AFAD Stations and Estimations of Station-specific Methodology and KAAH15 for the November 26, 2022, M_L6.0 Düzce Earthquake.

Lastly, specific emphasis is directed to the vicinity of Küçükçekmece Lake as both IERREWS and AFAD networks have stations around the lake and significant disagreements among estimations are recognised in this area. Figure 6.20 and Figure 6.21 show the PGA values estimated through station-specific methodology, KAAH15 and ASB14 as well as those observed at the stations of IERREWS and AFAD, respectively. The actual data from stations in both networks indicates that PGAs are around 10 cm/s^2 in the northeast-southwest direction while showing slightly lower levels in the opposite direction. KAAH15 and ASB14 both estimate the PGAs at these stations to be approximately half of the actual values whereas the estimations acquired via the station-specific methodology seem to be quite comparable to the actual PGAs. As aligned with the earlier discussions, despite its success in near-field zones, the hybrid dataset approach does not perform as effectively as the other two functional forms in estimating actual values for these local areas.

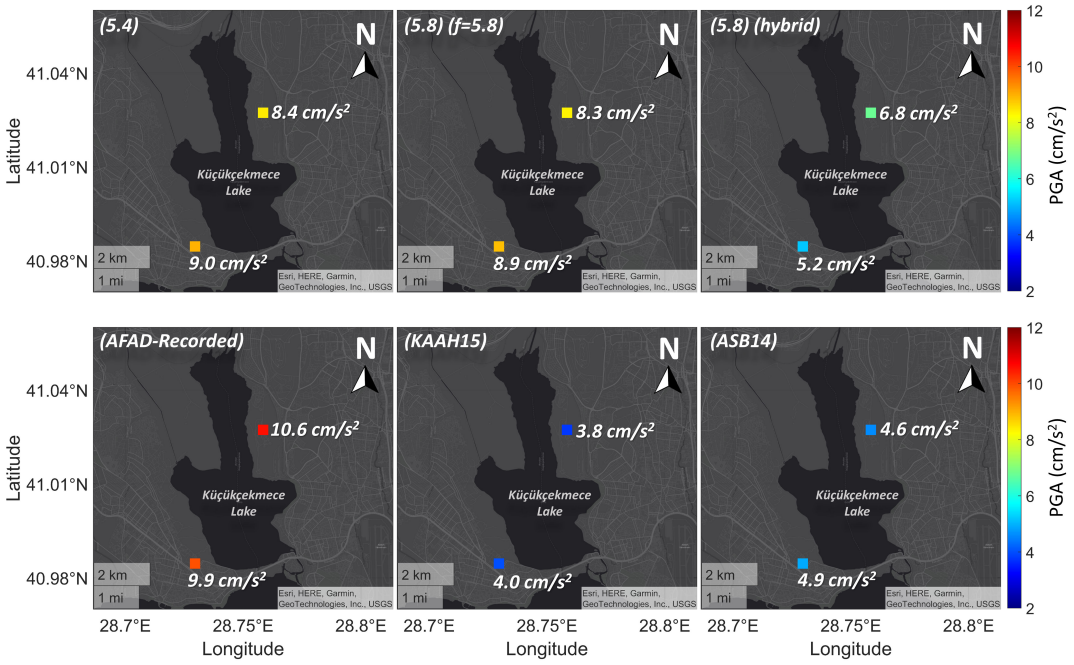


Figure 6.20. Comparison between PGAs Recorded by AFAD Stations around Küçükçekmece Lake and their Estimations of Station-specific Methodology, KAAH15 and ASB14 for the November 26, 2022, M_L6.0 Düzce Earthquake.

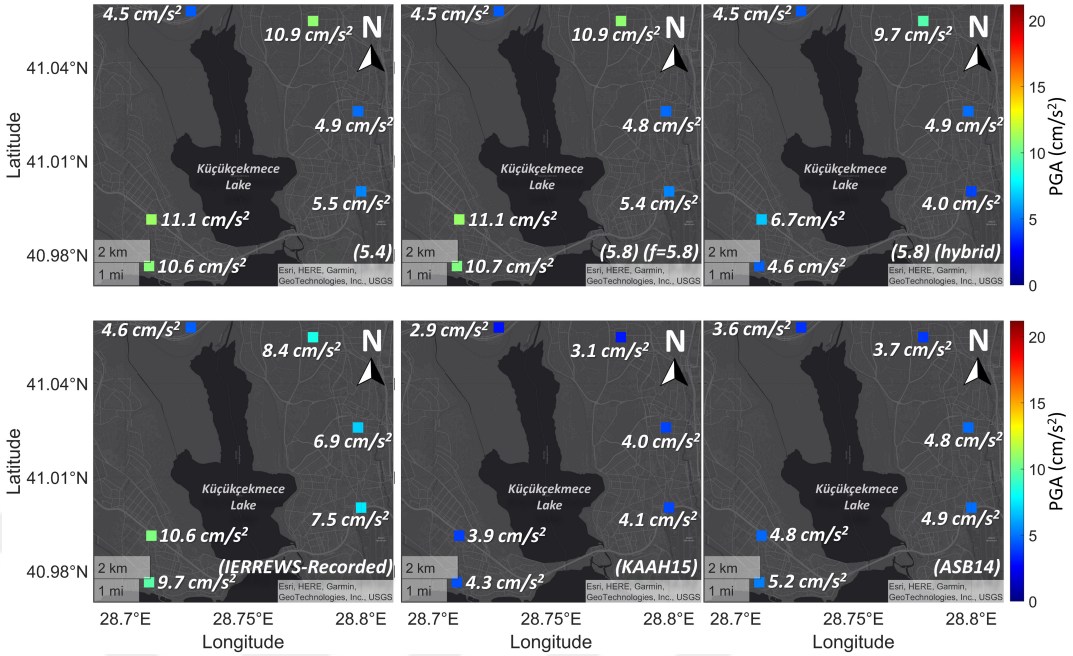


Figure 6.21. Comparison between PGAs Recorded by IERREWS Stations around Küçükçekmece Lake and Estimations of Station-specific Methodology, KAAH15 and ASB14 for the November 26, 2022, M_L6.0 Düzce Earthquake.

7. CONCLUSION

This thesis initially performs an assessment of consistency for the most suitable GMPEs for İstanbul to ascertain whether their estimation capabilities are sufficient. In pursuit of this objective, 31,054 raw horizontal-component recordings of the IERREWS dense network are collated using a three-step database criteria. Given the significance of low-frequency noises in influencing GMPs, high-pass filter frequencies are meticulously handpicked on a component basis. This is accomplished by conducting a visual examination concurrently on the time histories, Fourier amplitude spectra and slope of the displacement utilising a GUI developed within the framework of this thesis. The ultimate database comprises 6,534 individual horizontal-component recordings ($R_{EPI,max}$ = 200 km) from 78 small-to-moderate ($4.0 \leq M_L \leq 5.7$) and shallow (1.8 km $\leq$ h $\leq$ 20.2 km) seismic events near the Marmara region between 2012 and 2022.

Consistency evaluations are made between the frequently utilized GMPs, computed from the database's accelerograms, and the estimations of GMPEs that best align with our database. To facilitate interpretation, empirical relations are formulated for both the entire database and subsets based on magnitude via a two-stage nonlinear regression analysis. The comparisons of median distance scalings for GMPs, e.g. PGA, PGV, SAs (T=0.4; 0.6; 1.0; 2.0), AI and CAV, indicate that the GMPEs selected tend to overestimate both the actual GMPs and the estimations from the empirical models of this thesis. As magnitude increases, estimation lines of both GMPEs and the relation of this study converge, with this study's estimations showing a tendency to slightly exceed GMPEs. This finding may be an indication that there is a possibility of underestimation of GMPs by GMPEs for larger magnitudes than the M_L5.7. KAAH15's estimates are relatively more representative of actual GMPs, especially for near-field distances, when compared to other GMPEs. Despite the relative effectiveness of KAAH15, potentially linked to its supplying Türkiye-specific regression coefficients, its tendency to overestimate actual GMPs is particularly apparent. Additionally, total and between-event residuals endorse the overestimation tendencies of the GMPEs, whereas within-event residuals against R_{EPI}, V_{S30} and azimuth an-

gle imply equally both overestimation and underestimation with an approximate zero mean. Even with the superior consistency demonstrated by the empirical model of this thesis derived using the entire database with actual GMPs, it does not accurately predict all individual GMPs. These discrepancies in estimations versus actual GMPs may be connected to the influence of local aspects on GMPs. This argument prompts the embracing of a methodology that seeks to minimize the uncertainties mainly tied to regional implications.

Afterwards, this thesis introduces a methodology that emphasizes station-specific regression analyses, aiming to localise and improve the estimations of GMPs, particularly in Istanbul. The dense urban network of Istanbul provides an abundance of small-to-moderate magnitude events, establishing a sufficient database for conducting station-specific analyses. The methodology asserts that adopting a single-station regressions serves to reduce uncertainties associated with soil conditions and, to some extent, propagation paths and their inter-dependent effects on GMPs. Despite the absence of concrete evidence regarding azimuthal effects on GMPs, any potential influence stemming from azimuthal variations is indirectly incorporated into regression analyses. This is accomplished by converting ground motions from the EW and NS directions to the principal orientations of the ground motion time series.

After experimenting with various functional forms, which included different combinations of source and path parameters, the most straightforward functional form is chosen since augmenting the complexity of the functional form does not contribute to the improvement of the estimation capacity. As the selected form's linearity along the entire distance range compromises the reliability of near-field estimations, a regression coefficient (f) for distance modification is incorporated into the functional form. The first approach entails setting the coefficient f to a constant value (f = 5.8), determined through regression analysis of the entire database. In the second approach, the coefficient f is established through station-specific regressions for hybrid station-based subsets, combining actual PGAs and near-field estimations obtained from the regression of the entire database. The overall assessment, considering total, between-event, and within-event residuals, as well as a comparison with KAAH15 and ASB14,

indicates that the proposed station-specific methodology enhances the capability to estimate actual PGAs.

The last segment of the thesis is focused on generating spatial distribution maps for PGA in the southern part of Istanbul. The missing information in areas without deployed stations is estimated using Matlab's 2-D Delaunay triangulation algorithm. Subsequently, the southern part of Istanbul is partitioned into 4.714 cells, with each cell assigned the closest interpolated coefficient. The comparison of PGA distribution maps for two hypothetical events, M_L5.7 Silivri (September 26, 2019) and M_L6.0 Düzce (November 26, 2022) earthquakes reveals that functional forms considering unmodified distance terms and fixed coefficient f exhibit significantly larger PGAs than the estimations of functional forms utilizing the hybrid dataset approach. The integration of hybrid subsets seems to offer a partial resolution to near-field estimations, while the constant f approach generally results in outcomes almost resembling those of the linear base functional form. The residuals between the estimations of three functional forms of the station-specific methodology and KAAH15 display localized differences on both the European and Asian sides of Istanbul. These local differences are less distinctive in the estimations of the functional form involving hybrid datasets. Comparison of estimations with actual PGAs from recordings of IERREWS and AFAD's stations reveals that PGAs of stations around Küçükçekmece Lake and the shores of Bakırköy are better estimated by the station-specific methodology than by KAAH15. Additionally, the largest recorded PGA of the Düzce earthquake within the specified area matches the estimations of the station-specific methodology. These local discrepancies in the estimations might be originated from the regional impacts on GMPs.

While the station-specific methodology excels in capturing local large PGAs, there are lingering issues to be resolved in future research. First, this methodology hinges on the crucial requirement of having abundant data at each station. Secondly, despite having a sufficient number of recordings for conducting regression analyses within the database, a prominent challenge is the absence of large-magnitude events and near-field recordings. Estimating GMPs for strong events may necessitate the extrapolation to a magnitude range beyond that considered in this thesis. Optimizing the hybrid

dataset approach by using simulated ground motions considering its physical nature may elevate the estimation capability of the methodology. The IERREWS network is deficient in recording sites in the northern and western parts of Istanbul, particularly beyond the West of Büyükçekmece. Increasing the number of stations is strongly recommended for a more effective implementation of this methodology. Moreover, for a comprehensive analysis, it is essential to implement this methodology for other GMPs such as PGV, SA, AI, and CAV to fortify the conclusions drawn for PGA.

REFERENCES

1. Bozkurt, E., "Neotectonics of Turkey–A synthesis", *Geodinamica Acta*, Vol. 14, No. 1-3, pp. 3–30, 2001.

2. Rebuplic of Türkiye, M. o. I., "Türkiye'nin Nüfus Haritası", 2021, `https://www.icisleri.gov.tr/turkiyenin-nufus-haritasi-10072021`, accessed on November 03, 2023.

3. Emre, Ö., T. Duman, S. Özalp, H. Elmaci, Ş. Olgun and F. Şaroğlu, *Açıklamalı Türkiye Diri Fay Haritası, Ölçek 1: 1.250.000*, Maden Tetkik ve Arama Genel Müdürlüğü, Ankara, Türkiye, 2012.

4. Bohnhoff, M., F. Bulut, G. Dresen, P. E. Malin, T. Eken and M. Aktar, "An Earthquake Gap South of Istanbul", *Nature Communications*, Vol. 4, No. 1999, pp. 1–6, 2013.

5. KOERI-RETMC, "Boğaziçi University, Kandilli Observatory and Earthquake Research Institute, Regional Earthquake Tsunami Monitoring Center, Earthquake Catalog Search System", 2023, `http://www.koeri.boun.edu.tr/sismo/2/earthquake-catalog/`, accessed on April 22, 2023.

6. Le Pichon, X., N. Chamot-Rooke, C. Rangin and A. M. C. Sengör, "The North Anatolian Fault in the Sea of Marmara", *Journal of Geophysical Research: Solid Earth*, Vol. 108, No. B4, pp. 1–20, 2003.

7. Parsons, T., "Recalculated Probability of M $\geq$ 7 Earthquakes Beneath the Sea of Marmara, Turkey", *Journal of Geophysical Research: Solid Earth*, Vol. 109, No. B5, pp. 1–21, 2004.

8. Şengör, A., O. Tüysüz, C. Imren, M. Sakınç, H. Eyidoğan, N. Görür, X. Le Pichon

and C. Rangin, "The North Anatolian Fault: A New Look", *Annual Review of Earth and Planetary Sciences*, Vol. 33, pp. 37–112, 2005.

9. Hubert-Ferrari, A., A. Barka, E. Jacques, S. S. Nalbant, B. Meyer, R. Armijo, P. Tapponnier and G. C. King, "Seismic Hazard in the Marmara Sea Region Following the 17 August 1999 Izmit Earthquake", *Nature*, Vol. 404, No. 6775, pp. 269–273, 2000.

10. Atakan, K., A. Ojeda, M. Meghraoui, A. A. Barka, M. Erdik and A. Bodare, "Seismic Hazard in İstanbul Following the 17 August 1999 Izmit and 12 November 1999 Düzce Earthquakes", *Bulletin of the Seismological Society of America*, Vol. 92, No. 1, pp. 466–482, 2002.

11. Erdik, M., M. Demircioglu, K. Sesetyan, E. Durukal and B. Siyahi, "Earthquake Hazard in Marmara Region, Turkey", *Soil Dynamics and Earthquake Engineering*, Vol. 24, No. 8, pp. 605–631, 2004.

12. Kalkan, E., P. Gülkan, N. Y. Öztürk and M. Çelebi, "Seismic Hazard in the Istanbul Metropolitan Area: a Preliminary Re-Evaluation", *Journal of Earthquake Engineering*, Vol. 12, No. S2, pp. 151–164, 2008.

13. Mert, A., Y. M. Fahjan, L. J. Hutchings and A. Pınar, "Physically based Probabilistic Seismic Hazard Analysis Using Broadband Ground Motion Simulation: A Case Study for the Prince Islands Fault, Marmara Sea", *Earth, Planets and Space*, Vol. 68, No. 1, pp. 1–26, 2016.

14. Şeşetyan, K., M. B. Demircioğlu Tümsa and A. Akinci, "Evaluation of the Seismic Hazard in the Marmara Region (Turkey) based on Updated Databases", *Geosciences*, Vol. 9, No. 12, p. 489, 2019.

15. Erdik, M., N. Aydinoglu, Y. Fahjan, K. Sesetyan, M. Demircioglu, B. Siyahi, E. Durukal, C. Ozbey, Y. Biro, H. Akman *et al.*, "Earthquake Risk Assessment for Istanbul Metropolitan Area", *Earthquake Engineering and Engineering Vibration*,

Vol. 2, No. 1, pp. 1–23, 2003.

16. Durukal, E., M. Erdik and E. Uçkan, "Earthquake Risk to Industry in Istanbul and Its Management", *Natural Hazards*, Vol. 44, No. 2, pp. 199–212, 2008.

17. Ansal, A., A. Akinci, G. Cultrera, M. Erdik, V. Pessina, G. Tönük and G. Ameri, "Loss Estimation in Istanbul based on Deterministic Earthquake Scenarios of the Marmara Sea Region (Turkey)", *Soil Dynamics and Earthquake Engineering*, Vol. 29, No. 4, pp. 699–709, 2009.

18. Zülfikar, A. C., N. Ö. Z. Fercan, S. Tunç and M. Erdik, "Real-time Earthquake Shake, Damage, and Loss Mapping for Istanbul Metropolitan Area", *Earth, Planets and Space*, Vol. 69, No. 9, pp. 1–15, 2017.

19. Alcik, H., O. Ozel, N. Apaydin and M. Erdik, "A Study on Warning Algorithms for Istanbul Earthquake Early Warning System", *Geophysical Research Letters*, Vol. 36, No. 5, 2009.

20. Sesetyan, K., C. Zulfikar, M. Demircioglu, U. Hancilar, Y. Kamer and M. Erdik, "Istanbul Earthquake Rapid Response System: Methods and Practices", *Soil Dynamics and Earthquake Engineering*, Vol. 31, No. 2, pp. 170–180, 2011.

21. Alçık, H. and A. Pınar, "İstanbul'da Kurulu Deprem Erken Uyarı ve Yapısal Alarm Sistemleri", *İstanbul Yerbilimleri Dergisi*, Vol. 26, No. 2, pp. 65–72, 2013.

22. Pınar, A., M. O. Erdik, H. Alçık, C. Zulfikar, A. Mert and A. Korkmaz, "Developments in the Earthquake Early Warning System for Istanbul, NW Turkey", *Japan Geoscience Union Meeting*, Makuhari, Chiba, Japan, 2013.

23. Böse, M., *Earthquake Early Warning for Istanbul Using Artificial Neural Networks*, Ph.D. Thesis, Karlsruhe Institute of Technology, 2006.

24. Elgin, K. G., "Istanbul Seismic Risk Mitigation and Emergency Preparedness Project (ISMEP)", *ATC and SEI Conference on Improving the Seismic Perfor-*

mance of Existing Buildings and Other Structures, pp. 1129–1140, San Francisco, California, United States, 2009.

25. Köhler, N., *Real-time Information from Seismic Networks*, Ph.D. Thesis, Karlsruher Institut für Technologie (KIT), 2010.

26. Erdik, M., K. Sesetyan, M. Demircioglu, U. Hancilar, C. Zulfikar, E. Cakti, Y. Kamer, C. Yenidogan, C. Tuzun, Z. Cagnan *et al.*, "Rapid Earthquake Hazard and Loss Assessment for Euro-Mediterranean Region", *Acta Geophysica*, Vol. 58, No. 5, pp. 855–892, 2010.

27. Erdik, M., K. Şeşetyan, M. Demircioğlu, C. Zülfikar, U. Hancılar, C. Tüzün and E. Harmandar, "Rapid Earthquake Loss Assessment after Damaging Earthquakes", *Perspectives on European Earthquake Engineering and Seismology: Volume 1*, Vol. 34, pp. 53–95, 2014.

28. Hancilar, U., C. Tuzun, C. Yenidogan and M. Erdik, "ELER Software–A New Tool for Urban Earthquake Loss Assessment", *Natural Hazards and Earth System Sciences*, Vol. 10, No. 12, pp. 2677–2696, 2010.

29. Çaktı, E., E. Şafak, U. Hancılar, K. Şeşetyan, G. Durusoy, Ş. Dede, T. Tetik, Ö. Uzunkol, E. Yavuz, B. E. Konukcu, S. Günay, H. Mehmetoğlu, K. Duran and T. Kahraman, *İstanbul Deprem Hızlı Müdahale ve Erken Uyarı Sistemi*, Technical report, Boğaziçi University Kandilli Observatory and Earthquake Research Institute Department of Earthquake Engineering, İstanbul, Türkiye, 2021.

30. Hancilar, U., K. Sesetyan and E. Cakti, "Comparative Earthquake Loss Estimations for High-Code Buildings in Istanbul", *Soil Dynamics and Earthquake Engineering*, Vol. 129, p. 105956, 2020.

31. Douglas, J. and H. Aochi, "A Survey of Techniques for Predicting Earthquake Ground Motions for Engineering Purposes", *Surveys in Geophysics*, Vol. 29, No. 3, pp. 187–220, 2008.

32. Campbell, K. W., "Strong-motion Attentuation Relations", *International Geophysics Series*, Vol. 81, No. B, pp. 1003–1012, 2003.

33. Douglas, J., "Earthquake Ground Motion Estimation Using Strong-Motion Records: A Review of Equations for the Estimation of Peak Ground Acceleration and Response Spectral Ordinates", *Earth-Science Reviews*, Vol. 61, No. 1-2, pp. 43–104, 2003.

34. Douglas, J. and B. Edwards, "Recent and Future Developments in Earthquake Ground Motion Estimation", *Earth-Science Reviews*, Vol. 160, pp. 203–219, 2016.

35. Douglas, J., *Ground Motion Prediction Equations 1964 – 2021*, Compendium, Department of Civil and Environmental Engineering, University of Strathclyde, Glasgow, United Kingdom, 2022.

36. Esteva, L. and E. Rosenblueth, "Espectros de Temblores a Distancias Moderadas y Grandes", *Boletin Sociedad Mexicana de Ingenieria Sesmica*, Vol. 2, No. 1, pp. 1–18, 1964.

37. Ambraseys, N. N. and J. Bommer, "The Attenuation of Ground Accelerations in Europe", *Earthquake Engineering and Structural Dynamics*, Vol. 20, No. 12, pp. 1179–1202, 1991.

38. Idriss, I. M., "An NGA Empirical Model for Estimating the Horizontal Spectral Values Generated by Shallow Crustal Earthquakes", *Earthquake Spectra*, Vol. 24, No. 1, pp. 217–242, 2008.

39. Joyner, W. B. and D. M. Boore, "Peak Horizontal Acceleration and Velocity from Strong-Motion Records Including Records from the 1979 Imperial Valley, California, Earthquake", *Bulletin of Seismological Society of America*, Vol. 71, No. 6, pp. 2011–2038, 1981.

40. Niazi, M. and Y. Bozorgnia, "Behavior of Near-Source Peak Horizontal and Verti-

cal Ground Motions over SMART-1 Array, Taiwan", *Bulletin of the Seismological Society of America*, Vol. 81, No. 3, pp. 715–732, 1991.

41. Ambraseys, N. N. and J. J. Bommer, "On the attenuation of Ground Accelerations in Europe", *in Proceedings of Tenth World Conference on Earthquake Engineering*, pp. 675–678, Madrid, Spain, 1992.

42. Cauzzi, C. and E. Faccioli, "Anatomy of Sigma of a Global Predictive Model for Ground Motions and Response Spectra", *Bulletin of Earthquake Engineering*, Vol. 16, No. 5, pp. 1887–1905, 2018.

43. Boore, D. M., W. B. Joyner and T. E. Fumal, *Estimation of Response Spectra and Peak Accelerations from Western North American Earthquakes: An Interim Report Part 2*, Open-File Report 94-127, U.S. Geological Survey, Menlo Park, California, USA, 1994.

44. Spudich, P. and D. Boore, "A Revised Ground-Motion Prediction Relation for Use in Extensional Tectonic Regimes", *Bulletin of the Seismological Society of America*, Vol. 95, No. 3, pp. 1209–1209, 2005.

45. Abrahamson, N. A. and R. R. Youngs, "A Stable Algorithm for Regression Analyses Using the Random Effects Model", *Bulletin of the Seismological Society of America*, Vol. 82, No. 1, pp. 505–510, 1992.

46. Joyner, W. B. and D. M. Boore, "Methods for Regression Analysis of Strong-Motion Data", *Bulletin of the Seismological Society of America*, Vol. 83, No. 2, pp. 469–487, 1993.

47. Boore, D. M., W. B. Joyner and T. E. Fumal, "Equations for Estimating Horizontal Response Spectra and Peak Acceleration From Western North American Earthquakes: A Summary of Recent Work", *Seismological Research Letters*, Vol. 68, No. 1, pp. 128–153, 1997.

48. Ordaz, M., S. K. Singh and A. Arciniega, "Bayesian Attenuation Regressions: An Application to Mexico City", *Geophysical Journal International*, Vol. 117, No. 2, pp. 335–344, 1994.

49. Dahle, A., A. Climent, W. Taylor, H. Bungum, P. Santos, M. C. Real, C. Linholm, W. Strauch and F. Segura., "New Spectral Strong Motion Attenuation Models for Central America", *Fifth International Conference on Seismic Zonation*, Vol. 2, pp. 1005–1012, Nice, France, 1995.

50. Kuehn, N. and F. Scherbaum, "Ground-Motion Prediction Model Building: A Multilevel Approach", *Bulletin of Earthquake Engineering*, Vol. 13, No. 9, pp. 2481–2491, 2015.

51. Güllü, H. and E. Erçelebi, "A Neural Network Approach for Attenuation Relationships: An Application Using Strong Ground Motion Data from Turkey", *Engineering Geology*, Vol. 93, No. 3-4, pp. 65–81, 2007.

52. Derras, B., P. Y. Bard and F. Cotton, "Towards Fully Data Driven Ground-Motion Prediction Models for Europe", *Bulletin of Earthquake Engineering*, Vol. 12, No. 1, pp. 495–516, 2014.

53. Derras, B., P.-Y. Bard and F. Cotton, "V_{S30}, slope, H_{800} and f_0: Performance of Various Site-Condition Proxies in Reducing Ground-Motion Aleatory Variability and Predicting Nonlinear Site Response", *Earth, Planets and Space*, Vol. 69, No. 1, pp. 1–21, 2017.

54. Wiszniowski, J., "Estimation of a Ground Motion Model for Induced Events by Fahlman's Cascade Correlation Neural Network", *Computers & Geosciences*, Vol. 131, pp. 23–31, 2019.

55. Sobhaninejad, G., A. Noorzad and A. Ansari, "Genetic Algorithm (GA): A New Approach in Estimating Strong Ground Motion Attenuation Relations", *Fourth International Conference on Earthquake Geotechnical Engineering* , Thessaloniki,

Greece, 2007.

56. Cabalar, A. F. and A. Cevik, "Genetic Programming-Based Attenuation Relationship: An Application of Recent Earthquakes in Turkey", *Computers & Geosciences*, Vol. 35, No. 9, pp. 1884–1896, 2009.

57. Güllü, H., "Prediction of Peak Ground Acceleration by Genetic Expression Programming and Regression: a Comparison Using Likelihood-Based Measure", *Engineering Geology*, Vol. 141, pp. 92–113, 2012.

58. Power, M., B. Chiou, N. Abrahamson, Y. Bozorgnia, T. Shantz and C. Roblee, "An Overview of the NGA Project", *Earthquake Spectra*, Vol. 24, No. 1, pp. 3–21, 2008.

59. Douglas, J., "Use of Analysis of Variance for the Investigation of Regional Dependence of Strong Ground Motions", *13th World Conference on Earthquake Engineering*, Vancouver, B.C., Canada, 2004.

60. Douglas, J., "An Investigation of Analysis of Variance as A Tool for Exploring Regional Differences in Strong Ground Motions", *Journal of Seismology*, Vol. 8, No. 4, pp. 485–496, 2004.

61. Ambraseys, N. N., J. Douglas, S. Sarma and P. Smit, "Equations for the Estimation of Strong Ground Motions from Shallow Crustal Earthquakes Using Data from Europe and the Middle East: Horizontal Peak Ground Acceleration and Spectral Acceleration", *Bulletin of Earthquake Engineering*, Vol. 3, No. 1, pp. 1–53, 2005.

62. Campbell, K. W. and Y. Bozorgnia, "Next Generation Attenuation (NGA) empirical ground motion models: Can They Be Used in Europe ?", *1st European Conference on Earthquake Engineering and Seismology*, pp. 1–10, Geneva, Switzerland, 2006.

63. Campbell, K. W. and Y. Bozorgnia, "NGA Ground Motion Model for the Geometric Mean Horizontal Component of PGA, PGV, PGD and 5% Damped Linear Elastic Response Spectra for Periods Ranging from 0.01 to 10 s", *Earthquake Spectra*, Vol. 24, No. 1, pp. 139–171, 2008.

64. Chiou, B., R. Youngs, N. Abrahamson and K. Addo, "Ground-motion Attenuation Model for Small-to-Moderate Shallow Crustal Earthquakes in California and Its Implications on Regionalization of Ground-Motion Prediction Models", *Earthquake Spectra*, Vol. 26, No. 4, pp. 907–926, 2010.

65. Campbell, K. W., "Comprehensive Comparison among the Campbell–Bozorgnia NGA-West2 GMPE and Three GMPEs from Europe and the Middle East", *Bulletin of the Seismological Society of America*, Vol. 106, No. 5, pp. 2081–2103, 2016.

66. Akkar, S., M. A. Sandıkkaya, M. Şenyurt, A. Azari Sisi, B. Ö. Ay, P. Traversa, J. Douglas, F. Cotton, L. Luzi, B. Hernandez and et al., "Reference Database for Seismic Ground-Motion in Europe (RESORCE)", *Bulletin of Earthquake Engineering*, Vol. 12, No. 1, pp. 311–339, 2014.

67. Bindi, D., M. Massa, L. Luzi, G. Ameri, F. Pacor, R. Puglia and P. Augliera, "Pan-European Ground-Motion Prediction Equations for the Average Horizontal Component of PGA, PGV, and 5%-Damped PSA at Spectral Periods up to 3.0 s Using the RESORCE Dataset", *Bulletin of Earthquake Engineering*, Vol. 12, No. 1, pp. 391–430, 2014.

68. Bora, S. S., F. Scherbaum, N. Kuehn, P. Stafford and B. Edwards, "Development of A Response Spectral Ground-Motion Prediction Equation (GMPE) for Seismic-Hazard Analysis from Empirical Fourier Spectral and Duration Models", *Bulletin of the Seismological Society of America*, Vol. 105, No. 4, pp. 2192–2218, 2015.

69. Campbell, K. W. and Y. Bozorgnia, "NGA-West2 Ground Motion Model for the Average Horizontal Components of PGA, PGV, and 5% Damped Linear Accel-

eration Response Spectra", *Earthquake Spectra*, Vol. 30, No. 3, pp. 1087–1115, 2014.

70. Safak, E., M. Erdik, K. Beyen, D. Carver, E. Cranswick, M. Çelebi, E. Durukal, W. Ellsworth, T. Holzer, M. Meremonte, C. Mueller, O. Ozel and S. Toprak, "Kocaeli, Turkey, Earthquake of August 17, 1999: Reconnaissance Report, Chapter 5—Recorded Mainshock and Aftershock Motions", *Earthquake Spectra*, Vol. 16, pp. 97–112, 2000.

71. Boore, D. M., "Comparisons of Ground Motions from the 1999 Chi-Chi Earthquake with Empirical Predictions Largely based on Data from California", *Bulletin of the Seismological Society of America*, Vol. 91, No. 5, pp. 1212–1217, 2001.

72. Douglas, J., "On the Regional Dependence of Earthquake Response Spectra", *Indian Society of Earthquake Technology (ISET) Journal of Earthquake Technology*, Vol. 44, No. 1, pp. 71–99, 2007.

73. Scasserra, G., J. P. Stewart, P. Bazzurro, G. Lanzo and F. Mollaioli, "A Comparison of NGA Ground-Motion Prediction Equations to Italian Data", *Bulletin of the Seismological Society of America*, Vol. 99, No. 5, pp. 2961–2978, 2009.

74. Akkar, S. and Z. Çağnan, "A Local Ground-Motion Predictive Model for Turkey, and its Comparison with Other Regional and Global Ground-Motion Models", *Bulletin of the Seismological Society of America*, Vol. 100, No. 6, pp. 2978–2995, 2010.

75. Malcioglu, F. S., H. Süleyman and E. Çaktı, "Seismological and Engineering Characteristics of Strong Motion Data from 24 and 26 September 2019 Marmara Sea Earthquakes", *Bulletin of Earthquake Engineering*, Vol. 20, No. 11, pp. 5567–5599, 2022.

76. Boore, D. M., J. P. Stewart, E. Seyhan and G. M. Atkinson, "NGA-West2 Equations for Predicting PGA, PGV, and 5% Damped PSA for Shallow Crustal Earth-

quakes", *Earthquake Spectra*, Vol. 30, No. 3, pp. 1057–1085, 2014.

77. Kale, Ö., S. Akkar, A. Ansari and H. Hamzehloo, "A Ground-Motion Predictive Model for Iran and Turkey for Horizontal PGA, PGV, and 5% Damped Response Spectrum: Investigation of Possible Regional Effects", *Bulletin of the Seismological Society of America*, Vol. 105, No. 2A, pp. 963–980, 2015.

78. Tezcan, S. S., *Probability Analysis of Earthquake Magnitudes*, Türkiye Deprem Vakfı, İstanbul, Türkiye, 1995.

79. Inan, E., Z. Colakoglu, N. Koc, N. Bayülke and E. Coruh, *1976-1996 Yılları Arası İvme Kayıtları Olan Deprem Kataloğu*, Afet İşleri Genel Müdürlüğü, Deprem Araştırma Dairesi Başkanlığı, Ankara, Türkiye, 1996.

80. Aydan, Ö., M. Sezaki and R. Yarar, "The Seismic Characteristics of Turkish earthquakes", *11th World Conference on Earthquake Engineering*, Acapulco, Mexico, 1996.

81. Gülkan, P. and E. Kalkan, "Attenuation Modeling of Recent Earthquakes in Turkey", *Journal of Seismology*, Vol. 6, No. 3, pp. 397–409, 2002.

82. Ulusay, R., E. Tuncay, H. Sonmez and C. Gokceoglu, "An Attenuation Relationship based on Turkish Strong Motion Data and Iso-Acceleration Map of Turkey", *Engineering Geology*, Vol. 74, No. 3-4, pp. 265–291, 2004.

83. Kalkan, E. and P. Gülkan, "Empirical Attenuation Equations for Vertical Ground Motion in Turkey", *Earthquake Spectra*, Vol. 20, No. 3, pp. 853–882, 2004.

84. Özbey, C., A. Sari, L. Manuel, M. Erdik and Y. Fahjan, "An Empirical Attenuation Relationship for Northwestern Turkey Ground Motion Using A Random Effects Approach", *Soil Dynamics and Earthquake Engineering*, Vol. 24, No. 2, pp. 115–125, 2004.

85. Bindi, D., S. Parolai, H. Grosser, C. Milkereit and E. Durukal, "Empirical Ground-

Motion Prediction Equations for Northwestern Turkey Using the Aftershocks of the 1999 Kocaeli Earthquake", *Geophysical Research Letters*, Vol. 34, No. 8, 2007.

86. Akyol, N. and Ö. Karagöz, "Empirical Attenuation Relationships for Western Anatolia, Turkey", *Turkish Journal of Earth Sciences*, Vol. 18, No. 3, pp. 351–382, 2009.

87. Ulutas, E. and M. F. Ozer, "Empirical Attenuation Relationship of Peak Ground Acceleration for Eastern Marmara Region in Turkey", *Arabian Journal for Science and Engineering*, Vol. 35, No. 1, p. 187, 2010.

88. Gülerce, Z., B. Kargoığlu and N. A. Abrahamson, "Turkey-adjusted NGA-W1 Horizontal Ground Motion Prediction Models", *Earthquake Spectra*, Vol. 32, No. 1, pp. 75–100, 2016.

89. Erken, A., G. Şengül Nomaler and Z. Gündüz, "The Development of Attenuation Relationship for Northwest Anatolia Region", *Arabian Journal of Geosciences*, Vol. 11, No. 21, pp. 1–15, 2018.

90. Sandıkkaya, M. A., S. Akkar, Ö. Kale and E. Yenier, "A Simulation-Based Regional Ground-Motion Model for Western Türkiye", *Bulletin of Earthquake Engineering*, Vol. 21, No. 7, pp. 3221–3249, 2023.

91. Zátopek, A., "The Propagation of East Alpine Earthquakes in the Bohemian Mass", *General Assembly of International Union of Geodesy and Geophysics (IUGG)*, Oslo, Norway, 1948.

92. Procházková, D. and V. Kárník, *Atlas of Isoseismal Maps. Central and Eastern Europe*, Geophysical Institute of the Czechoslovak Academy of Sciences, Prague, Czech Republic, 1978.

93. Procházková, D., "Earthquake Pattern in Central Europe", *Acta Universitatis Carolinae, Mathematica et Physica*, Vol. 34, No. 1, pp. 3–66, 1993.

94. Cultrera, G., A. Rovelli, G. Mele, R. Azzara, A. Caserta and F. Marra, "Azimuth-dependent Amplification of Weak and Strong Ground Motions within a Fault Zone (Nocera Umbra, Central Italy)", *Journal of Geophysical Research: Solid Earth*, Vol. 108, No. B3, pp. ESE 10–1—ESE 10–14, 2003.

95. Wang, D. and L. Xie, "Attenuation of Peak Ground Accelerations from the Great Wenchuan Earthquake", *Earthquake Engineering and Engineering Vibration*, Vol. 8, No. 2, pp. 179–188, 2009.

96. Calderoni, G., A. Rovelli and S. K. Singh, "Stress Drop and Source Scaling of the 2009 April L'Aquila Earthquakes", *Geophysical Journal International*, Vol. 192, No. 1, pp. 260–274, 2013.

97. Málek, J., J. Brokešová and J. Vackář, "Mid-European Seismic Attenuation Anomaly", *Tectonophysics*, Vol. 712, pp. 557–577, 2017.

98. Somerville, P. G., N. F. Smith, R. W. Graves and N. A. Abrahamson, "Modification of Empirical Strong Ground Motion Attenuation Relations to Include the Amplitude And Duration Effects of Rupture Directivity", *Seismological Research Letters*, Vol. 68, No. 1, pp. 199–222, 1997.

99. Abrahamson, N. A., "Effects of Rupture Directivity on Probabilistic Seismic Hazard Analysis", *Proceedings of the 6th International Conference on Seismic Zonation*, Vol. 1, pp. 151–156, Palm Springs, CA, USA, 2000.

100. Spudich, P. and B. S. Chiou, "Directivity in NGA Earthquake Ground Motions: Analysis Using Isochrone Theory", *Earthquake Spectra*, Vol. 24, No. 1, pp. 279–298, 2008.

101. Rupakhety, R., S. Sigurdsson, A. Papageorgiou and R. Sigbjörnsson, "Quantification of Ground-Motion Parameters and Response Spectra in the Near-fault Region", *Bulletin of Earthquake Engineering*, Vol. 9, No. 4, pp. 893–930, 2011.

102. Kurzon, I., F. L. Vernon, Y. Ben-Zion and G. Atkinson, "Ground Motion Prediction Equations in the San Jacinto Fault Zone: Significant Effects of Rupture Directivity and Fault Zone Amplification", *Pure and Applied Geophysics*, Vol. 171, No. 11, pp. 3045–3081, 2014.

103. Ripperger, J., P. Mai and J.-P. Ampuero, "Variability of Near-Field Ground Motion from Dynamic Earthquake Rupture Simulations", *Bulletin of the Seismological Society of America*, Vol. 98, No. 3, pp. 1207–1228, 2008.

104. Ramirez-Guzman, L., R. W. Graves, K. B. Olsen, O. S. Boyd, C. Cramer, S. Hartzell, S. Ni, P. Somerville, R. A. Williams and J. Zhong, "Ground-motion Simulations of 1811–1812 New Madrid Earthquakes, Central United States", *Bulletin of the Seismological Society of America*, Vol. 105, No. 4, pp. 1961–1988, 2015.

105. Sokolov, V., F. Wenzel, J. Wen-Yu and W. Kuo-Liang, "Uncertainty and Spatial Correlation of Earthquake Ground Motion in Taiwan", *TAO: Terrestrial, Atmospheric and Oceanic Sciences*, Vol. 21, No. 6, p. 9, 2010.

106. Mena, B. and P. M. Mai, "Selection and quantification of Near-Fault Velocity Pulses Owing to Source Directivity", *Georisk*, Vol. 5, No. 1, pp. 25–43, 2011.

107. Vyas, J. C., P. M. Mai and M. Galis, "Distance and Azimuthal Dependence of Ground-Motion Variability for Unilateral Strike-Slip Ruptures", *Bulletin of the Seismological Society of America*, Vol. 106, No. 4, pp. 1584–1599, 2016.

108. Stamatovska, G. S., "A New Ground Motion Model-Methodological Approach", *Acta Geodaetica et Geophysica Hungarica*, Vol. 41, No. 3-4, pp. 409–423, 2006.

109. Stamatovska, G., "Ground Motion Models—State of the Art", *Acta Geodaetica et Geophysica Hungarica*, Vol. 43, No. 2-3, pp. 267–284, 2008.

110. Stamatovska, S. G., "The Latest Mathematical Models of Earthquake Ground Motion", *Seismic Waves-Research and Analysis*, IntechOpen, 2012.

111. Tsuno, S., M. Noyori and H. Yamanaka, "Azimuthal Dependence on Amplifications for Long-Period Ground Motions Propagating in the Kanto Basin, Japan", *Journal of Seismology*, Vol. 26, No. 2, pp. 373–385, 2022.

112. Chiou, B., R. Darragh, N. Gregor and W. Silva, "NGA Project Strong-Motion Database", *Earthquake Spectra*, Vol. 24, No. 1, pp. 23–44, 2008.

113. "Güralp 5T Operator's Guide", Güralp Systems Limited, Aldermaston, England, 2009.

114. Campbell, K. W., "Near-source Attenuation of Peak Horizontal Acceleration", *Bulletin of the Seismological Society of America*, Vol. 71, No. 6, pp. 2039–2070, 1981.

115. OYO Inc., J., *Production of Microzonation Report and Maps on European Side (South)*, Final report, Istanbul Metropolitan Municipality, İstanbul, Türkiye, 2007.

116. OYO Inc., J., *Production of Microzonation Report and Maps on Asian Side*, Final report, Istanbul Metropolitan Municipality, İstanbul, Türkiye, 2009.

117. Harmandar, E., *Spatial Variation of Strong Ground Motion*, Ph.D. Thesis, Boğaziçi University, Kandilli Observatory and Earthquake Research Institute, 2009.

118. The MathWorks, Inc., "Matlab Version: 9.13 (R2022b)", `https://www.mathworks.com`, 2023.

119. Boore, D. M., "On Pads and Filters: Processing Strong-motion Data", *Bulletin of the Seismological Society of America*, Vol. 95, No. 2, pp. 745–750, 2005.

120. Malcioglu, F. S. and B. Taskin, "Investigation of the Effect of Noise Content in the Recorded Strong Motions in Structural Behavior", *International Conference on Earthquakes and Structures*, Seoul, Korea, 2011.

121. Tento, A., L. Franceschina and A. Marcellini, "Expected Ground Motion Evaluation for Italian Sites", *10th World Conference on Earthquake Engineering*, Vol. 1, pp. 489–494, Madrid, Spain, 1992.

122. Mollova, G., "Effects of Digital Filtering in Data Processing of Seismic Acceleration Records", *EURASIP Journal on Advances in Signal Processing*, Vol. 2007, No. 029502, pp. 1–9, 2007.

123. Puglia, R., E. Russo, L. Luzi, M. D'Amico, C. Felicetta, F. Pacor and G. Lanzano, "Strong-motion Processing Service: A Tool to Access and Analyse Earthquakes Strong-Motion Waveforms", *Bulletin of Earthquake Engineering*, Vol. 16, No. 7, pp. 2641–2651, 2018.

124. Malhotra, P. K., "Response Spectrum of Incompatible Acceleration, Velocity and Displacement Histories", *Earthquake Engineering & Structural Dynamics*, Vol. 30, No. 2, pp. 279–286, 2001.

125. Bazzurro, P., B. Sjoberg, N. Luco, W. Silva, R. Darragh *et al.*, "Effects of Strong Motion Processing Procedures on Time Histories, Elastic and Inelastic Spectra", *Invited Workshop on Strong Motion Record Processing, Consortium of Organizations for Strong-Motion Observation Systems (COSMOS)*, Richmond, CA, USA, 2004.

126. Akkar, S. and J. J. Bommer, "Influence of Long-Period Filter Cut-Off on Elastic Spectral Displacements", *Earthquake Engineering & Structural Dynamics*, Vol. 35, No. 9, pp. 1145–1165, 2006.

127. Boore, D. M., "Effect of Baseline Corrections on Displacements and Response Spectra for Several Recordings of the 1999 Chi-Chi, Taiwan, Earthquake", *Bulletin of the Seismological Society of America*, Vol. 91, No. 5, pp. 1199–1211, 2001.

128. Heng, L., Y. Yunsheng, Z. Shuiming, C. Yongjian and L. Dongning, "Baseline Correction for Digital Strong-Motion Records by Using the Pre-Event Portion",

Geodesy and Geodynamics, Vol. 2, No. 1, pp. 43–46, 2011.

129. Chiu, H.-C., "Stable Baseline Correction of Digital Strong-Motion Data", *Bulletin of the Seismological Society of America*, Vol. 87, No. 4, pp. 932–944, 1997.

130. Gregor, N. and B. Bolt, "Peak Strong Motion Attenuation Relations for Horizontal and Vertical Ground Displacements", *Journal of Earthquake Engineering*, Vol. 1, No. 02, pp. 275–292, 1997.

131. Akkar, S. and D. M. Boore, "On Baseline Corrections and Uncertainty in Response Spectra for Baseline Variations Commonly Encountered in Digital Accelerograph Records", *Bulletin of the Seismological Society of America*, Vol. 99, No. 3, pp. 1671–1690, 2009.

132. Pacor, F., R. Paolucci, G. Ameri, M. Massa and R. Puglia, "Italian Strong Motion Records in ITACA: Overview and Record Processing", *Bulletin of Earthquake Engineering*, Vol. 9, No. 6, pp. 1741–1759, 2011.

133. Douglas, J. and D. M. Boore, "High-frequency Filtering of Strong-Motion Records", *Bulletin of Earthquake Engineering*, Vol. 9, No. 2, pp. 395–409, 2011.

134. Boore, D. M., A. Azari Sisi and S. Akkar, "Using Pad-Stripped Acausally Filtered Strong-Motion Data", *Bulletin of the Seismological Society of America*, Vol. 102, No. 2, pp. 751–760, 2012.

135. Malcioglu, F. S. and T. Tetik, "Effect of High-Pass Cut-Off Frequency on Structural Response under the Strong Ground Motion", *Society for Earthquake and Civil Engineering Dynamics Conference*, London, United Kingdom, 2019.

136. Malcioglu, S. and H. Süleyman, "A Practical Approach for the Selection of the Corner Frequency of High-Pass Filters in Processing Earthquake Records", *36th General Assembly of the European Seismological Commission*, Valletta, Malta, 2018.

137. Boore, D. M. and S. Akkar, "Effect of Causal and Acausal Filters on Elastic and Inelastic Response Spectra", *Earthquake Engineering & Structural Dynamics*, Vol. 32, No. 11, pp. 1729–1748, 2003.

138. Kotha, S. R., G. Weatherill, D. Bindi and F. Cotton, "A Regionally-Adaptable Ground-Motion Model for Shallow Crustal Earthquakes in Europe", *Bulletin of Earthquake Engineering*, Vol. 18, No. 9, pp. 4091–4125, 2020.

139. Akkar, S., M. A. Sandıkkaya and J. J. Bommer, "Empirical Ground-Motion Models for Point-and Extended-Source Crustal Earthquake Scenarios in Europe and the Middle East", *Bulletin of Earthquake Engineering*, Vol. 12, No. 1, pp. 359–387, 2014.

140. Hermkes, M., N. M. Kuehn and C. Riggelsen, "Simultaneous Quantification of Epistemic and Aleatory Uncertainty in GMPEs Using Gaussian Process Regression", *Bulletin of Earthquake Engineering*, Vol. 12, No. 1, pp. 449–466, 2014.

141. Sandıkkaya, M. A., S. Akkar and P.-Y. Bard, "A Nonlinear Site-Amplification Model for the Next Pan-European Ground-Motion Prediction Equations", *Bulletin of the Seismological Society of America*, Vol. 103, No. 1, pp. 19–32, 2013.

142. Sandıkkaya, M. A. and S. Akkar, "Cumulative Absolute Velocity, Arias Intensity and Significant Duration Predictive Models from a Pan-European Strong-Motion Dataset", *Bulletin of Earthquake Engineering*, Vol. 15, No. 5, pp. 1881–1898, 2017.

143. Heaton, T. H., F. Tajima and A. W. Mori, "Estimating Ground Motions Using Recorded Accelerograms", *Surveys in Geophysics*, Vol. 8, No. 1, pp. 25–83, 1986.

144. Kadirioğlu, F. T. and R. F. Kartal, "The New Empirical Magnitude Conversion Relations Using An Improved Earthquake Catalogue for Turkey and Its Near Vicinity (1900-2012)", *Turkish Journal of Earth Sciences*, Vol. 25, No. 4, pp. 300–310, 2016.

145. Campbell, K. W. and Y. Bozorgnia, "A Comparison of Ground Motion Prediction Equations for Arias Intensity and Cumulative Absolute Velocity Developed Using a Consistent Database and Functional Form", *Earthquake Spectra*, Vol. 28, No. 3, pp. 931–941, 2012.

146. Foulser-Piggott, R. and K. Goda, "Ground-motion Prediction Models for Arias Intensity and Cumulative Absolute Velocity for Japanese Earthquakes Considering Single-Station Sigma and Within-Event Spatial Correlation", *Bulletin of the Seismological Society of America*, Vol. 105, No. 4, pp. 1903–1918, 2015.

147. Strasser, F. O., J. J. Bommer and N. A. Abrahamson, "Truncation of the Distribution of Ground-Motion Residuals", *Journal of Seismology*, Vol. 12, No. 1, pp. 79–105, 2008.

148. Atik, L. A., N. Abrahamson, J. J. Bommer, F. Scherbaum, F. Cotton and N. Kuehn, "The Variability of Ground-Motion Prediction Models and its Components", *Seismological Research Letters*, Vol. 81, No. 5, pp. 794–801, 2010.

149. Baltay, A. S., T. C. Hanks and N. A. Abrahamson, "Uncertainty, Variability, and Earthquake Physics in Ground-Motion Prediction Equations", *Bulletin of the Seismological Society of America*, Vol. 107, No. 4, pp. 1754–1772, 2017.

150. Kaklamanos, J., L. G. Baise and D. M. Boore, "Estimating Unknown Input Parameters When Implementing the NGA Ground-Motion Prediction Equations in Engineering Practice", *Earthquake Spectra*, Vol. 27, No. 4, pp. 1219–1235, 2011.

151. Gallovič, F., "Azimuthal Dependence of the Ground Motion Variability from Scenario Modeling of the 2014 Mw6.0 South Napa, California, Earthquake Using an Advanced Kinematic Source Model", *Pure and Applied Geophysics*, Vol. 174, No. 9, pp. 3467–3478, 2017.

152. Penzien, J. and M. Watabe, "Characteristics of 3-Dimensional Earthquake Ground Motions", *Earthquake Engineering & Structural Dynamics*, Vol. 3, No. 4,

pp. 365–373, 1974.

153. Kubo, T. and J. Penzien, "Analysis of Three-Dimensional Strong Ground Motions along Principal Axes, San Fernando Earthquake", *Earthquake Engineering & Structural Dynamics*, Vol. 7, No. 3, pp. 265–278, 1979.

154. Kubo, T. and J. Penzien, *Time and Frequency Domain Analyses of Three Dimensional Ground Motions*, Earthquake Engineering Research Center, University of California Berkeley, Berkeley, California, 1976.

155. Lay, T. and T. C. Wallace, *Modern Global Seismology*, Elsevier, United States of America, 1995.

156. Stein, S. and M. Wysession, *An Introduction to Seismology, Earthquakes, and Earth Structure*, Blackwell Publishing, Hoboken, New Jersey, United States of America, 2003.

157. Kaklamanos, J. and L. G. Baise, "Model Validations and Comparisons of the Next Generation Attenuation of Ground Motions (NGA–West) Project", *Bulletin of the Seismological Society of America*, Vol. 101, No. 1, pp. 160–175, 2011.

158. Strasser, F. O., N. A. Abrahamson and J. J. Bommer, "Sigma: Issues, Insights, and Challenges", *Seismological Research Letters*, Vol. 80, No. 1, pp. 40–56, 2009.

159. Bommer, J. J., J. Douglas and F. O. Strasser, "Style-of-faulting in Ground-Motion Prediction Equations", *Bulletin of Earthquake Engineering*, Vol. 1, No. 2, pp. 171–203, 2003.

160. Sadigh, K., C.-Y. Chang, J. Egan, F. Makdisi and R. R. Youngs, "Attenuation Relationships for Shallow Crustal Earthquakes based on California Strong Motion Data", *Seismological Research Letters*, Vol. 68, No. 1, pp. 180–189, 1997.

161. Spudich, P., W. Joyner, A. Lindh, D. Boore, B. u. Margaris and J. Fletcher, "SEA99: A Revised Ground Motion Prediction Relation for Use in Extensional

Tectonic Regimes", *Bulletin of the Seismological Society of America*, Vol. 89, No. 5, pp. 1156–1170, 1999.

162. Campbell, K. W., "The Dependence of Peak Horizontal Acceleration on Magnitude, Distance, and Site Effects for Small-Magnitude Earthquakes in California and Eastern North America", *Bulletin of the Seismological Society of America*, Vol. 79, No. 5, pp. 1311–1346, 1989.

163. Richter, C. F., "Elementary Seismology", *Engineering and Science*, Vol. 22, No. 2, pp. 10–10, 1958.

164. Denham, D. and G. Small, "Strong Motion Data Centre: Bureau of Mineral Resources, Canada", *Bulletin of the New Zealand Society for Earthquake Engineering*, Vol. 4, No. 1, pp. 15–30, 1971.

165. Ambraseys, N., "Ground Motions in the Near Field of Small-Magnitude Earthquakes", *in Proceedings of the Commission on the Safety of Nuclear Installations, Organisation of Economic Cooperation in Europe*, Vol. 1, pp. 113–136, 1975.

166. Humbert, N. and E. Viallet, "An Evaluation of Epistemic and random uncertainties included in Attenuation Relationship Parameters", *14th World Conference on Earthquake Engineering*, Beijing, China, 2008.

167. Trifunac, M. D., "Preliminary Analysis of the Peaks of Strong Earthquake Ground Motion—Dependence of Peaks on Earthquake Magnitude, Epicentral Distance, and Recording Site Conditions", *Bulletin of the Seismological Society of America*, Vol. 66, No. 1, pp. 189–219, 1976.

168. Cotton, F., G. Pousse, F. Bonilla and F. Scherbaum, "On the Discrepancy of Recent European Ground-Motion Observations and Predictions from Empirical Models: Analysis of KiK-net Accelerometric Data and Point-Sources Stochastic Simulations", *Bulletin of the Seismological Society of America*, Vol. 98, No. 5, pp. 2244–2261, 2008.

169. Atkinson, G. M. and G. Viegas, "Point-Source Decay of Ground-Motion Amplitudes at¡ 10 km", *The Seismic Record*, Vol. 3, No. 1, pp. 21–28, 2023.

170. Boore, D. M., J. P. Stewart, A. A. Skarlatoudis, E. Seyhan, B. Margaris, N. Theodoulidis, E. Scordilis, I. Kalogeras, N. Klimis and N. S. Melis, "A Ground-Motion Prediction Model for Shallow Crustal Earthquakes in Greece", *Bulletin of the Seismological Society of America*, Vol. 111, No. 2, pp. 857–874, 2021.

171. Ambraseys, N. N., K. u. Simpson and J. J. Bommer, "Prediction of Horizontal Response Spectra in Europe", *Earthquake Engineering & Structural Dynamics*, Vol. 25, No. 4, pp. 371–400, 1996.

172. Yenier, E. and G. M. Atkinson, "Equivalent Point-Source Modeling of Moderate-To-Large Magnitude Earthquakes and Associated Ground-Motion Saturation Effects", *Bulletin of the Seismological Society of America*, Vol. 104, No. 3, pp. 1458–1478, 2014.

173. Atkinson, G. M., E. Yenier, N. Sharma and V. Convertito, "Constraints on the Near-Distance Saturation of Ground-Motion Amplitudes for Small-To-Moderate Induced Earthquakes", *Bulletin of the Seismological Society of America*, Vol. 106, No. 5, pp. 2104–2111, 2016.

174. Young, R. R., S. M. Day and J. P. Stevens, "The Specialty Conference: Earthquake Engineering and Soil Dynamics II-Recent Advances in Ground Motion Evaluation", *ASCE Geotechnical Special Publication 20* , Hawai, USA, 1988.

175. Crouse, C., "Ground-motion Attenuation Equations for Earthquakes on the Cascadia Subduction Zone", *Earthquake Spectra*, Vol. 7, No. 2, pp. 201–236, 1991.

176. Atkinson, G. M. and D. M. Boore, "Empirical Ground-Motion Relations for Subduction-Zone Earthquakes and Their Application to Cascadia and Other Regions", *Bulletin of the Seismological Society of America*, Vol. 93, No. 4, pp. 1703–1729, 2003.

177. Campbell, K. W., "Prediction of Strong Ground Motion Using the Hybrid Empirical Method and Its Use in the Development of Ground-Motion (Attenuation) Relations in Eastern North America", *Bulletin of the Seismological Society of America*, Vol. 93, No. 3, pp. 1012–1033, 2003.

178. Aoi, S., T. Kunugi, H. Nakamura and H. Fujiwara, "Deployment of New Strong Motion Seismographs of K-NET and KiK-net", *Earthquake Data in Engineering Seismology: Geotechnical, Geological, and Earthquake Engineering book series*, Vol. 14, pp. 167–186, 2011.

179. Persson, P.-O. and G. Strang, "A Simple Mesh Generator in MATLAB", *SIAM Review*, Vol. 46, No. 2, pp. 329–345, 2004.

180. Arias, A., "A Measure of Earthquake Intensity", *Seismic Design for Nuclear Plants*, pp. 438–483, 1970.

181. Bolt, B. A., "Duration of Strong Ground Motion", *in Proceedings of the 5th World Conference on Earthquake Engineering*, Vol. 1, pp. 1304–1313, Rome, Italy, 1973.

182. Bommer, J. J. and A. Martínez-Pereira, "The Effective Duration of Earthquake Strong Motion", *Journal of Earthquake Engineering*, Vol. 3, No. 02, pp. 127–172, 1999.

183. Earthquake Loss Estimation Routine, ELER v.3.0, Boğaziçi University, Department of Earthquake Engineering, İstanbul, Türkiye, 2010.

184. Erdik, M., Y. Fahjan, O. Ozel, H. Alcik, A. Mert and M. Gul, "Istanbul Earthquake Rapid Response and the Early Warning System", *Bulletin of Earthquake Engineering*, Vol. 1, No. 1, pp. 157–163, 2003.

185. Housner, G. W., "Intensity of Earthquake Ground Shaking Near the Causative Fault", *3rd World Conference on Earthquake Engineering*, Vol. III, pp. 94–115, Auckland and Wellington, New Zealand, 1965.

186. Lopez, O. A., A. K. Chopra and J. J. Hernandez, "Critical Response of Structures to Multicomponent Earthquake Excitation", *Earthquake Engineering & Structural Dynamics*, Vol. 29, No. 12, pp. 1759–1778, 2000.

187. The Regents of the University of California, "PEER Ground Motion Database", 2013, `https://ngawest2.berkeley.edu/`, accessed on December 10, 2023.

188. Ang, A. H.-S., W. H. Tang and S. Ross, *Probability Concepts in Engineering*, John Wiley & Sons, New Jersey, United States of America, 2007.

189. Sarma, S. K. and B. J. Casey, "Duration of Strong Motion in Earthquakes", *9th European Conference on Earthquake Engineering*, pp. 174–183, Moscow, Russia, 1990.

190. Stamatovska, G. S., "New Ground Motion Model: Methodological Approach", 2009, `https://www.researchgate.net/publication/338682223`, accessed on January 19, 2020.

191. Trifunac, M. D. and A. G. Brady, "A study on the Duration of Strong Earthquake Ground Motion", *Bulletin of the Seismological Society of America*, Vol. 65, No. 3, pp. 581–626, 1975.

APPENDIX A: COEFFICIENTS FOR M_L-BASED REGRESSIONS

Table A.1. Regression coefficients for M_L-based subsets.

M_L	Ground Motion Parameter	b_1	a_2	a_3	a_4	a_5	a_6	b_2
4.0	**PGA**	4.7950	1.0775	0.4296	1.1046	1.0383	9.6059	-0.6201
	PGV	6.1923	1.1060	0.2149	1.0103	0.9123	11.1193	-0.8485
	SA (T=0.4 s)	7.4973	1.0885	0.3484	-6.5785	-1.8990	20.9518	-1.0590
	SA (T=0.6 s)	8.0941	1.0981	0.2776	0.7827	0.7217	20.5820	-1.1564
	SA (T=1.0 s)	7.9648	1.1025	0.2450	1.0324	0.8321	28.6956	-1.1357
	SA (T=2.0 s)	5.8333	1.1441	0.0750	1.1233	0.7024	9.7310	-0.7913
	AI	10.3303	1.3619	0.3293	1.5108	1.5923	12.8739	-1.5187
	CAV	5.8877	1.0864	0.3636	-0.1000	0.3518	20.3864	-0.7979
4.1	**PGA**	3.3404	1.0805	0.4123	0.9496	0.9969	8.0560	-0.3805
	PGV	5.2255	1.1111	0.1888	1.0275	0.9274	0.0274	-0.6849
	SA (T=0.4 s)	6.2586	1.0912	0.3340	1.0427	0.8875	-0.0005	-0.8496
	SA (T=0.6 s)	6.6515	1.0968	0.2928	1.0487	0.8706	0.4918	-0.9129
	SA (T=1.0 s)	7.6307	1.1059	0.2262	1.0589	0.8440	-0.0792	-1.0707
	SA (T=2.0 s)	6.1132	1.1194	0.1278	1.0733	0.8066	-0.0944	-0.8287
	AI	8.1084	27.0463	3.7768	-19.5025	-6.3377	7.9938	-1.1161
	CAV	4.9946	1.0941	0.3123	1.0990	0.7377	-0.0203	-0.6469
4.2	**PGA**	3.7495	1.0903	0.3452	1.0382	0.9021	-0.0106	-0.4494
	PGV	6.1038	1.1180	0.1435	1.0552	0.8581	-0.0827	-0.8311
	SA (T=0.4 s)	7.7085	1.0935	0.3219	1.0566	0.8552	-0.0502	-1.0885
	SA (T=0.6 s)	7.8793	1.1035	0.2498	1.0787	0.7991	-0.0698	-1.1167
	SA (T=1.0 s)	8.6678	1.1138	0.1748	1.0930	0.7622	-0.0458	-1.2446
	SA (T=2.0 s)	7.8010	1.1278	0.0734	1.1080	0.7240	-0.0880	-1.1056
	AI	8.5909	1.1203	0.1292	0.9328	1.1719	-0.0996	-1.2326
	CAV	5.6101	1.0947	0.3133	1.1076	0.7261	-0.2232	-0.7500

Table A.1. Sample table that spans multiple pages. (cont.)

$\mathbf{M_L}$	**Ground Motion Parameter**	b_1	a_2	a_3	a_4	a_5	a_6	b_2
4.3	**PGA**	-16.4566	118.9213	18.4460	-152415	-62209	51.2189	-0.5085
	PGV	5.7269	1.0669	0.5182	0.8598	1.3189	35.5874	-0.7668
	SA (T=0.4 s)	6.2984	1.0475	0.6583	0.8978	1.2587	33.5889	-0.8578
	SA (T=0.6 s)	7.2909	1.0693	0.5012	0.9596	1.0978	21.9427	-1.0193
	SA (T=1.0 s)	7.8579	1.0851	0.3870	0.9814	1.0213	12.0824	-1.1118
	SA (T=2.0 s)	7.1726	1.0870	0.2928	0.9994	1.0115	12.5881	-1.0029
	AI	8.7964	0.9934	1.0487	717.3773	294.9283	46.0536	-1.2571
	CAV	5.3447	1.0469	0.6625	0.8783	1.1408	39.8925	-0.7038
4.4	**PGA**	4.1231	1.0105	0.9248	-65.2282	-26.4689	78.8781	-0.5038
	PGV	5.7728	0.8324	0.2946	4.9933	2.8553	28.3276	-0.7764
	SA (T=0.4 s)	7.3906	1.0787	0.4375	0.9920	1.0191	0.0490	-1.0348
	SA (T=0.6 s)	8.1994	1.0955	0.3169	1.0366	0.9148	-0.3037	-1.1663
	SA (T=1.0 s)	9.1714	1.1039	0.2570	1.0336	0.9211	0.1326	-1.3234
	SA (T=2.0 s)	9.7312	1.1170	0.1627	1.0422	0.9006	0.0750	-1.4173
	AI	14.7654	-7.0220	19.8822	62813.7	26754.13	504.3590	-1.2243
	CAV	5.6423	1.0788	0.4359	-10.5447	-4.0544	30.7894	-0.7532
4.5	**PGA**	3.6594	1.0706	0.4976	0.9483	1.1162	0.1189	-0.4365
	PGV	5.0137	1.1045	0.2571	0.9817	1.0414	-0.0261	-0.6586
	SA (T=0.4 s)	5.7853	1.0755	0.4628	0.9838	1.0362	0.1102	-0.7817
	SA (T=0.6 s)	6.6099	1.0873	0.3790	1.0149	0.9661	0.0293	-0.9163
	SA (T=1.0 s)	7.6633	1.1040	0.2602	1.0544	0.8782	-0.0030	-1.0883
	SA (T=2.0 s)	6.8687	1.1216	0.1355	1.0722	0.8380	-0.0589	-0.9603
	AI	11.7133	473.8753	66.8922	76330.4	33926.1	36.3176	-1.2533
	CAV	6.1300	0.9688	1.2220	-5.6463	-1.0141	137.0506	-0.8299

Table A.1. Sample table that spans multiple pages. (cont.)

M_L	Ground Motion Parameter	b_1	a_2	a_3	a_4	a_5	a_6	b_2
4.6	**PGA**	3.3220	0.1955	6.6917	-1.8849	7.1657	367.7562	-0.3152
	PGV	5.4942	0.4264	5.0821	-1.2416	5.7627	365.5232	-0.6841
	SA (T=0.4 s)	6.9260	0.5746	4.0087	-0.6144	4.5420	335.6181	-0.9273
	SA (T=0.6 s)	8.0442	0.6746	3.3005	-0.2772	3.7025	446.4727	-1.1155
	SA (T=1.0 s)	7.9200	9.5877	1.3686	6.2482	3.1281	30.3159	-1.2114
	SA (T=2.0 s)	8.3087	1.1269	0.1041	1.0814	0.8259	20.3767	-1.1944
	AI	6.8859	0.0734	7.5554	-2.6060	8.7668	294.1781	-0.8830
	CAV	4.6652	1.0714	0.5279	-4128.19	-1919.55	58.2076	-0.5986
4.7	**PGA**	1.8062	1.0447	0.6853	0.7862	1.3579	14.9517	-0.1329
	PGV	3.5436	1.0750	0.4715	0.8016	1.3756	13.3968	-0.4142
	SA (T=0.4 s)	4.6939	1.0526	0.6289	0.8511	1.3043	1.0868	-0.5972
	SA (T=0.6 s)	5.8503	1.0535	0.6221	1.4422	1.6519	4.7127	-0.7829
	SA (T=1.0 s)	7.2435	1.0416	0.7183	-807.294	-392.623	19.8057	-1.0056
	SA (T=2.0 s)	6.8438	1.0606	0.5727	-3.3408	-0.5738	19.3307	-0.9430
	AI	5.7477	1.0415	0.7081	10.8450	7.0229	23.7185	-0.7655
	CAV	4.7477	1.0446	0.6859	9.1519	5.2484	33.1472	-0.6052
4.8	**PGA**	4.6953	0.9482	1.3633	0.4273	2.1189	1.1247	-0.5941
	PGV	5.6741	0.9457	1.3811	0.2969	2.3546	1.2415	-0.7524
	SA (T=0.4 s)	4.5604	0.9135	1.6073	0.3186	2.3320	1.2211	-0.5694
	SA (T=0.6 s)	6.8360	0.9137	1.6056	0.3011	2.3675	1.1747	-0.9379
	SA (T=1.0 s)	6.7416	0.9240	1.5337	0.3107	2.3484	1.3221	-0.9234
	SA (T=2.0 s)	6.4466	0.5256	4.3305	-1.3452	5.1620	165.7504	-0.8425
	AI	10.7541	0.8437	2.0974	-0.3079	3.5302	1.1740	-1.5665
	CAV	6.0960	0.9528	1.3313	0.5199	1.9368	0.9989	-0.8213

Table A.1. Sample table that spans multiple pages. (cont.)

$\mathbf{M_L}$	**Ground Motion Parameter**	b_1	a_2	a_3	a_4	a_5	a_6	b_2
4.9	**PGA**	5.4542	1.0489	0.6574	0.8291	1.3165	-0.1101	-0.7168
	PGV	7.6297	1.1146	0.1968	0.9866	1.0248	0.1043	-1.0705
	SA (T=0.4 s)	7.0527	1.0752	0.4728	0.9690	1.0573	0.0931	-0.9748
	SA (T=0.6 s)	8.7772	1.1100	0.2292	1.1074	0.8011	-0.5384	-1.2537
	SA (T=1.0 s)	10.4896	1.1348	0.0554	1.1811	0.6649	0.3215	-1.5298
	SA (T=2.0 s)	11.5547	1.1523	-0.0673	1.1861	0.6554	0.3203	-1.7017
	AI	12.1345	1.0677	0.5258	0.5925	1.7540	0.0861	-1.7871
	CAV	7.3942	1.0570	0.6003	0.9360	1.1193	0.0368	-1.0279
5.0	**PGA**	NA	NA	NA	NA	NA	NA	NA
	PGV	NA	NA	NA	NA	NA	NA	NA
	SA (T=0.4 s)	NA	NA	NA	NA	NA	NA	NA
	SA (T=0.6 s)	NA	NA	NA	NA	NA	NA	NA
	SA (T=1.0 s)	NA	NA	NA	NA	NA	NA	NA
	SA (T=2.0 s)	NA	NA	NA	NA	NA	NA	NA
	AI	NA	NA	NA	NA	NA	NA	NA
	CAV	NA	NA	NA	NA	NA	NA	NA
5.1	**PGA**	-2.1989	1.0849	0.4051	0.9537	1.0765	0.0038	0.5189
	PGV	1.4517	1.1179	0.1738	0.9464	1.0886	0.0175	-0.0862
	SA (T=0.4 s)	4.3202	1.0617	0.5680	0.6118	1.0682	12.9600	-0.5536
	SA (T=0.6 s)	4.3975	1.0824	0.4229	0.9224	1.1284	0.0919	-0.5684
	SA (T=1.0 s)	5.3675	1.0900	0.3692	0.9252	1.1208	0.0063	-0.7290
	SA (T=2.0 s)	6.8145	1.0938	0.3425	1.9065	1.7499	10.3880	-0.9680
	AI	1.3194	1.1243	0.1293	0.8055	1.3211	-0.0220	-0.0651
	CAV	3.5950	1.0786	0.4493	1.0527	0.9122	0.0043	-0.4357

Table A.1. Sample table that spans multiple pages. (cont.)

$\mathbf{M_L}$	**Ground Motion Parameter**	b_1	a_2	a_3	a_4	a_5	a_6	b_2
5.2	**PGA**	4.8486	1.2150	-0.5105	1.5432	0.1616	1.1171	-0.6370
	PGV	5.6583	1.2995	-1.1040	1.7777	-0.2075	1.2853	-0.7751
	SA (T=0.4 s)	5.0118	1.1855	-0.3034	1.4605	0.2880	1.1125	-0.6601
	SA (T=0.6 s)	4.7794	2.9944	-13.0123	8.1602	-10.1049	453.5266	-0.8095
	SA (T=1.0 s)	4.3287	3.1843	-14.3462	8.8556	-11.1587	452.1482	-0.7571
	SA (T=2.0 s)	3.4274	3.7528	-18.3402	10.6881	-14.1232	511.0141	-0.6717
	AI	9.4422	2.3268	-8.3219	5.6565	-6.2240	259.5334	-1.4857
	CAV	4.8503	2.7598	-11.3643	7.4179	-8.9162	421.1436	-0.7966
5.3	**PGA**	NA	NA	NA	NA	NA	NA	NA
	PGV	NA	NA	NA	NA	NA	NA	NA
	SA (T=0.4 s)	NA	NA	NA	NA	NA	NA	NA
	SA (T=0.6 s)	NA	NA	NA	NA	NA	NA	NA
	SA (T=1.0 s)	NA	NA	NA	NA	NA	NA	NA
	SA (T=2.0 s)	NA	NA	NA	NA	NA	NA	NA
	AI	NA	NA	NA	NA	NA	NA	NA
	CAV	NA	NA	NA	NA	NA	NA	NA
5.4	**PGA**	NA	NA	NA	NA	NA	NA	NA
	PGV	NA	NA	NA	NA	NA	NA	NA
	SA (T=0.4 s)	NA	NA	NA	NA	NA	NA	NA
	SA (T=0.6 s)	NA	NA	NA	NA	NA	NA	NA
	SA (T=1.0 s)	NA	NA	NA	NA	NA	NA	NA
	SA (T=2.0 s)	NA	NA	NA	NA	NA	NA	NA
	AI	NA	NA	NA	NA	NA	NA	NA
	CAV	NA	NA	NA	NA	NA	NA	NA

Table A.1. Sample table that spans multiple pages. (cont.)

$\mathbf{M_L}$	**Ground Motion Parameter**	b_1	a_2	a_3	a_4	a_5	a_6	b_2
5.5	**PGA**	NA	NA	NA	NA	NA	NA	NA
	PGV	NA	NA	NA	NA	NA	NA	NA
	SA (T=0.4 s)	NA	NA	NA	NA	NA	NA	NA
	SA (T=0.6 s)	NA	NA	NA	NA	NA	NA	NA
	SA (T=1.0 s)	NA	NA	NA	NA	NA	NA	NA
	SA (T=2.0 s)	NA	NA	NA	NA	NA	NA	NA
	AI	NA	NA	NA	NA	NA	NA	NA
	CAV	NA	NA	NA	NA	NA	NA	NA
5.6	**PGA**	NA	NA	NA	NA	NA	NA	NA
	PGV	NA	NA	NA	NA	NA	NA	NA
	SA (T=0.4 s)	NA	NA	NA	NA	NA	NA	NA
	SA (T=0.6 s)	NA	NA	NA	NA	NA	NA	NA
	SA (T=1.0 s)	NA	NA	NA	NA	NA	NA	NA
	SA (T=2.0 s)	NA	NA	NA	NA	NA	NA	NA
	AI	NA	NA	NA	NA	NA	NA	NA
	CAV	NA	NA	NA	NA	NA	NA	NA
5.7	**PGA**	4.3626	0.7515	2.8553	-2.0137	2.3473	54.6270	-0.4981
	PGV	6.2123	0.7971	2.5146	-1.1200	3.2382	51.2471	-0.7999
	SA (T=0.4 s)	6.3856	0.6233	3.8125	-1.8163	3.9548	66.9624	-0.8011
	SA (T=0.6 s)	6.5337	0.6954	3.2739	-1.4357	3.5566	58.1281	-0.8357
	SA (T=1.0 s)	7.7896	0.8133	2.3936	-0.7953	2.8817	45.5390	-1.0538
	SA (T=2.0 s)	7.1987	0.8299	2.2700	-0.8310	2.9242	40.8307	-0.9621
	AI	10.7175	0.6166	3.8632	-2.4554	4.6238	47.7274	-1.4905
	CAV	6.6079	0.8393	2.2003	-0.4356	2.5066	43.1223	-0.8693

APPENDIX B: RESULTS FOR FUNCTIONAL FORM (5.4)

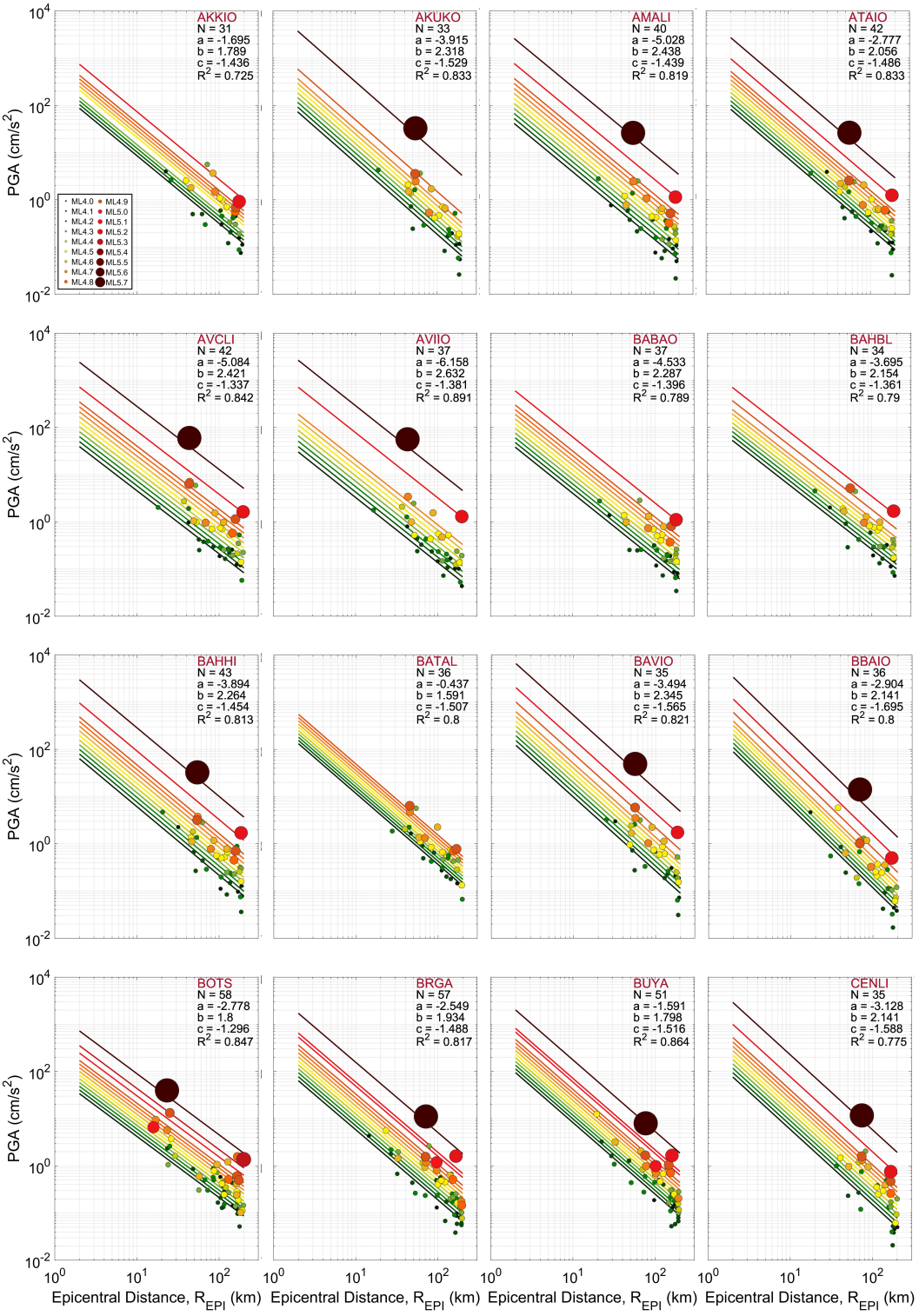


Figure B.1. Distance Scalings of the Functional Form (5.4) for All Stations.

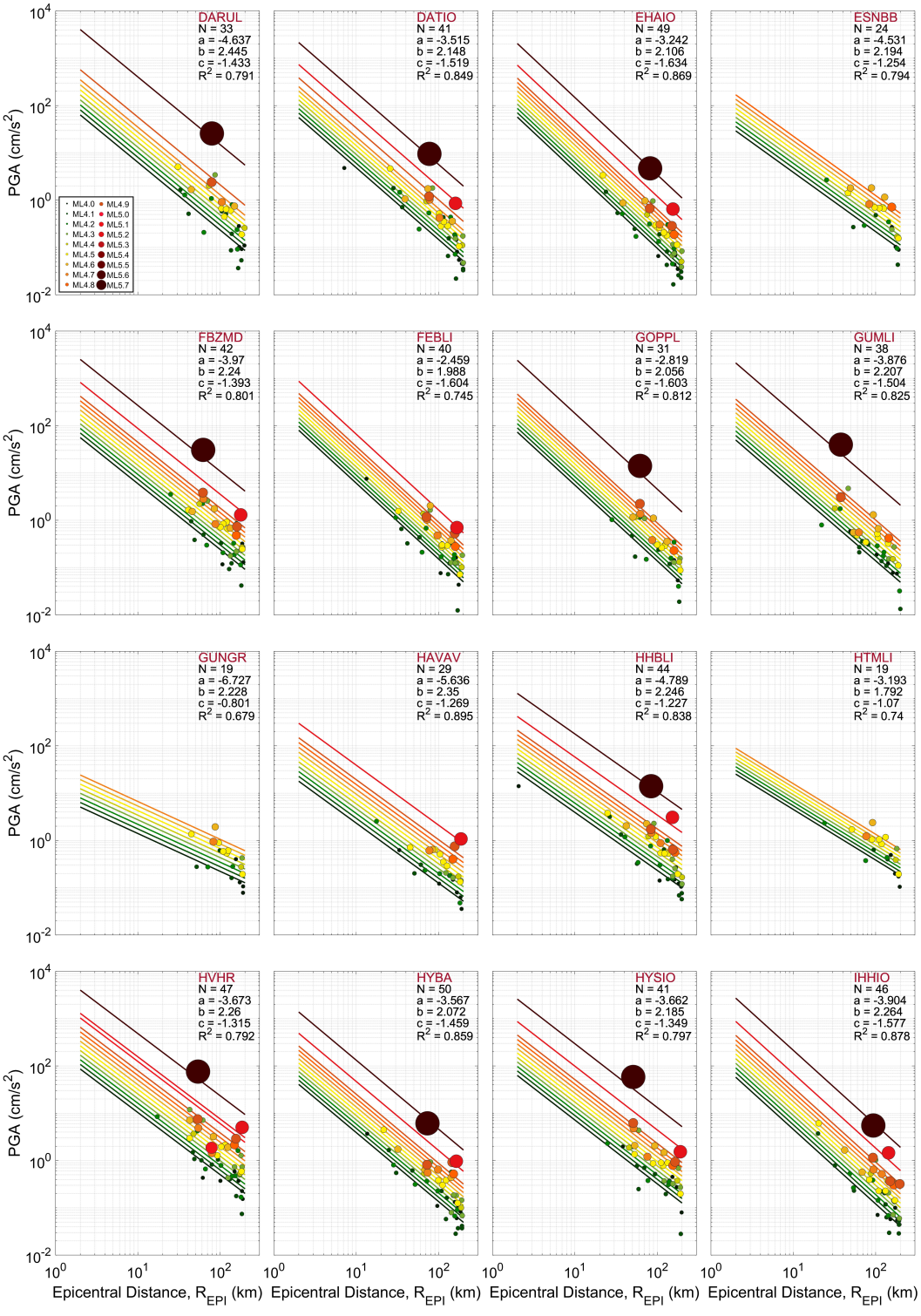


Figure B.2. Distance Scalings of the Functional Form (5.4) for All Stations (cont.).

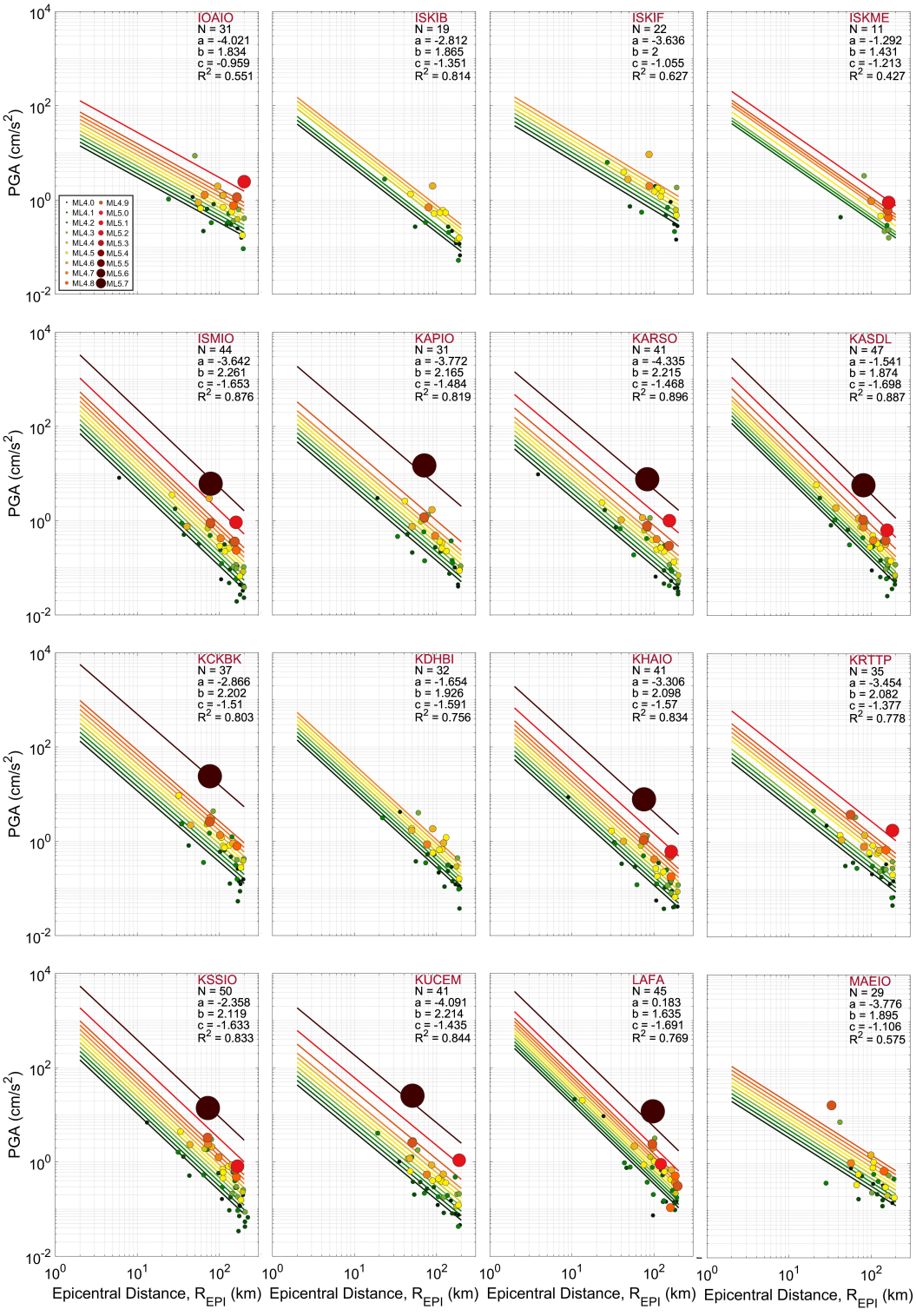


Figure B.3. Distance Scalings of the Functional Form (5.4) for All Stations (cont.).

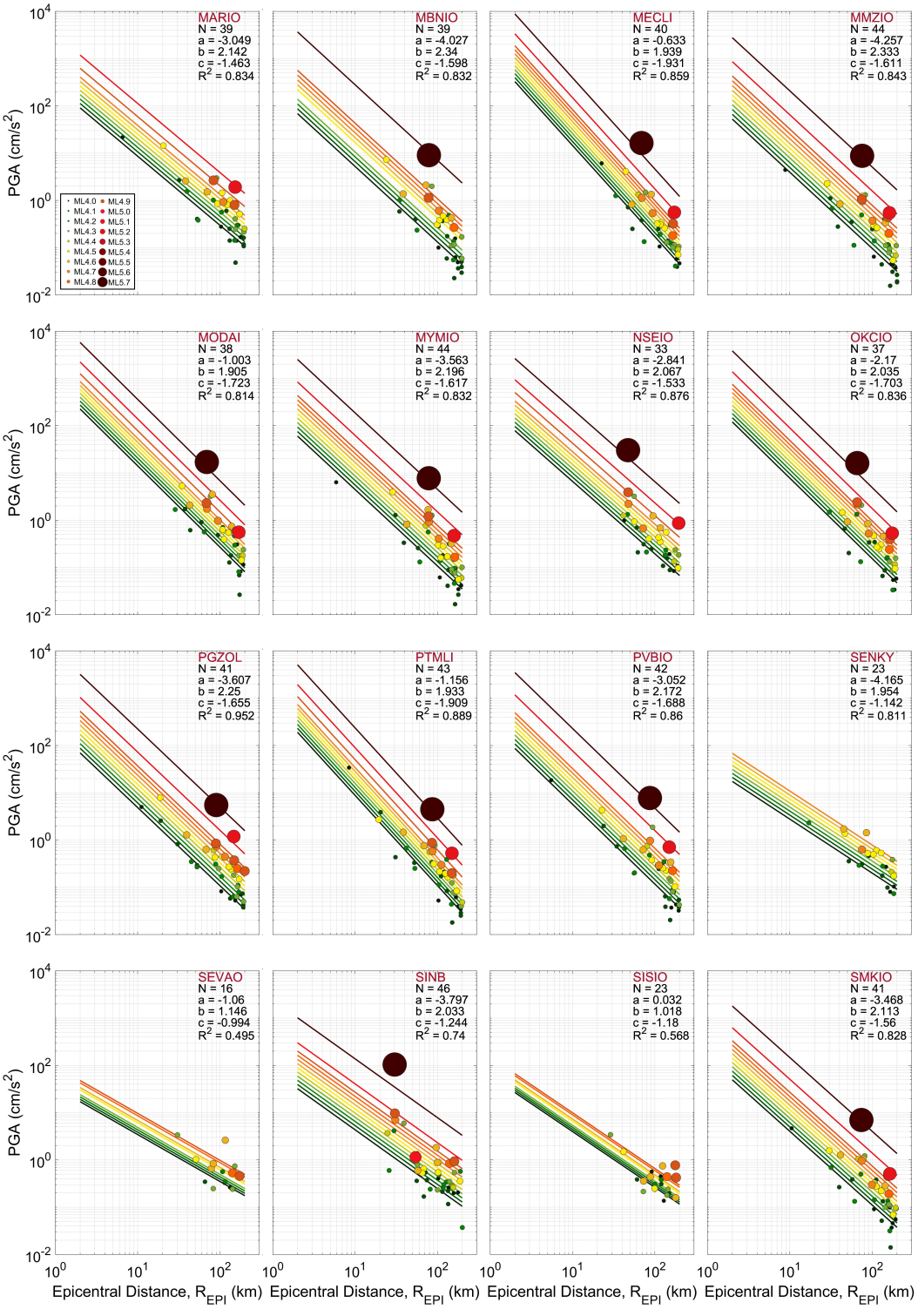


Figure B.4. Distance Scalings of the Functional Form (5.4) for All Stations (cont.).

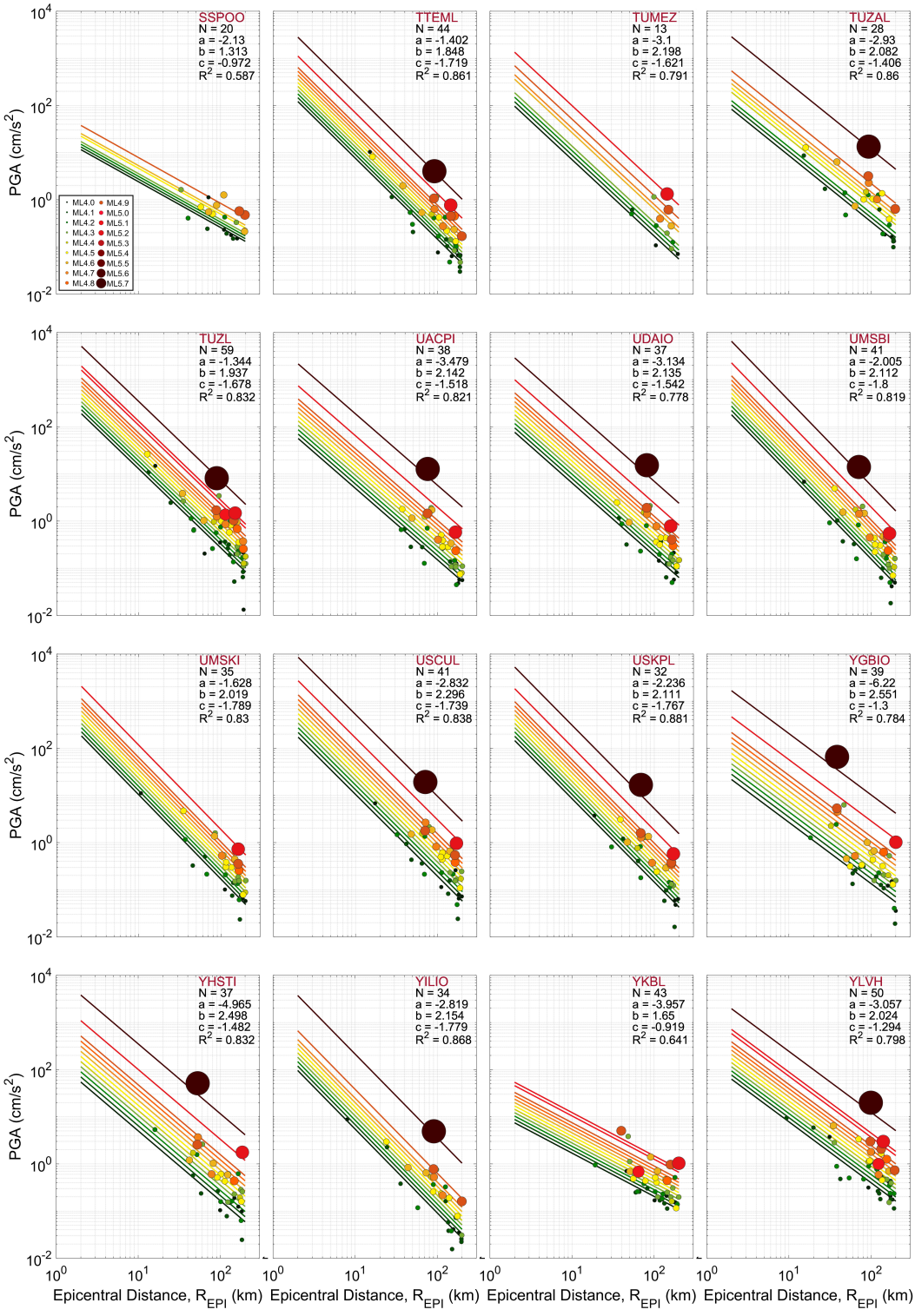


Figure B.5. Distance Scalings of the Functional Form (5.4) for All Stations (cont.).

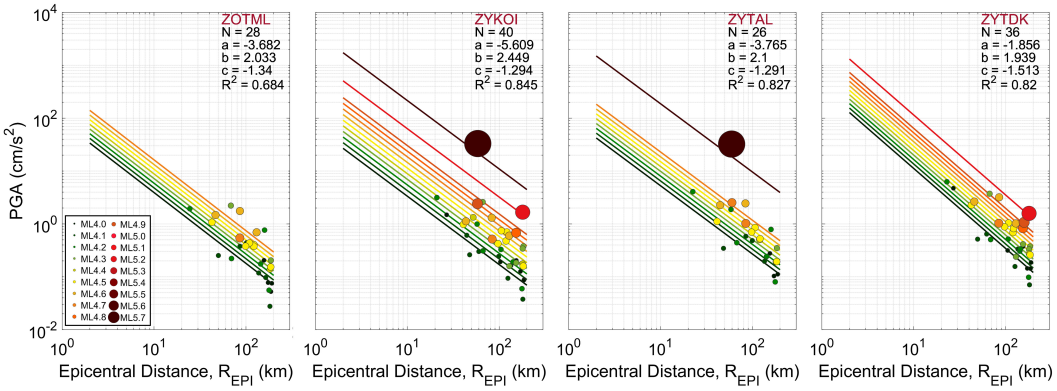


Figure B.6. Distance Scalings of the Functional Form (5.4) for All Stations (cont.).

APPENDIX C: RESULTS FOR FUNCTIONAL FORM (5.8) (f = 5.8)

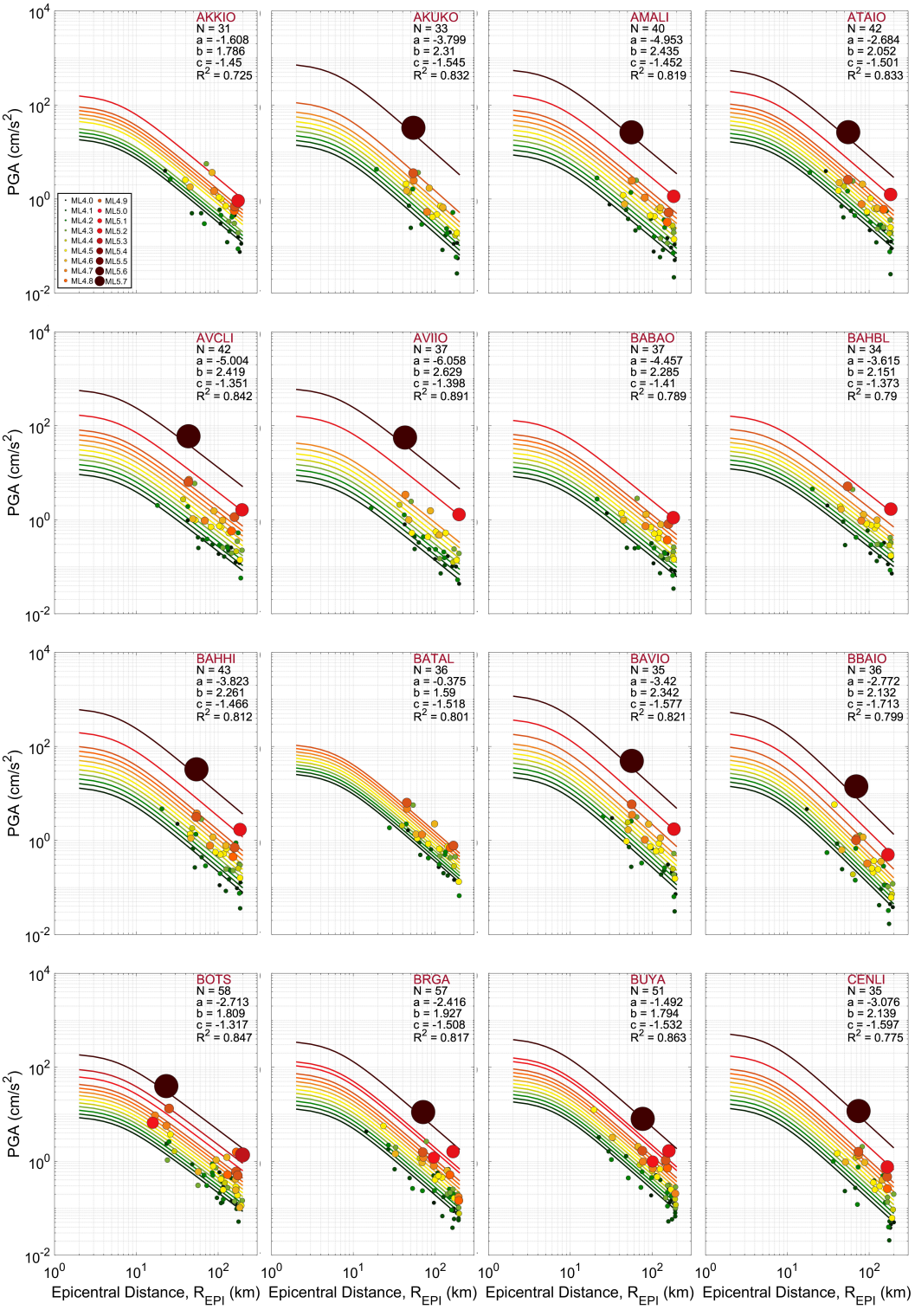


Figure C.1. Distance Scalings of the Functional Form (5.8) (f = 5.8) for All Stations.

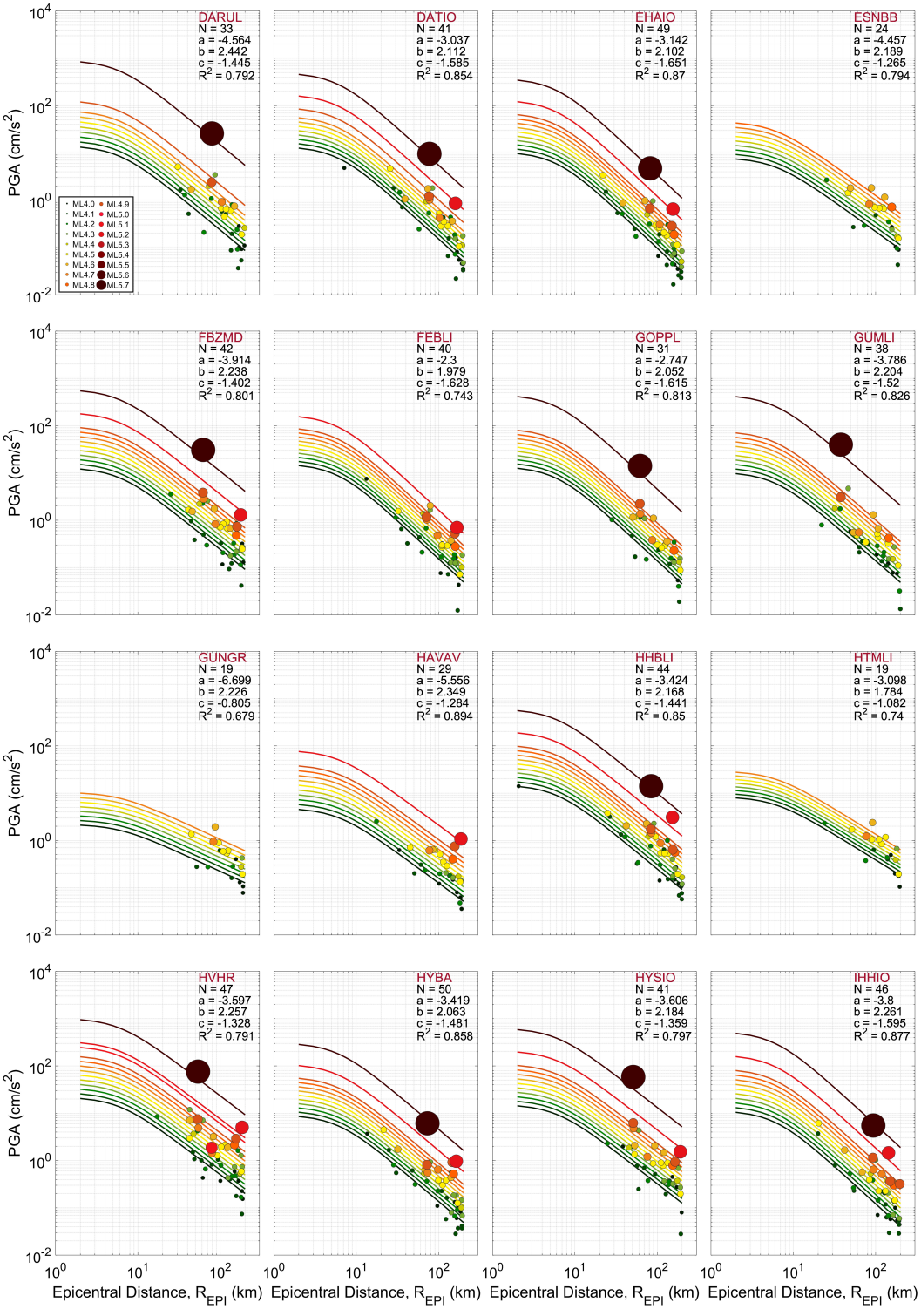


Figure C.2. Distance Scalings of the Functional Form (5.8) (f = 5.8) for All Stations (cont.).

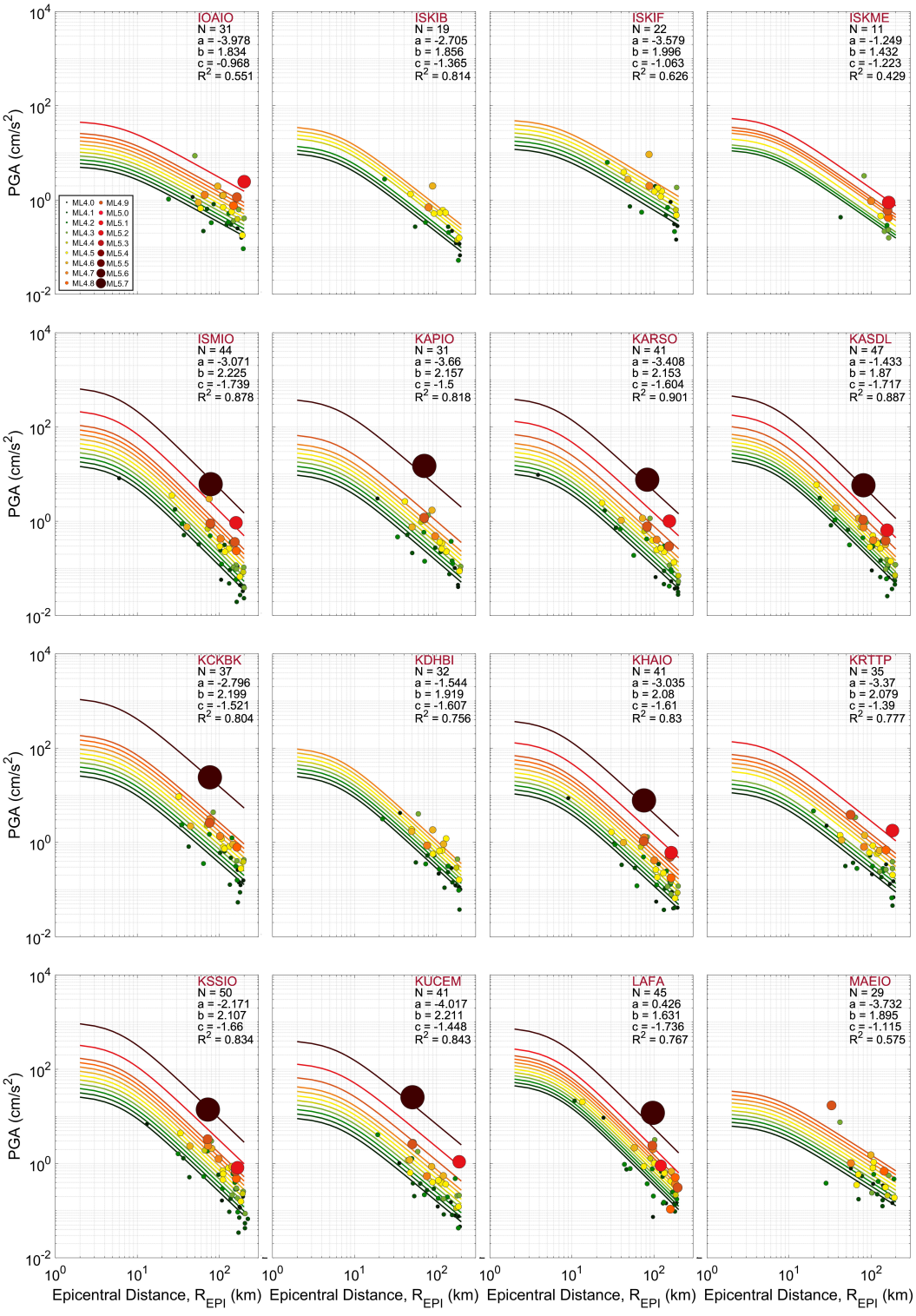


Figure C.3. Distance Scalings of the Functional Form (5.8) (f = 5.8) for All Stations (cont.).

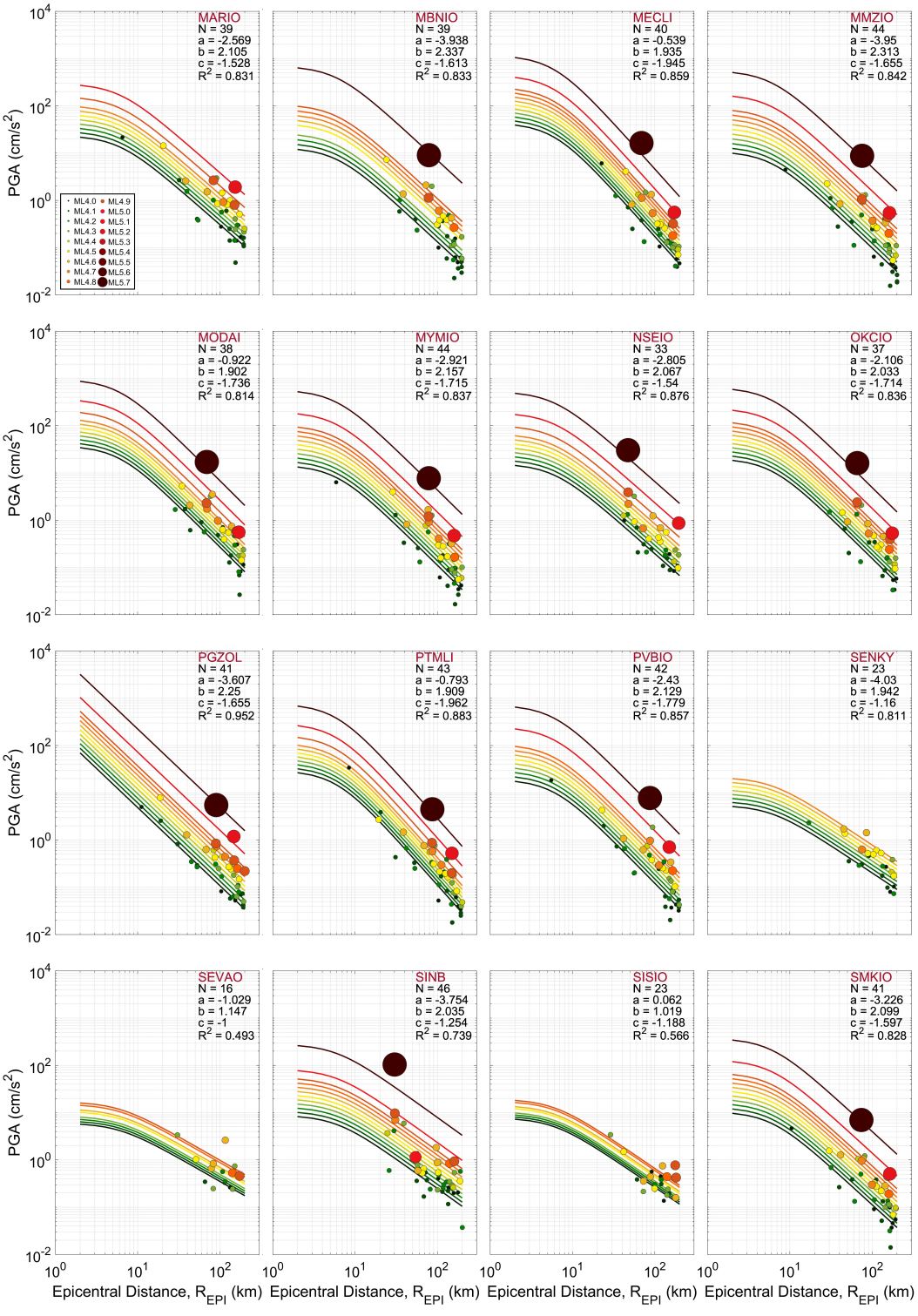


Figure C.4. Distance Scalings of the Functional Form (5.8) (f = 5.8) for All Stations (cont.).

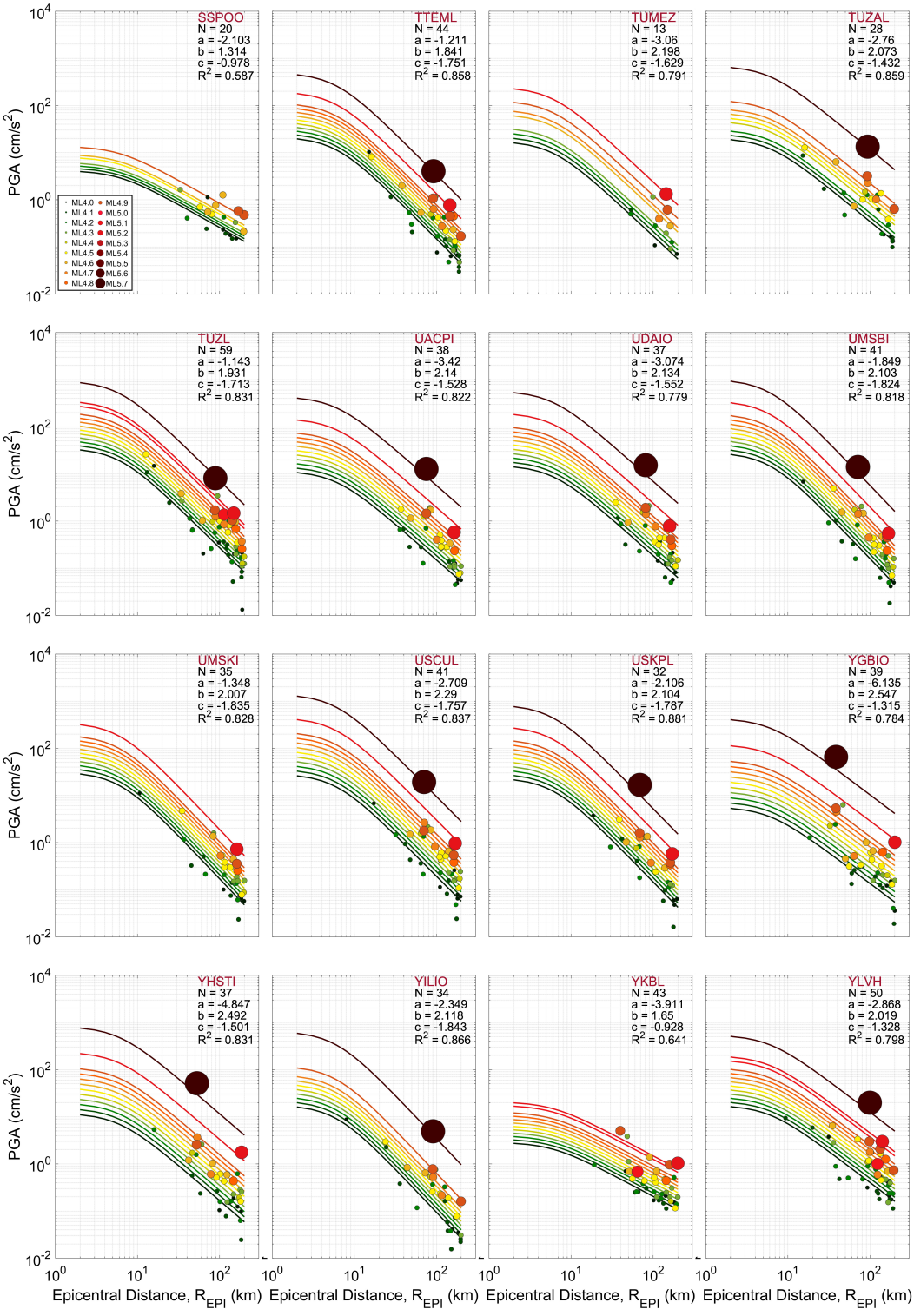


Figure C.5. Distance Scalings of the Functional Form (5.8) (f = 5.8) for All Stations (cont.).

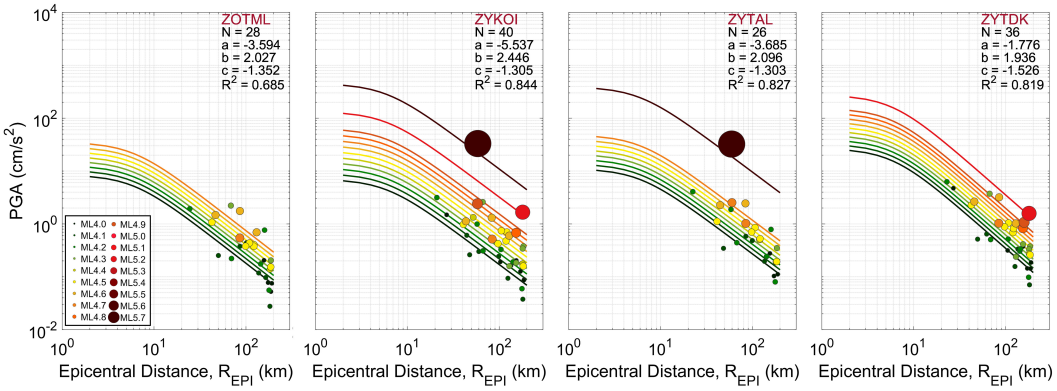


Figure C.6. Distance Scalings of the Functional Form (5.8) (f = 5.8) for All Stations (cont.).

APPENDIX D: RESULTS FOR FUNCTIONAL FORM (5.8) (HYBRID)

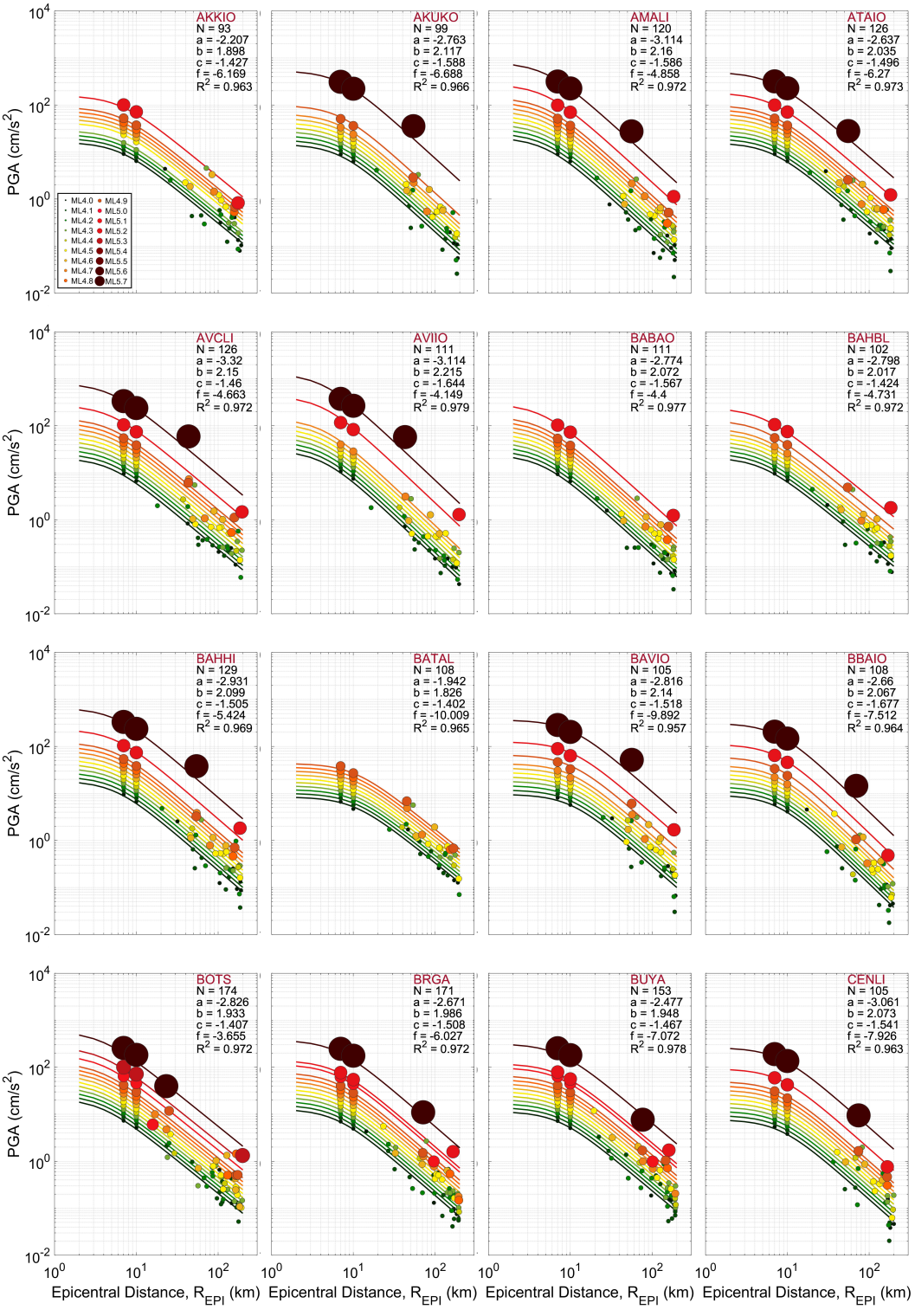


Figure D.1. Distance Scalings of the Functional Form (5.8) (hybrid) for All Stations.

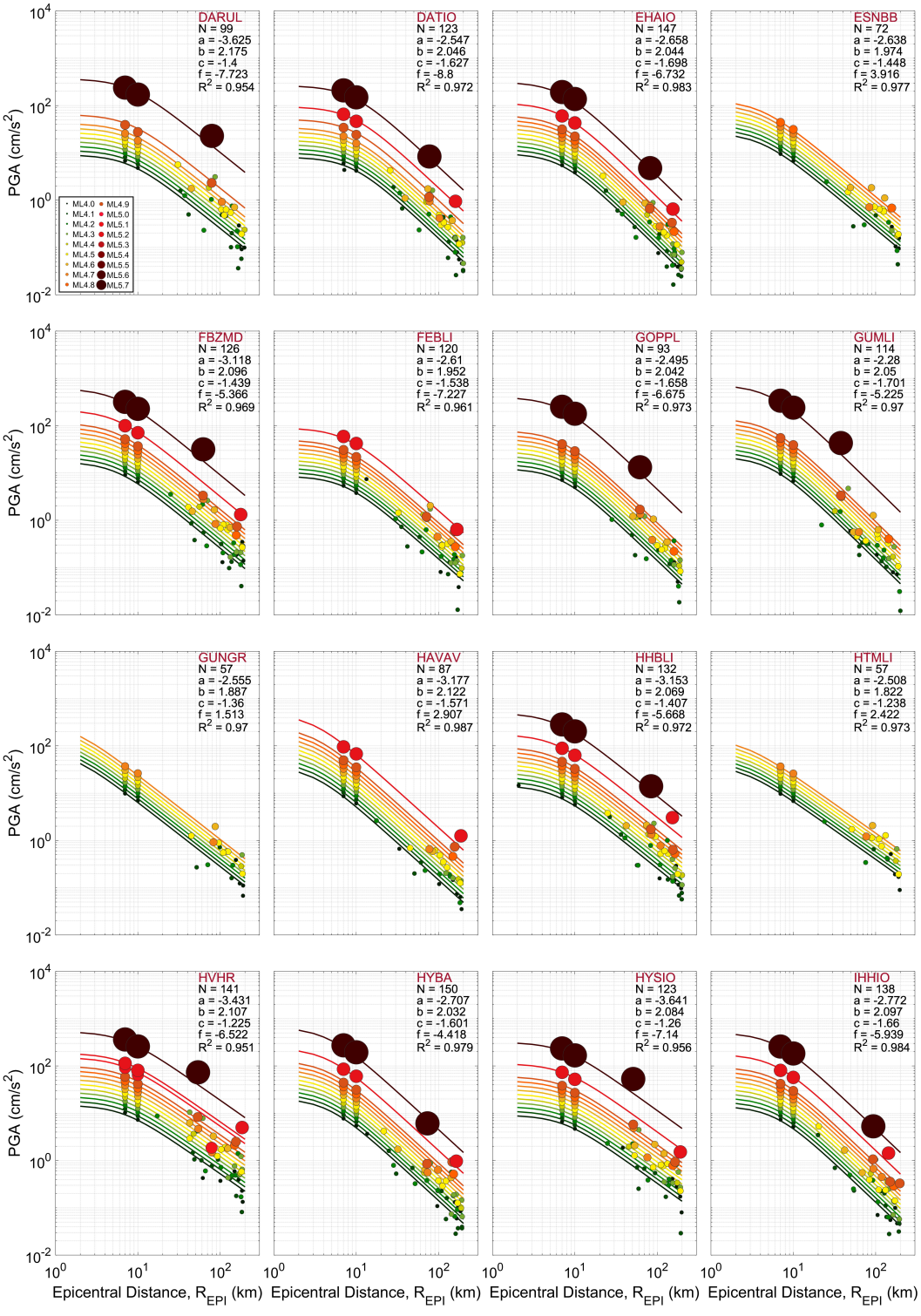


Figure D.2. Distance Scalings of the Functional Form (5.8) (hybrid) for All Stations (cont.).

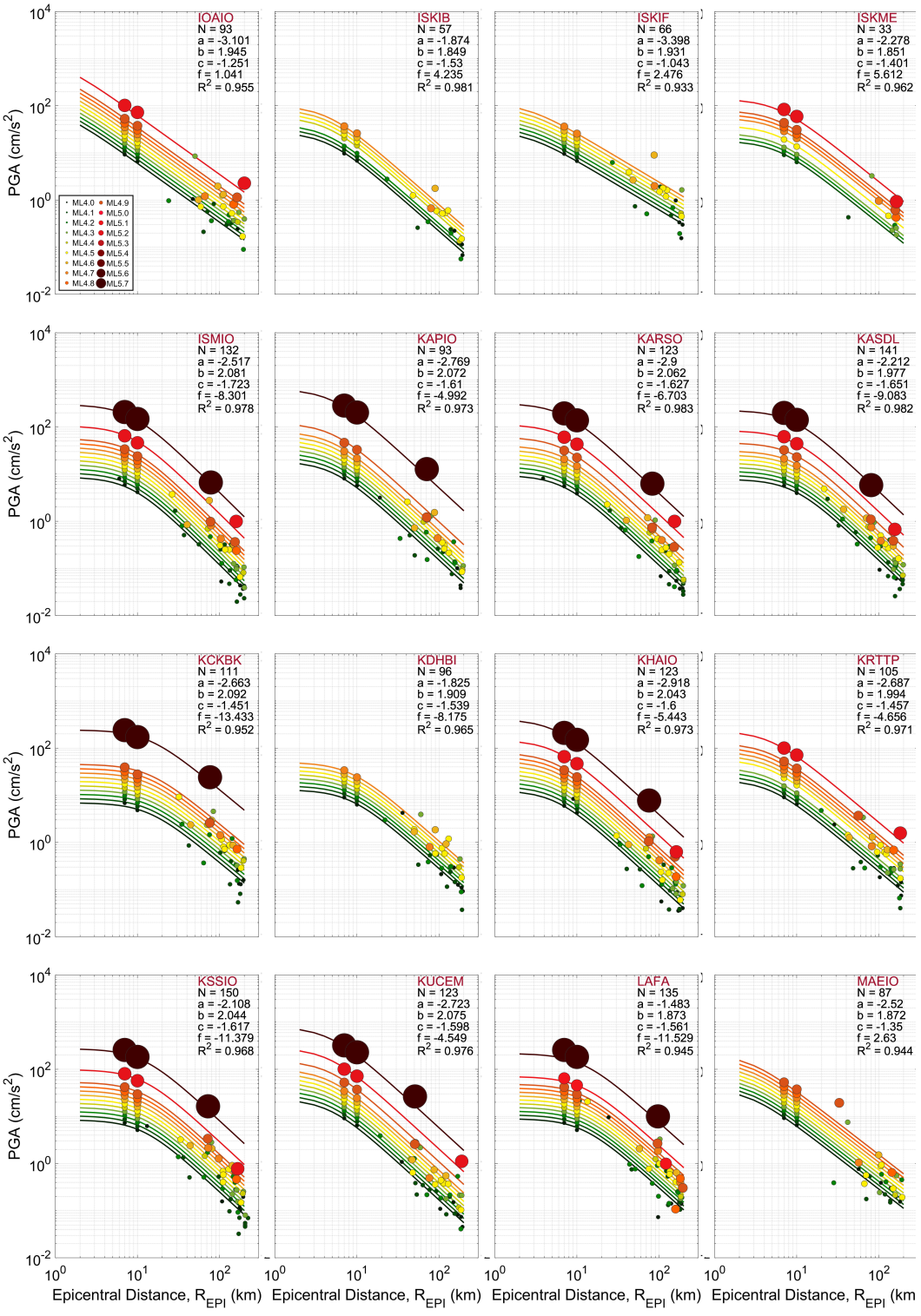


Figure D.3. Distance Scalings of the Functional Form (5.8) (f = 5.8) for All Stations (cont.).

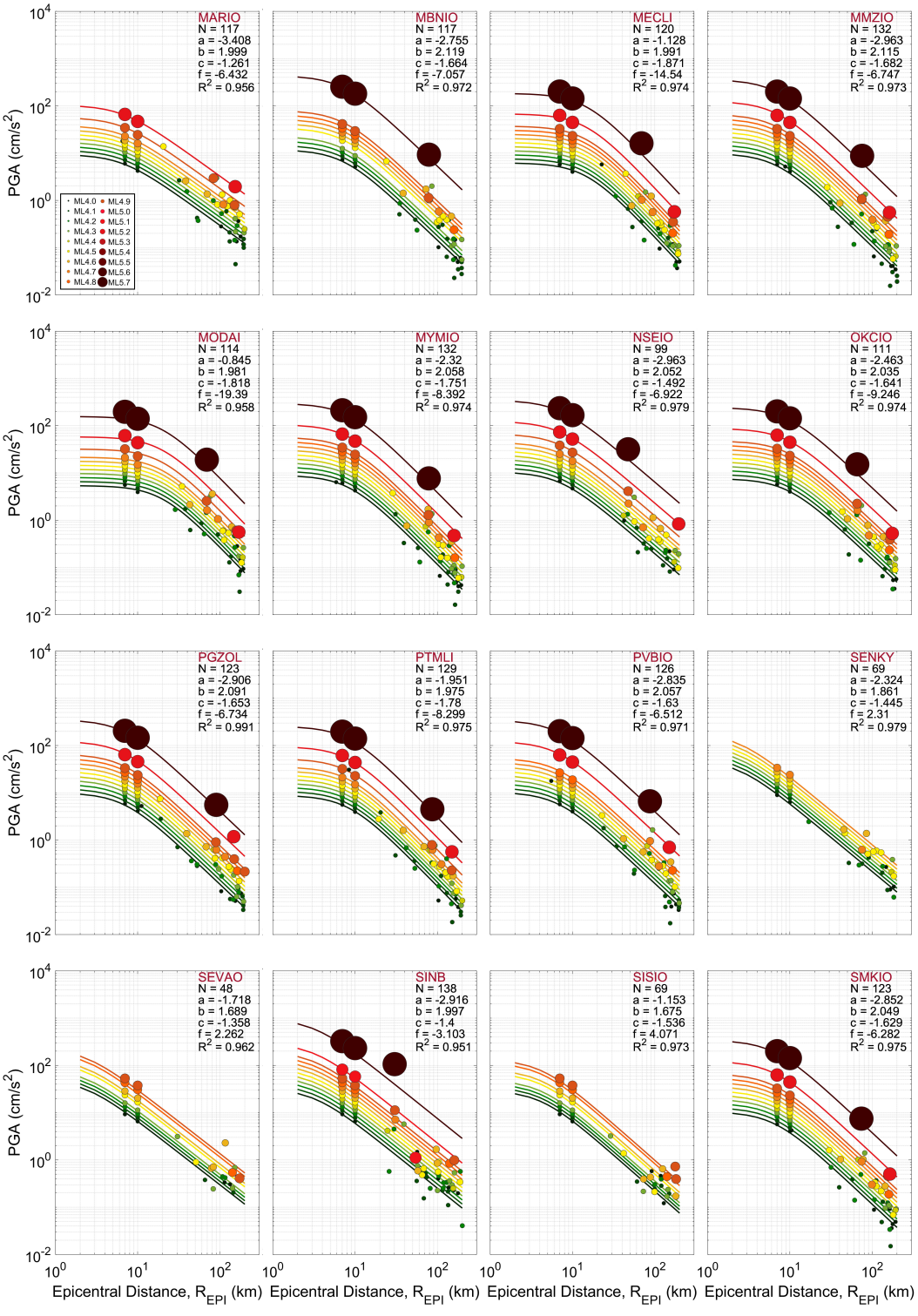


Figure D.4. Distance Scalings of the Functional Form (5.8) (f = 5.8) for All Stations (cont.).

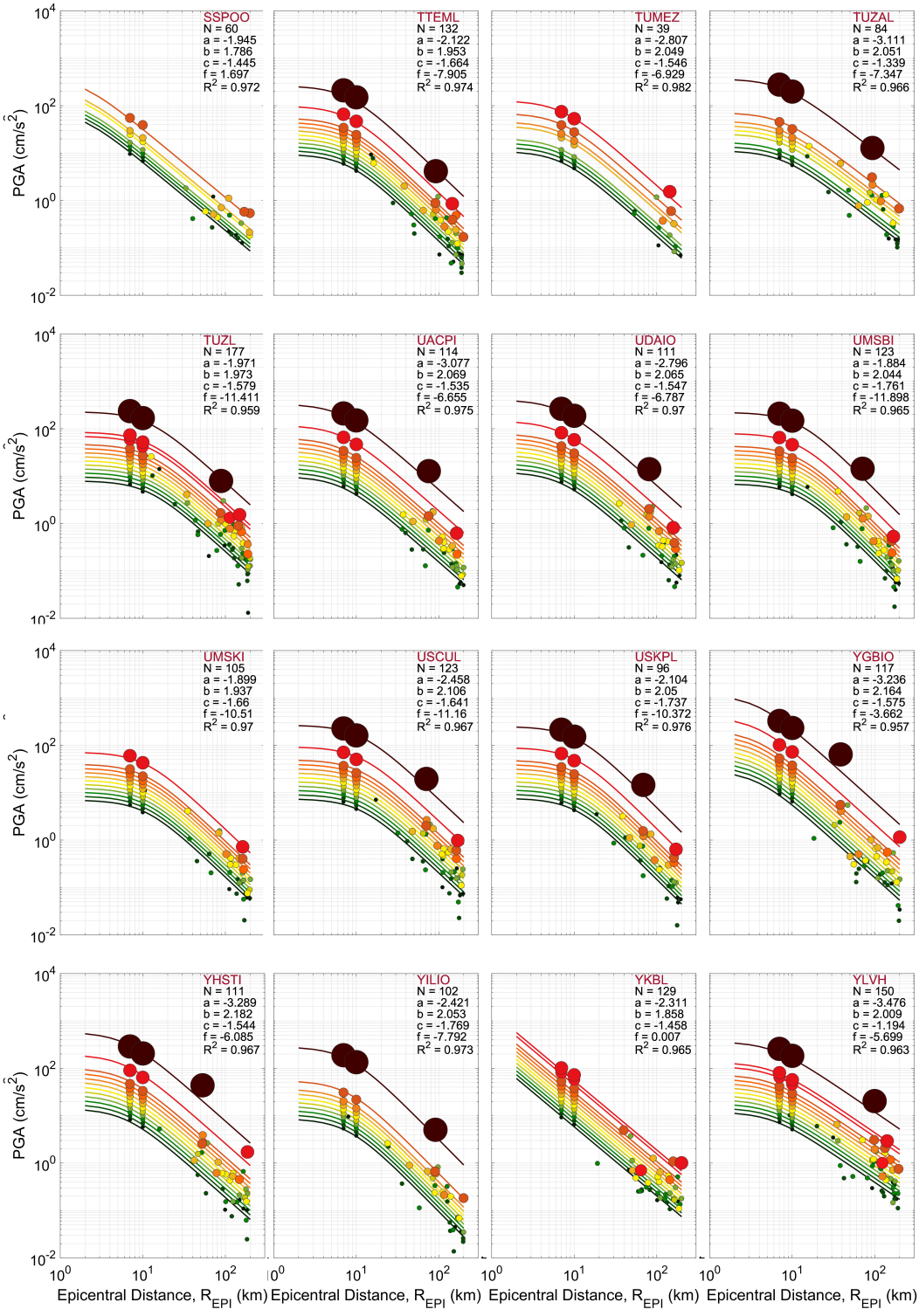


Figure D.5. Distance Scalings of the Functional Form (5.8) (f = 5.8) for All Stations (cont.).

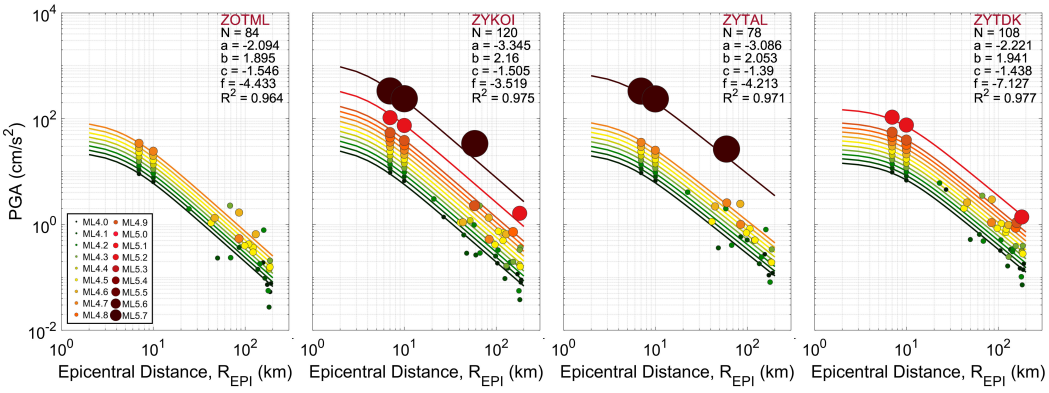


Figure D.6. Distance Scalings of the Functional Form (5.8) (f = 5.8) for All Stations (cont.).